Alpha-event characterization for germanium detectors

Garbini Lucia

München 2016

Alpha-event characterization for germanium detectors

Garbini Lucia

Dissertation
an der Fakultät für Physik
der Ludwig–Maximilians–Universität
München

vorgelegt von
Garbini Lucia
aus Umbertide (PG)

München, den 17 März, 2016

Erstgutachter: Prof. Dr. Jochen Schieck
Zweitgutachter: Prof. Dr. Thomas Kuhr
Tag der mündlichen Prüfung: 2 Mai, 2016

Zusammenfassung

Eine detaillierte Studie alpha-induzierter Ereignisse auf der passivierten Oberfläche eines Germaniumdetektors wird präsentiert. Germanium Detektoren werden sowohl bei der Suche nach neutrinolosem Doppelbetazerfall von ^{76}Ge als auch bei der Suche nach Dunkler Materie eingesetzt. Um die Sensitivität über das in den heutigen Experimenten erreichte hinaus zu verbessern, ist es nötig die aktive Masse der Experimente um eine Größenordnung auf eine Tonne zu steigern und gleichzeitig den Untergrund um eine Größenordnung zu reduzieren. Die Auswahl der Detektoroptionen, um beide Suchen zu ermöglichen und den Untergrund zu reduzieren, ist eine der großen Herausforderungen für solch ein Experiment. Oberflächenkontaminationen auf Materialien in der nahe Umgebung der Detektoren oder auf den Detektoren selber führen oft zu Untergründen, die in einigen Fällen die Sensitivität von Experimenten begrenzt haben.

Die Charakterisierung von alpha-induzierten Ereignissen birgt die Möglichkeit, sie im Experiment als solche zu erkennen und sie auf diese Weise als Untergrund zu eliminieren. Ein speziell für solche Studien konzipierter segmentierter vollständig koaxialer Detektor wurde im GALATEA Teststand des MPI für Physik in München mit Hilfe einer ^{241}Am Quelle untersucht. Zur Charakterisierung der alpha-induzierten Ereignisse wurden Pulsformanalysen durchgeführt. Die Eigenschaften des Detektors im Volumen direkt unter der passivierten Endplatte wurden ebenfalls untersucht. Ein Teil dieser Untersuchung war die Bestimmung der effektiven Totzone des Detektors. Die hier vorgelegten Studien suggerieren, dass gewisse Veränderungen im Detektordesign zur Verbesserung der Identifikation von alpha-induzierten Ereignissen in germaniumbasierten Experimenten führen würden.

Abstract

A detailed study of alpha interactions on the passivated surface of a germanium detector is presented. Germanium detectors can be used to search for both neutrinoless double beta decay of ^{76}Ge and direct interaction of dark matter. In order to increase the sensitivity to both neutrinoless double beta decay and dark matter beyond the current state of the art, the next generation of germanium-based experiments has to have a mass of about one ton and has to reduce the background by a factor of ten. The choices of detector technology facilitating both searches and the background reduction are one of the biggest challenges for such an experiment. Surface contaminations on the material close to the detectors or on the detectors themselves, can generate a background due to alpha particles, which was found to be limiting in some experiments.

The characterization of events induced by alpha particles will help to identify such events and thus eliminate them as sources of background. An especially designed segmented true-coaxial detector was probed with alpha particles from an ^{241}Am source inside the test-stand GALATEA, located at the MPI für Physik in Munich. Pulse shape analysis was performed to identify the characteristics of alpha events. The properties of the detector directly underneath the passivation layer on the end-plate were also studied. As part of the detector characterization, the thickness of the effective dead layer was determined.

The studies presented here suggest improvements on detector design, which would allow an effective reduction of alpha background in next generation of germanium-based experiments.

"Nobody said it was easy!!"
Coldplay, The Scientist
A Rush of Blood to the Head
2002

Contents

List of Figures

List of Tables

Introduction

This thesis presents a detailed study of interactions of alpha particles on the surface of a germanium detector. The work was carried out as a part of an R&D project targeting the development of novel germanium detectors for basic research in experimental physics.

One of the main goals of experimental physics is to test the Standard Model (SM), which is one of the most successful theories ever formulated for particle physics. Phenomena like neutrino oscillations and the existence of Dark Matter require at least an extension of the SM.

The neutrinos of the SM are neutral massless particles. The observation of neutrino oscillations [1,2], for which Ray Davis in 2002 and Arthur B. McDonald and Takaaki Kajita in 2015 received Nobel prizes, shows that neutrinos have finite masses. Since only mass differences can be determined from oscillation experiments, the absolute neutrino mass scale is still unknown. Furthermore, the question whether neutrinos are Majorana or Dirac particle is still without an experimental answer.

The SM was formulated to describe the phenomena associated with known "visible" matter. The existence of a "non-visible" Dark Matter (DM) was proven through its gravitational interaction with visible matter at different cosmological scales [3]. However, the nature of DM is still unknown. A wide variety of possible DM candidates have been proposed over the past years. The most studied DM candidates are Weakly Interacting Massive Particles (WIMPs), for which stringent limits on the WIMP-nucleon cross section depending on the WIMP mass have been set.

Both the neutrino and the DM sector can be investigated using germanium detectors. Lepton Number Violation (LNV), the nature of neutrinos and the neutrino mass hierarchy can be probed searching for neutrinoless double beta ($0\nu\beta\beta$) decay of the isotope ^{76}Ge [4]. Low recoil-energy interactions of DM can be searched using low-threshold germanium detectors [5].

The latest result on $0\nu\beta\beta$ decay obtained with a germanium-based experiment was published in Summer 2013 by the GERDA collaboration, who obtained a lower limit on the half life of ^{76}Ge of $\mathcal{T}^{0\nu}_{1/2} > 2.1 \times 10^{25}$ y [6]. The latest germanium-based result on direct DM searches was published in 2015 by the CDMS collaboration who obtained a limit on the WIMP-nucleon spin-independent scattering cross-section of $1.8 \cdot 10^{-44}\,\mathrm{cm}^2$ ($1.18 \cdot 10^{-41}\,\mathrm{cm}^2$) for a 60 GeV (8.6 GeV) WIMP mass [7].

If the background is sufficiently low, the experimental sensitivity, both to $0\nu\beta\beta$ and DM searches, increases with the exposure of the experiment. The next generation of

germanium-based experiments has to have an about 10 times increased mass of about one ton. At the same time, the background rate has to be reduced by at least a factor 10. One of the challenges is the development of new detector technologies which combine the different experimental requirements for $0\nu\beta\beta$ and DM searches. The second challenge is the reduction of background. Deep underground laboratories such as CJPL [8] and SNOLAB [9] guarantee an effective reduction of the background coming from cosmic rays. Radiopure materials are available to shield the germanium detectors from environmental neutrons and gammas. However, the reduction of the radiation from the materials close to the detectors like from their holders and from the detector surfaces remains a major challenge. One of the biggest problems, often creating an irreducible background, is alpha radiation. Alpha particles are produced in the decay of polonium and lead contaminating either the detector surfaces or the components close to the detectors.

The first goal of the work presented here was to characterize events induced by alpha particles interacting on the passivated surfaces of germanium detectors. To achieve this goal, an especially designed segmented true-coaxial detector was probed with alpha particles from an ^{241}Am source.

The second goal was to determine the detector properties just below the passivated surface of a true-coaxial detector, especially underneath the end-plates where charge trapping is expected. The determination of the thickness of the dead layer was part of this goal. This is also important for the evaluation of the active volume which is crucial for both $0\nu\beta\beta$ and DM searches.

The measurements were performed with a special test detector in the GALATEA [10] test-facility located at the MPI für Physik, Munich. GALATEA was designed to operate germanium detectors in vacuum. Its most innovative aspect is the possibility to have radioactive sources inside the vacuum tank, thereby allowing the probing of detectors with low penetrating sources like alpha or beta emitters. A system of three motors moves radioactive sources to perform full 3D scans. The task of finalization and commissioning of the GALATEA test-stand was a major part of the work on which this thesis is based.

The thesis is structured as follows:

chapter 1: an overview of the open questions in particle physics is given. The chapter focuses mainly on neutrinos and Dark Matter;

chapter 2: experimental aspects of both $0\nu\beta\beta$ and DM searches with germanium detectors are discussed. Results from past experiments are presented. Running and future experiments are introduced;

chapter 3: basic concepts about interaction between radiation and matter are discussed. The main characteristics of germanium detectors are introduced. The detectors used to perform measurements presented in this thesis are briefly described;

chapter 4: the GALATEA test-stand is briefly described. Background and calibration measurements performed to check the stability and reliability of the test-stand are discussed in detail;

chapter 5: the energy calibration of segmented germanium detectors developed for the measurements presented here is described. Origin and effects of the cross talk are discussed. A fully automized and robust calibration procedure is presented. Emphasis is given to the presence of events with charge trapping, which bias the determination of cross talk;

chapter 6: the basic concepts of the Pulse Shape Analysis are introduced. The processing of the pulses is discussed. Parameters to characterize pulses are introduced. Events with charge trapping are discussed in detail;

chapter 7: the choice of an ^{241}Am source to probe the detector surfaces is motivated. The signature of alpha events on the surface is given and first evidence for such events is presented;

chapter 8: a review of the results based on data from a 2-D scan of the upper end-plate of the test detector is given. Alpha events are characterized. Pulse Shape Analysis is used to examine zones of low electric field and quantify the effects of charge trapping. The thickness of the dead layer and its dependence on the radius are extracted. The consequences for $0\nu\beta\beta$ experiments are discussed.

Chapter 1

Open questions in particle physics

The Standard Model (SM) [11–13] is one of the most successful theories ever conceived for particle physics. It was developed in the early 1970s by S. L. Glashow, S. Weinberg and A. Salam. It describes matter in terms of fundamental particles (fermions and gauge bosons) and fundamental forces (electro-weak and strong forces). It has successfully described most of the experimental results in particle physics and predicted a wide variety of phenomena. Over time, the SM has become a well-tested theory (e.g. [14] and references therein). One of the latest successes was the discovery of the Higgs boson in July 2012 at the LHC, both by CMS [15] and ATLAS [16].

Even though the SM is currently the best description particle physicists have of the subatomic world, it is not complete. There is experimental evidence like neutrino oscillations or the existence of dark matter which require at least an extension of the SM framework. Both the neutrino and the dark matter sector can be investigated using germanium detectors. Lepton Number Violation (LNV), the nature of neutrinos and the neutrino mass hierarchy can be probed searching for neutrinoless double beta decay of the isotope ^{76}Ge (e.g. [4]). Improved knowledge of the description of the neutrino oscillation patterns, including active-to-sterile neutrino oscillations, could be obtained using neutrino coherent scattering on germanium nuclei [17]. Low recoil-energy interactions of dark matter with germanium would shed light on the nature of dark matter (e.g. [5]).

In this chapter, the neutrino and dark matter sectors are briefly introduced. In Sec. 1.1.1, neutrinos are described in the SM framework. Features of neutrinos not explained in the SM framework are described in Sec. 1.1.2. In Sec. 1.2.1, astrophysical and cosmological evidence for the existence of dark matter is reported. A selected list of possible candidates for dark matter detectable with germanium detectors is found in section 1.2.2.

1.1 Neutrinos

The existence of neutrinos was postulated by W. Pauli in 1931 to explain the spectra observed for nuclear beta decay without challenging energy conservation. The spectra measured for beta decay were not typical 2-body decay spectra with peaks at the Q-values

of the decays. Observed were continuum spectra up to the Q-values, characteristic for 3-body decays:

$$(Z, A) \rightarrow (Z + 1, A) + e^- + \bar{\nu_e} \ . \tag{1.1}$$

The particle emitted together with the electron had to be an electrically neutral fermion in order to conserve charge and spin. The name "neutrino" was chosen by E. Fermi after the discovery of the neutron by J. Chadwick and collaborators [18]. Only in 1956, C. L. Cowan and F. Reines experimentally confirmed the existence of neutrinos [19]. The experiment was performed in a shallow underground laboratory in the Savannah river nuclear plant, only about 10 m away from the reactor core. The anti-electron neutrinos produced in the reactor were detected via inverse beta decay:

$$\bar{\nu_e} + p \rightarrow n + e^+ \ . \tag{1.2}$$

The signature of this interaction was the coincidence of the two photons produced by e^+e^- annihilation in the detector material and the photon produced in the de-excitation of Cadmium after neutron capture.

1.1.1 Neutrinos in the Standard Model

At the time of the development of the SM, neutrinos were thought to be massless Dirac particles. In the SM, there are three[1] families of quarks and leptons. Each family contains a charged lepton l and its neutrino partner ν_l. The internal symmetry which describes the electroweak interaction is a combination of two gauge groups $SU(2)_L \times U(1)_Y$. The corresponding quantum numbers are the electroweak isospin T_3 and the hypercharge Y, connected trough the Gell-Mann-Nishijima relation:

$$Q = T_3 + Y \ , \tag{1.3}$$

where Q is the electric charge. According to the symmetry, the families of leptons are grouped in a left handed doublet and a right handed singlet like:

$$\begin{pmatrix} l^- \\ \nu_l \end{pmatrix}_L \ , \ l_R \, . \tag{1.4}$$

Right handed neutrinos do not exist in the SM.

The lepton number is defined for each flavour l as:

$$L_l = n_l - n_{\bar{l}} \, , \tag{1.5}$$

where n_l is the number of leptons (charged and neutral) and $n_{\bar{l}}$ is the number of anti-leptons. This quantum number is found to be conserved in electro-weak interactions. New limits on lepton-number violation can be found in [22].

[1] The number of light neutrinos can be inferred from measurements of the decay width of the Z^0 gauge boson done at LEP [20] and SLC [21]

1.1.2 Neutrino oscillations

Over time, the description of neutrinos as given in the SM was found to be insufficient to explain all phenomena. The first evidence that neutrinos can oscillate was found studying the solar and atmospheric neutrino fluxes.

Solar neutrino problem

A large amount of electron neutrinos are produced in the sun in its nuclear reaction chains. The main reactions of the pp chain are listed in Table 1.1 together with the corresponding neutrino fluxes and neutrino energies predicted by the Standard Solar Model (SSM) [23]. Reactions with Carbon, Nitrogen and Oxygen (CNO) are omitted because of their relatively low contribution to the solar luminosity and the neutrino fluxes.

	Reaction	Flux $[cm^{-2}s^{-1}]$	E_ν[MeV]
pp	$p + p \rightarrow {}^2\mathrm{H} + e^+ + \nu_e$	$5.99(1.00 \pm 0.01) \cdot 10^{10}$	$\leqslant 0.42$
pep	$p + e^- + p \rightarrow {}^2\mathrm{H} + \nu_e$	$1.42(1.00 \pm 0.02) \cdot 10^{8}$	1.44
hep	${}^3\mathrm{He} + p \rightarrow {}^4\mathrm{He} + e^+ + \nu_e$	$7.93(1.00 \pm 0.16) \cdot 10^{3}$	$\leqslant 18.77$
^{7}Be	${}^7\mathrm{Be} + e^- \rightarrow {}^7\mathrm{Li} + \nu_e$	$4.84(1.00 \pm 0.11) \cdot 10^{9}$	0.86
^{8}B	${}^8\mathrm{B} \rightarrow {}^8\mathrm{Be}^* + e^+ + \nu_e$	$5.69(1.00 \pm 0.16) \cdot 10^{6}$	$\leqslant 15$

Table 1.1: List of the main reactions in the nuclear pp chain. For each reaction, the predicted neutrino flux and energy are given.

Figure 1.1 shows a comparison between the measured and predicted neutrino count rate for seven different experiments combined into 5 results. Depending on the energy threshold and on the detection technique of the experiment, different reactions in different proportion contribute to the total predicted flux. The ^{37}Cl experiment (R.J.Davis and collaborators [25]) shows one third of the predicted rate. The ^{71}Ga experiments, sensitive to the low energy solar neutrinos, show about half of the predicted rate (GALLEX [26], GNO [27] and SAGE [28] independently but in agreement). Similarly, water Čerenkov experiments, performing better with high energy solar neutrinos, show a measured rate lower than expected (Kamiokande [29] and super-Kamiokande [30]).

Both low and high energy neutrinos were observed to be missing but not to the same extent. The data were available before the year 2000 and suggested an oscillation scenario. However, only in June 2001, the Solar Neutrino Observatory, SNO, experiment was able to confirm it. Using heavy water (D_2O) as target material, it was possible to detect all neutrino flavours, i.e. also muon and tau neutrinos. The measured total neutrino flux was in agreement with the expected neutrino flux [1]. This result demonstrated that electron neutrinos created in the nucleus of the sun changed their flavour along the path to the earth. In October 2015, the Nobel prize in Physics was awarded to Arthur B. McDonald as the head of the SNO collaboration at the time of the discovery of neutrino oscillations.

Already in 1969 B. Pontecorvo and V. Gribov [31] postulated that lower energy solar neutrinos could change from electron neutrino to another type as they travel in the vacuum from the Sun to the Earth. At higher neutrino energies, the process of oscillation is enhanced by interactions with electrons in the Sun or in the Earth. This enhancement is known as the MSW effect, as it was proposed in the early 1980s by L. Wolfenstein [32], S. Mikheyev and A. Smirnov [33].

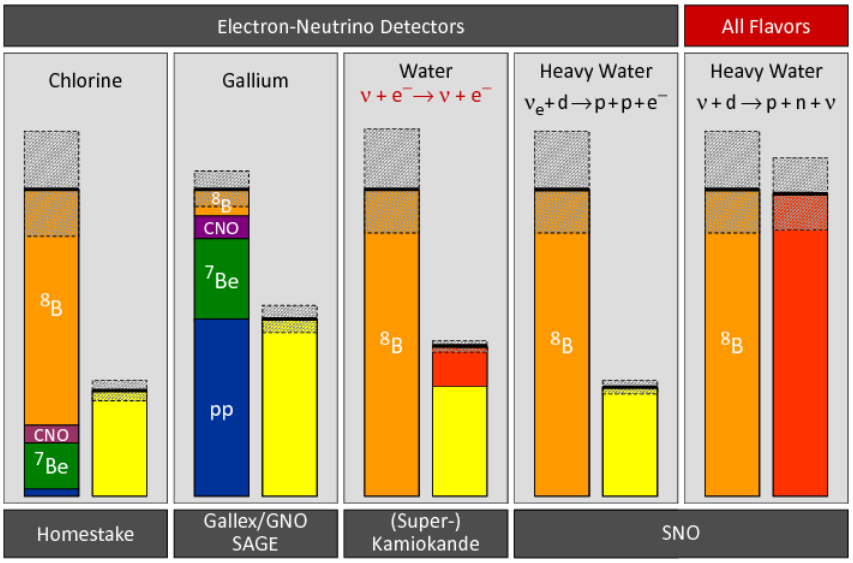

Figure 1.1: Solar neutrino predictions (left bars) and measurements (right bars) for seven solar neutrino experiments bundled in 5 results. For each experiment, the total prediction (in arbitrary units normalized to one) is shown with its error. The fractional contribution of different source reactions are shown in different colors. Each experimental result is shown with its uncertainty. Yellow experimental bars are for electron neutrinos, red bars for all flavors, from [24].

Atmospheric neutrinos anomaly

Cosmic rays interact in the upper atmosphere and create pions, kaons and other unstable particles that produce electron and muon neutrinos in their decays. Several experiments, born as proton decay experiments, measured atmospheric neutrino fluxes. What, at the beginning, was simply a source of background, became a central topic of investigation.

The double ration, R, for neutrino fluxes is defined as

$$R = \frac{\left(\Phi_{\nu_e}/\Phi_{\nu_\mu}\right)_{Data}}{\left(\Phi_{\nu_e}/\Phi_{\nu_\mu}\right)_{MC}} \ , \tag{1.6}$$

where

- $\left(\frac{\Phi_{\nu_e}}{\Phi_{\nu_\mu}}\right)_{Data}$ is the ratio between the measured electron and muon neutrino flux;
- $\left(\frac{\Phi_{\nu_e}}{\Phi_{\nu_\mu}}\right)_{MC}$ is the ratio between the expected electron and muon neutrino flux.

Figure 1.2 shows R for several experiments. The first experiments showing a double ratio significantly differing from 1 were water Čerenkov detectors: Irvine-Michigan-Brookhaven detector (IBM) [35] in the US and Kamiokande in Japan [36]. This discrepancy was not confirmed by European tracking calorimeters like NUSEX [37] and Frejus [38]. Only after the results obtained by the Soudan collaboration [39] were presented, it became evident that the deficit in the muon

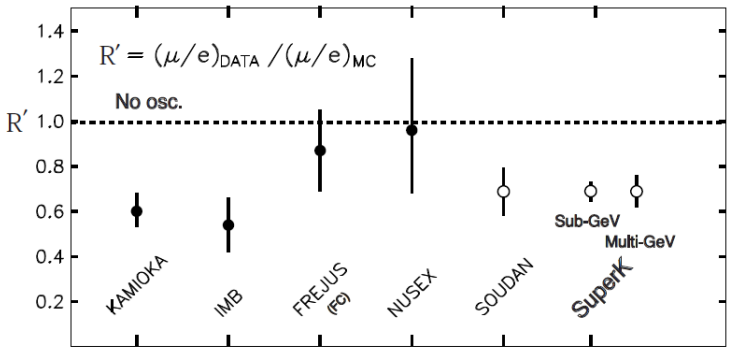

Figure 1.2: Comparison of measured double ratios for different experiment with the expected value of 1, from [34].

neutrino flux was not an artefact of Čerenkov detectors, but a real physics effect that needed an explanation. The solution to this puzzle came from the Super-Kamiokande collaboration [2, 40]. The deficit in the muon neutrino flux was demonstrated to occur only for upward-going muons, where the neutrinos had passed through the Earth before interacting. Muon neutrinos produced in the atmosphere oscillate to tau neutrinos travelling through the earth. The Super-Kamiokande analysis of 1998 provided the discovery of a second kind of neutrino oscillation. In October 2015, the Physics nobel prize was awarded to Takaaki Kajita as the head of the Super-Kamiokande collaboration at the time of the discovery of atmospheric neutrino oscillations.

Oscillation formalism

Neutrino oscillations can be described as a periodic change of neutrino flavours with time, and therefore, with the distance from the production point of the neutrinos. A neutrino produced as ν_α becomes ν_β after some propagation. The Feynman diagram that describes this process is depicted in Fig. 1.3.

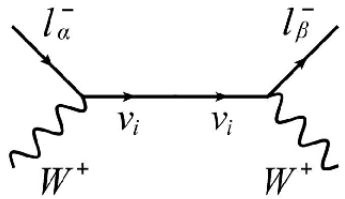

Figure 1.3: Feynman diagram for ν_i production and detection resulting in observed ν_α-ν_β oscillation, with ν_i being the mass eigenstate which propagates in time, from [41].

Neutrinos can only oscillate from one flavor state to another if they have masses. Neutrino flavor eigenstates (ν_α, with $\alpha = e$, μ, τ) are superpositions of three different mass eigenstates (ν_i

with $i = 1, 2, 3$):

$$|\nu_\alpha\rangle = \sum_i U^*_{\alpha,i} |\nu_i\rangle \ , \tag{1.7}$$

where U_{ij} is a unitary matrix, usually called Pontecorvo-Maki-Nakagawa-Sakata (PMNS) matrix [42]. One of the possible representations of U_{PMNS} is

$$U_{PMNS} = \begin{pmatrix} c_{12}c_{13} & s_{12}c_{13} & s_{13}e^{i\delta} \\ -s_{12}c_{23} - c12s_{13}s_{23}e^{i\delta} & c_{12}c_{23} - s_{12}s_{13}s_{23}e^{i\delta} & c_{13}s_{23} \\ s_{12}s_{23} - c_{12}s_{13}c_{23}e^{i\delta} & -c_{12}s_{23} - s_{12}s_{13}s_{23}e^{i\delta} & c_{13}c_{23} \end{pmatrix} \ , \tag{1.8}$$

where $c_{ij} = cos(\theta_{ij})$ and $s_{ij} = sin(\theta_{ij})$ are the cosine and the sine of the mixing angle between the ν_i and ν_j mass eigenstates respectively; δ is the Dirac CP phase, which quantifies the CP-violation in the lepton sector. The relation between the flavour eigenstates and the mass eigenstates, ignoring the phases, can be obtained as a product of three Euler rotations as depicted in Fig.1.4.

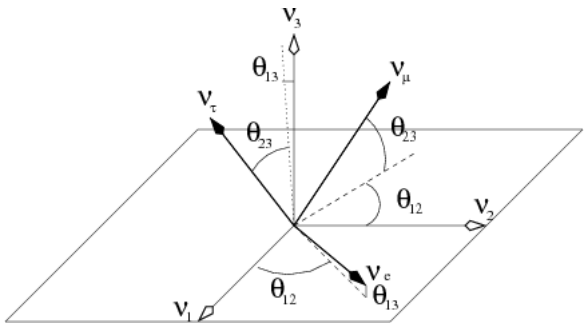

Figure 1.4: The relation between the neutrino flavour eigenstates ν_e, ν_μ and ν_τ and the neutrino mass eigenstates ν_1, ν_2 and ν_3 in terms of the three mixing angles θ_{12}, θ_{13}, θ_{23}, from [43].

The Feynman diagram for neutrino oscillation demonstrates (e.g. [44]) that a neutrino produced in the ν_α eigenstate becomes a superposition of all the flavour eigenstates, after travelling a distance L:

$$|\nu_\alpha(L)\rangle \approx \sum_\beta \left[\sum_i U^*_{\alpha,i} e^{-i\left(\frac{m_i^2}{2E}\right)L} \right] |\nu_i\rangle \ , \tag{1.9}$$

where m_i is the mass of the mass eigenstate ν_i and E is the average energy of the different mass eigenstates. The probability to find the ν_β eigenstate after a distance L is $|\langle\nu_\beta|\nu_\alpha(L)\rangle|^2$.

Both for solar and atmospheric neutrinos, oscillations can be described in a two-flavour framework. In this framework, the probability for change of flavour is (e.g. [44]):

$$P(\nu_\alpha \to \nu_\beta) = sin^2 2\theta sin^2\left(1.27\Delta m^2_{12}[eV^2]\frac{L[km]}{E[GeV]}\right) \ , \tag{1.10}$$

where θ is the mixing angle and Δm^2_{12} is the squared mass difference defined as $\Delta m^2_{12} = |m_1^2 - m_2^2|$.

Neutrino oscillations have not only been observed in solar and atmospheric neutrinos, but also in accelerator and reactor neutrinos. A complete and updated review of all the results on the neutrino oscillation parameters can be found in [45].

1.1.3 Neutrino masses

The discovery of neutrino oscillations proved that neutrinos have masses. The SM does not contain a right handed neutrino ν_R, which would be a singlet under the SM gauge groups, i.e. a sterile particle. It is however possible to introduce a "Dirac mass term" like for all the other fermions of the SM [46], thus introducing a sterile neutrino ν_R:

$$\mathcal{L}_{Yukawa} = -\frac{1}{2} y_{ij} \overline{L_i} \tilde{H} \nu_{jR} + h.c. \;\; \rightarrow \;\; -\frac{1}{2} v y_{ij} \overline{\nu_{iL}} \nu_{jR} + h.c. \,, \tag{1.11}$$

where y_{ij} is the Yukawa coupling describing the interaction between the SM Higgs doublet, the SM lepton doublet and the right handed neutrino, v is the vacuum expectation value (VEV) of the Higgs field and $v y_{ij} = (m_D)_{ij}$ is the Dirac mass of the neutrinos.

However, as neutrinos are the only neutral fermions in the SM, it is also possible to write a "Majorana mass term", represented by the Weinberg operator, without introducing a sterile neutrino [47]:

$$\mathcal{L}_{Weinberg} = -\frac{y_{ij}}{\Lambda} (\overline{L_i^C} \tilde{H}^*)(\tilde{H}^\dagger L_j) \;\; \rightarrow \;\; -\frac{v^2 y_{ij}}{\Lambda} \cdot \overline{(\nu_{iL})^C} \nu_{jL} \,, \tag{1.12}$$

where Λ is a new physics scale and $\frac{v^2 y_{ij}}{\Lambda} = (m_M)_{ij}$ is the Majorana mass of the neutrinos. This operator implies the existence of processes with LNV of 2 ($\Delta L = 2$) and that neutrinos are Majorana particles. Many other models to introduce neutrino mass terms are described in detail in [48] and references therein.

The oscillation experiments previously discussed measured the squared mass difference for the solar neutrinos, called "small splitting", to be $\Delta^2 m_{sol} \sim 7.50^{+0.19}_{-0.17} \cdot 10^{-5}$ eV^2 and for the atmospheric neutrinos, i.e. the "big splitting", the measurement was $\Delta^2 m_{atm} \approx 2.457^{+0.047}_{-0.047} \cdot 10^{-3}$ eV^2 [45]. The sign of Δm_{sol} is known to be positive due to the MSW effect in neutrino oscillations inside the dense sun. The sign of Δm_{atm} cannot be measured from oscillation experiments. Thus two different hierarchies are possible.

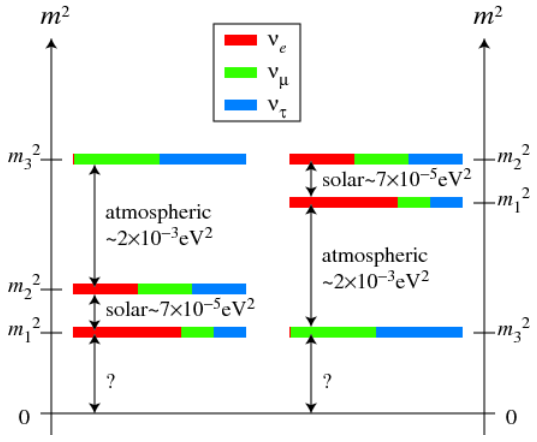

Figure 1.5: Comparison between the two possible neutrino mass hierarchies, from [43].

In Fig. 1.5, a comparison between the two hierarchies is shown. Neutrino mass eigenstates are represented as a mixture of flavour eigenstates. In both hierarchies, neutrinos are arranged

in a pair (ν_1, ν_2) with ν_1 being the lighter state, and a "lone" state ν_3 that can be either lighter or heavier than the pair. The absolute scale is not yet known.

There are mainly three ways to determine the absolute neutrino mass (e.g. [49] and references therein), i.e. cosmological constraints, direct measurements and neutrinoless double beta decay which will be discussed in detail in the next section 1.1.4. The investigations presented in this thesis aim to develop technology for such searches.

Cosmological constraints: The sum of the three neutrino masses is limited by the energy density of neutrinos at present which depends on the neutrinos decoupling temperature (e.g. [50] and references therein). In the early universe, neutrinos, as many other particles, were in thermal equilibrium: the production and annihilation rates were the same. The interaction rates governing the neutrino abundances dropped with the universe expanding. The neutrino freeze out temperature was a few MeV. Particles that freeze out stay at the temperature of the universe at their decoupling time. Taking into account the reheating of the photons at 1 MeV due to e^+e^- annihilation, the temperature of neutrinos today, $T^3_{\nu 0}$, can be expressed in terms of the temperature of photons today, $T^3_{\gamma 0}$, as:

$$T^3_{\nu 0} = \frac{4}{11} T^3_{\gamma 0} = \frac{n_{\gamma 0}}{2} \pi^2 \zeta(3), \tag{1.13}$$

where the $n_{\gamma 0}$ is the number density of the photons at present which can be obtained from Cosmic Microwave Background and structure formation data. Using the Gershtein-Zeldovich limit [51] on the energy density of neutrinos today, the upper bound on the sum of the three neutrino masses is found to be $\sum_i m_i < 0.194$ eV by the Planck collaboration [52].

Direct measurements:

Time-of-flight measurements: this is a method to directly measure the absolute mass of electron neutrinos. Time-of-flight measurements require a very long baselines experiments with very strong sources. These requirements are met only by cataclysmic astrophysical events like a core-collapse supernovae. From the observation of neutrinos from the supernova SN1987a in the Large Magellanic Cloud, upper limits of 5.7 eV/c^2 (95 % C.L.) [53–55] were determined.

Precision investigations of weak decays: The most sensitive and model-independent direct method to measure neutrino masses remains the investigation of the end-point region of β-decay spectra. If the charged lepton produced in a weak decay carries away all available kinetic energy, the neutrino is produced at rest, i.e. the end point of the spectrum provides information on the mass of the neutrino. Tritium is one of the best isotope for experiments targeting m_{ν_e}, because of its small Q-value of $Q = 18.6$ keV and small nuclear corrections:

$$^3\mathrm{H} \rightarrow {}^3\mathrm{He} + e^- + \bar{\nu_e}\,. \tag{1.14}$$

The experimental challenge is the rarity of events close to the end point of the spectrum. The Mainz collaboration published an upper limit on the electron neutrino mass of $m(\nu_e) < 2.3$ eV (95% C.L.) [56]. Another Tritium-based experiment, Troitsk, published an upper limit of $m(\nu_e) < 2.05$ eV (95 % C.L.) [57]. New results on the

neutrino mass are expected from KATRIN, a next-generation tritium-based experiment in the commissioning phase [58]. Its goal is a sensitivity of $m_{\nu_e} \lesssim 0.2$ eV. Limits on the mass of ν_μ come from pion decay measurements done at Paul Scherrer Institute (PSI) [59]. Limits on the mass of ν_τ come from tau decay studies, performed at ALEPH (LEP) [60]; they are currently $m_{\nu_\mu} < 0.17$ MeV (90% C.L.) and $m_{\nu_\tau} < 18.2$ MeV (95% C.L.).

1.1.4 Neutrinoless double beta decay

Double Beta Decay ($2\nu\beta\beta$-decay) is a second order weak process present in the SM. It is defined as the transition of a nucleus with mass number A and atomic number Z, to another nucleus with the proton number larger by two units. Two electrons and two electron anti-neutrinos are emitted:

$$(A, Z) \rightarrow (A, Z + 2) + 2e^- + 2\bar{\nu_e}\,. \tag{1.15}$$

This reaction was introduced for the first time by M. Goeppert-Mayer in 1935 [61]. $2\nu\beta\beta$-decay happens in isotopes for which single beta decay is energetically forbidden or strongly suppressed due to a large change of spin. A complete list of all isotopes for which $2\nu\beta\beta$ is expected can be found in e.g. [44]. It has been observed for a number of those isotopes [62–65]. In Fig. 1.6, the specific situation for ^{76}Ge, ^{76}Se and ^{76}As is shown.

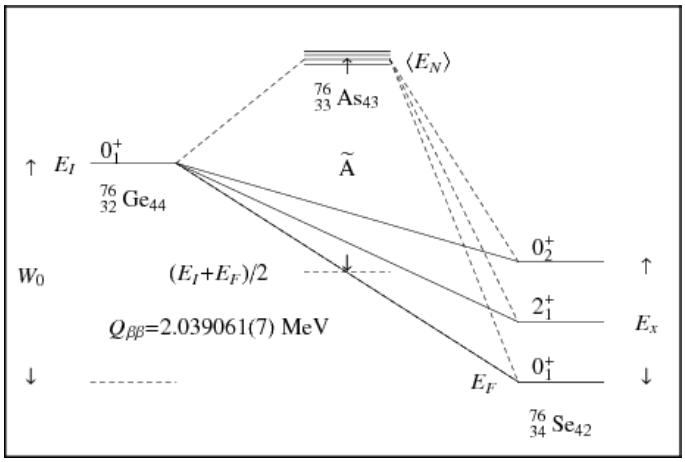

Figure 1.6: $^{76}_{32}\mathrm{Ge}_{44} \rightarrow {}^{76}_{34}\mathrm{Se}_{42}$ as an example for $2\nu\beta\beta$-decay, from [66]. The decay into $^{76}_{33}\mathrm{Ge}_{43}$ is energetically forbidden.

In 1937, the concept of neutrino-less double beta decay ($0\nu\beta\beta$-decay) was introduced [67,68]. Similarly to $2\nu\beta\beta$-decay, it is defined as the transition of a nucleus to another nucleus with the proton number larger by two units. Only two electrons are emitted:

$$(A, Z) \rightarrow (A, Z + 2) + 2e^-\,. \tag{1.16}$$

$0\nu\beta\beta$-decay is not allowed in the SM because it violates the lepton number by 2 units ($\Delta L = 2$). In principle, 35 nuclei can undergo $0\nu\beta\beta$-decay, though realistically only nine emerge as interesting candidates and are experimentally under investigation, namely ^{48}Ca, ^{76}Ge, ^{82}Se, ^{96}Zr,

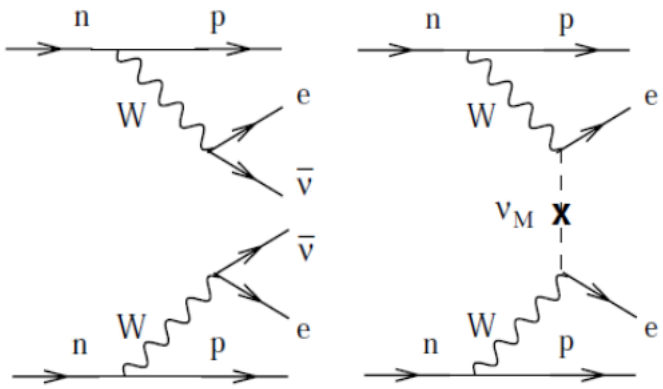

Figure 1.7: Feynman diagrams for neutrino accompanied double beta decay on the left and neutrino-less double beta decay on the right, from [69].

^{100}Mo, ^{116}Cd, ^{130}Te, ^{136}Xe and ^{150}Nd. Experimental aspects of $0\nu\beta\beta$-decay searches, especially those related to germanium, will be discussed in section 2.1.

In Fig. 1.7, the Feynman diagrams for $2\nu\beta\beta$-decay, left, and $0\nu\beta\beta$-decay, right, are depicted. The phenomenological model most considered for $0\nu\beta\beta$-decay requires a light Majorana neutrino as mediator. Majorana neutrinos are considered well motivated by many theorists. However, several other non-SM particles could also mediate the process, as widely discussed in [70, 71]. Calculating the Feynman diagram in Fig. 1.7, the decay rate, $\Gamma^{\mathcal{N}}_{0\nu\beta\beta}$, of a nucleus $\mathcal{N}$ for $0\nu\beta\beta$-decay can be expressed as (e.g. [72] and references therein):

$$\Gamma^{\mathcal{N}}_{0\nu\beta\beta} = \mathcal{G}^{\mathcal{N}}_{0\nu\beta\beta}(Q,Z)[y^{-1}] \cdot \left|\frac{\langle m_{\beta\beta}\rangle}{m_e}\right|^2 \left|\mathcal{M}^{\mathcal{N}}_{0\nu\beta\beta}\right|^2 \tag{1.17}$$

where:

- $\mathcal{G}^{\mathcal{N}}_{0\nu\beta\beta}(Q,Z)$ is the phase space factor for $0\nu\beta\beta$-decay. It depends on the Q-value of the double beta decay as Q^5 and on the atomic number, Z, of $\mathcal{N}$;
- $\mathcal{M}^{\mathcal{N}}_{0\nu\beta\beta}$ is the nuclear matrix element for $\mathcal{N}$, which is the biggest source of uncertainty; different nuclear models [73] are used generating values for $\mathcal{M}_{0\nu}$ of up to a factor of three different;
- $m_{\beta\beta}$ is the effective Majorana mass, defined as:

$$m_{\beta\beta} = \sum_i U_{ei}^2 m_i \ , \tag{1.18}$$

  where U_{ei} are the mixing matrix elements introduced in 1.7;
- m_e is the electron mass;

Experiments searching for $0\nu\beta\beta$-decay aim to measure the half life of the decay, $\mathcal{T}^{0\nu\beta\beta}_{1/2}$, defined as [74]:

$$\mathcal{T}^{\mathcal{N},0\nu\beta\beta}_{1/2} = \frac{ln(2)}{\Gamma^{\mathcal{N}}_{0\nu\beta\beta}} \ . \tag{1.19}$$

A lower bound on $\mathcal{T}_{\frac{1}{2}}^{0\nu\beta\beta}$ can be translated to an upper bound on $m_{\beta\beta}$. The latter can be parametrized by the smallest neutrino mass, m_{min}. In the scenario of the normal hierarchy, the three neutrino masses can be expressed as:

$$m_1 = m_{min}\ , \quad m_2 = \sqrt{m_{min}^2 + \Delta m_{sol}^2}\ , \quad m_3 = \sqrt{m_{min}^2 + \Delta m_{atm}^2 + \Delta m_{sol}^2}\,, \tag{1.20}$$

while in the scenario of the inverted hierarchy, the expressions are

$$m_1 = \sqrt{m_{min}^2 + \Delta m_{atm}^2}\ , \quad m_2 = \sqrt{m_{min}^2 + \Delta m_{sol}^2 + \Delta m_{atm}^2}\ , \quad m_3 = m_{min}\,. \tag{1.21}$$

A comparison of the resulting dependence of $m_{\beta\beta}$ on m_{min} for the two scenarios is shown in Fig. 1.8.

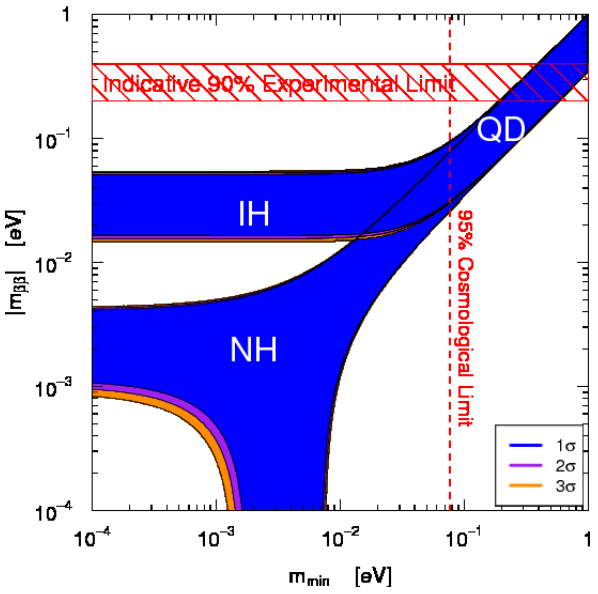

Figure 1.8: Dependence of the effective Majorana mass $m_{\beta\beta}$ on the smallest neutrino mass m_{min} for the Normal Hierarchy (NH), the Inverted Hierarchy (IH) and the Quasi Degenerate (QD) spectra, from [4].

The two bands are obtained varying the mixing parameters in the definition of $m_{\beta\beta}$ (see Eq. 1.18) within their experimental uncertainties. The cosmological constraints on m_{min} (see section 1.1.3) and the experimental upper bound on $m_{\beta\beta}$ [75] are also shown. The latter is shown with the uncertainty introduced by the uncertainty on $\mathcal{M}_{0\nu\beta\beta}^{^{76}\mathrm{Ge}}$. Figure 1.8 shows that in the case of an inverted hierarchy, a lower bound of about 0.01 eV for $m_{\beta\beta}$ exists. Thus, if neutrinos are Majorana particles, $0\nu\beta\beta$-decay has to exist. This is not the case for a normal hierarchy. For $2 \times 10^{-3} < m_{min} < 7 \times 10^{-3}$ eV, the effective Majorana mass can be zero. In that case, $0\nu\beta\beta$-decay does not occur. The goal of $0\nu\beta\beta$-decay experiments in the near future is either to measure $0\nu\beta\beta$-decay or rule out the inverted hierarchy. However, if $0\nu\beta\beta$-decay is observed, the only possibility to establish the hierarchy is to have an independent upper bound on the lowest neutrino mass around 10^{-2} eV.

$0\nu\beta\beta$-decay has not been observed yet. The status and techniques of searches for $0\nu\beta\beta$-decay will be discussed in chapter 2.

1.2 Dark Matter

The first cosmological observation of gravitational anomalies was published by F. Zwicky in 1933 [76]. Measuring the velocity dispersions of 8 galaxies in the Coma cluster, he found them to far exceed the expected values based on General Relativity (GR). He claimed that the measured velocities were only possible with an average matter density 400 times larger than the density of the luminous matter. Since then, many other observations at different cosmological scales have shown deviations from the expectations for the movement of observable objects. Mainly two approaches have been used to address these issues: either questioning and modifying GR or postulating the presence of a "non-visible", gravitationally interacting Dark Matter (DM). The 2006 observation of a pair of colliding galaxy clusters, known as the "Bullet Cluster" [77], poses a significant challenge for all theories proposing a modified gravity solution like MOND (MOdiefied Newtonian Dynamics) [78]. Models containing DM particles are favoured. However, the latest results from a mono-jet analysis published by the ATLAS collaboration set really low upper bounds on DM nucleon scattering cross-sections [79, 80].

Evidence for the existence of DM are discussed in section 1.2.1; DM candidates detectable with germanium detectors are listed and shortly described in section 1.2.2.

1.2.1 Evidence for Dark Matter

Evidence for DM comes from the observation of its gravitational effect on visible matter, radiation and large scale structures.

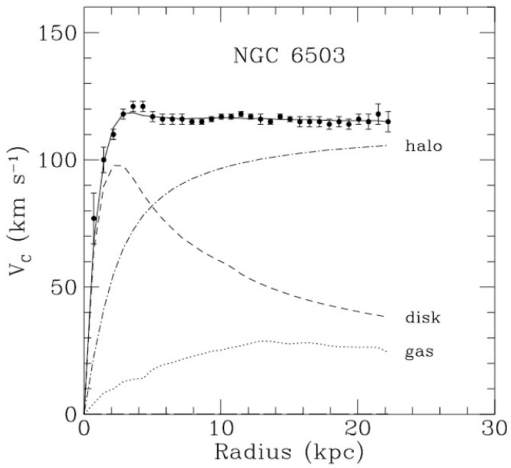

Figure 1.9: Galactic rotation curve for NGC 6503 together with the predictions from the disk and gas contributions plus the dark matter halo contribution needed to match the data, from [81].

Rotation curves: the orbital velocities of visible stars or gas in a galaxy are expected to decrease at bigger radii, if there is nothing but the observed luminous matter present. An example of a measured galactic rotation curve is shown in Fig. 1.9. The prediction for the rotation curve from gas plus luminous matter (disk) does not match the data points. Introducing a contribution from a dark halo that permeates all the galaxy produces a prediction which matches the data points well.

Gravitational lensing: in GR, the effect of gravity is described as a distortion of space. Gravitational lensing is nothing but the effect of this deformation on light. If a cluster of matter is between a light source (e.g. a galaxy cluster) and an observer, the image of the source gets distorted. An example of the effect of gravitational lensing on the image of a galaxy cluster is shown in Fig. 1.10. From the distortion of the image, it is possible to not only evaluate the mass of the "lensing" cluster but also the distribution of the matter in the "lensing" cluster [82]. The observed distortion cannot be explained considering only the observed luminous matter. The contribution from non-visible matter is necessary to match the observations.

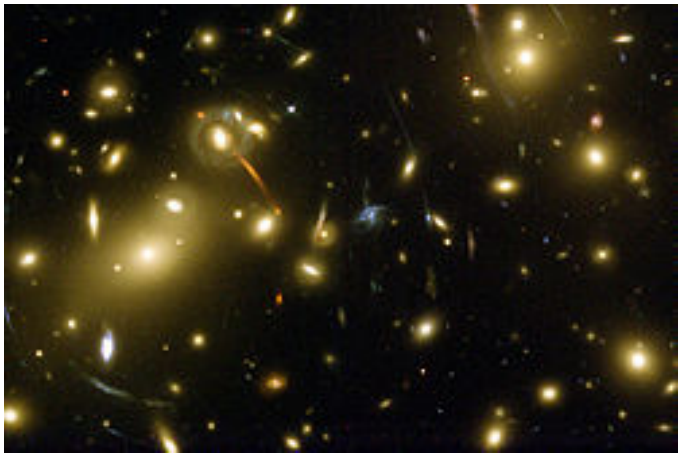

Figure 1.10: Strong gravitational lensing produced by the presence of the cluster of galaxies Abell 2218. Point-like sources get deformed into arcs. Figure credit: NASA/ESA

Large scale structures: the total mass of luminous matter observed is not sufficient to explain the formation of the large scale structures observed. Another component, like DM, is necessary to explain the observed clumping of ordinary matter. The large scale structure is in good agreement with simulations accounting for a cold, i.e. non relativistic, DM, disfavouring warm DM [83].

1.2.2 Dark Matter candidates

A wide variety of possible DM candidates have been proposed over the past years. A few selected DM candidates, which are, in principle, detectable with germanium detectors, are briefly discussed in the following. A complete review on DM candidates can be found in e.g. [3].

From the Big Bang Nucleosynthesis (BBN) and the Cosmic Microwave Background (CMB) data, the constraints on the amount of baryonic matter disfavour the existence of baryonic DM candidates or at least reduce them to a very small fraction. The amount of DM in the universe at present can only be explained by introducing non-baryonic candidates. The non-baryonic candidates can be grouped in Weakly Interacting Massive Particles (WIMPs) and non-WIMPs.

- WIMPs

  Lightest Super-Symmetric Particle (LSP): In the Minimal Supersymmetric extension of the SM (MSSM) (e.g. [84]), the LSP is a stable particle which might be a good candidate for DM. It must be a colourless and electrically neutral particle, otherwise it would have been observed due to its interaction with ordinary matter via the strong and electromagnetic forces [85]. The most studied of the possible LSPs is the neutralino χ, which is a linear combination of the super partners of the Higgs and the gauge bosons. The neutralino is a Majorana fermion. A nice review on the experimental results on χ-nucleon scattering cross-sections can be found in [86];

  non-SUper SYmmetric (SUSY) WIMPs: Already after the first run of the LHC, the limits on possible SUSY parameters are quite stringent (e.g. [87, 88]). It is therefore necessary to think about possible alternatives like Kaluza-Klein particles [89], heavy fourth generation neutrinos [90] or mirror DM [91];

- non-WIMP candidates

  Axions: They arise from the Peccei-Quinn solution to the strong CP problem [92]. The introduction of this pseudo-particle adds a new spontaneously-broken global symmetry which dynamically relaxes strong CP-violation in our universe to zero. Axions can couple to photons in the presence of strong electromagnetic fields via the Primakoff effect [93], and therefore also with valence electrons. Searches [94] have been performed for both relic axions and axions produced in the Sun, setting strong limits on the photon and electron couplings of sub-keV axions.

The experimental status and techniques of DM searches with germanium detectors, will be discussed in chapter 2.

Chapter 2

Searches for new physics with germanium detectors

Germanium detectors are widely used in a vast range of applications from basic research to applied science. Several international collaborations like the European AGATA [95] and the American GRETINA [96] collaborations, have chosen germanium detectors for nuclear physics experiments. Many particle physics projects also use germanium detectors to search for physics beyond the Standard Model. In this chapter germanium based experiments looking for new physics are discussed. Such projects focus either on the properties of neutrinos or dark matter.

In section 2.1, the search for $0\nu\beta\beta$-decay is discussed, and in section 2.2, dark matter searches. In both sections, the general experimental requirements for each search are introduced. Results obtained by first experiments are discussed and running and future experiments are described. In section 2.3, the R&D project at the heart of this thesis, important for both $0\nu\beta\beta$ and DM-searches, is introduced.

2.1 Neutrinoless Double Beta Decay

As discussed in section 1.1.4, $0\nu\beta\beta$-decay is a possible rare decay that would only be observable in nuclei for which single beta decay is energetically forbidden. A number of large-scale experiments are running or are under construction to search for $0\nu\beta\beta$-decay. In case for evidence of $0\nu\beta\beta$-decay, an observation with several isotopes is needed. A complete overview on $0\nu\beta\beta$-searches is given in [97]. The dominant experimental technique used so far is pure calorimetry: the energy of the electrons is measured via scintillation light (e.g. Xenon-based experiments), ionization (e.g. Germanium-based experiments) or heat deposition, i.e. bolometers, (e.g. Tellurium-based experiments). In the following, the focus will be on germanium-based experiments.

2.1.1 Experimental aspects

The isotope ^{76}Ge, for which $2\nu\beta\beta$-decay has been observed, is a candidate for $0\nu\beta\beta$-searches. Germanium is a semiconductor. Therefore, it can be used as source and detector material simultaneously.

$0\nu\beta\beta$-events are to be identified through energy depositions at the Q-value of the $2\nu\beta\beta$-decay (see section 1.1.4) as shown in Fig. 2.1. Sources of background are cosmic rays (e.g. muon induced events), natural radioactivity of the materials surrounding the detectors and internal radioactivity from cosmogenic activation, e.g. ^{60}Co and ^{68}Ge. An often limiting background is due to α-particles coming from lead or polonium surface contamination.

The observable for $0\nu\beta\beta$-experiments is the half-life, $\mathcal{T}^{0\nu}_{1/2}$. It is directly related to the number of expected $0\nu\beta\beta$-events, $N_{0\nu\beta\beta}$, in an observation of duration t [72]:

$$\begin{aligned} N_{0\nu\beta\beta} &= N_{^{76}\mathrm{Ge}} \cdot \Gamma^{^{76}\mathrm{Ge}}_{0\nu\beta\beta} \cdot t \cdot \epsilon = \\ &= \frac{M \cdot \eta}{m^{mol}_{^{76}\mathrm{Ge}}} \cdot N_A \cdot \Gamma^{^{76}\mathrm{Ge}}_{0\nu\beta\beta} \cdot t \cdot \epsilon \end{aligned} \tag{2.1}$$

where M is the total mass, η and $m^{mol}_{^{76}\mathrm{Ge}}$ are the isotopic abundance and the molar mass of ^{76}Ge, respectively. N_A is the Avogadro number. $\Gamma^{^{76}\mathrm{Ge}}_{0\nu\beta\beta}$ is the decay rate as defined in Eq. 1.17, with $\mathcal{N} = {}^{76}$Ge, ϵ is the detection efficiency of the experiment. The product $M \cdot t$ is referred to as exposure. The "Region Of Interest" (ROI) of the $0\nu\beta\beta$-search is an energy window around the Q-value of the decay. In the ROI, also a number of background events, N_B, is expected. N_B is proportional to the exposure and to the width of the ROI (ΔE):

$$N_B = b \cdot M \cdot t \cdot \Delta E \ , \tag{2.2}$$

where b is the background index, often given in counts/(keV $\cdot$ kg $\cdot$ y). The index b is assumed to be constant across the ROI.

Two different scenarios are considered:

1. $N_B < N_{0\nu\beta\beta}$: a number of events, N_{obs}, is observed during a time t. N_B is measured[1]. Thus, $N_{0\nu\beta\beta}$ is

   $$N_{0\nu\beta\beta} = N_{obs} - N_B \, . \tag{2.3}$$

   Given Eqs. 2.1 and 1.19, $\mathcal{T}^{^{76}\mathrm{Ge},0\nu\beta\beta}_{1/2}$ is obtained as:

   $$\mathcal{T}^{^{76}\mathrm{Ge},0\nu\beta\beta}_{1/2} = \frac{M \cdot \eta}{m^{mol}_{^{76}\mathrm{Ge}}} \cdot N_A \cdot \frac{ln(2) \cdot t \cdot \epsilon}{N_{obs} - N_B} \, . \tag{2.4}$$

   By using Eq. 1.17, it is also possible to obtain the effective Majorana mass $m_{\beta\beta}$ in terms of N_{obs} and N_B;

2. $N_B \gg N_{0\nu\beta\beta}$: only lower (upper) bounds are set for $\mathcal{T}^{^{76}\mathrm{Ge},0\nu\beta\beta}_{1/2}$ ($m_{\beta\beta}$). The bound is evaluated using a Taylor expansion of the sensitivity, as:

   $$S = \frac{N_{0\nu\beta\beta}}{\sqrt{N_{0\nu\beta\beta} + N_B}} \simeq \frac{N_{0\nu\beta\beta}}{\sqrt{N_B}} \, . \tag{2.5}$$

[1] It is common to measure the background events outside the ROI and extrapolate the value into the ROI.

By introducing $N_{0\nu\beta\beta}$ and N_B as given in Eqs. 2.1 and 2.3, the sensitivity becomes:

$$S = \frac{\eta N_A}{m^{mol}_{^{76}\mathrm{Ge}}} \cdot \frac{ln(2)}{\mathcal{T}^{^{76}\mathrm{Ge},0\nu\beta\beta}_{1/2}} \cdot \epsilon \cdot \sqrt{\frac{M \cdot t}{b \cdot \Delta E}} \,. \tag{2.6}$$

For $N_{obs} \approx N_B$, it is possible to set a limit with 90% Confidence Level (CL) on $\mathcal{T}^{^{76}\mathrm{Ge},0\nu\beta\beta}_{1/2}$ as:

$$\mathcal{T}^{^{76}\mathrm{Ge},0\nu\beta\beta}_{1/2} > \frac{\eta \cdot N_A \cdot ln(2)}{1.64 \cdot m^{mol}_{^{76}\mathrm{Ge}}} \cdot \epsilon \cdot \sqrt{\frac{M \cdot t}{b \cdot \Delta E}} \,. \tag{2.7}$$

The upper limit on the effective Majorana mass is found combining Eqs. 2.7 and 1.17.

From Eqs. 2.1 and 2.7, the main requirements for $0\nu\beta\beta$-experiments follow:

1. The isotope should have:
   a) a high isotopic abundance in order to have a good signal-to-background ratio. The natural abundance of ^{76}Ge is 7.6% [98]. Current generation experiments use enriched material with up to 88% enrichment in ^{76}Ge;
   b) a high Q-value since the decay rate scales with Q^5 and the natural background is lower at higher energies. ^{76}Ge has a Q-value of 2039 keV;
2. The germanium detectors used have to be large enough not to loose too many *ee* events at the surface;
3. The better the energy resolution, the smaller the ROI can be. The smaller the ROI, the smaller N_B is. Figure 2.1 shows how important a good energy resolution is to distinguish the $0\nu\beta\beta$-decay signal (a single peak at $K_e/Q = 1$) from the irreducible background from $2\nu\beta\beta$-decays (continuum spectrum up to $K_e/Q = 1$);
4. By increasing the mass, the sensitivity increases if the background is low enough.
5. The background has to be low enough to make the mass usable. Different sources of background are reduced using different strategies:
   a) background coming from cosmic rays is substantially reduced using deep underground laboratories;
   b) layered shields protect from γ-s due to natural radioactivity in the surrounding rocks;
   c) muon-induced prompt signals are vetoed;
   d) low-Z shields are used to reduce the number of muon-induced neutrons created close to the detectors in order to prevent the creation of meta-stable states;
   e) the materials surrounding the detectors are selected as radio-pure as possible, e.g some low-background experiment use 2000 years old Roman lead (roughly 10^3 times lower radioactivity).
6. In preparation of the experiments:

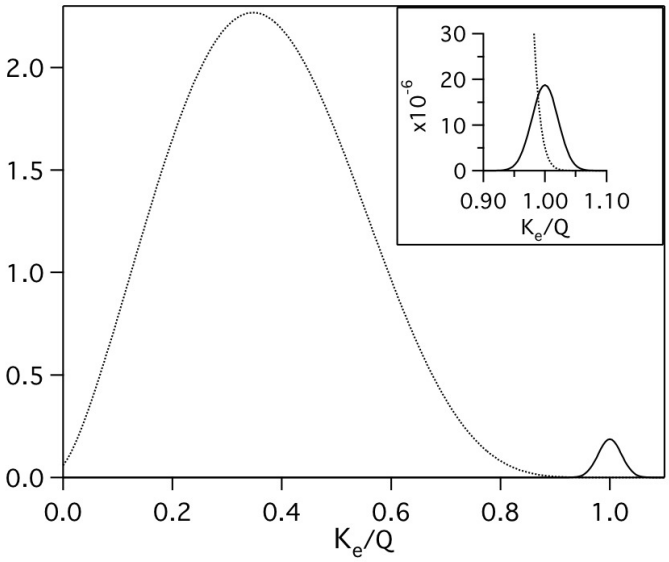

Figure 2.1: Spectra of electron kinetic energies, K_e, scaled with the Q-value of the $\beta\beta$-decay for the $2\nu\beta\beta$ (dotted curve) and $0\nu\beta\beta$ decays (solid curve), from [99]. In the top right part, a zoom of the energy spectra is shown around the Q-value of $2\nu\beta\beta$-decay.

a) as the interaction of cosmic rays with stable germanium isotope produces radioactive isotopes like ^{60}Co and ^{68}Ge, with half lives longer than the life time of the experiments, shielded transportation is used after crystal growing and enrichment processes [100];

b) as one of the most limiting background comes from α-particles produced by ^{210}Pb and ^{210}Po, it is important to maximally reduce lead or polonium contaminations. Contamination with lead or polonium are possible either on the surfaces of the detectors or on the materials surrounding the detectors. When an α-particle with an energy of about 5 MeV is emitted close to or on the surfaces of the detector, it can be detected with an energy within the ROI.

7. These techniques reduce N_B significantly. It can be reduced further by methods to identify and reject background events in the ROI [101]:

   a) **granularity**: large scale experiments have a modular structure based on many germanium detectors. This allows the usage of anti-coincidence techniques to reject Compton scattering background events. The number, the size and the mass of the detectors can be selected to optimize the rejection power;

   b) **segmentation**: a single detector can have several segments (see section 3.3). This allows the usage of anti-coincidence techniques between different segments to reject multi-segment events as background events. The number of segments and the way to divide the crystal can be optimized for background rejection. However, the higher number of segments requires more cabling introducing new possible sources of background;

c) **pulse shape discrimination**: the pulse shapes of electron-like (i.e. signal) and photon-like (i.e. background) events are different and this can be used to reject the latter [102]. Methods for background rejection based on pulse shape analysis will be discussed in chapters 6 and 7.

2.1.2 First experiments

The first $0\nu\beta\beta$-experiments based on germanium were the International Germanium EXperiment (IGEX) [103], in the Canfranc underground laboratory in Spain, and Heidelberg-Moscow (HdM) [104] in the Laboratori Nazionali del Gran Sasso (LNGS), in Italy.

The IGEX experiment ran from 1991 to 2000 with a total exposure of $8.8\,\mathrm{kg}\cdot\mathrm{y}$ and a background index of $0.17\,\mathrm{counts}/(\mathrm{kg}\cdot\mathrm{keV}\cdot\mathrm{y})$. In the final configuration, the experiment used 6 p-type High Purity Germanium (HPGe) detectors. The lower limit on the half life was found to be [105] $\mathcal{T}_{1/2}^{0\nu\beta\beta} > 1.57\times10^{25}\,\mathrm{y}$. The upper limit on the effective Majorana mass was placed in the interval $[0.33\,\mathrm{eV}, 1.35\,\mathrm{eV}]$ depending on the nuclear matrix element used.

The Heidelberg-Moscow experiment ran from August 1990 to May 2003 with a total exposure of $71.1\,\mathrm{kg}\cdot\mathrm{y}$ and a background index of $0.11\,\mathrm{counts}/(\mathrm{kg}\cdot\mathrm{keV}\cdot\mathrm{y})$. The experiment used 5 p-type HPGe detectors. Part of the HdM collaboration made a controversial claim of a discovery with 4.2 σ significance and a half-life of: $\mathcal{T}_{1/2}^{0\nu\beta\beta} = 1.2^{+0.4}_{-0.2}\times10^{25}\,\mathrm{y}$ [106] (Klapdor Kleingrothaus, KK, claim), while the official result of the collaboration was a lower limit of: $\mathcal{T}_{1/2}^{0\nu\beta\beta} > 1.9\times10^{25}\,\mathrm{y}$ [107].

2.1.3 Running and future experiments

The current experiments searching for $0\nu\beta\beta$-decay, are the European GERmanium Detector Array (GERDA) [108], shown in Fig. 2.2a, and the American Majorana Demonstrator, MD, [109], shown in Fig. 2.2b.

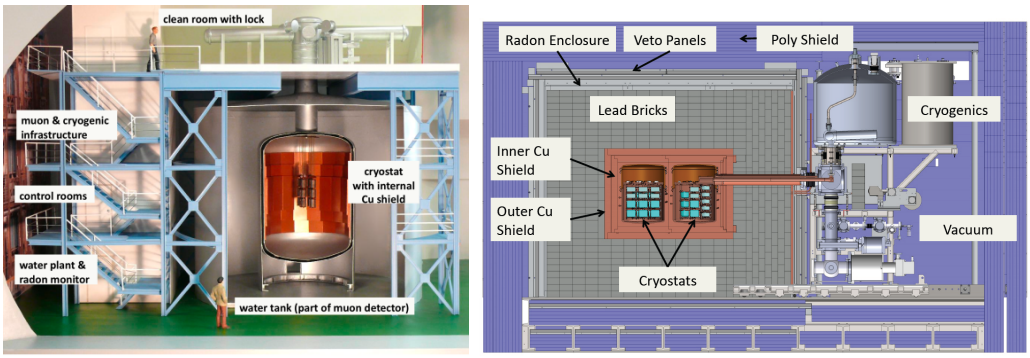

(a) (b)

Figure 2.2: (a) GERDA setup, from [110]; (b) Majorana Demonstrator setup, from [111].

GERDA is located in the Laboratori Nazionali del Gran Sasso (LNGS) in Italy, with an overburden of 1400 m (3800 meter water equivalent, m.w.e.). The first phase of data taking

(phase-I) ran from November 2011 to May 2013. The detectors used in the array were 8 closed-end p-type enriched HPGe detectors from the HdM and IGEX experiments [112], and 5 newly produced Broad Energy Germanium (BEGe) detectors [113]. All the detectors were operated fully immersed in liquid argon (LAr) which cooled down the detectors and acted as part of the shielding system. A water tank (diameter d=10 m and height h=9 m filled with 580 m^3 of water) surrounds the LAr tank (d=4 m and h=6 m filled with 64 m^3 of high-purity liquid argon) to further reduce the natural radioactivity background (see Fig. 2.2a).

GERDA phase-I reached an exposure of 21.6 $kg \cdot y$ with $b = 1.1 \times 10^{-2}$counts/(keV $\cdot$ kg $\cdot$ y). No signal was observed and a lower limit on the half life was set as $\mathcal{T}^{0\nu}_{1/2} > 2.1 \times 10^{25}$ y [6]. Combining the GERDA result with the previous IGEX and HdM results provides a limit of $\mathcal{T}^{0\nu}_{1/2} > 3.0 \times 10^{25}\, y$, resulting in an upper limit on the effective Majorana mass in the range of [0.2 eV, 0.4 eV], depending on the choice of nuclear matrix element. The KK claim is strongly disfavoured.

GERDA Phase-II is still in the commissioning phase. The goal is to lower b to 10^{-3} and reach an exposure of around 200 $kg \cdot y$, improving the sensitivity by a factor of 10. The background will be reduced using new detector assembly techniques, new front end electronics and instrumenting the LAr to use it as a veto system. New detectors were produced for GERDA Phase-II. One option had been segmented n-type true-coaxial detectors [114]. Such detectors were used to provide the results presented in this thesis. For technical reasons related to crystal pulling and pulse shape discrimination (PSD) capabilities, p-type BEGe detectors were used for GERDA. Thirty newly produced BEGe detectors with a total mass of about 20 kg were added for GERDA Phase-II.

The Majorana Demonstrator is located in the Sanford Underground Research Facility (SURF) in the Homestake Mine, which has an overburden of 1478 m of rock (4260 m.w.e).

The MD baseline foresees 30 kg of enriched germanium detectors operated in vacuum. Two separate cryostats, each one with its own vacuum system, house multiple detector strings. One of the goals of the Majorana collaboration is to proof the scalability of such an experiment and to suggest a scheme for the development of a tonne-scale ^{76}Ge experiment. As in all $0\nu\beta\beta$-decay searches, the background reduction plays a central role in the development of the experiment. A multilayer shield system, shown in Fig 2.2b, is used to minimize the background index. The background index aimed for is around 0.75×10^{-3}counts/(keV $\cdot$ kg $\cdot$ y). MD was in the commissioning phase at the beginning of 2016. The main question for the MD is whether the high-Z shield used allows the background reduction at the relatively small overburden of SURF.

Table 2.1 summarizes the main aspects of the two experiments, GERDA and MD. The main difference between the two experiments is the shielding against external radiation [115]. GERDA uses high-purity liquid argon enclosed in a large water tank, i.e. low atomic number, Z, materials. MD uses high-purity electro-formed copper with an external lead shield, i.e. high Z materials. Given the Z-dependence of muon induced neutron production, in order to avoid neutron background, MD needs a bigger overburden in comparison to GERDA.

2.2 Dark Matter

As already discussed in section 1.2, DM particles have not been observed yet. Several large scale experiments are running or are under construction to search for them. Three different search methods are used: collider searches (e.g. at LHC with ATLAS and CMS [116]), indirect detection

	GERDA		MD
	Phase-I	**PhaseII**	
Detectors	8 closed-end coaxial from IGEX and HdM, 5 new BEGe	Phase-I plus 30 new BEGe	p-type point contact
Total Mass [kg]	≈ 20	≈ 40	≈ 30
b [counts/(keV $\cdot$ kg $\cdot$ y)]	1.1×10^{-2} (achieved)	10^{-3} (goal)	0.75×10^{-3} (goal)
Exposure [kg $\cdot$ y]	21.6	≈ 200	≈ 200
Overburden [m.w.e]	3800		4260
μ veto	water Čerenkov light		plastic scintillators
shielding for γs and neutrons from natural radioactivity	high-purity liquid argon and ultra-pure water		electro-formed copper, lead

Table 2.1: Comparison of the main technical characteristics of GERDA and MD.

(e.g using neutrino telescopes [117, 118] or satellites [119–122]) and direct detection (based on different calorimetric techniques e.g scintillation light, ionization or heat deposition). A complete overview of DM-searches is given elsewhere [123, 124]. In the following section, the focus will be on direct detection experiments using germanium detectors.

2.2.1 Experimental aspects

Germanium detectors are used as target to search for possible interactions of DM particles [125]. The signature of such interactions would be a nuclear recoil with an energy deposition below 100 keV. Background events can be divided into nuclear recoil and electron recoil events. The electron-recoil background comes from α-particles, electrons, and photons. These originate from natural radioactivity in the surroundings of the detectors or from surface contaminations. Neutrons dominate the nuclear-recoil background. They are either muon-induced or due to natural radioactivity in the surroundings.

The experimental sensitivity of a direct detection experiment is defined as the minimum upper limit on the DM-nucleon scattering cross-section such experiment can set. The lower the upper limit, the more sensitive the experiment is.

Figure 2.3 illustrates the dependence of the sensitivity to the DM-nucleon scattering cross-section as a function of the exposure, MT, on different detector parameters. The black line shows the sensitivity for a reference detector. The red line shows the effects of an increased background rate: the sensitivity reaches its best value after a short exposure and longer exposure does not improve it. Assuming a constant background, enlarging the target mass improves the sensitivity with time (blue line). The green line shows how an improved discrimination between background and signal events lead to a higher sensitivity, i.e. a lower upper limit on the scattering

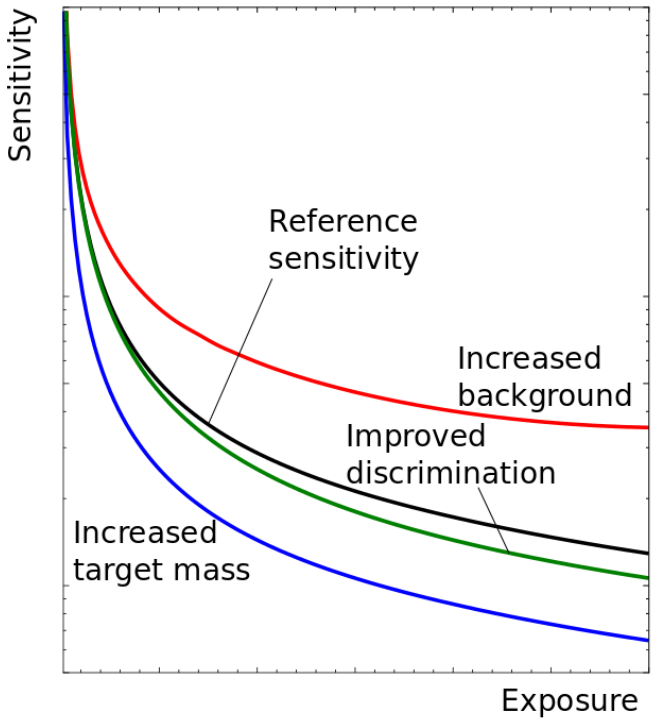

Figure 2.3: Evolution of the sensitivity versus the exposure, from [126]. For more information see text.

cross section. The main experimental requirements for a direct dark matter detection experiment follow:

1. increasing the target mass improves the sensitivity *only* if the background stays constant;
2. the background rate has to be as low as possible. All the techniques for background reduction discussed for $0\nu\beta\beta$-searches are also valid for DM-searches;
3. given a target mass, improving background discrimination techniques enhances the sensitivity for longer data taking period. Background and signal events can be distinguished using the following features:
   a) temporal variation in the signal event rates, i.e. annual modulation. The WIMP event rate and spectrum are expected to vary as the relative motion between the laboratory frame and the WIMP wind varies along the earth's orbit around the sun [127];
   b) directional variation of the recoiling nuclei. Signal events, unlike background events, are expected to exhibit a non-uniform directionality correlated with the relative directions of the laboratory frame and the WIMP wind [128];
   c) different detector response to signal and background events. For a given energy deposition, the relative scintillation, ionization and phonon signals (or one of their com-

binations) are often different for electron recoils, i.e background, and nuclear recoils, i.e. signal.

2.2.2 First experiments

The **Coherent Germanium Neutrino Technology (CoGeNT)** [129] experiment, was a Dark Matter direct detection experiment located in the Soudan Underground Laboratory with 2090 m.w.e. overburden. The detector element was a single p-type Point Contact (PPC) germanium detector of 443 g, optimized for low energy-deposition. The detector was surrounded by an Oxygen-free high thermal conductivity (OFHC) copper cryostat. A multilayer shield made of lead, borated polyethylene and aluminum, together with an active muon veto, reduced the effect of natural radioactivity coming from the vicinity. In early 2014, the collaboration reported an annual modulation appearing in the counting rate from their detector. The energy spectrum exhibited an exponential excess of unknown origin [130] with, however, a low statistical significance (2.2σ).

2.2.3 Running and future experiments

The running direct detection experiments based on germanium detectors are the Cryogenic Dark Matter Search (CDMS) experiment [5], located in the Soudan Underground Laboratory, and the China Dark Matter Experiment, CDEX [131], located in the China JinPing underground Laboratory (CJPL [8]).

CDMS uses both germanium and silicon detectors at ultra low temperature ($\approx 40\,\mathrm{mK}$) to have heat (trough phonons collection) and ionization signals. Pulse shape analysis was used in CDMS to further discriminate against surface events which could otherwise be misidentified as nuclear recoils. The latest results obtained by the CDMS collaboration is a limit on the WIMP-nucleon spin-independent scattering cross-section of $1.8 \times 10^{-44}\,\mathrm{cm}^2$ ($1.18 \times 10^{-41}\,\mathrm{cm}^2$) for a 60 GeV (8.6 GeV) WIMP mass [7]. The CDMS collaboration is planning the SuperCDMS experiment with a $\mathrm{M} = 200\,\mathrm{kg}$ at the Canadian underground laboratory SNOLAB [9] with 6010 m.w.e. overburden.

CDEX in its first stage, CDEX-1, uses two high-purity germanium detectors operated at temperatures around $\approx 100\,\mathrm{K}$: a 20 g low energy-threshold germanium (ULEGe) detector and a 1 kg p-type point-contact germanium (PPCGe) detector [132]. The ULEGe detector is used to investigate how to lower the energy threshold and be sensitive to extremely low recoil energies, i.e. to low-mass WIMP interactions. The PPCGe detector allows the CDEX collaboration to test software techniques to reject background events using pulse shape analysis. CDEX-1 has been running since 2011. The latest limits on WIMP-nucleon interaction cross-section were published in April 2014 [133].

The main difference between CDMS and CDEX is the operating temperature of the germanium detectors. Operating germanium detectors in the mK temperature range allows to use both the ionization and the phonon channel to reject the background. On the other hand, operating germanium detectors at such low temperature is more difficult and the scalability to higher masses is still under study. The shielding strategies are both based on a combination of low-Z and high-Z materials.

2.3 Germanium detector R&D project

As mentioned in the previous sections, one of the limiting backgrounds, both for $0\nu\beta\beta$ and DM searches, comes from α-particles. It is very difficult to totally avoid ^{210}Pb or ^{210}Po contamination both on the material close to the detector and on the detector itself. Therefore, a method to characterize α-events is needed. Knowing the characteristics of α-events, it is possible to reject them as background. The main goal of this work is to do this characterization probing germanium detectors with α-particles produced by radioactive sources like ^{241}Am.

Chapter 3

Germanium detectors

Germanium detectors were first developed during the 1960s. The first germanium detectors to measure radioactivity were built using the ion lithium drifting technology. They were called Ge(Li) detectors, similarly to the Si(Li) detectors. Unlike for the wide-spread silicon detectors, a large reduction of the impurity level became possible for germanium detectors during 1970s and 1980s. This allowed the production of High Purity Germanium (HPGe) detectors which can be very big and especially suitable for gamma ray detection.

Germanium detectors are widely used in basic research, see chapter 2, but they also have commercial applications like screening for radioactivity [134], wine authentication [135, 136], low background material screening [137, 138] or medical scanning [139]. An analysis using HPGe detectors to measure the potassium content in several food samples is discussed in appendix A.

In the following, basic concepts of HPGe detectors as radiation detectors are explained. The basics of interactions between radiation and matter is discussed in section 3.1, focusing mainly on photons and α-particles. The working principles of semiconductor detectors, from a brief characterization of semiconductor materials to the description of the principle of a p-n junction, are presented in section 3.2. Germanium semiconductor detectors are discussed in section 3.3. In section 3.3.2, the commercial and R&D detectors available at the MPI are described in detail.

3.1 Interactions of radiation with matter

Radiation interacts with matter through a variety of processes, for an overview see [140]. In the following, only a brief description of the relevant processes is presented.

Radiation is categorized in charged particle radiation (light charged particles and heavy charged particles) and neutral radiation (photons and neutrons). For the work presented in this thesis, mainly gamma- and alpha-emitters were used as radioactive sources. Therefore, the following focuses on the interactions of photons (see section 3.1.1) and heavy charged particles (see section 3.1.2) with matter.

3.1.1 Photons

There are three main interaction mechanisms for photons in matter: photoelectric absorption, Compton scattering and pair production. All of these processes result in a partial or complete

transfer of the incident photon energy to an electron of the target. The cross section of each process depends on the atomic number of the target material, Z, and the energy of the incident photon, $h\nu$, where h is the Planck's constant and ν is the frequency of the photon. Figure 3.1 shows the relative importance of the three processes in the parameter space of Z and $h\nu$.

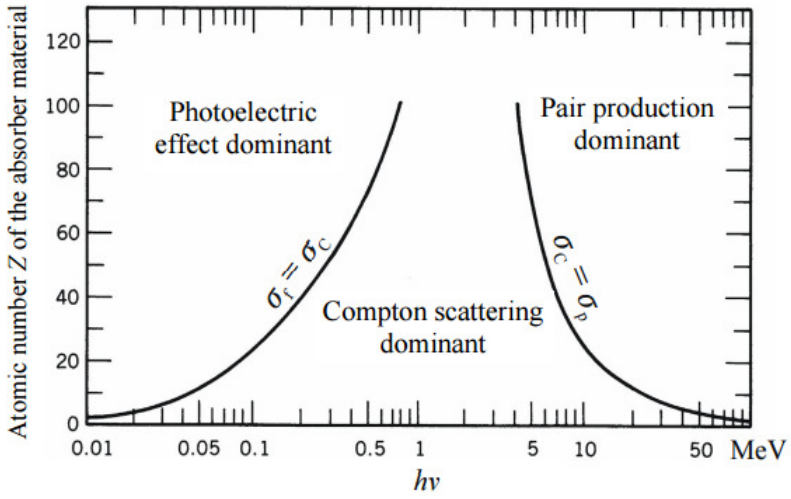

Figure 3.1: Relative importance of the three major types of photon interaction with matter in the parameter space of the incident photon energy, $h\nu$, and the atomic number, Z, of the absorber. The solid lines show the values of Z and $h\nu$ where two neighboring effects are equal, from [141].

Photoelectric absorption: This is the dominant interaction mechanism for photons with energies below 200 keV. The probability of photoelectric absorption varies approximately as Z^5 and $(h\nu)^{-3}$. As the incident photon energy is completely absorbed by an atomic shell electron, the latter is ejected out of the shell. The energy of the ejected photo-electron, E_e is:

$$E_e = h\nu - E_b\,, \tag{3.1}$$

where E_b is the binding energy of the electron. If the photo-electron is ejected from an inner shell the rearrangement of the electrons from the outer shells will produce X-rays. They might be re-absorbed causing Auger-electrons to be emitted.

Compton scattering: This is the dominant interaction mechanism for photons with energies from 200 keV up to 3 MeV; the Compton scattering cross section was one of the first to be calculated using electrodynamics. It is known as the Klein-Nishina formula [140]. If the energy of the incident photon is high enough, the target electron can be considered as free. The incident photon transfers part of its energy to the recoil quasi-free electron and is deflected by an angle θ_C with respect its original direction. Energy and momentum conservation force the energy of the scattered photon, $h\nu'$, to be:

$$h\nu' = \frac{h\nu}{1+\gamma(1-cos\theta_C)}\,, \tag{3.2}$$

where $\gamma = h\nu/m_e c^2$ and m_e is the mass of the electron. The transferred energy can vary from $h\nu/(1+2\gamma)$, for $\theta_C = 180°$ to the full energy $h\nu$, for $\theta_C = 0$.

Pair production: It becomes relevant for photon energies exceeding $2m_e$ (1.02 MeV). The energy of the incident photon is totally converted and an electron and positron pair is created. The excess energy of the incident photon above 1.02 MeV becomes kinetic energy of the new pair of particles. Momentum conservation allows this process only in the presence of a nucleus. No simple expression for the probability of pair production exists. However, the cross section depends on Z^2.

3.1.2 Charged particles

Charged particles are commonly divided into two categories: electrons and positrons, and heavy charged particles such as α-particles, protons, and pions.

When charged particles penetrate matter, they lose their initial energy and are deflected trough either collisions with the electrons or elastic scattering from nuclei. The collisions with electrons (with extremely high cross sections of about $10^{-18} - 10^{-16}\,\mathrm{cm}^2$) are the dominant effect. These collisions can be classified as soft or hard collisions; while in the former only atomic excitation takes place, in the latter the transferred energy is enough to cause ionization. The amount of energy transferred in each individual collision is a very small fraction of the initial energy. However, since the number of collisions per unit path length is large, a substantial energy loss is observed even in relatively thin layers of material. A 5.5 MeV α-particle, for example, loses all its energy in only 32 μm of germanium.

One of the main parameters to characterize the interaction between charged particles and matter is the stopping power. It is defined as the average energy loss per unit path length, and usually known as dE/dx. A first derivation, using classical arguments, was done by N. Bohr [142]. The quantum mechanical version of Bohr's calculation, was completed by H. Bethe and F. Bloch ([143] and references therein). The Bethe-Block formula gives the mean energy loss, of a heavy charged particle of mass m_0 (with $m_0 \gg m_e$), charge z and a velocity β:

$$-\frac{dE}{dx} = 4\pi N_A r_e^2 m_e c^2 z^2 \frac{Z}{A}\frac{1}{\beta^2}\left[\frac{1}{2} ln \frac{2m_e c^2 \beta^2 \gamma^2 T_{max}}{I^2} - \beta^2 - \frac{\delta(\beta\gamma)}{2}\right], \tag{3.3}$$

where:

N_A is the Avogadro number,

r_e and m_e are the classical radius and the mass of the electron;

Z and A are the atomic number and atomic mass of the absorber;

I is the characteristic ionization constant, which is material dependent;

T_{max} is the maximum kinetic energy which can be transferred to a free electron in a single collision; it is defined as

$$T_{max} = \frac{2m_e c^2 \beta^2 \gamma^2}{1 + 2\gamma(\frac{m_e}{m_0}) + (\frac{m_e}{m_0})^2} \approx 2m_e c^2 \beta^2 \gamma^2\,; \tag{3.4}$$

$\delta(\beta\gamma)$ is a density effect correction due to energy loss in the ionization process.

The dependency of the stopping power on m_0 is only present in T_{max}. As shown in Eq. 3.4, for $m_0 \gg m_e$ the dependency on m_0 is lost. The Bethe-Block formula is not valid for electrons and positrons.

3.2 Semiconductor detectors

3.2.1 Semiconductor materials

In crystalline materials, the close and periodic arrangement of atoms in the lattice leads to energy bands for the electron states. The band structure consists of a valence band, an energy gap and a conduction band. In the valence band, all the outer shell electrons bound to a specific site of the lattice are collected. Electrons in the conduction band are free to migrate through the crystal and contribute to the electrical conductivity. The size of the band gap is determined by the lattice structure. It allows the classification of materials as insulators, semiconductors or metals. If the energy gap is about 1 eV, the material is considered a semiconductor, while if it is bigger than 5 eV the material is an insulator.

In the absence of thermal excitation, semiconductor materials have a full valence band and an empty conduction band. However, at non-zero temperatures, some thermal energy is shared among the electrons in the crystal. An electron in the valence band can gain sufficient energy to be elevated to the conduction band, leaving a vacancy (hole) in the valence band. The concentration of thermally generated electrons (holes), $n_i(T)$, at the absolute temperature T can be expressed as:

$$n_i(T) = CT^{\frac{3}{2}} e^{\left(-\frac{E_g}{2kT}\right)}, \tag{3.5}$$

where C is a proportionality factor dependent on the material, E_g is the energy band gap and k is the Boltzmann constant. Under stable conditions, an equilibrium concentration is established.

In pure or intrinsic materials, all electron-hole pairs are created by thermal excitation. Real materials, however, always have small levels of residual impurities. They effectively dominate the electrical properties of the material. Doped materials can be divided into two classes:

n-type materials: they have "donor" impurities (N_D) which have one valence electron more than the semiconductor material; these excess electrons are lightly bound to the original impurity site and lie in the band gap close to the conduction band. Thermal excitation can easily move these electrons to the conduction band. The net result is that the equilibrium concentration of electron-hole pairs thermally generated vanishes and the resistivity of the material is drastically reduced;

p-type materials: these materials show the presence of "acceptor" impurities (N_A) which have one valence electron less than the semiconductor material; electrons thermally excited can fill these holes and create an excess of holes from the semiconductor atoms in the valence band that will destroy the equilibrium concentration of electron-hole pairs thermally generated, i.e. also the resistivity of a p-type doped material is also drastically reduced.

3.2.2 Semiconductors as radiation detectors

In order to use semiconductor materials as radiation detectors, a junction between n- and p-type semiconductor materials is necessary. The junction is normally formed in a single crystal by creating a change in the impurity content from one side to the other. The different densities of conduction electrons and holes in the differently doped regions determine a diffusion of charge carriers in the junction region. The diffusion results in a net negative space charge on the p side and a net positive space charge on the n side of the junction. The accumulated space charge creates an electric field that, at equilibrium, prevents any further diffusion. The region where the electric field is created is called depletion zone.

When radiation creates electrons (holes) in the depletion zone of a p-n junction, the electric field in the depletion region sweeps out the electrons and the holes and their motion constitutes a basic electrical signal. However, in an unbiased junction the thickness of the depletion zone is quite small and the electric field is not strong enough to have a high charge collection efficiency. Therefore the p-n junction has to be reverse biased (a negative voltage, V, is applied to the p side of the junction) in order to effectively collect a signal. As the applied bias V is increased, the thickness of the depletion zone, d, i.e. the active volume of the detector, increases, while its capacitance, C, decreases:

$$d = \left(\frac{2\epsilon V}{eN}\right)^{\frac{1}{2}}, \tag{3.6}$$

$$C = \frac{\epsilon}{d} = \left(\frac{e\epsilon N}{2V}\right)^{\frac{1}{2}}, \tag{3.7}$$

where ϵ is the dielectric constant of the medium, N is the dopant concentration[1] and e is the electric charge. At a given applied voltage, the depletion region is larger and the capacitance smaller if the dopant concentration is reduced. For large germanium detectors, it is crucially important to have a low impurity concentration, such that C can be suppressed by a reasonable V.

Germanium and silicon are the most common semiconductor materials for radiation detectors. The main difference is that germanium can be purified to a much higher level. Thus, HPGe detectors can have sizes of several centimeters. Therefore, they can be used as total absorption detectors for gamma rays up to a few MeV.

Semiconductor detectors are made from n-type or p-type bulk material. For n-type detectors, the p-n junction is produced with a heavily p^+ doped surface layer. For p-type detectors, the junction is created with a heavily n^+ doped surface layer.

As the charge carriers move towards the electrodes due to the electric field, mirror charges are induced in the electrodes. These are read out using charge sensitive amplifiers. The amplitude of the signal thus created is proportional to the deposited energy. The evolution of the signal contains information about the position and possibly on the nature of the interaction.

[1] In a p-n junction the donor concentration on the n-side and the acceptor concentration in the p-side are usually not the same. N is the dopant concentration in the side of the junction with a lower dopant concentration.

3.3 Semiconductor Germanium detectors

Germanium detectors can be found in different geometries: planar or cylindrical. The maximum obtainable depletion depth for planar detector is about 2 cm, the corresponding total active volume can reach about 30 cm^3. Cylindrical detectors, can have a much larger active volume, up to about 800 cm^3. The following section is focused on germanium detectors in cylindrical configurations.

Figure 3.2 shows two different cylindrical geometries: the true coaxial geometry obtained by removing the core of the crystal and the closed-end geometry obtained by removing only part of the core. The closed-end configuration is usually preferred over the true-coaxial configuration for commercial detectors due to the smaller leakage current. The closed-end configuration also provides a planar front surface for low penetrating sources, if the electrical contact is thin enough. However, the geometry of closed-end detectors results in electric field lines, which are not fully radial, and in regions with reduced field strength in the corners of the crystal. The fully radial and easy to compute field is an advantage of the true-coaxial configuration.

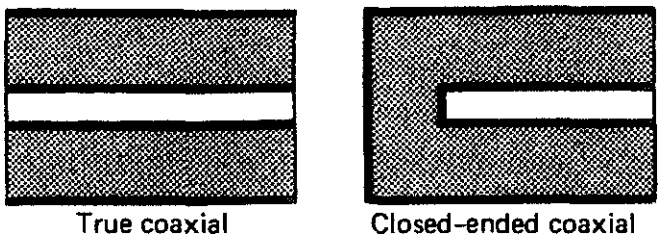

Figure 3.2: Cross-section of cylindrical detectors in two common configurations: true-coaxial on the left and closed-end on the right; the solid black lines represent electrical contacts, from [144].

Germanium detectors can be based on p- or n-type materials as already mentioned in section 3.2. Figure 3.3 shows a radial schematic for the two coaxial configurations. For n-type (p-type) detectors, the p^+ (n^+) contact is on the outer while the n^+ (p^+) contact is on the inner surface. In both configurations, the rectifying contact is on the outer surface in order to have the depletion zone growing inward and the lowest possible depletion voltage. The n^+ contacts are usually formed by diffusing lithium into the surface. The resulting layer has a thickness of up to 1 mm and has to be considered dead. The p^+ contacts are produced by implanting boron ions, accelerated to about 20 keV, into the crystal. The resulting layer has a thickness of a couple of hundred nanometers, a much thinner dead layer.

One of the biggest achievements in manufacturing germanium detectors in the last two decades is a two dimensional segmentation of the outer contact. It was developed for nuclear physics [146] in order to determine three-dimensional positions of gamma-ray interactions with an accuracy of $0.2 - 0.5$ mm. The localization technique is based on segmentation plus the analysis of the pulse shapes of the signals. Segmented germanium detectors can also be used to increase the sensitivity to neutrino-less double beta decay (see chapter 2) by background reduction through identification of multi-site events [114, 147].

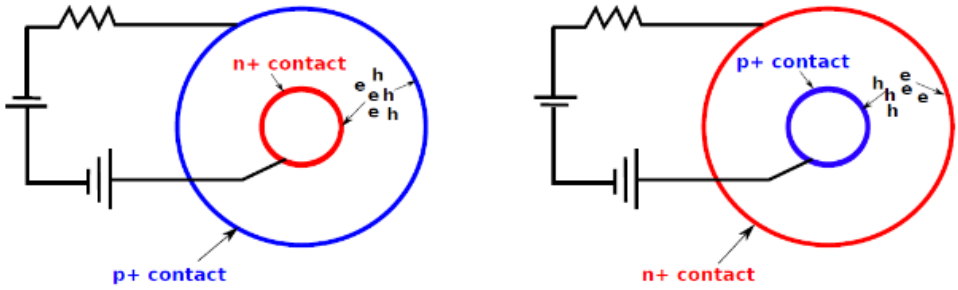

Figure 3.3: Cross sections perpendicular to the cylindrical axis of the crystal for two different types of germanium detectors: an n-type detector on the left and a p-type detector on the right, from [145].

3.3.1 Operational characteristics

Due to their small band gap (0.7eV), germanium detectors can only be operated below $\approx 100\,\mathrm{K}$ such that large thermally induced leakage current is avoided.

The dominant characteristic of germanium detectors is their excellent energy resolution. The overall energy resolution achievable for a germanium detector is due to a combination of several effects. The full width at half maximum (FWHM), W_T^2, of a typical peak in an energy spectrum can be expressed as a function of the deposited energy, E, like:

$$W_T^2 = W_D^2(E) + W_X^2(E^2) + W_E^2\,, \tag{3.8}$$

where:

$W_D^2 = (2.35)^2 F \cdot e \cdot E$ is due to the statistical fluctuation of the number of charge carriers produced by the energy deposition in the crystal; F is the Fano factor[2], e is the energy necessary to create an electron-hole pair, which in germanium is 2.96 eV;

$W_X^2 \propto E^2$ is due to an incomplete charge collection efficiency; this term is significant for large detectors or for detectors with a low electric field;

$W_E^2 =$ constant representing electronic noise.

The energy resolution of several germanium detectors are shown in section 3.3.2.

The intrinsic efficiency is defined as:

$$\epsilon_i = \frac{N(E)_{FEP}}{N(E)}\,, \tag{3.9}$$

where $N(E)_{FEP}$ is the number of counts in the full-energy peak at an energy E and $N(E)$ is the number of gamma-rays, emitted by the source with energy E, entering the detector. ϵ_i depends on the energy of the gamma-ray. In germanium detectors, ϵ_i is close to 100% for gamma-ray energies up to a few hundreds keV.

[2]The number of charge carriers can not be described by simple Poisson statistics; the Fano factor was introduced to quantify the effect [148].

3.3.2 Germanium detectors at the MPI

Research and development at the MPI is performed on detector prototypes with new ground-breaking features. Commercial germanium detectors are used as reference detectors. In the following, a brief description of two commercial germanium detectors, XtRa and REGe, and the R&D detector, Super Siegfried used for this thesis is given.

Commercial detectors: XtRa and REGe

The crystals are housed in thin aluminium vacuum cryostats. The detectors are electrically isolated from, but thermally connected to copper rods which, immersed in LN_2, acts as cooling fingers. Figure 3.4 shows a REGe detector.

Figure 3.4: REGe detector with the aluminium cryostat on the left and the LN_2 reservoir on the right.

Two different kinds of commercial germanium detectors were used:

XtRa: an eXTended Range p-type closed-end coaxial detector produced by Canberra. A thinned window contact on the front surface extends its sensitive range down to less than 5 keV. The outer n^+ contact is a Lithium diffusion layer about 0.5 mm thick;

REGe: a Reverse-Electrode n-type closed-end coaxial detector produced by Canberra. The outer p^+ contact is a Boron implantat of about 200 nm thick.

Parameter	XtRa	REGe
Detector type	p-type	n-type
Energy range	3 keV to several MeV	
Recommended temperature	~ 100 K	
Operation voltage	+3000 V	−4500 V

Table 3.1: Main geometrical and physical specifications of XtRa and REGe, from [149, 150].

The main technical characteristics of XtRa and REGe as given by the manufacturer are listed in Table 3.1.

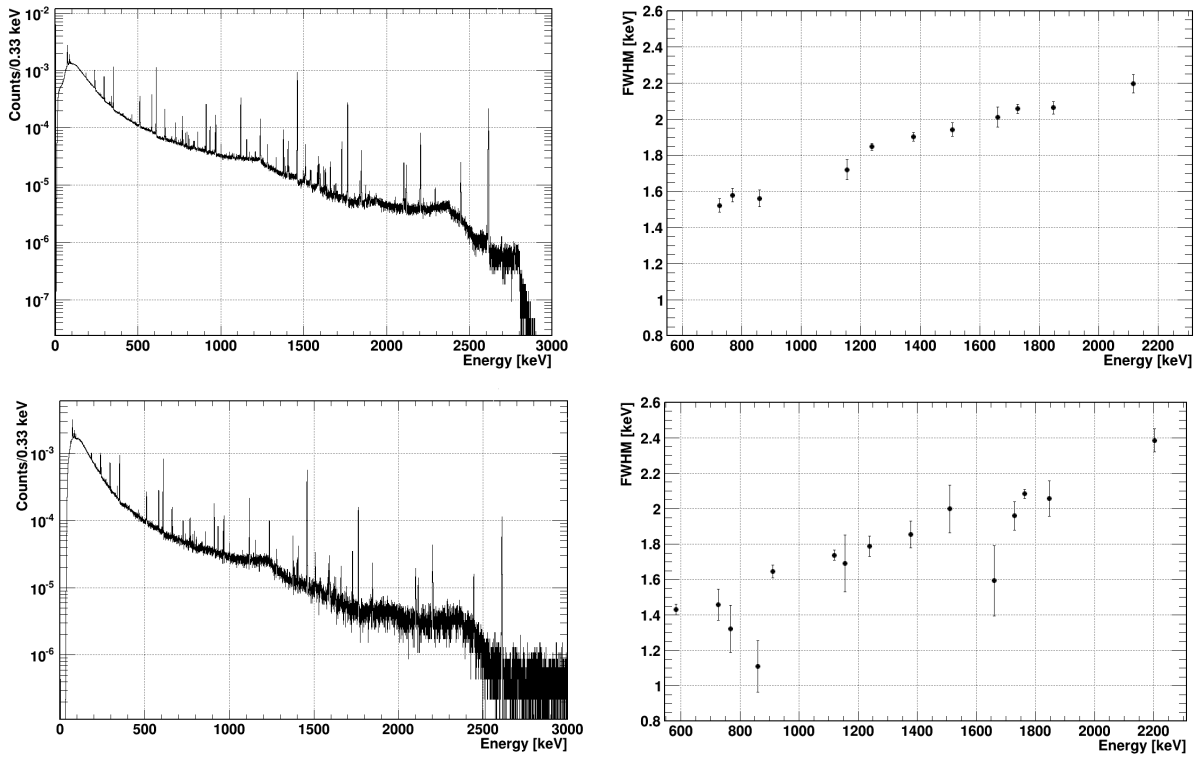

Figure 3.5: Top row: XtRa detector performance; Bottom row: REGe detector performance; on the left, the natural radioactive background spectra normalized to the number of events; on the right the FWHM as a function of the energy. The error bars represent the statistical uncertainties.

Figure 3.5 shows the detection performance of both detectors: XtRa on the top and REGe at the bottom. On the left, the energy spectrum of the natural radioactive background as measured by each detector is shown. All the main characteristic gamma lines are resolved with good energy resolution. On the right, the FWHM as a function of the energy is shown for each detector. The FWHM and its uncertainty are evaluated as described in appedix B. For both detectors, the FWHM is between 1 and 2.5 keV over the energy range. The two detectors have about the same performance. The measurements presented in appendix A were performed on XtRa and REGe.

R&D Detector

The MPI owns a number of true-coaxial R&D detectors. They are operated in various test setups. Available are the vacuum cryostat K1 [114], the Gerdalinchen facility for submersion in LN_2 [151] and the 3d scanning facility GALATEA [10, 145, 152]. A number of true-coaxial detectors have been characterized [153–155]. The main focus was the effect of segmentation (see Sec. 3.3) to enhance the sensitivity for $0\nu\beta\beta$-decay. In the following, there is a brief description of the detector used for the measurements presented in this thesis.

Super Siegfried (SuSie) Figure 3.6 shows the Super Siegfried (SuSie) detector ready for installation in the GALATEA test-facility. The main parameters of SuSie, as reported by the manufacturer, are also listed.

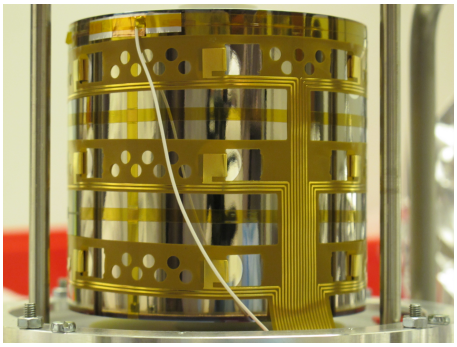

Parameter	Super Siegfried
Height	70.0 mm
Outer radius	37.5 mm
Inner radius	5.0 mm
Mass	1634.5 g
Impurity level, bottom	$1.30 \times 10^{10}/\mathrm{cm}^3$
Impurity level, top	$0.44 \times 10^{10}/\mathrm{cm}^3$
Operation voltage	+3000 V

Figure 3.6: Super Siegfried: on the left, a picture of SuSie, ready for installation in GALATEA, see chapter 4; on the right, a list of the main parameters of SuSie, from [156].

SuSie, already previously characterized in detail [157], is a true-coaxial n-type HPGe detector with an 18+1-fold segmentation. The inner n^+ electrode (core) is lithium drifted while the outer p^+ electrodes (segments) are boron implants. The detector was produced by Canberra France. A 5 mm thick segment, unsegmented in ϕ, was created at the top of the detector. This additional segment makes SuSie suitable for studies of surface effects using low penetrating sources. This will be discussed in detail later in the thesis. The Boron implant of the top segment covers only the outer surface. The top surface is protected by a passivation layer. The remaining outer p^+ contact is 6-fold segmented in ϕ and 3-fold segmented in z.

During the operation of SuSie in GALATEA, a reprocessing of the detector was necessary. At that point, it was decided to change the metalization scheme of the segments. From now on SuSie I refers to the detector before and SuSie II after reprocessing.

SuSie I The 18 regular segments of the detector were partially metallized. Only a circular area with a radius of about 2 mm in the middle of each segment was metallized. The top segment had only a sector on the side surface metallized (see Fig. 3.7, top). Reducing the metalization reduces the material on the crystal and therefore the background expected in the region of interest for either $0\nu\beta\beta$-decay or dark matter searches. However, the partial metalization affects the field, and thus the charge collection efficiency and the energy resolution of the detector. Such effects are still under discussion;

SuSie II: has all the segments, including the top one, fully metallized (see Fig. 3.7, bottom).

The individual segments are read out using a Kapton printed-circuit-board (PCB). The contacts between the segments and the PCB are created with "snap-contacts" [114]. The contact to the top segment was made using a 2 cm metallic strip. The read out cable was soldered to the metal strip.

The measurements on surface events were performed on SuSie I and SuSie II. In chapter 4, the operation of SuSie I and SuSie II in GALATEA is discussed in detail.

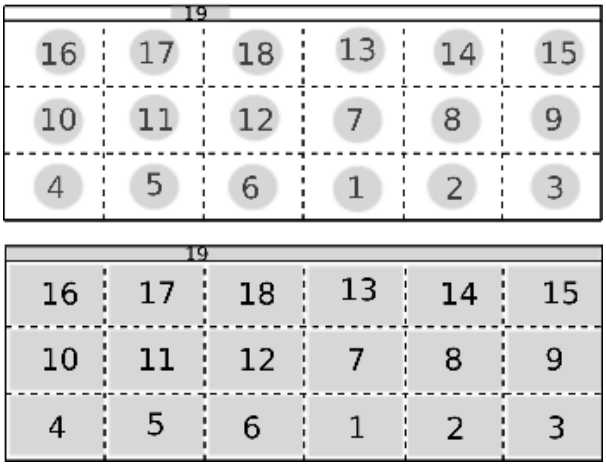

Figure 3.7: Unfolded view of the metalization scheme for the Super Siegfried detector; top: SuSie I with all the segments partially metallized (circular area not to scale); bottom: SuSie II with all the segments fully metallized.

Chapter 4

Detector operation in the GALATEA test-facility

GALATEA is a test-facility to characterize HPGe detectors. It is important to have a test-stand where detectors can be probed with different kinds of movable radioactive sources. The most important aspect of GALATEA is that the radioactive sources are placed inside the vacuum tank that hosts the detector. Thus, low penetrating sources like alpha and beta emitters can be used to study surface effects on germanium detectors.

In section 4.1, GALATEA is briefly described, with the focus on the main aspects of the apparatus and the monitoring system. In section 4.2, measurements in the GALATEA test-facility on SuSie I and SuSie II (see Sec. 3.3.2) are presented.

4.1 The experimental setup

The GALATEA test-facility has already previously been described in detail [10, 145, 152]. The optimization of its performance was a substantial part of the work for this thesis. Figure 4.1 shows the interior of the main vacuum tank of the test-facility. On the right, the inside is illustrated in a 3D design drawing. On the left, two pictures, taken during the installation of SuSie I in GALATEA, show all the components depicted in the sketch. The main technical features of the test-facility GALATEA are:

Vacuum: The vacuum in which germanium detectors are operated has to be better than 10^{-4} mbar. The GALATEA tank reaches pressures of around 5×10^{-9} mbar, when the cold volume is pumped. However, micro-phonic effects from the working pump would make detector operation impossible. Therefore the pump is switched off during measurements. A shutter separates the tank from the pump volume. Metal seals and a careful conditioning-procedure [152] allow to maintain a good vacuum ($\mathcal{O}(10^{-6})$ mbar) for several weeks without pumping when the system is cold. The improvement of the quality of the vacuum in GALATEA to this level was a major success.

Cryogenic temperature: As shown in Fig. 4.1, a liquid nitrogen (LN_2) tank (cryo-tank) is located at the bottom of the vacuum tank. The detector holder sits on top of a copper cooling

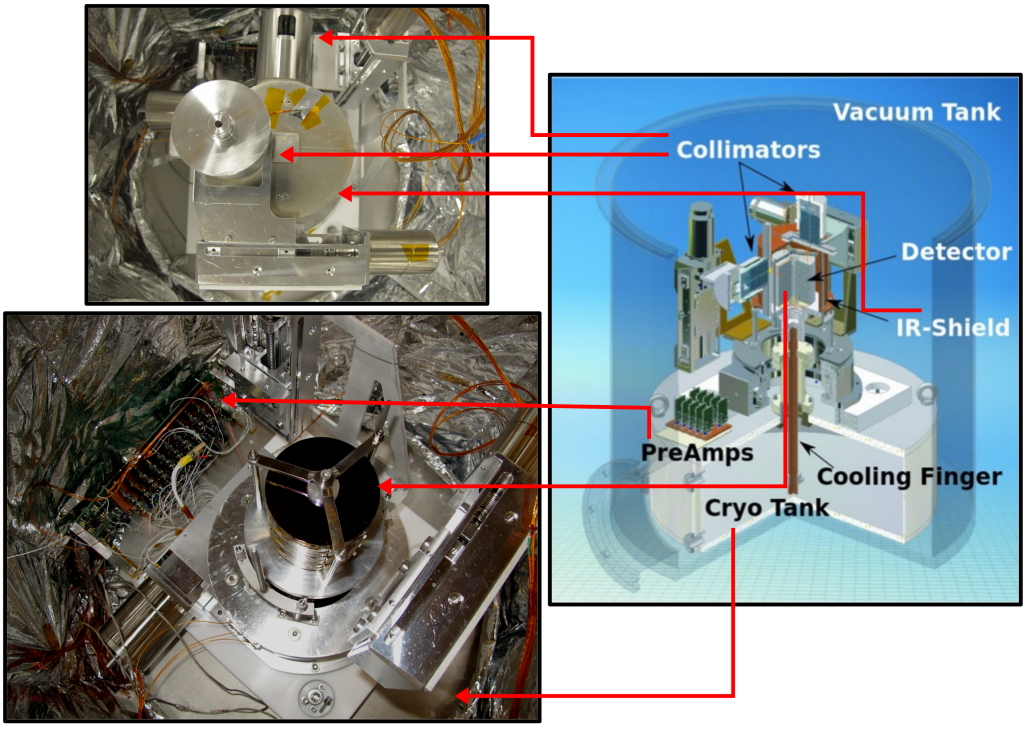

Figure 4.1: The inside of the GALATEA tank: on the left, pictures taken during the commissioning phase and on the right, a sketch of the complete setup.

finger, which is immersed in the cryo-tank. The operational temperature of the detector is usually between $100 - 110\,\mathrm{K}$;

IR-shield: Uncontrolled infra-red radiation from the outer wall would make detector operation impossible. A shield made of electropolished and silver coated copper surrounds the detector. In addition, the inside of the tank is thermally insulated from the outer wall by a mash holding a multiple layers of cryogenic foil as shown in Fig. 4.2. The substantial improvement of the temperature due to this outer shield separated from the wall was another success of the optimization work.

Scanning system: it consists of two collimators operated with tungsten or plastic segments to collimate gamma, alpha or beta particles. The top left picture in Fig. 4.1 shows the two collimator-systems. They are moved by three motors which allow a complete scan of the detector. The top collimator can be moved horizontally along the radius of the detector. The side collimator can be moved vertically along the height of the detector. Both the collimators can be rotated around the axis of the detector, i.e. along the azimuthal angle. The IR-shield has two slits for the radioactive sources. The absence of material between source and detector allows the usage of low

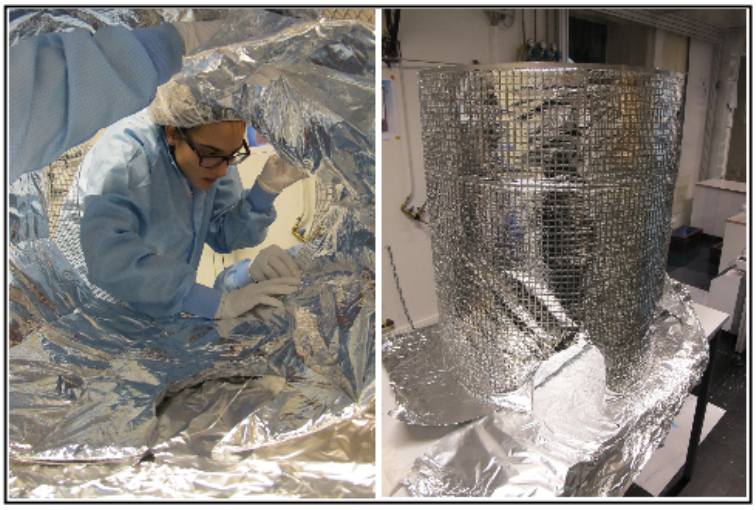

Figure 4.2: Mounting of the mash holding a multiple layers of cryogenic foil.

penetrating sources to study interactions close to the detector surface. The commissioning of the scanning system was another substantial part of the work for this thesis. During the data taking in December 2013, a problem with the rotation of the IR-shield was discovered. The shield had to slide over the holder. Unfortunately, it cold-fused and the rotational stage dragged the detector holder along. This caused major damage to the setup and the detector. Diligent tests revealed that the shielding hat was not a viable long-term solution. A solution with the hat lifted during rotation is being implemented;

Electronics: An electronic board holding the charge-sensitive pre-amplifiers to read out the signals from the detector and the HV circuit to bias the detector, is mounted on top of the cryo-tank. The read-out cables are kept as short as possible to minimize capacitances and thus optimize detector resolution.

DAQ system: The measurements in GALATEA were performed with a DGF Pixie-4 multi-channel data acquisition system produced by XIA [158]. The software used to communicate with the Pixie-4 modules was the graphical user interface IGOR from Wavemetrics [159].

4.1.1 Environmental monitoring

The system is equipped with 15 sensors to monitor the environment of the detector during operation. Its commissioning was a part of the work for this thesis. Reliable monitoring is a prerequisite for the safe operation of GALATEA. Figure 4.3 shows the main parameters during a typical operational cycle from a pumping and cooling phase to the detector operation phase. These data were taken during the first data taking period in August 2013. The parameters are:

Pressure: It is monitored using two pressure gauges with different working ranges placed in

two different locations. A full range gauge is placed at the side of the tank while a BARION sensor is placed at the top of the lid [1]. Figure 4.3a shows the behaviour of the pressure during a complete operational cycle. The blue (red) line represents the pressure measured by the full range gauge (BARION sensor). During pumping and cooling the pressure can reach values around 5×10^{-9} mbar. The volume is not pumped during operation and the pressure rises to around 3 to 4×10^{-6} mbar. As soon as the tank is pumped again, the pressure drops to the high-vacuum regime again.

Liquid Nitrogen Level: The cryo-tank is automatically refilled from a reservoir outside of the tank. A LN-level controller based on a capacitance measurement [152] is used. Figure 4.3b shows the behaviour of the capacitance for several refilling cycles during data taking. Once the cryo-tank is refilled, the capacitance goes up to about 24 pF. After it decreases to around 19 pF, the controller starts the automatic refilling. The time between refillings is usually around 20-30 hours.

Temperature: The detector should never be the coldest point inside the tank. Otherwise it would act like a cold pump and attract remnant particles floating inside the tank. The temperatures inside and outside the tank are monitored using pt-100 sensors. Figure 4.3c shows the behaviour of the temperatures inside the tank during a complete operational cycle. The temperatures follow the refilling cycles. The lowest temperature is always registered by the sensor placed on top of the cryo-tank. Figure 4.3d shows the behaviour of the temperatures outside the tank during a complete operational cycle; these temperatures are only minimally affected by the LN refilling.

4.2 Detector operation in GALATEA

Inside GALATEA, detectors are tested and characterized using different sources:

- alpha particles from sources like ^{241}Am, are collimated and used to probe the surfaces of a detector. Surface effects are studied, and dead layers evaluated. Alpha events are characterized. Measurements on alpha particles probing SuSie I are discussed in detail later in this thesis;
- low energy gamma-rays from sources like ^{133}Ba or ^{152}Eu are collimated and used to scan the outer layers of the detectors and determine crystallographic axes or segment boundaries;
- medium or high energy gamma-rays from sources like ^{60}Co or ^{228}Th placed outside the tank and used to perform bulk measurements. Bulk events are used to optimize the noise level, study the influence of the monitoring sensors, and test the data-quality and selection software.

In the following, the performances of the GALATEA test-facility is demonstrated via several bulk measurements.

[1] The full range gauge can measure pressures up to 1 bar. The BARION sensor measures pressures lower than 10^{-3} mbar. The BARION sensor is more reliable in the high-vacuum pressure range.

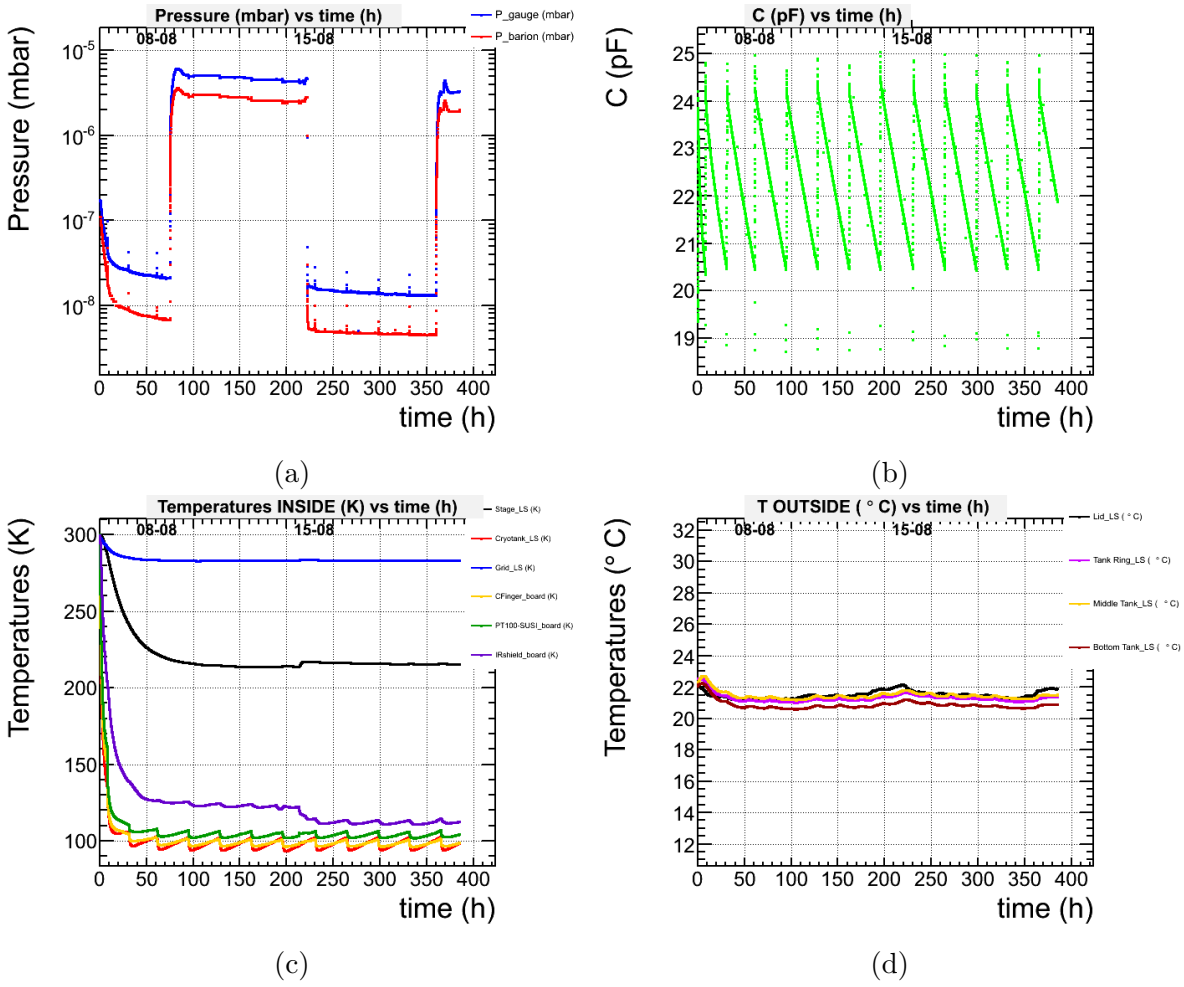

Figure 4.3: Online monitoring during 11 LN refilling cycles after initial coll down. Measurements were taken for 5 cycles before pumping resumed.

4.2.1 Natural radioactive background

The natural radioactive background (BKG) is regularly recorded between the measurements of a scan. This is important to test the stability of the setup and the detector itself. A scan consists of a set of measurements with changing position of the radioactive source. An entire scan can last more than a week. During a scan, two sources are present inside GALATEA: one mounted in the top collimator (top source) and one in the side collimator (side source). During a BKG measurement, both sources are moved as far as possible away from the detector (see Fig. 4.4).

Figure 4.5 shows an example of the background energy spectra obtained with SuSie I in December 2013 (BKG11, as listed in Table D.1). On the top left (right), the energy spectra from the core (segment 19 on the top) are shown. The spectra from the bulk segments are shown below.

The core spectrum shows all the main lines of the natural radioactive background. During

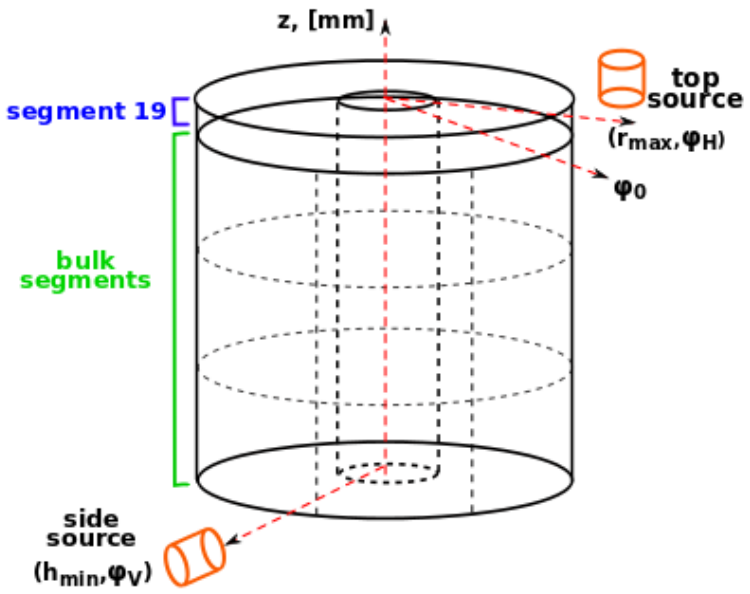

Figure 4.4: Sketch (not to scale) of the relative positions of the detector and the sources inside GALATEA during a background measurement.

this BKG measurement, a ^{152}Eu source was placed in the side collimator while a ^{241}Am source was inside the top collimator. Even tough the collimators were placed as shown in Fig. 4.4, some of the high energy lines from the ^{152}Eu are still visible in the core spectrum. From the intensity of the lines in the bulk segments, it is possible to deduce the azimuthal position of the side collimator (between segment 4 and segment 3). The strongest lines in the spectrum are listed in Table 4.1. Segment 19 does not show the strong lines because in most cases, it is too thin to fully contain the full energy.

Detector stability

Regularly taken BKG measurements were used to test the stability of the detector. This was done by monitoring output values that should be constant in time like the count rates from natural radioactivity. The energy resolution of the detector should also not change. Any significant change in one of these parameters would indicate a problem of the system or of the detector itself.

Figure 4.6 shows the count rate in the core (top) and the core resolution (bottom) as a function of time for three different gamma lines from natural radioactivity. The lines are in three different energy ranges: 609.38 keV and 1764.49 keV from ^{214}Bi, and 2614.50 keV from ^{228}Tl. Eleven BKG measurements were taken between August 29 and December 17, 2013 (see Table D.1). The count rate and the FWHM together with their uncertainties were calculated as explained in appendix B. The error bars represent the statistical uncertainties. The count rate and the resolution are stable for all three lines during the three months under investigation. It was a major step towards the full operation of GALATEA to establish long-term stability for a system with the electronics operated inside the vacuum tank.

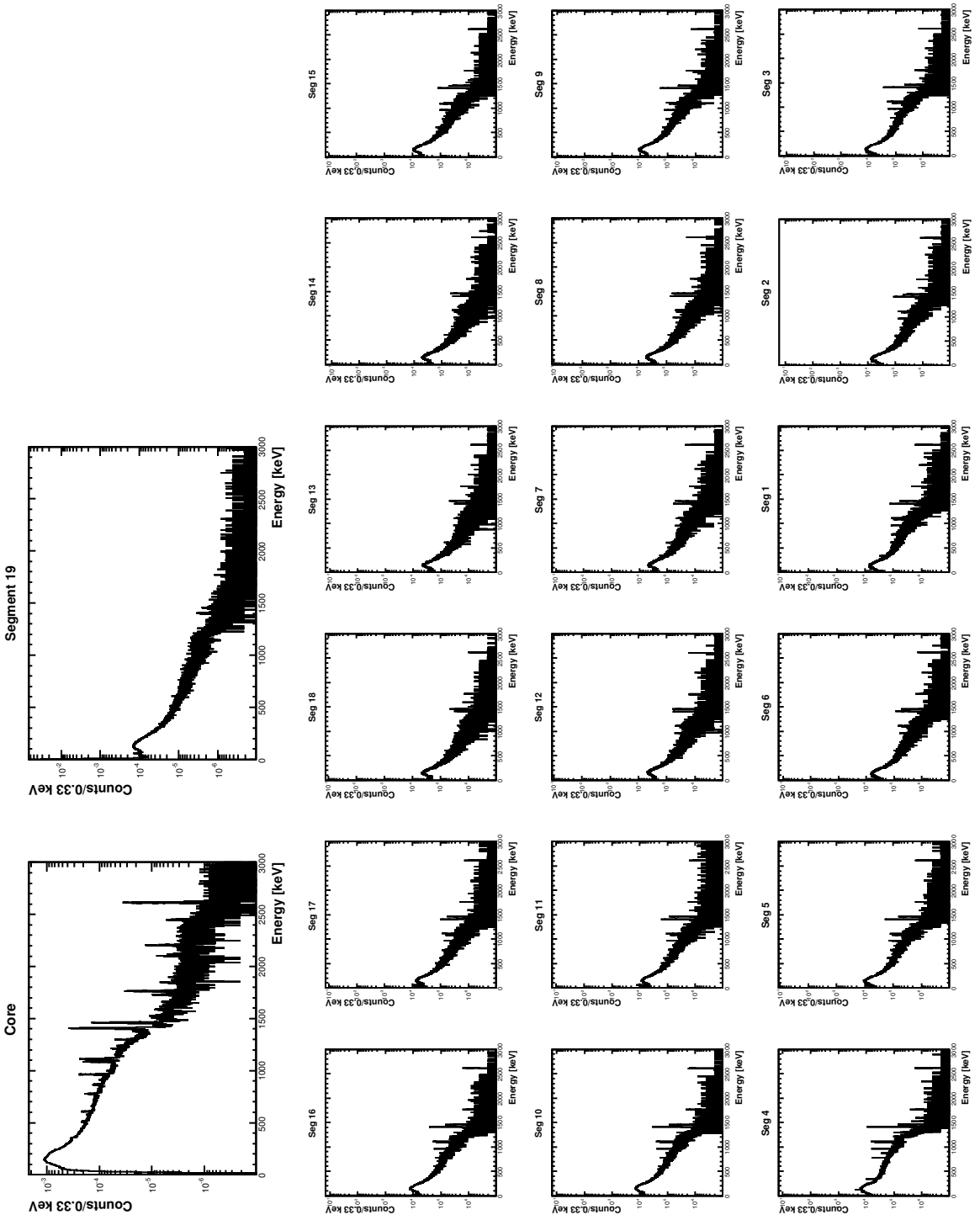

Figure 4.5: Natural background spectra of the core (top left), the top segment (top right) and the 18 regular segments of SuSie I measured in December 2013 (BKG11 measurement as listed in Table D.1).

BKG Radiation	Energy [keV]	Internal Source	Energy [keV]
annihilation peak	511.00	^{152}Eu	778.90
^{208}Tl (Th chain)	583.25	^{152}Eu	964.08
^{214}Bi (U chain)	609.38	^{152}Eu	1085.90
^{40}K	1460.99	^{152}Eu	1112.10
^{214}Bi (U chain)	1764.68	^{152}Eu	1408.00
^{208}Tl (Th chain)	2614.50		

Table 4.1: List of the strongest lines in the core energy spectrum shown in Fig. 4.5: on the left, the lines due to natural background; on the right, the lines due to the internal ^{152}Eu source. For each line, the source and the line energy are listed.

Detector performance

After the accident described in section 4.1, SuSie had to be reprocessed after its first operation in GALATEA. After the reprocessing, background measurements were taken to again characterize the detector. In the following, the performance of SuSie I and SuSie II in background measurements is compared.

Figure 4.7 (top) shows a comparison between the background measured in the core with SuSie I (black) and SuSie II(red); on the bottom, a comparison of the energy resolutions as a function of the energy for the two detectors is given. The energy resolution in general is improved by a factor of 2 for SuSie II. It has to be noted, however, that the two BKG measurements were performed under different conditions:

1. the radioactive sources inside GALATEA during the two measurements were not the same; the top source was ^{241}Am during both measurements; the side source was ^{152}Eu (^{133}Ba) during the measurement performed with SuSie I (SuSie II). The red spectrum indeed does not show the 1085.90 keV and the 1408.00 keV lines form the ^{152}Eu source. The black spectrum as well does not show the 133.60 keV and the 356.00 keV lines from the ^{133}Ba source;

2. the DAQ trigger threshold on the core channel was reduced to make measurements with the 30.63 and 80.40 keV lines of ^{133}Ba possible. The different shape of the spectra in the low energy region is due to the different trigger threshold;

3. features like a web-cam were added to the setup.

Missing peaks are due to 1. The difference in the low energy Compton spectrum are due to 1 and 2. Number 3 has no influence. The improvement in resolution is unlikely to be due to the setup. More likely, it is due to the new metalization scheme. An investigation of this is still ongoing.

4.2.2 Calibration and noise

Measurements to calibrate a detector operated in GALATEA are done with uncollimated high-energy gamma sources placed on top of the lid of the tank, approximately $30-40$ cm from the top

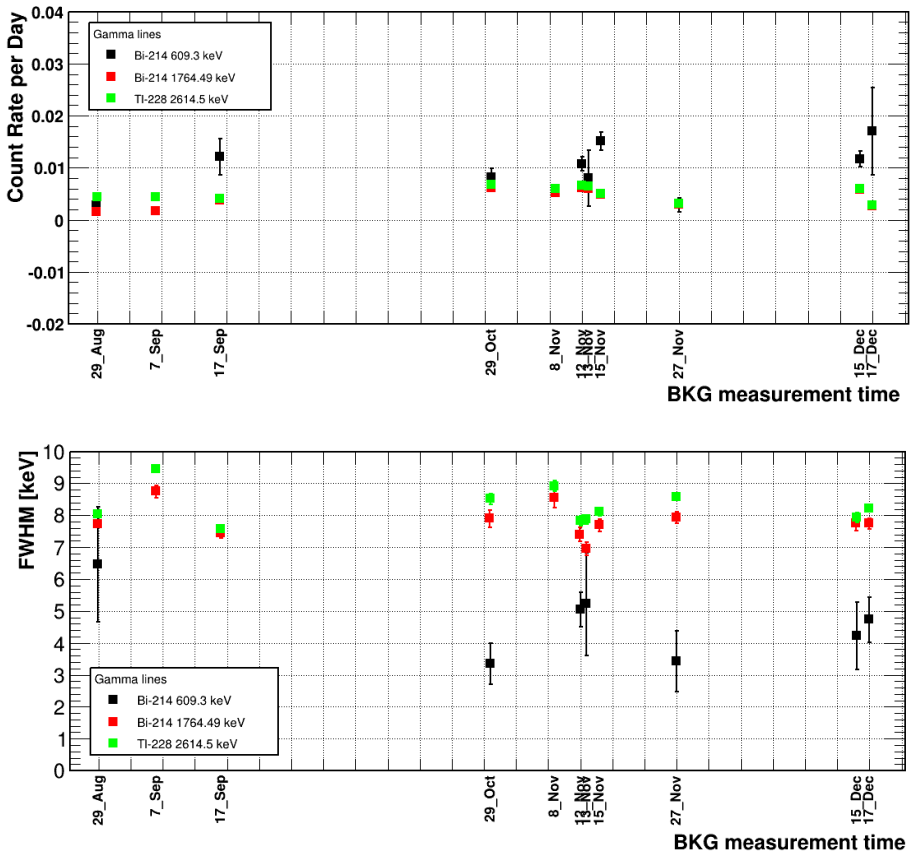

Figure 4.6: Core count-rates per day (top) and core energy-resolutions (bottom) for three background lines as a function of time: the 609.38 keV line from ^{214}Bi in black, the 1764.49 keV from ^{214}Bi in red and the 2614.5 keV line from ^{228}Tl in green. The error bars represent the statistical uncertainties calculated as introduced in appendix B. The results are based on measurements from BKG set as listed in Table D.1.

surface of the detector. Using a ^{228}Th as a calibration source, studies to optimize the noise level were performed. The electronic noise not only comes from the electronics read-out itself, but also from any electronic device connected to the setup, e.g. all the monitoring devices. Calibration measurements were performed with different configurations of the monitoring sensors in order to establish which of the sensors induce noise. A complete list of the measurements is available in Table D.1. Figure 4.8 shows a comparison between the energy resolution as a function of the energy for different sensor configurations.

The best energy resolution, i.e. the lowest noise level, was obtained for the configuration with all the monitoring sensors off (all sensors OFF). The worst energy resolution was obtained when all the sensors were on (all sensors ON). The data visualised in Fig. 4.8 seem to indicate that only the combined usage of the two pressure sensors (pressure OFF others ON) drastically increase the noise level. Using only one of the two sensors (only Single Gauge ON or only BARION

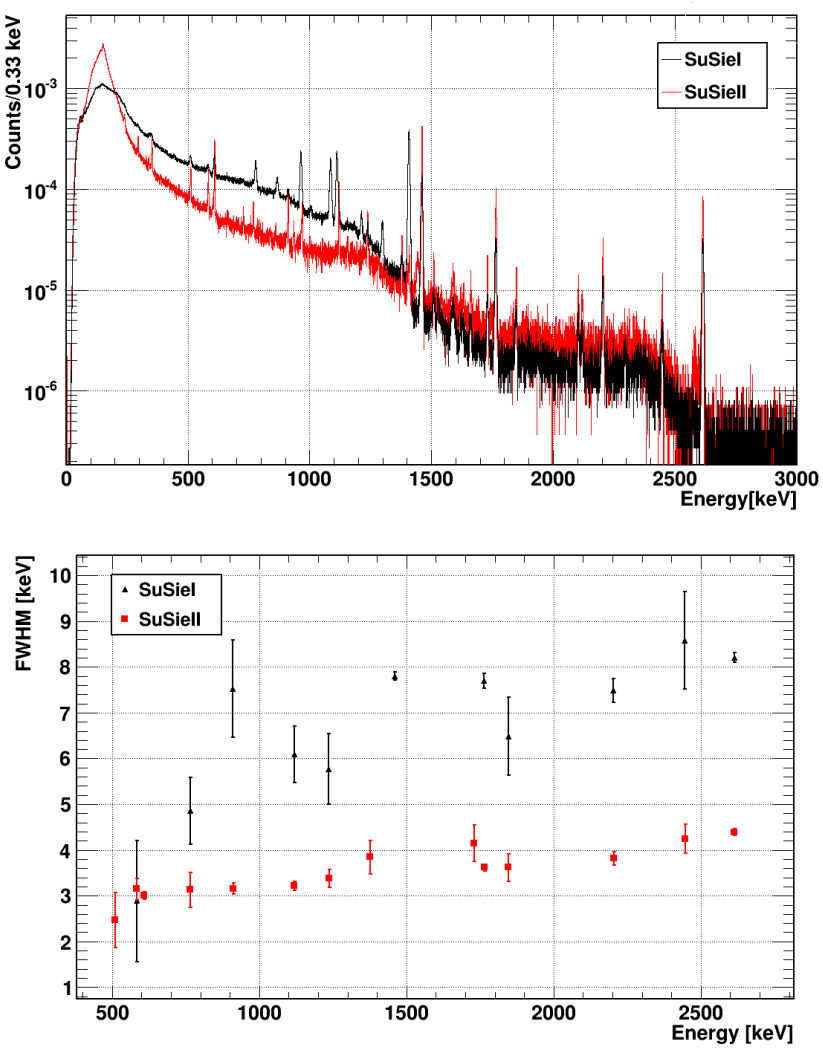

Figure 4.7: Top: comparison of natural radioactive background spectra measured with SuSie I (black line) and SuSie II (red line). Bottom: comparison of the FWHM, computed as described in appendix B, as a function of the energy for SuSie I (black) and SuSie II (red); the error bars represent the statistical uncertainty on the FWHM.

sensor ON, see section 4.1), the noise level is still reasonable. However, during the data taking for this thesis all sensors were switched on during all measurements. This is also true for SuSie II measurements where the resolutions was much improved.

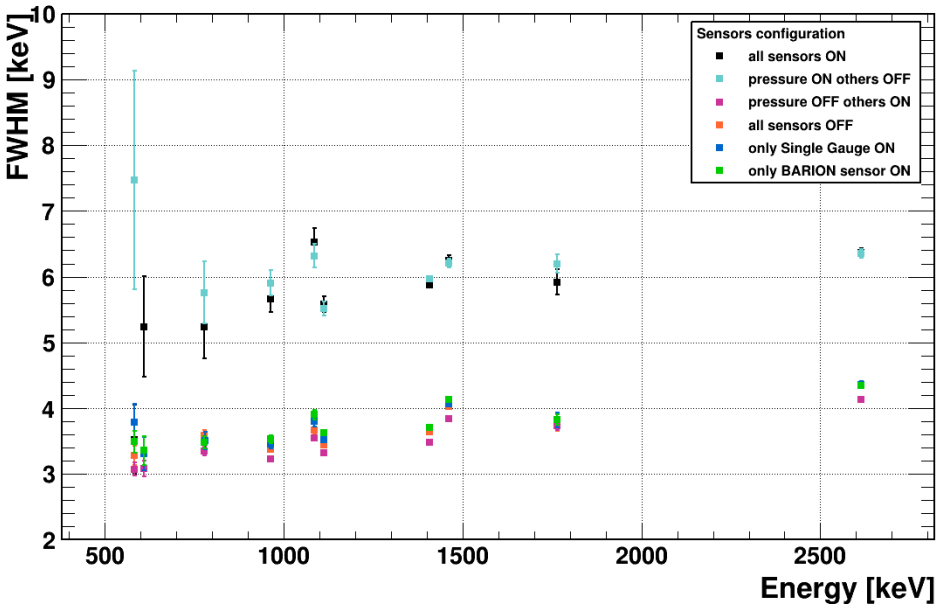

Figure 4.8: Effect on the energy resolution of different configuration of the monitoring sensors. The FWHM and their uncertainties were obtained as described in appendix B. The error bars represent the statistical uncertainties of the FWHM.

Chapter 5

Cross talk and energy calibration of segmented detectors

One of the most important properties of germanium detectors is their extremely good energy resolution. In segmented germanium detectors, cross talk can, however, affect this resolution. Cross talk has therefore to be taken into account. In this chapter, a robust and automized procedure to calibrate any kind of germanium detector is presented.

Different sources and effects of cross talk are described in section 5.1. In section 5.2, the calibration procedure for segmented detector is described step by step from the core calibration to the cross talk correction and calibration of each segment. In section 5.3, the stability in time of the calibration factors is presented.

5.1 Cross talk

Cross talk in segmented germanium detectors is well established [160, 161]. It worsens the energy resolution and deteriorates the pulses, thereby disturbing energy measurements and pulse shape analysis. In this section, different sources of cross talk and their effects are described.

5.1.1 Origin of cross talk

Cross talk can be described as the electromagnetic induction of a signal in a neighbouring "signal-processing" system. In the following, the possible sources of cross talk operating a segmented detector such as SuSie, in a system like GALATEA, are listed:

intrinsic cross talk: it is due to the capacitive coupling between the detector electrodes. This kind of cross talk is usually really small ($\mathcal{O}(0.1\%)$). Figure 5.1a shows how the intrinsic cross talk is originated in an n-type coaxial detector: the lithium drift creates an n^+-contact in the bore hole which can capacitively couple to the p^+-contacts of each outer segment, creating core-to-segment cross talk; p^+-contacts of different outer segments can also couple to each other, creating segment-to-segment cross talk. The amount of cross talk depends on the coupling capacities C_{0i} or C_{ij} between the core and the i^{th} segment and between the i^{th} and j^{th} segment respectively. Intrinsic cross talk is symmetric;

due to cables: a signal collected on the relevant electrode is brought to a pre-amplifier through a read-out cable. The signal from the core is amplified by a FET directly connected to the core electrode, see section 4.1. Cables close to each other induce cross talk. This kind of cross talk can be asymmetric due to the different strength of the signals brought trough nearby cables. The negative core signal, already amplified is transmitted on a cable which runs close to the cables from the outer segment electrodes with unamplified signals. Shielded cables cannot be used due to their large capacity per unit length and the routing options for the cables are limited. The resulting core-to-segment cross talk is large. It dominates in the setup used for this work. Figure 5.1b shows what happens when there is an energy deposition in segment i. If segment j is not hit by the radiation, in absence of cross talk no energy deposition is expected in segment j. The solid (dashed) line represents the signal in segment j in the presence (absence) of core-to-segment$_j$ cross talk.

due to pre-amplifiers: as the pre-amplifiers collecting signals from the detector are mounted parallel to each other, they act like capacitors charging up in close proximity. Cross talk can be introduced between segments with pre-amplifiers mounted close to each other on the electronics board, see Fig. 4.1. This kind of cross talk is symmetric.

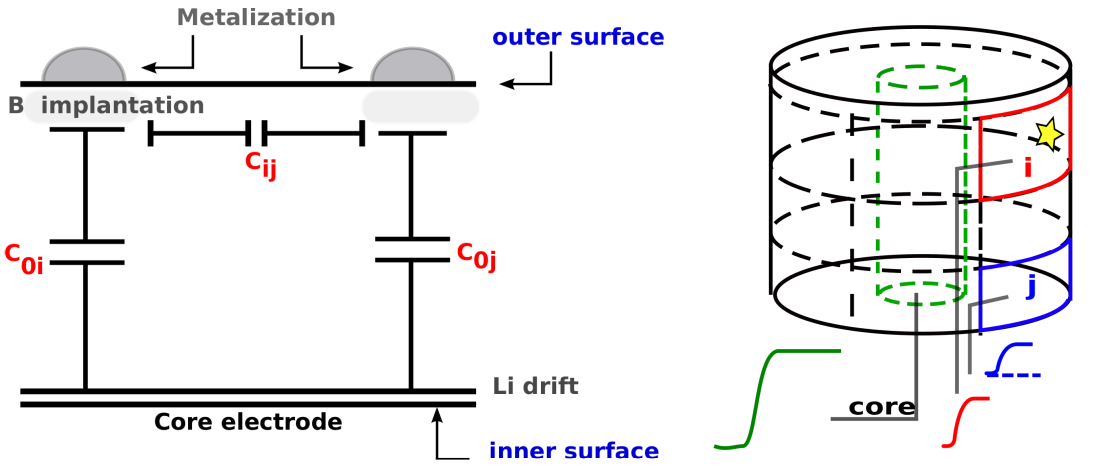

(a) (b)

Figure 5.1: Schematics for different sources of cross talk which occur for SuSie mounted in GALATEA: a)intrinsic cross talk induced by the capacitive coupling either between the central core electrode and each outer segment electrode or between neighbouring outer electrodes; b) core-to-segment$_j$ cross talk in the cables due to the proximity of cables. The green solid line is the signal from the core, the red line the signal from the hit segment, i.e. segment i. The solid (dashed) blue line is the signal from segment j in the presence (absence) of core-to-segment$_j$ cross talk.

The cross talk depends on the speed, amplitude and risetime of the signal. It has two different components:

- proportional component: it is proportional to the inducing signal, i.e. to the charge. This dominates for long risetimes. In the following, it is shown that the proportional component is dominant in the system used for this work;
- differential component [162]: it is proportional to the derivative of the inducing signal, i.e. to the current. It can result in spurious transient signals. This becomes important for short risetimes with large currents. Evidence of differential cross talk is shown in chapter 7.

5.1.2 Effects of cross talk

Proportional cross talk affects the energy spectra. The energy resolution of the detector gets worse. Per construction, the cross talk from the capacitive coupling of the electrodes and from the pre-amplifiers is small. Due to the cabling and to the amplification of the core signal, the biggest cross talk is the core-to-segment one. Cross talk from cables between segments is smaller as none of the signals is amplified.

The effect of cross talk was studied using a non collimated ^{228}Th source placed on top of the GALATEA lid. The internal radioactive sources were placed as for background measurements as shown in Fig. 4.4. All the results shown in this chapter refer to the ^{228}Th calibration dataset CAL01 as listed in Tab. D.1 in appendix D.

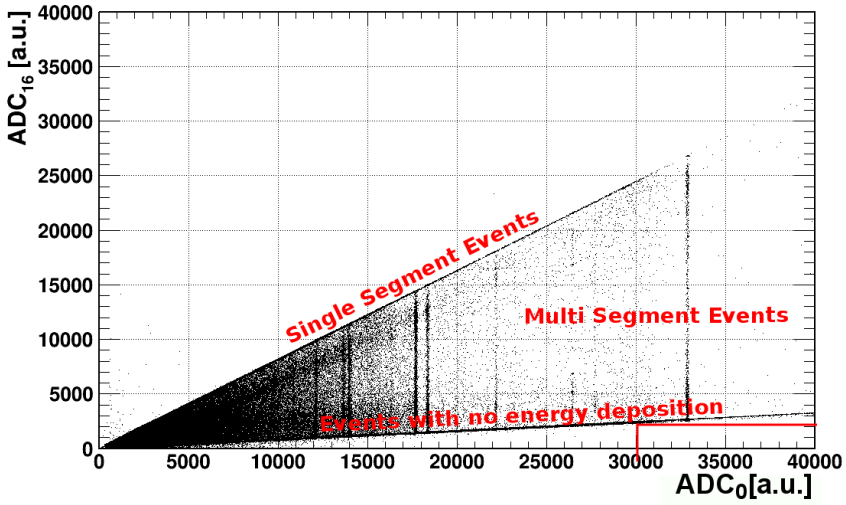

Figure 5.2: Correlation plot between ADC counts from segment 16 and the core. The effect of the cross talk is visible as the absence of events with zero segment-16 energy for higher core energies.

Figure 5.2 shows the correlation plot between ADC counts from the core and ADC counts from segment 16. The cross talk in segment 16 is $\approx 7\%$ ($\approx 2000/30000$). In the correlation plot, three different populations of events can be identified:

1. the events on the upper line are segment-16 single segment events (SSE). The incident radiation interacts only in segment 16 and a net energy deposition is recorded only in segment 16 and in the core;

2. the events on the lower line are the events without energy deposition in segment 16. In the absence of cross talk, this class of events would be distributed in a horizontal line around zero ADC counts in segment 16;

3. the events between the lines are multi segments events (MSE), i.e. events with energy depositions in multiple segments. The vertical lines are the gamma lines from the natural radioactive background, from the calibration source, ^{228}Th, and the radioactive sources inside GALATEA. In the absence of cross talk, the sum of the energies recorded in all the segments should be equal to the core energy, within the energy resolution.

In the following section, two different methods are introduced to quantify the amount of core-to-segment cross talk for all segments.

5.2 Calibration of segmented detectors

The procedure used to calibrate segmented germanium detectors consists of three steps:

1. the core calibration, described in section 5.2.1, where the core is assumed to be cross-talk-free;

2. the extraction of first order core-to-segment cross talk and calibration factors, described in section 5.2.2. Two similar methods are compared;

3. the extraction of second order cross talk factors, described in section 5.2.3, where segment-to-core and segment-to-segment cross talk are evaluated.

The procedure was proven to be flexible and suitable for different cross-talk situations[1]. The improvement and automation of the procedure was a big part of the work for this thesis.

5.2.1 Core calibration

Any segment-to-core cross talk is neglected. The core is independently calibrated using known gamma lines. The relation between the energy, E_0, and the ADC counts, ADC_0, in the core, is assumed to be linear:

$$E_0 = o_0 + s_0 \cdot ADC_0 \,, \tag{5.1}$$

where o_0 and s_0 are the offset and the slope of the calibration function.

The main steps of the core calibration procedure are:

1. **description of radioactive sources**: a list of expected gamma lines (source_lines) has to be provided. An example of a source description, which can be used in the algorithm, is reported in appendix E;

2. **analysis of the core spectrum**: the TSpectrum [163] tool in the ROOT [164] analysis software framework is used to extract a list of the strongest lines in the measured spectrum (data_lines);

[1] The procedure has been successfully applied to data from true-coaxial and Broad-Energy segmented detectors mounted in different setups.

3. **pre-calibration**: a first mapping between the source_lines and the data_lines is performed as follows (see Fig. 5.3):

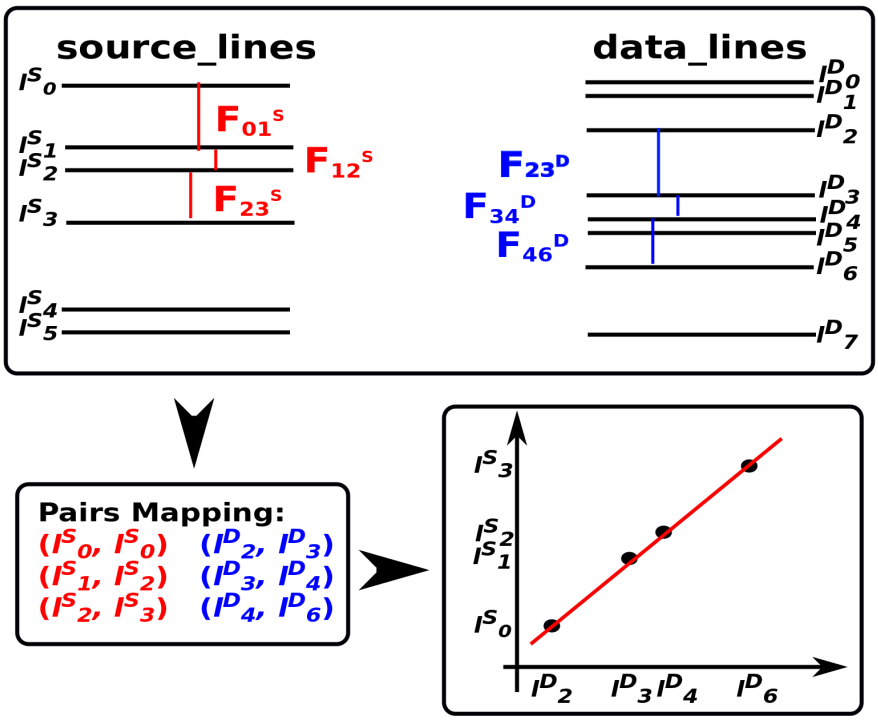

Figure 5.3: Pre-calibration algorithm: the mapping is done between the source_lines and the data_lines minimizing the factor C defined in eq. 5.3. Once the mapping is obtained, the ADC values of the mapped data_lines are correlated with the energies of the mapped source_lines and a linear fit is performed.

a) the normalized distances between lines from the same list is defined as:

$$F_{ij}^{\text{list}} = \frac{l_j^{\text{list}} - l_i^{\text{list}}}{l_i^{\text{list}}}\,, \tag{5.2}$$

where i and j are ascending indexes running either on the data_lines (for list = D), or on the source_lines lists (for list = S), i.e. l_i^S is the energy of the i^{th} line in the source_lines and l_i^D is the ADC value of the i^{th} line in the ADC spectrum.

b) for each pair of lines among the source_lines with F_{ij}^S, the algorithm looks for the best corresponding pair of lines among the data_lines with F_{kl}^D by minimizing the value:

$$C = \left| 1 - \frac{F_{ij}^D}{F_{kl}^S} \right| ; \tag{5.3}$$

c) once the mapping is established, the ADC counts of the selected data_lines are correlated with the energies of the selected source_lines and a linear fit is performed. Two preliminary calibration parameters, o_0^{pre} and s_0^{pre} are determined;

4. **optimization of the mapping:**

a) the ADC core spectrum is divided into sub-ranges around values defined as:

$$ADC_0^i = \frac{E_0^i - o_0^{pre}}{s_0^{pre}}\,, \tag{5.4}$$

where $i = 1, ..., L$ with L being the total number of lines with energy E_0^i;

b) the lines in the different energy sub-ranges are fitted with a modified Gaussian (see appendix B). A typical result of the fitting procedure is shown in Fig. 5.4a;

c) the mean value of a Gaussian, μ_0^i, is accepted for the optimized mapping if

$$E_0^i - (o_0^{pre} + s_0^{pre} \cdot \mu_0^i) < 0.1\,\mathrm{keV}\,. \tag{5.5}$$

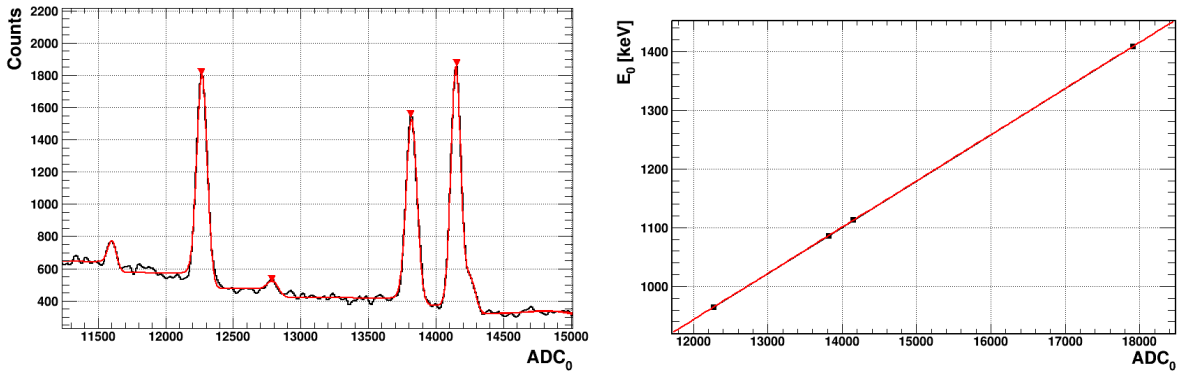

(a) (b)

Figure 5.4: Optimization of the core pre-calibration: a) ADC core spectrum (histogram) in the middle energy range and the result of the fit (red line) performed with multiple skewed Gaussian as reported in appendix B; b) Correlation between the energy and the ADC values for the lines in the optimized mapping. A fit performed according to Eq. 5.1 is shown as a red line.

5. **extraction of the calibration factors**: using the optimized mapping, a new linear fit is performed and the final calibration factors, o_0 and s_0, are obtained, see Fig. 5.4b. The values of the calibration factors obtained for the calibration measurement CAL01 are:

$$o_0 = (-0.877 \pm 0.861)\,\mathrm{keV} \qquad \mathrm{s}_0 = (0.078 \pm 6 \cdot 10^{-7})\,\mathrm{keV}\,. \tag{5.6}$$

A significant value of the offset would reveal segment-to-core cross talk, but o_0 is compatible with zero with a CL of 95%. Thus the segment-to-core cross talk can be neglected. In section 5.2.3, another test on the segment-to-core cross talk is shown.

The described procedure can be used to calibrate any number of cross-talk-free channels. The performance of this calibration procedure was tested using data from all the commercially available detectors described in section 3.3.2.

5.2.2 Extraction of first order cross-talk and segment-calibration factors

Two similar methods are described to evaluate both core-to-segment cross-talk and segment-calibration factors. Both methods are based on the correlation between the ADC counts in the core and the ADC counts in the segments. The results of the two methods were compared and proven to be compatible. The easier and more robust method was selected to be a step of the standard calibration procedure.

Ratio Method: it is based on the distribution of the ratio $R_{0,i}$ defined as:

$$R_{0,i} = \frac{ADC_i}{ADC_0}\,, \tag{5.7}$$

where ADC_i are the ADC counts in segment i (with i=1, ..., 19, for SuSie). Figure 5.5 shows the distribution of $R_{0,16}$ from the ^{228}Th calibration measurement CAL01 as listed in Table D.1.

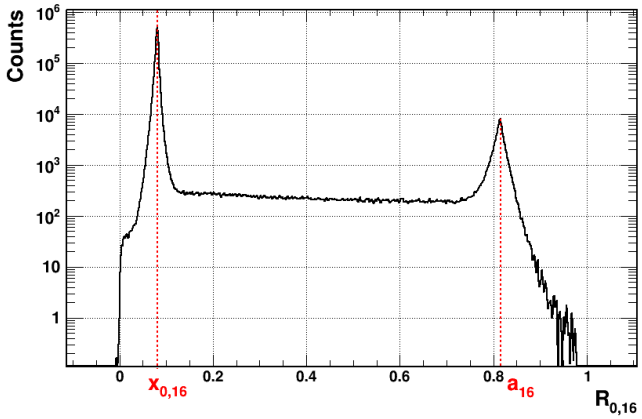

Figure 5.5: Distribution of $R_{0,16}$ as defined in Eq. 5.7 with $i = 16$ for all the events of the ^{228}Th calibration measurement CAL01 as listed in Table D.1.

The distribution shows two clearly distinct peaks:

1. the peak close to 0 contains all events without energy deposition in segment i. In absence (presence) of core-to-segment cross talk, these events would show $R_{0,i} \approx 0$ ($R_{0,i} \approx x_{0,i} \neq 0$). Thus $x_{0,i}$ is the core-to-segment cross-talk factor for segment i;

2. the peak close to 1 contains all the segment-i SSE. From the position of the second peak, it is possible to extract the calibration factor for segment i relative to the core. Solving Eq. 5.1 respect to ADC_0 and assuming $o_0 = 0$:

$$ADC_0 = E_0 \cdot k_0 \quad \text{with } k_0 = \frac{1}{s_0}\,. \tag{5.8}$$

Taking into account core-to-segment cross talk, an equation equivalent to Eq. 5.8 can be written for any segment i as:

$$ADC_i - x_{0,i} \cdot ADC_0 = E_i \cdot k_i \quad \text{with } k_i = \frac{1}{s_i} \tag{5.9}$$

where s_i is the slope of the calibration function for segment i. For segment-i SSE, with an energy deposition $\bar{E}$:

$$ADC_0 = \bar{E} \cdot k_0 \quad ADC_i = \bar{E} \cdot k_i + x_{0,i} \cdot ADC_0\,. \tag{5.10}$$

The ratio $R_{0,i}$ is therefore:

$$R_{0i} = \frac{k_i}{k_0} + x_{0,i} = \frac{s_0}{s_i} + x_{0,i} = a_i\,, \tag{5.11}$$

where a_i is shown in Fig. 5.5. Solving 5.11 with respect to s_i, the calibration slope for segment i is extracted as:

$$s_i = \frac{s_0}{a_i - x_{0,i}}. \tag{5.12}$$

The calibration offset for each segment is set equal to o_0 as obtained for the core calibration, i.e. $o_i = o_0$.

Global Fit Method: it is based on the minimization of a χ^2-like test statistic whose parameters are the core-to-segment cross talk and the calibration factors.

a) For events without energy deposition in segment i, the test statistic is defined as:

$$\sum_{n=0}^{N_{NE}} (\delta^n)^2 = \sum_{n=0}^{N_{NE}} (x_{0,i} \times ADC_0^n + ADC_i^n)^2 \tag{5.13}$$

where N_{NE} is the total number of events without an energy deposition in segment i;

b) for segment-i SSE, the test statistic is defined as:

$$\sum_{n=0}^{N_{SSE_i}} (\delta^n)^2 = \sum_{n=0}^{N_{SSE_i}} (E_0^n - o_i + s_i \times (x_{0,i} \times ADC_0^n + ADC_i^n))^2\,, \tag{5.14}$$

where N_{SSE_i} is the total number of segment-i SSE and E_0^n is the core calibrated energy.

The global fit method had some problems: too big computing-power consumption, the need for a huge number of events and very precise initial parameters for the minimization to converge. These issues led to the choice of the ratio method as the standard. The global fit method was, however, used to cross check the determination of the core-to-segment cross talk corrections. The results obtained with the two methods were in agreement.

	Super Siegfried I		Super Siegfried II	
i	$x_{0,i}$	s_i [keV/a.u.]	$x_{0,i}$	s_i [keV/a.u.]
1	0.026	0.106	0.003	0.105
2	0.061	0.111	0.004	0.112
3	0.050	0.127	0.009	0.126
4	0.150	0.130	0.017	0.131
5	0.189	0.141	0.003	0.142
6	0.102	0.113	0.003	0.114
7	0.085	0.112	0.006	0.112
8	0.087	0.131	0.002	0.131
9	0.147	0.104	0.003	0.104
10	0.077	0.130	0.003	0.130
11	0.055	0.127	0.006	0.127
12	0.049	0.134	0.005	0.134
13	0.050	0.125	0.003	0.125
14	0.016	0.127	0.005	0.128
15	0.104	0.104	0.005	0.105
16	0.081	0.108	0.004	0.109
17	0.110	0.126	0.003	0.126
18	0.288	0.105	0.006	0.106
19	0.308	0.129	0.006	0.128

Table 5.1: List of the $x_{0,i}$ and s_i for all segments as extracted using the ratio method with data of the ^{228}Th calibration measurements done with SuSie I in October 2013 and SuSie II in July 2015, in GALATEA.

Table 5.1 shows the core-to-segment cross-talk factors and the calibration factors extracted from ^{228}Th calibration measurements done with SuSie I (measurement CAL01 as listed in Table D.1) and SuSie II (measurement performed in June 2015). The read-out cables and the metalization scheme were changed during the reprocessing of the detector. A remarkable reduction of the core-to-segment cross talk, $x_{0,i}$, was observed. For SuSie I, the highest core-to-segment cross-talk factor was observed for segment 19 as 0.308. For SuSie II, the highest core-to-segment cross talk is observed for segment 4 as 0.017. The slopes, s_i, do not show big changes. This was expected since the pre-amplifier configuration did not change between the two different data taking periods.

In terms of the core-to-segment cross talk and the calibration factors for segment i (with $i = 1, ...19$), the calibrated energy in segment i, E_i, is related to ADC_i as:

$$E_i = o_i + s_i \cdot (ADC_i - x_{0,i} \cdot ADC_0)\,. \tag{5.15}$$

Figure 5.6 shows calibrated energy spectra from the core for different event multiplicities[2]. The spectra are depicted around two of the strongest gamma lines from ^{152}Eu. In case of an imperfect

[2]The multiplicity of an event is defined as the number of segments with a significant energy deposition, i.e. SSE have multiplicity 1.

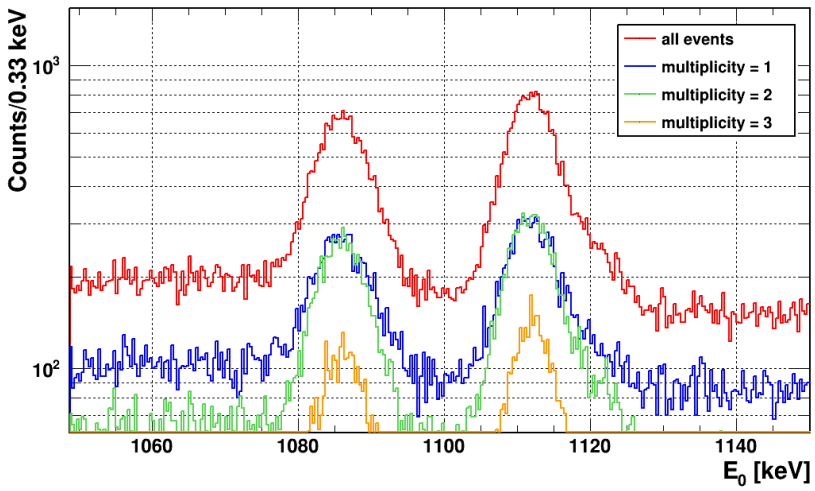

Figure 5.6: Calibrated core energy spectra around the two gamma lines from the ^{152}Eu at 1085 and 1112 keV for different multiplicities. The red line is the energy spectrum for any multiplicity, the blue line is for SSE (multiplicity = 1), the green line is obtained for events with multiplicity 3 and the orange line for multiplicity 4.

cross talk correction, energy spectra for higher multiplicities would show a worse resolution and a shift in energy. For each event multiplicity, a fit of the two gamma lines was performed as described in appendix B. Mean, μ, and standard deviation, σ, values as obtained from the fitting procedure are listed in Table 5.2. Statistical uncertainties as obtained from the fit are listed too. Mean values of the same γ-line for different multiplicities are compatible within their uncertainties. The energy resolutions do not worsen for higher multiplicity. The applied cross talk correction was thus proven to be sufficient.

	$\gamma-$ line at 1085 keV		$\gamma-$ line at 1112 keV	
Multiplicity	μ [keV]	σ [keV]	μ [keV]	σ [keV]
all	1085.93 ± 0.05	4.75 ± 0.06	1111.86 ± 0.04	4.14 ± 0.05
1	1085.87 ± 0.09	5.38 ± 0.13	1111.81 ± 0.08	4.61 ± 0.10
2	1086.03 ± 0.07	4.50 ± 0.08	1111.78 ± 0.06	3.81 ± 0.08
3	1086.08 ± 0.11	4.19 ± 0.13	1111.88 ± 0.09	3.87 ± 0.11

Table 5.2: List of the mean, μ, and standard deviation, σ, values of two different γ-lines from the calibrated energy spectra shown in Fig. 5.6.

5.2.3 Second order cross-talk factors

Only after applying the first order cross-talk correction, effects of second order cross talks can be investigated. Second order cross talk was investigated only for SuSie I. Segment-to-core and

segment-to-segment cross talk are evaluated using SSE. The selection of SSE is based on the distribution of $R^{\mathrm{cal}}_{0,i}$ defined a:

$$R^{\mathrm{cal}}_{0,i} = \frac{E_i}{E_0}\,, \tag{5.16}$$

where E_0 and E_i are the calibrated energies in the core and in segment i as defined in Eqs. 5.1 and 5.15, respectively. Figure 5.7 shows the distribution of $R^{\mathrm{cal}}_{0,16}$, for the ^{228}Th calibration measurement CAL01. As already previously discussed in section 5.2.2, the peak around 1 contains SSE. Segment-i SSE are thus selected asking for:

$$0.95 < R^{\mathrm{cal}}_{0,i} < 1.05\,. \tag{5.17}$$

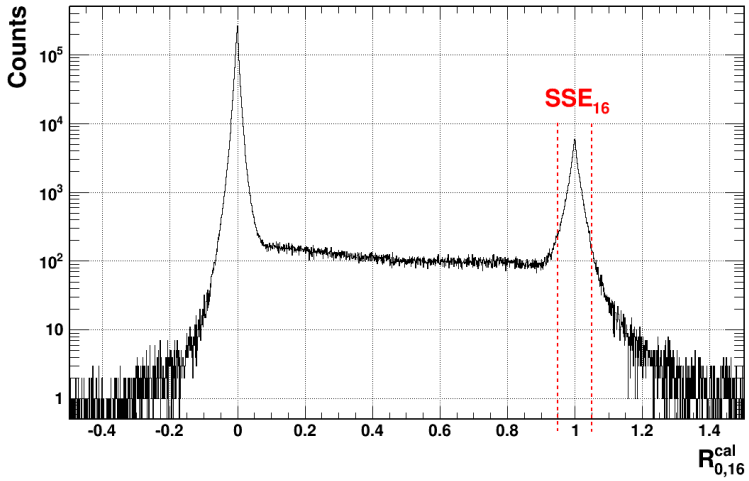

Figure 5.7: Distribution of $R^{\mathrm{cal}}_{0,i}$ as defined in Eq. 5.16, with $i = 16$, for the ^{228}Th calibration measurement CAL01 as listed in Table D.1.

Segment-to-core cross talk: it is expected to be small by construction. A first evaluation in terms of o_0 of the core calibration was presented in section 5.2.1. In the presence of segment-to-core cross talk, core spectra obtained for SSE in different segments would look different, i.e. γ-lines would show a shift in energy proportional to the segment-to-core cross talk. Fitting two representative γ-lines from core spectra for segment-i SSE and comparing the μ^j_0 (with $j = 1085\,, 1112\,\mathrm{keV}$) values, it is possible to quantify the segment$_i$-to-core cross talk. Figure 5.8 shows the μ^j_0 values with $j = 1085\,\mathrm{keV}$ ($j = 1112\,\mathrm{keV}$) in black (red), as functions of the segment-i. The error bars represent the uncertainties on the mean values as extracted from the fitting procedure. The variations observed are smaller than 2 keV, indicating that any segment-to-core cross talk has to be below 0.2%. As the variations do not seem to be correlated between the two lines, they are most likely due to systematic uncertainties of the fits. Thus no evidence of segment-to-core cross talk was found.

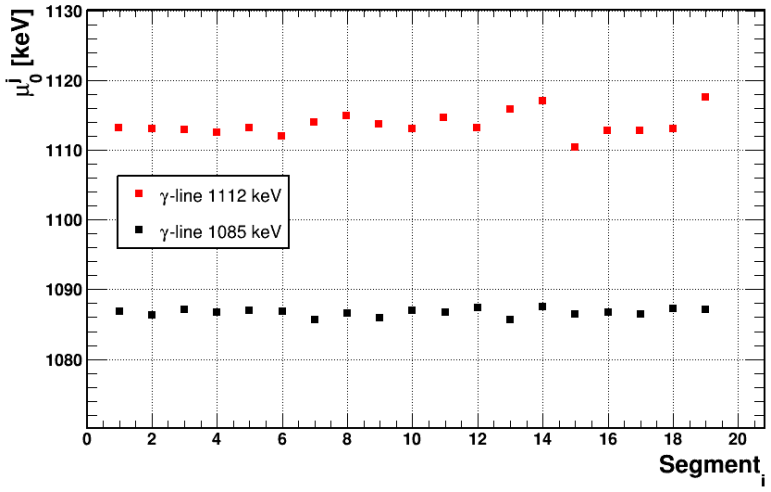

Figure 5.8: μ_0^j values extracted from core energy spectra obtained with segment-i SSE (with $i = 1, ..., 19$), as functions of segment-i, for $j =$ 1085 keV ($j = 1112$ keV) in black (red).

Segment-to-segment cross talk: $R^{\text{cal}}_{i,j}$ is defined as:

$$R^{\text{cal}}_{i,j} = \frac{E_j}{E_i}\,, \tag{5.18}$$

where E_i and E_j are the calibrated energies as defined in Eq. 5.15. In the absence of segment$_i$-to-segment$_j$ cross talk, no energy deposition is expected in segment j for segment-i SSE, i.e. $R^{\text{cal}}_{i,j}$ is expected to be around zero. In the presence of segment$_i$-to-segment$_j$ cross talk, $R^{\text{cal}}_{i,j}$ is expected to be around the cross talk factor $x_{i,j}$. Figure 5.9 shows a comparison between $R^{\text{cal}}_{16,10}$ and $R^{\text{cal}}_{16,18}$. The extracted segment-to-segment cross talk factors are shown with dashed vertical lines as $x_{16,10} = 7.3 \cdot 10^{-5}$ and $x_{16,18} = -4.1 \cdot 10^{-3}$.

5.2.4 Cross-talk factors and charge trapping

As already previously pointed out in sections 3.3.2 and 4.2.1, SuSie I had all the segments only partially metallized. Effects of the partial metalization are still under investigation. However, there are hints of reduced charge collection efficiency in partially metallized segments. The lower the charge collection efficiency, the higher the probability of charge trapping which is discussed in detail later in section 6.4. Figure 5.10 shows the effects of electron trapping in the distributions of $R^{\text{cal}}_{0,i}$ for segment 8, $i = 8$, and segment 18, $i = 18$. The distributions show peaks at negative values, i.e. for values of $E_i < 0$. "Negative energies" are features of events with electron trapping.

In order to evaluate second order cross talk factors only events without charge trapping, i.e. only events with $R^{\text{cal}}_{0,i} > R^{thr}_{0,i}$, where $R^{thr}_{0,i}$ is some threshold to be set, can be used. By including events with charge trapping, cross-talk factors are biased. Figure 5.11 shows how the segment$_2$-to-segment$_8$ cross talk is evaluated with (black) and without (red) events with charge trapping. The cross talk factor extracted without charge trapping events is about 30% lower.

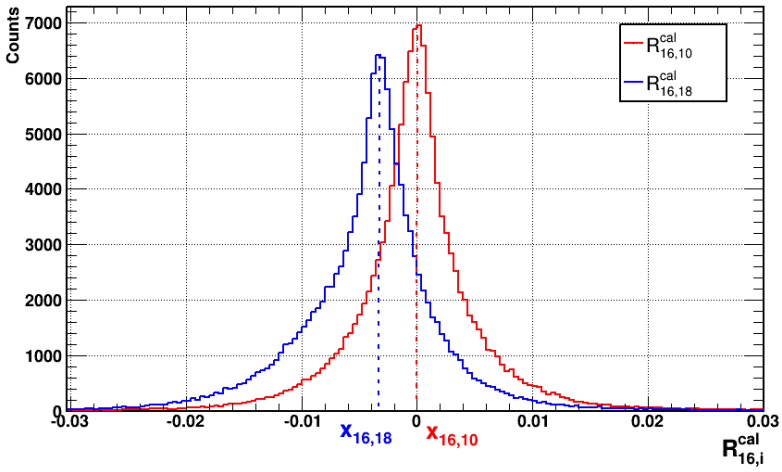

Figure 5.9: Comparison of $R^{\mathrm{cal}}_{16,i}$ for $i = 10$ (red) and $i = 18$ (blue), from the ^{228}Th calibration measurement CAL01 as listed in Table D.1.

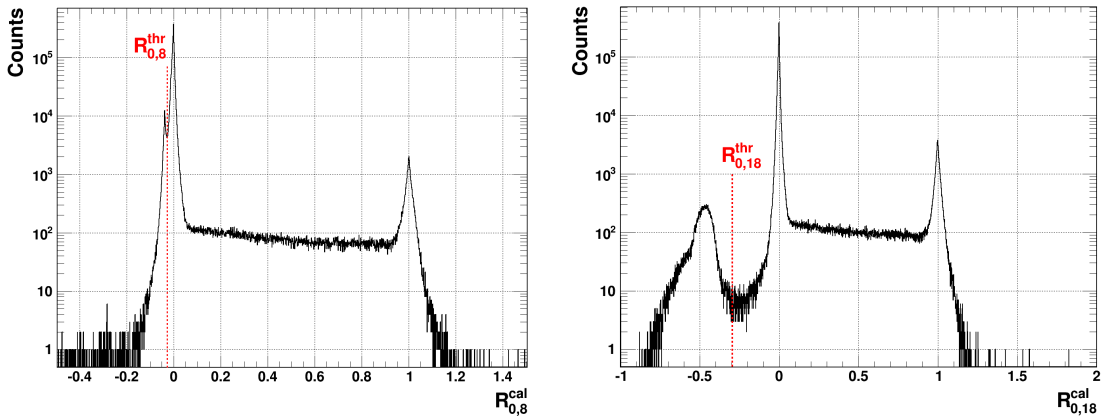

(a) (b)

Figure 5.10: Distributions of $R^{\mathrm{cal}}_{0,i}$: a) for $i = 8$; b) for $i = 18$. In red thresholds, $R^{thr}_{0,i}$, are indicated.

All the segment-to-segment cross talk factors listed in Table 5.3 were extracted using only events without charge trapping.

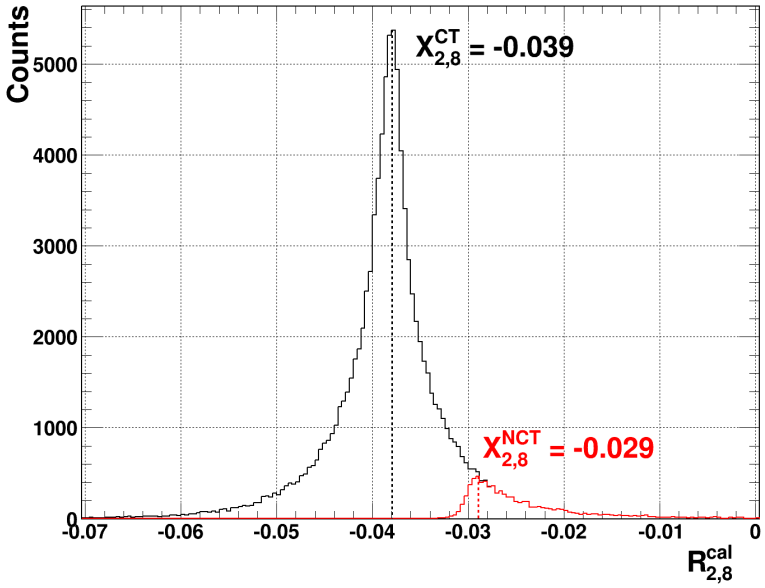

Figure 5.11: Comparison of $R^{\mathrm{cal}}_{2,8}$ obtained with (black) and without (red) events with charge trapping. The cross talk factors extracted from the two distributions are shown with dashed vertical lines.

Receiver segment	Emitter segment 1	2	3	4	5	6	7	8	9	10	11	12	13	14	15	16	17	18	19
1	+1	-0.0206	-0.005	+0.0002	+0.0002	-0.0002	+0.0006	-0.0042	-0.001	-0.0002	+0.0002	-0.0002	+0.0002	-0.0006	-0.0002	+0.0002	-0.0002	-0.0002	-0.0002
2	-0.001	+1	+0.0022	+0.001	+0.001	+0.001	+0.001	-0.0002	-0.0002	+0.001	+0.001	+0.001	+0.001	+0.001	+0.0006	+0.001	+0.001	+0.001	+0.001
3	-0.001	+0.0006	+1	+0.0006	+0.0006	+0.0006	+0.001	+0.0006	+0.0006	+0.0006	+0.001	+0.0006	+0.0006	+0.0006	+0.0006	+0.0006	+0.0006	+0.0006	+0.0006
4	-0.0034	+0.0022	-0.0002	+1	+0.0038	-0.011	+0.001	+0.001	+0.0014	+0.0018	-0.0038	+0.0018	+0.0018	-0.0006	+0.0018	-0.003	+0.0018	-0.0014	+0.0018
5	-0.0078	+0.0014	-0.011	+0.001	+1	+0.0006	-0.0002	-0.0006	+0.0002	-0.0078	+0.001	-0.0022	+0.0002	-0.0014	+0.0002	+0.0006	-0.001	+0.0002	+0.0002
6	-0.001	+0.0002	-0.0006	-0.0018	+0.0022	+1	-0.0002	-0.0002	-0.001	+0.0002	-0.005	+0.0002	+0.0006	-0.001	-0.0002	-0.005	+0.0006	-0.003	+0.0006
7	-0.0102	-0.0054	-0.0042	-0.0002	+0.0002	-0.0002	+1	-0.005	-0.0074	+0.0002	-0.0002	-0.0006	-0.0118	-0.0022	-0.0066	-0.0002	-0.0058	-0.0002	+0.0002
8	-0.0106	-0.029	-0.0026	-0.0002	-0.0002	-0.0002	+0.0002	+1	-0.0122	-0.0002	-0.0002	-0.0002	-0.0006	-0.0006	-0.005	-0.0006	-0.0006	-0.0006	-0.0002
9	+0.0002	-0.0006	-0.0034	+0.0006	+0.001	+0.001	-0.0022	+0.0006	+1	+0.0006	+0.001	+0.0006	+0.0006	+0.0006	+0.0006	+0.0006	+0.0006	+0.0006	+0.0006
10	-0.0002	+0.0026	-0.0022	+0.0022	-0.0006	+0.0022	+0.0002	+0.0018	+0.0002	+1	+0.003	-0.0034	+0.0022	-0.0018	+0.0022	+0.0002	+0.0014	-0.0006	+0.0026
11	-0.0002	+0.0006	-0.0014	+0.0014	+0.0022	-0.001	+0.0006	+0.0006	+0.0002	+0.001	+1	+0.001	+0.0014	-0.0002	+0.001	-0.0058	+0.001	-0.001	+0.0018
12	-0.0006	-0.0002	-0.0002	-0.0002	-0.0002	-0.0006	-0.0002	-0.0006	-0.0002	-0.0034	+0.0006	+1	-0.0042	-0.0202	-0.001	-0.007	-0.009	-0.039	-0.0002
13	+0.0014	-0.0006	-0.0018	+0.001	+0.0014	+0.001	-0.0018	+0.001	-0.0018	+0.001	+0.0018	+0.001	+1	-0.0022	-0.005	+0.0014	-0.0006	+0.001	+0.0014
14	+0.0006	-0.0026	-0.0018	+0.0006	+0.001	+0.0006	-0.0018	+0.0006	-0.001	+0.001	+0.0014	+0.0006	+0.0002	+1	+0.0002	+0.0006	+0.0006	-0.0002	+0.0006
15	-0.001	-0.0026	-0.0082	+0.0002	+0.0002	+0.0002	-0.003	-0.0046	-0.0074	-0.0002	+0.0002	+0.0002	-0.0034	-0.0006	+1	-0.0002	+0.0002	+0.0002	+0.0002
16	+0.0006	+0.0002	-0.0014	+0.0006	+0.001	+0.0006	+0.0014	+0.001	+0.0002	+0.0006	-0.001	+0.0006	+0.001	+0.0002	+0.0006	+1	+0.0002	-0.0054	+0.0006
17	-0.0006	+0.001	+0.001	+0.0018	+0.0022	+0.0018	+0.0014	+0.0002	+0.001	+0.0018	+0.0022	-0.0006	-0.0034	-0.0034	+0.0006	+0.0006	+1	-0.0038	+0.0014
18	-0.0006	-0.0006	-0.0018	-0.0002	+0.0002	-0.0002	-0.0002	-0.0006	-0.0006	-0.0002	-0.0002	-0.0002	-0.0006	-0.0034	-0.0006	-0.0034	-0.0006	+1	-0.0006
19	+0.0006	+0.001	+0.0002	-0.0026	-0.0014	-0.005	+0.0006	+0.0006	+0.0002	+0.0002	-0.0018	-0.0002	-0.001	+0.0002	-0.0006	-0.0026	-0.0006	-0.001	+1

Table 5.3: Segment-to-segment cross talk factors extracted using the ^{228}Th calibration measurement CAL01, as listed in Table D.1. The red values are the $|x_{i,j}| > 0.01$, for which the cross talk correction is applied.

All the 19 times 19 segment-to-segment cross talk factors were evaluated, as previously discussed. Table 5.3 shows a list of all the measured $x_{i,j}$ values for SuSie I. Only 10 of the 361 values are of $\mathcal{O}(1\%)$. All the others are of $\mathcal{O}(0.1\%)$. As the effects of charge trapping in SuSie I biases the determination of segment-to-segment cross talk factors, they were only applied if they were larger than 1%.

5.3 Time stability of calibration factors

As already previously mentioned in section 4.2, calibration and background measurements are regularly performed between the measurements of a scan. A deterioration of the energy resolutions was observed when the energy calibration for a measurement of a scan was performed using calibration factors extracted from a calibration measurement not close enough in time.

The core-to-segment cross talk and calibration factors for segment i extracted using a ^{228}Th measurement are referred to as $x_{0,i}^{^{228}\mathrm{Th}}$ and $s_i^{^{228}\mathrm{Th}}$. Analogously $x_{0,i}^l$ and s_i^l represent the factors extracted using the l^{th} measurement of a scan. For each segment i, ratios are defined as:

$$R_x^l(i) = \frac{x_{0,i}^l}{x_{0,i}^{^{228}\mathrm{Th}}} \tag{5.19}$$

$$R_s^l(i) = \frac{s_i^l}{s_i^{^{228}\mathrm{Th}}}\,. \tag{5.20}$$

The closer $R_x^l(i)$ and $R_s^l(i)$ are to 1, the better the performance of an energy calibration done with the ^{228}Th measurement would be. Figure 5.12 shows the time dependence of $R_x^l(i)$ and $R_s^l(i)$. Time 0 indicates the time of the last calibration. Periodic oscillation close to 1 are observed for all the segments. Deviations from 1 are more visible for $R_x^l(i)$ than for $R_s^l(i)$. The level of LN_2 in the cryotank inside GALATEA varies with time. The temperature of the entire setup (see Fig. 4.3c) follows this variation in time. The cross talk factors seem to follow this variation as well. Moreover, measurements of a scan are performed with different positions of the internal sources. The movements within the system can cause movements of the cables, i.e. changes of the relative distances between the cables. This can modify the cross talk factors. It is clear that cross talk factors have to be carefully monitored.

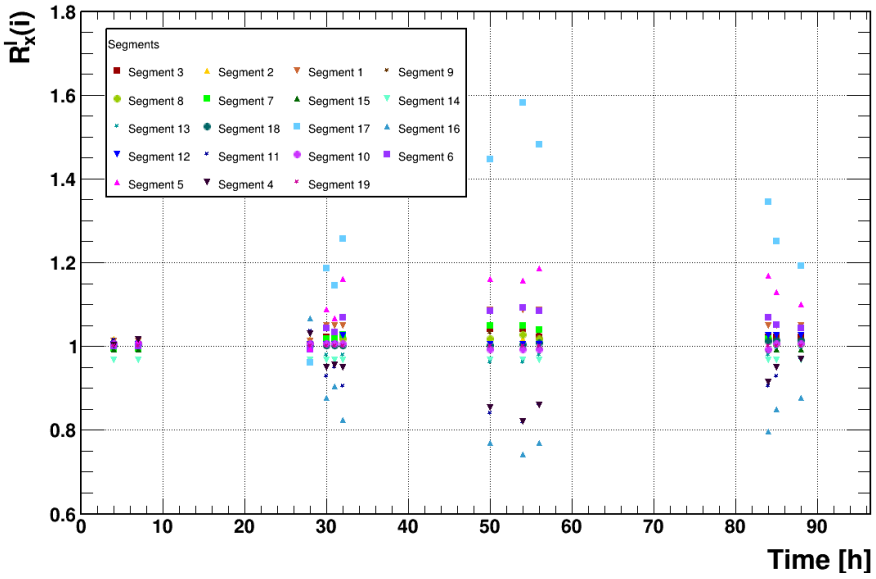

(a)

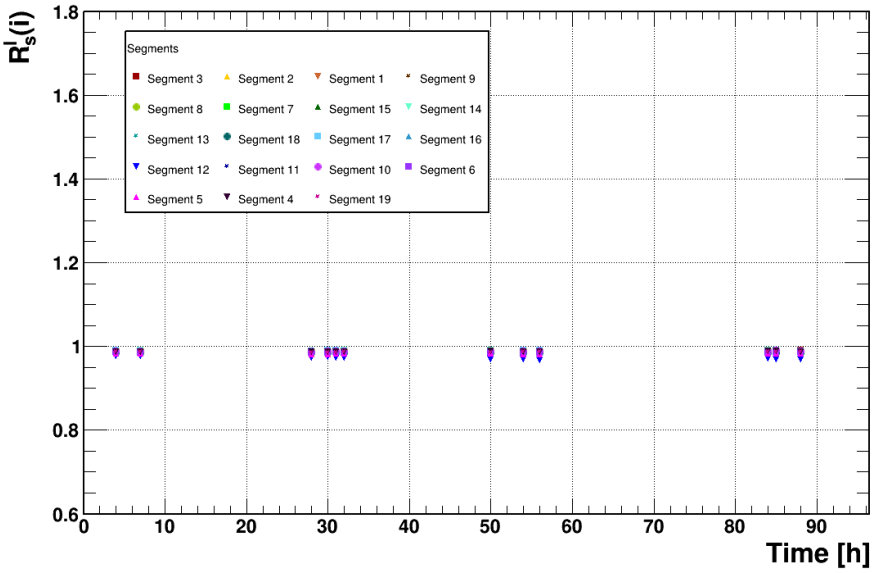

(b)

Figure 5.12: $R^l_x(i)$ and $R^l_s(i)$ as function of time from the latest calibration measurement for different segments. This reflects measurements performed with SuSie I in Autumn 2013.

Chapter 6

Pulse shapes and charge trapping

The shapes of the electrical pulses from a germanium detector contain a lot of information about the distribution of the charge depositions in the detector. From the shape of the pulse, it is possible to infer the number and the position of the energy deposits. This characterizes the event. The analysis of the time evolution of electrical pulses is usually referred to as Pulse Shape Analysis (PSA). Several background reduction techniques in $0\nu\beta\beta$ and DM searches are based on PSA.

In this chapter, the foundation for PSA is introduced. The processing from the raw pulse to the calibrated pulse is discussed in section 6.1. A list of all the parameters extracted from a pulse is presented in section 6.2. In section 6.3, an algorithm to classify the pulses is presented. In section 6.4, the phenomenon of charge trapping is discussed.

6.1 Pulse processing

In this section, all the steps from the raw pulse to the calibrated pulse are presented. The pulses were recorded with a sampling frequency of 75 MHz, i.e. pulses are sampled every 13.33 ns. The number of samples for each pulse is 1023, i.e. the pulse is recorded for a total time of ≈ 13600 ns.

6.1.1 Pre-processing

The steps used to pre-process the pulses are:

Baseline subtraction: the baseline of a pulse is defined as the value that would have been observed at the time of the start of the pulse if there had been no pulse [165]. Pulse heights are measured relative to the baseline. The value of the baseline of a pulse in channel i (with $i = 0, ..., 19$), $\bar{p}_i^{BL}$, is calculated as:

$$\bar{p}_i^{\mathrm{BL}} = \left(\frac{\sum_k^{N_{BL}} p_i^{\mathrm{raw}}(k)}{N_{BL}}\right), \tag{6.1}$$

where $p_i^{\mathrm{raw}}(k)$ is the value of the raw pulse at the k^{th} sample and N_{BL} is the number of samples used for the calculation. With the DAQ settings as used for this work, N_{BL} is

300. The output of the baseline subtraction for channel i is a pulse with a value at the k^{th} sample, $p^{\mathrm{BL}}(k)$, defined as:

$$p_i^{\mathrm{BL}}(k) = p_i^{\mathrm{raw}}(k) - \bar{p}_i^{\mathrm{BL}} \,. \tag{6.2}$$

Figure 6.1 shows the effect of the baseline subtraction on a core pulse.

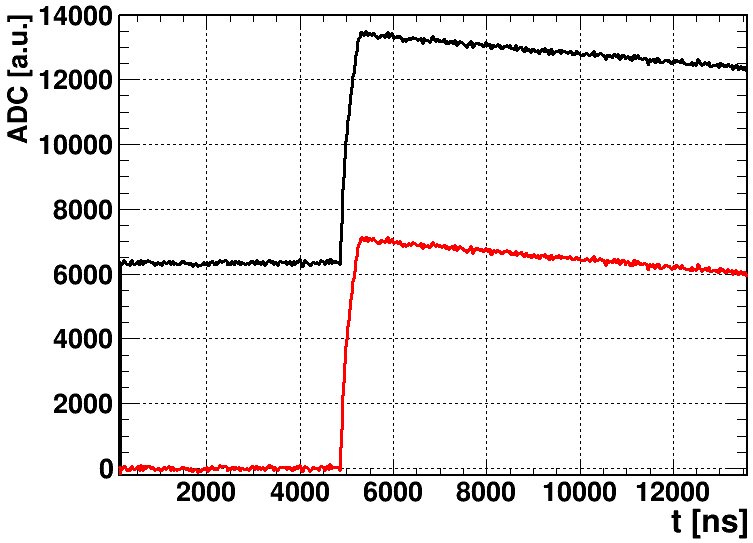

Figure 6.1: Effect of the baseline subtraction: a core pulse before (black) and after baseline subtraction (red).

Pre-amplifier decay correction: the tail of any pulse exponentially decays with the time constant of the discharging process of the pre-amplifier. Without a correction for this decay, the pulse-height can easily be underestimated. The time constant of the decay is a characteristic of a specific pre-amplifier[1]. If the pre-amplifier is not exchanged, the decay constant does not change. It is therefore enough to extract the decay constants from a long measurement at the beginning of a data taking period. The time constant is extracted as follows:

a) in each event, the tail of the pulse is fitted with an exponential decay function as:

$$f(t) = f_0 \cdot e^{-\frac{t}{\tau}} \tag{6.3}$$

where τ is the fitted decay time;

b) the distribution of the extracted decay times is fitted with a log-normal function, as shown in figure 6.2a. The median of the distribution for pre-amplifier i, τ_i^{extr} (with $i = 0, ..., 19$), is extracted.

[1]The pre-amplifiers used have a nominal decay time of about 50 μs. It is, however, important to determine the exact values to properly correct the pulses.

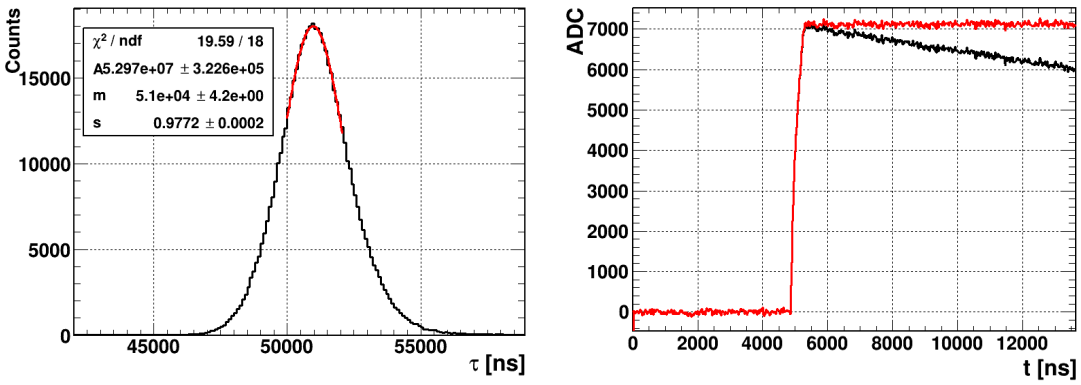

(a) (b)

Figure 6.2: a) Distribution (histogram) of the decay constants extracted from all events for the core amplifier, and a fit (red line) performed using a log-normal distribution. The extracted median is referred to as $\tau^{extr} = 51.0\,\mu$s. b) Comparison of a core pulse before (black) and after (red) the pre-amplifier decay correction.

The decay constants were extracted using the background measurement BKG11 as listed in Tab. D.1. Once the decay constants are extracted, all pulses are corrected accordingly. The output of the pre-amplifier decay correction in channel i is a pulse with a value at the k^{th} sample, $p_i^{\mathrm{DC}}(k)$, defined as:

$$p_i^{\mathrm{DC}}(k) = p_i^{\mathrm{BL}}(k) - p_i^{\mathrm{BL}}(k-1) + p_i^{\mathrm{DC}}(k-1)e^{-13.33\,\mathrm{ns}/\tau_{\mathrm{i}}^{\mathrm{extr}}}\,. \tag{6.4}$$

The effect of the correction on a core pulse is shown in Fig. 6.2b.

6.1.2 Offline reconstruction of pulse height

The used DAQ system has an internal algorithm to extract the pulse height for each channel. Negative pulses are foreseen and set to zero online. The pulse heights were also calculated offline.

Figure 6.3 shows the correlation between the pulse height in segment 8 as reconstructed offline and as reconstructed online by the DAQ. For the majority of events, the offline and online reconstruction agree. However, the offline reconstruction delivers negative pulse-heights. The DAQ cannot do that. Such pulses will be discussed in section 6.4.

The offline reconstruction works as follows. It is based on an "Asymmetric Trapezoidal Filter" (ATF). Figure 6.4 shows the results of the ATF. In black, the core pulse is shown after baseline subtraction and pre-amplifier decay correction. In red the average of the baseline, $\bar{p}_i^{\mathrm{BL}}$ (as defined in Eq. 6.1), is shown together with the average of the tail, $\bar{p}_i^{\mathrm{T}}$, defined as:

$$\bar{p}_i^{\mathrm{T}} = \left(\frac{\sum_{k=k_S}^{N_T} p_i^{\mathrm{DC}}(k)}{N_T}\right), \tag{6.5}$$

where k_S is the starting sample on the tail to to start the average, N_T is the number of samples in the pulse tail. k_S was chosen as $k_S = 525$ for all events and all channels. With the DAQ settings

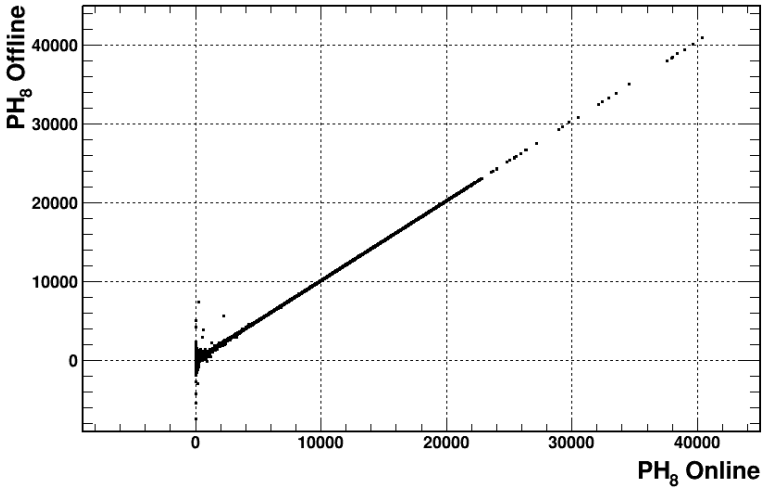

Figure 6.3: Correlation between the ADC reconstructed offline and the ADC reconstructed online by the DAQ in segment 8. The correlation plot was obtained using the background measurement CAL01, as listed in Tab. D.1.

as used for this work $t(k_S) \approx 7000\,\text{ns}$. With these settings the pulse height reconstruction is not affected by long pulses, expected for surface events.

The output of the ATF is obtained as:

$$PH_i = \bar{p}_i^{\mathrm{T}} - \bar{p}_i^{\mathrm{BL}}\,, \tag{6.6}$$

where PH_i, $\bar{p}_i^{\mathrm{T}}$ and $\bar{p}_i^{\mathrm{BL}}$ are obtained in ADC counts and $\bar{p}_i^{\mathrm{BL}}$ is close to zero after baseline subtraction.

6.1.3 Energy calibration of pulses

The pre-processed pulses are first cross-talk corrected and than calibrated with constants previously extracted as described in chapter 5 using the offline pulse-height reconstruction.

The output of the energy calibration is a pulse with a value of the k^{th} sample, $p_i^{\mathrm{cal}}(k)$, of:

$$p_i^{\mathrm{cal}}(k) = o_i + s_i \cdot p_i^{\mathrm{DC}}(k) \;\; for\; i = 0 \tag{6.7}$$

$$p_i^{\mathrm{cal}}(k) = o_i + s_i \cdot (p_i^{\mathrm{DC}}(k) + x_{0,i} \cdot p_0^{\mathrm{DC}}(k)) \;\; for\; i = 1,..,19 \tag{6.8}$$

The cross talk correction is done under the assumption that the core and the segments have the same response function. This simple approach to cross-talk correction at pulse level is valid for proportional cross talk. No satisfying method has been established for a proper correction of the differential cross talk.

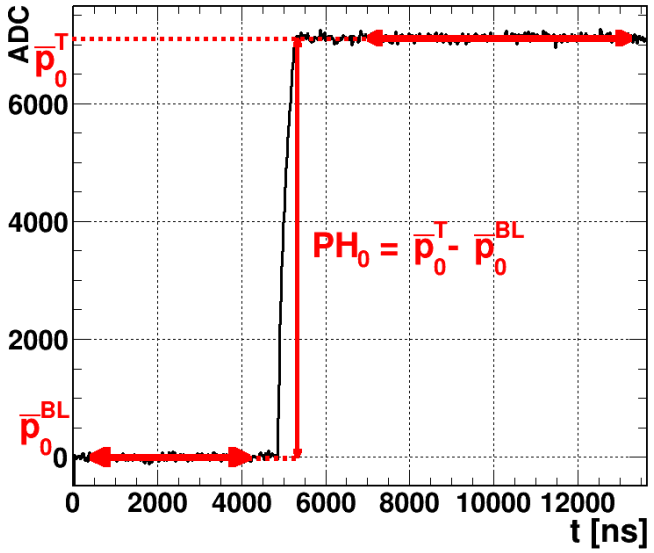

Figure 6.4: Pre-processed core pulse (black histogram), with a sketch to illustrate the working principle of the asymmetric trapezoidal filter.

6.2 Pulse parameters

Pulse-Height is extracted using the ATF as introduced in section 6.1.2. Once the pulse in channel i is pre-processed and calibrated, the pulse-height, PH_i, is obtained in keV and thus corresponds to the energy recorded in the i^{th} channel, i.e. $PH_i = E_i$.

Maxima Positive, M_i^+, and negative, M_i^-, maxima of the pulse in the i^{th} channel are defined. Figure 6.5 illustrates the definition of M_0^+ and M_0^- for a core pulse.

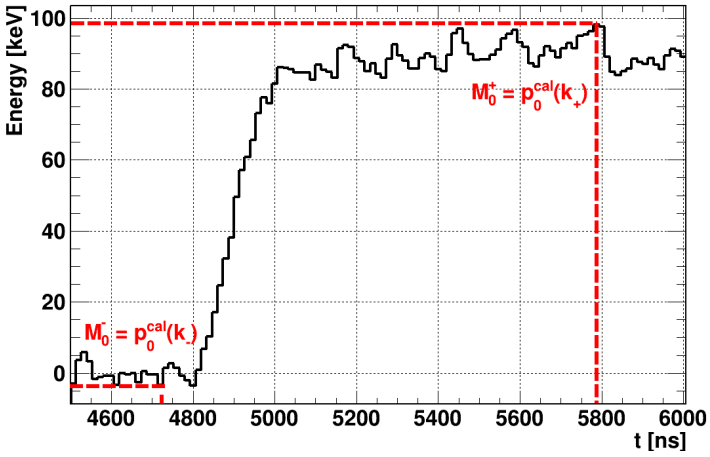

Figure 6.5: Definition of both positive, $M_0^+ = p_0^cal(k_+)$ and negative, $M_0^- = p_0^cal(k_-)$, maxima in a core pulse.

The values of the maxima of the i^{th} pulse are $M_i^+ = p_i^{\rm cal}(k_+)$, $M_i^- = p_i^{\rm cal}(k_-)$), with:

$$p_i^{\rm cal}(k_+) > p_i^{\rm cal}(l) \;\forall\, l \;|\, t(l) \;\in\; (4500, 6000\,{\rm ns})\,, \tag{6.9}$$
$$p_i^{\rm cal}(k_-) < p_i^{\rm cal}(l) \;\forall\, l \;|\, t(l) \;\in\; (4500, 6000\,{\rm ns})\,, \tag{6.10}$$

Noise level It is a characteristic of the system and depends on the electronic noise introduced by the read-out circuits. It is different for each channel. If the system is not changed, the noise levels remain the same. Thus, it is enough to extract the noise level for each segment only once from a long measurement. The noise level is extracted as follows:

1. in each event, the standard deviation σ_i^n of the $p_i^{\rm cal}(k)$ values for $k = 1, .., 300$ is calculated, where n is the index for the n^{th} event;

2. the distribution of the σ_i^n from all events in each channel is fitted with a log-normal function and the median, m, is extracted. Figure 6.6 shows the σ_0 distribution (black histogram) and the result of the fit (red line). The fit parameters are also listed.

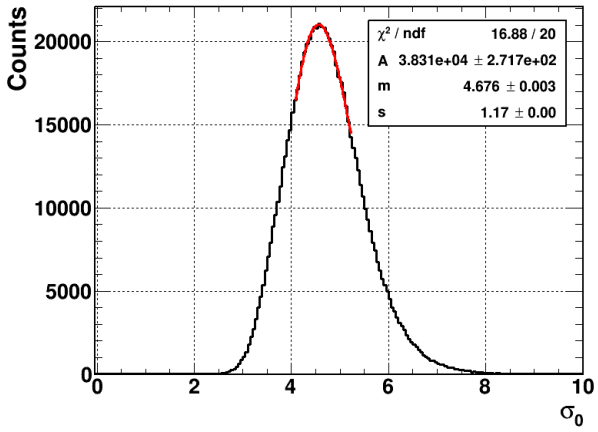

Figure 6.6: Distribution of σ_0 (black histogram) and the result of a fit (red line) with a log-normal function. The parameters as extracted from the fitting procedure and the obtained χ^2 are also listed.

The noise level for each channel was extracted using the background measurement BKG11 as listed in Tab. D.1.

Risetime: the timing structure of a pulse contains a lot of information about the event:

1. it strongly depends on where electron-hole pairs are created, i.e. on the interaction point;

2. it is different for single- or multi-site events;

3. charge trapping or regions of low electric fields can increase the risetime.

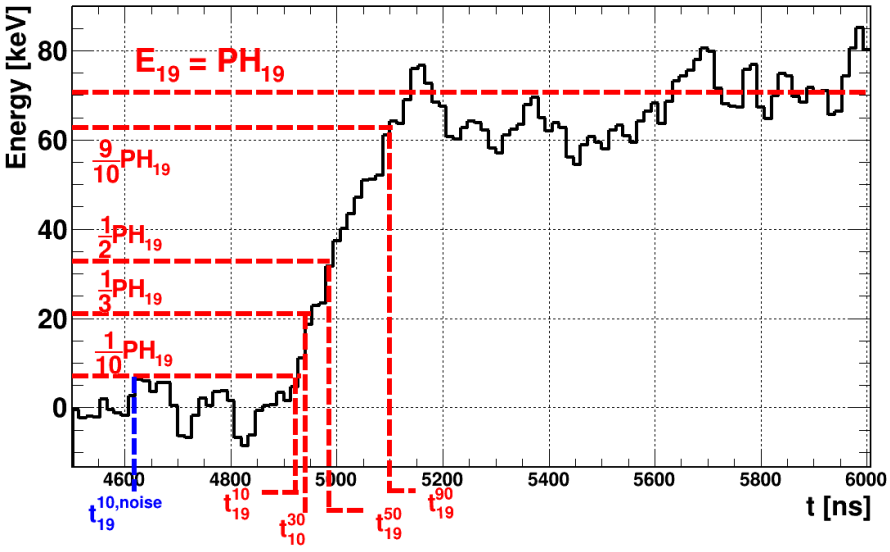

Figure 6.7: Pulse from segment 19, the top segment in SuSie I (black histogram). t_{19}^{n}, with $n = 10, 30, 50, 90$ are pointed at with dashed red lines, $t_{19}^{10,\mathrm{noise}}$ is shown in purple, for definitions see text.

Figure 6.7 shows a calibrated pulse from segment 19, the top segment in SuSie I. The times when the pulse reaches n% of its pulse-height, $PH_{19} = E_{19}$, t_{19}^{n} with $n = 10, 30, 50, 90$, are shown as dashed red lines.

The value of t_i^{50} is extracted as the time corresponding to the k^{th} sample, $t_i(k)$, such that:

$$p_i^{\mathrm{cal}}(k-1) < \frac{PH_i}{2} \quad \wedge \quad p_i^{\mathrm{cal}}(k+1) > \frac{PH_i}{2}\,, \tag{6.11}$$

where k is an ascending index in from 350 to 500 with $t(k) \in (4500\,\mathrm{ns}, 6500\,\mathrm{ns})$.

The value of t_i^{10} is extracted as the time corresponding to the l^{th} sample, $t(l)$, such that:

$$p_i^{\mathrm{cal}}(l-1) > \frac{PH_i}{10} \quad \wedge \quad p_i^{\mathrm{cal}}(l+1) < \frac{PH_i}{10}\,, \tag{6.12}$$

where l is a descending index from k to 350, i.e. $t(l) \in (t(k), 4500\,\mathrm{ns})$. The downward search is a safe-guard against noise. In pulses with high levels of noise, as in the segment 19 pulse shown in Fig. 6.7, using an ascending index would lead to the extraction of $t_i^{10,\mathrm{noise}}$, i.e. a value 300 ns lower than the real value. t_i^{30} is extracted using the same procedure.

Analogously, t_i^{90} is extracted as the time corresponding to the m^{th} sample, $t_i(m)$, such that:

$$p_i^{\mathrm{cal}}(m-1) < \frac{9 \cdot PH_i}{10} \quad \wedge \quad p_i^{\mathrm{cal}}(m+1) > \frac{9 \cdot PH_i}{10}\,, \tag{6.13}$$

where m is an ascending index between k and 500, i.e. $t(m) \in (t(k), 6500\,\mathrm{ns})$.

The rise time of the pulse in the i^{th} channel, RT_i^{10-90}, is defined as:

$$RT_i^{10-90} = t_i^{90} - t_i^{10}\,. \tag{6.14}$$

The bandwidths of the amplification system is around 15 MHz while the smallest risetimes are around 150 ns. Thus, the influence of the electronics on the risetime can be neglected. Pulse shapes can be drastically different for different events. For events really close to the surface, like alpha events, the charge collection process is sometimes modified. Charge carriers can be permanently or temporarily trapped. Traps are either shallow or deep. This reduces the reproducibility and the possible usage of RT_i^{10-90} distributions. Nevertheless, the first part of the pulse is sometimes more reproducible and can characterize groups of events. Therefore, a shorter risetime, RT_i^{10-30}, (see Fig. 6.7) is defined as:

$$RT_i^{10-30} = t_i^{30} - t_i^{10}\,, \tag{6.15}$$

where t_i^{30} is the time when the pulse reaches the 30% of its height.

6.3 Pulse classification

In segmented detectors several kinds of pulses are observed. Figure 6.8 shows sketches of the different classes of pulses:

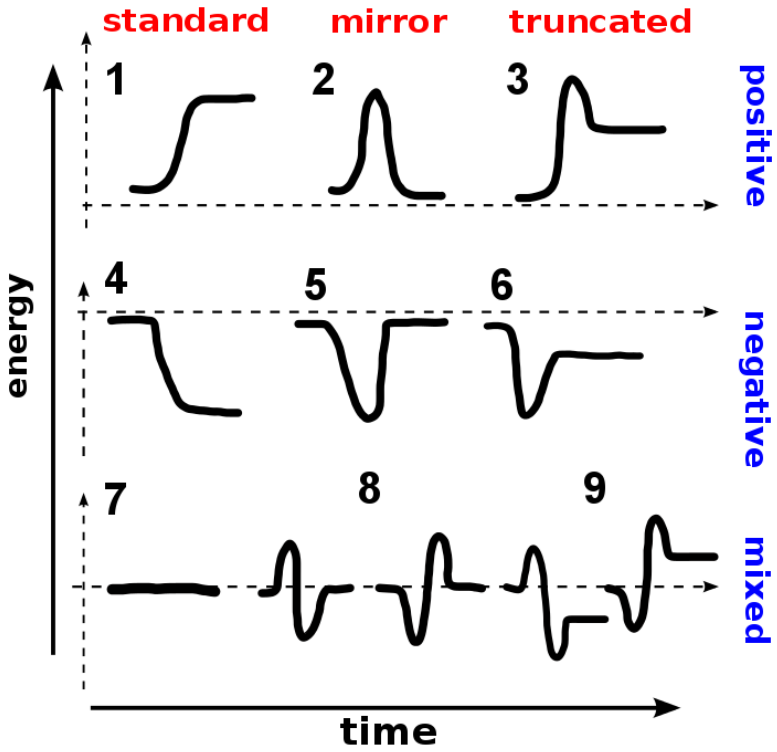

Figure 6.8: Sketch for all classes of pulses as recorded in a segmented germanium detector. They are grouped according to the three different polarities observed.

1. "standard" pulses are recorded for the core and for segments whose electrodes are collecting charge carriers, i.e. for segments where energy is deposited. The sign of a "standard" pulse depends on the collected charge carrier; in an n-type detector such as SuSie, the core (segments) show a negative (positive) pulse. For all events shown in this thesis, the signal from the core is inverted offline and shown as a positive pulse;

2. "mirror" pulses are recorded in segments close to the collecting segments. The charges drifting towards the collecting electrodes induce mirror charges in the electrodes of the neighbouring segments. Mirror pulses go back to the baseline as soon as all charge carriers are collected. The polarity of mirror pulses is related to the sign of the inducing charge carriers: electron (hole) drift induces negative (positive) mirror charges. Thus, the polarity of mirror pulses contains information about the radial position of the interaction. In an n-type detector, positive (negative) mirror pulses occur for interactions happening close to the core (outer surface). Mixed mirror pulses occur for interactions happening at medium radii. However, the number of mixed mirror pulses is smaller than the one predicted by simulations [166];

3. "truncated" mirror pulses are recorded in segments close to the collecting segments if charge trapping occurs. A fraction of the charge carriers is not collected and thus induced pulses do not go back to the baseline. The sign of such an "apparent energy deposition" is related to the sign of the trapped charge carriers, i.e. if electrons (holes) are trapped the truncated pulse fakes a "negative energy deposit" (positive signal).

6.3.1 The classification algorithm

An algorithm was developed to classify each pulse in each event. The pulse classification of the i^{th} pulse is based on the relations among the following parameters:

1. the maxima, M_i^+ and M_i^-, as defined in section 6.2;

2. the pulse-height, E_i, in the i^{th} pulse, as defined in section 6.2;

3. standard deviation of the noise, σ_i, in the i^{th} pulse, as defined in section 6.2.

Applying the algorithm flowchart from Fig. 6.9 to the pulse shown in Fig. 6.10, the classification works as follows:

a) is $E_i > 0$? **yes**;

b) is $|M_i^+ - E_i| > 3 \cdot \sigma_i$? **no**;

c) is $E_i > 3 \cdot \sigma_i$? **no**;

d) is $||M_i^-| - |E_i|| > 3 \cdot \sigma_i$? **yes**.

The pulse in Fig. 6.10 is therefore classified as a negative mirror pulse. Figure 6.11 shows examples of all the classes mentioned in Fig. 6.9 for $E_i > 0$. Figure 6.12 shows examples of all the classes mentioned in Fig. 6.9 for $E_i < 0$.

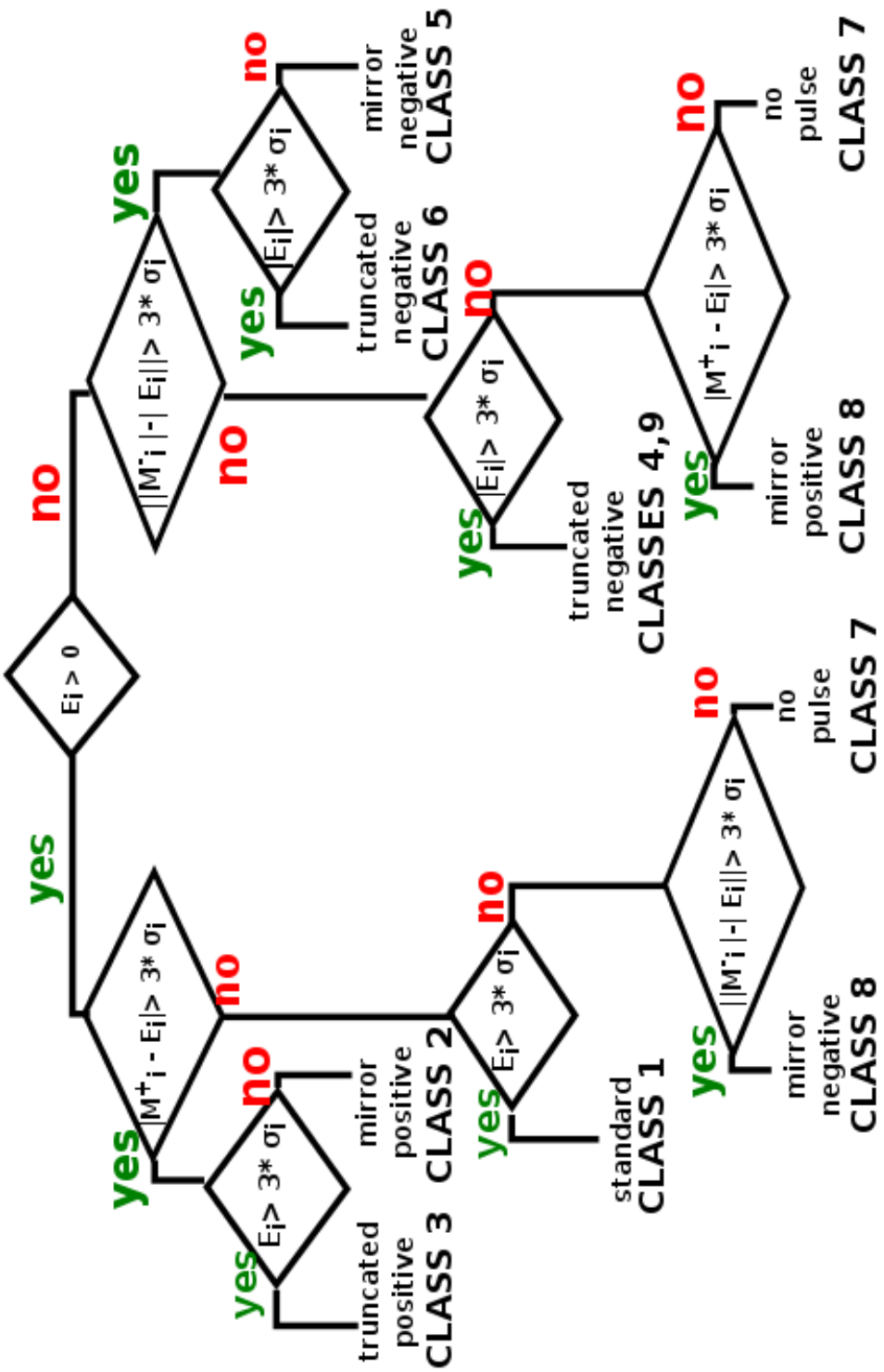

Figure 6.9: Flowchart of the algorithm for pulse characterization.

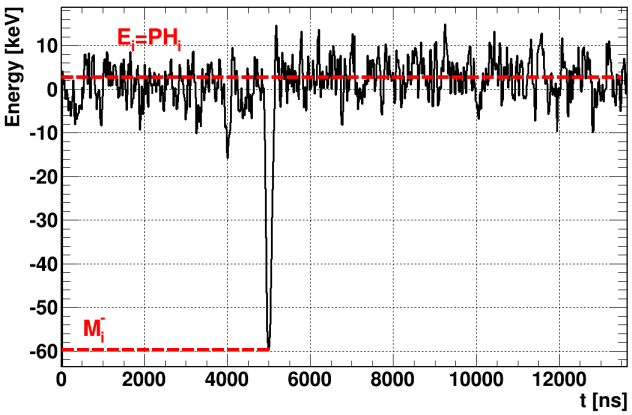

Figure 6.10: A typical negative mirror pulse, used as an example to describe the classification algorithm.

6.4 Special pulses: charge trapping

The phenomenon of charge trapping in germanium detectors is well established [167, 168]. In germanium, trapping sites can be formed during crystal growth, both through contamination and thermal excitations [169,170]. Trapping sites were observed also in radiation damaged detectors [171] and in areas of the detector with distorted and weak electrical field lines. The trapping of charge carriers during their drift and their possible release have a significant effect on pulses. It causes position-dependent pulse-height deficits and corresponding truncated mirror pulses. When electrons (holes) are trapped, negative (positive) truncated mirror pulses are recorded.

Figure 6.13 shows the $R^{\text{cal}}_{0,i}$, as defined in Eq. 5.16, distributions for segment 19, $i = 19$, the top segment of SuSie I and for segment 18, $i = 18$. As shown in section 5.2.4, charge trapping causes a third "peak" in the $R^{\text{cal}}_{0,i}$ distribution, neither around 0 nor around 1. The events with $R^{\text{cal}}_{0,19} > 1.75$ are events with electron trapping. These events show a peak at $R^{\text{cal}}_{0,18} \approx -0.3$ in segment 18 which is directly underneath segment 19. Figure 6.14 shows such an event. The energy deposit is in segment 19. Some of the electrons are trapped before being collected by the core electrode. The result is the presence of negative truncated mirror pulses in segments 18 and 13 and a reduced pulse-height recorded for the core.

This electron trapping is also observed in other segments. Figure 6.15 shows the $R^{\text{cal}}_{0,i}$ distributions for $i = 2$ and for $i = 8$. The $R^{\text{cal}}_{0,2}$ does not show a clearly distinct "third peak" as $R^{\text{cal}}_{0,19}$. However, events with $R^{\text{cal}}_{0,8} < -0.025$ show electron trapping. The energy deposit is in segment 2. Some of the electrons are trapped before being collected by the core electrode. This results in a truncated negative mirror pulse in segment 8. The effect is smaller than for segments 19 and 18 because the amount of trapped charge is smaller. A corresponding event is shown in Fig. 6.16.

Hole trapping will be discussed in detail in chapter 8.

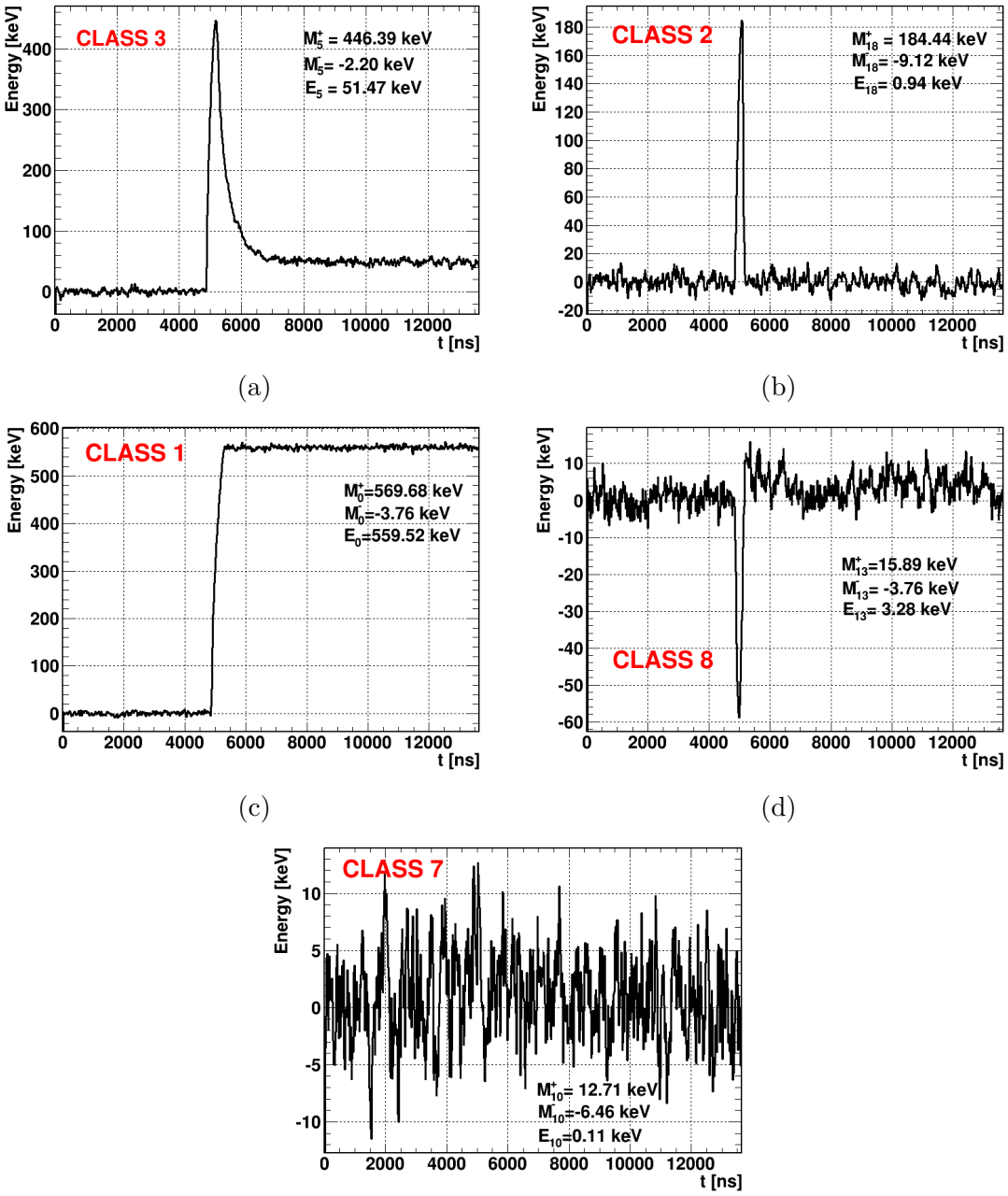

Figure 6.11: Examples of differently classified pulses from different events and different segments with $E_i > 0\,\text{keV}$ as defined in Fig. 6.9. For each pulse, A_i^+, A_i^- and E_i are listed: (a) truncated positive mirror pulse, (b) positive mirror pulse, (c) standard signal, (d) negative mirror pulse, (e) no pulse.

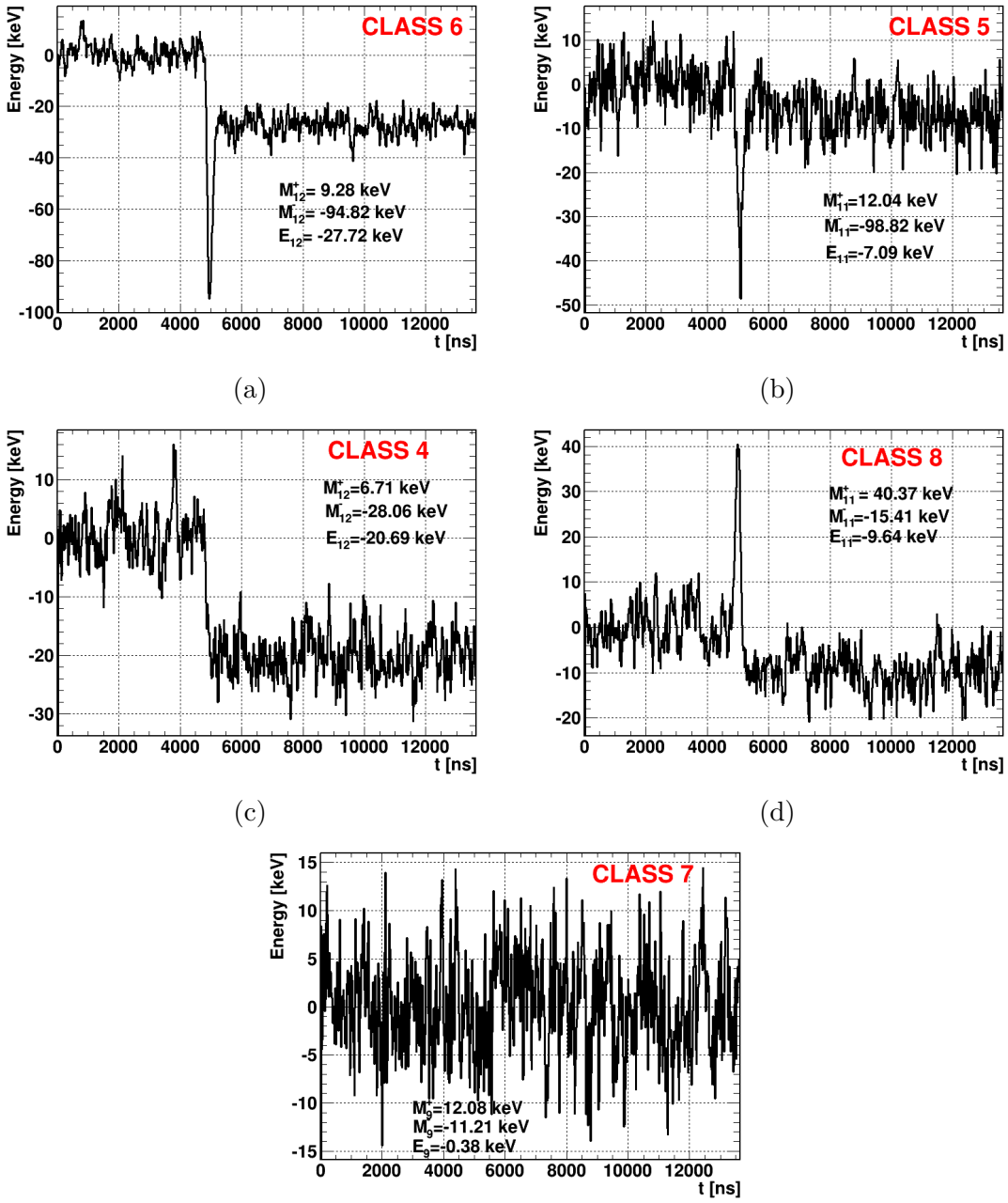

Figure 6.12: Examples of differently classified pulses from different events and different segments with $E_i < 0\,\text{keV}$ as defined in Fig. 6.9. For each pulse, A_i^+, A_i^- and E_i are listed. (a)truncated negative mirror pulse, (b) negative mirror pulse, (c) truncated negative mirror pulse, (d) positive mirror pulse, (e) no pulse.

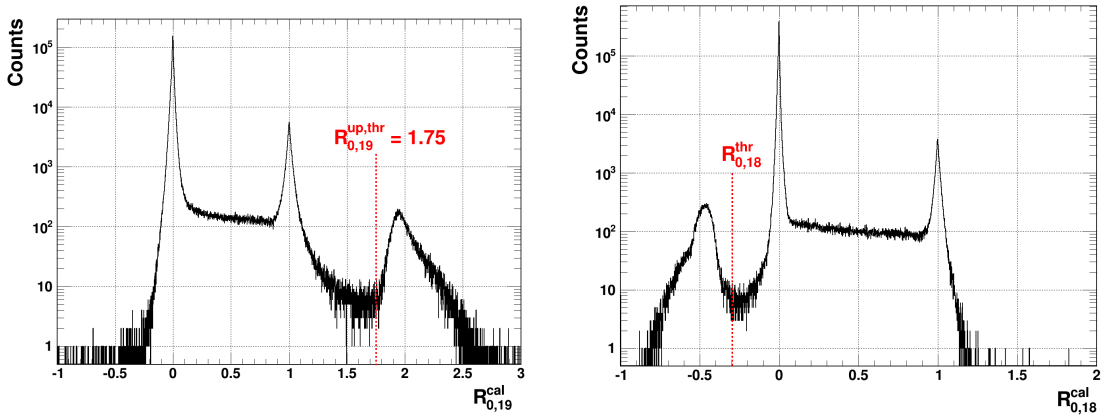

(a) (b)

Figure 6.13: Distributions of $R^{\text{cal}}_{0,i}$: a) for $i = 19$; b) for $i = 18$. In red the $R^{thr}_{0,i}$ thresholds used for calibration are shown as dashed red lines. The distributions were obtained with the ^{228}Th measurement referred to as CAL01, in Tab. D.1.

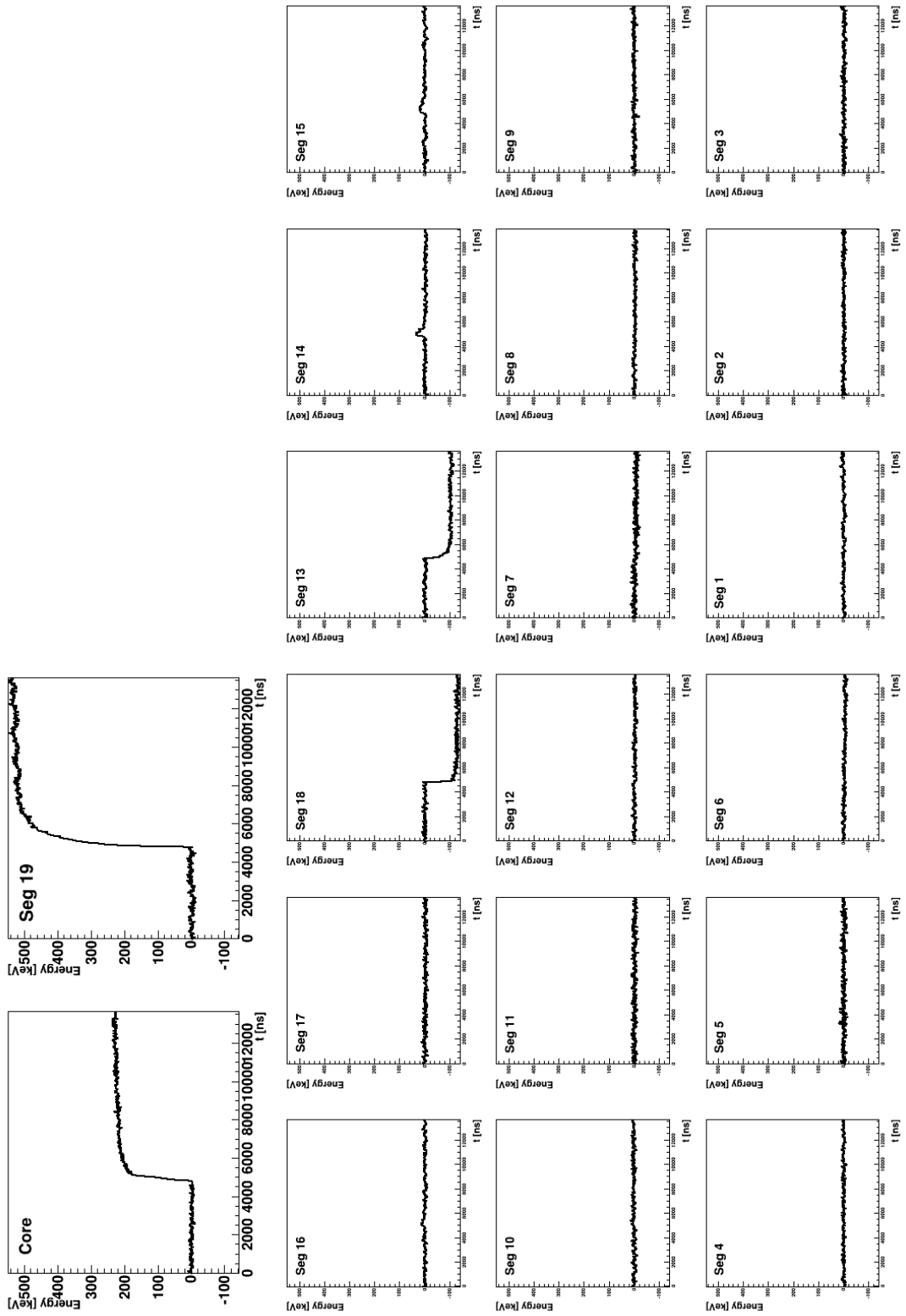

Figure 6.14: Calibrated and cross talk corrected pulses from the core (top left), from segment 19 (top right) and from the regular 18 segments for a typical event with electron trapping in segment 19.

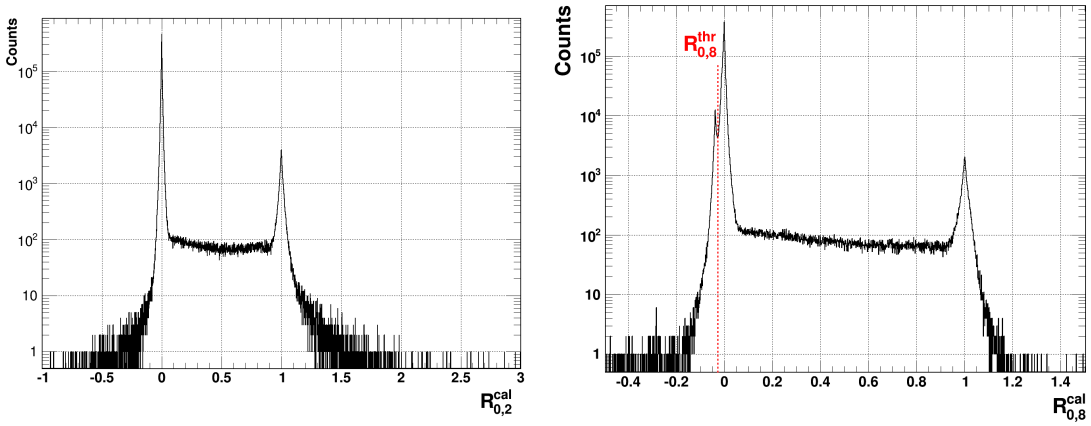

(a) (b)

Figure 6.15: Distributions of $R^{\text{cal}}_{0,i}$: (a) for $i = 2$ (b) for $i = 8$. In red the $R^{thr}_{0,i}$ threshold is shown as a dashed red line for $R^{\text{cal}}_{0,8}$. The distributions were obtained with the ^{228}Th measurement referred to as CAL01, in Tab. D.1.

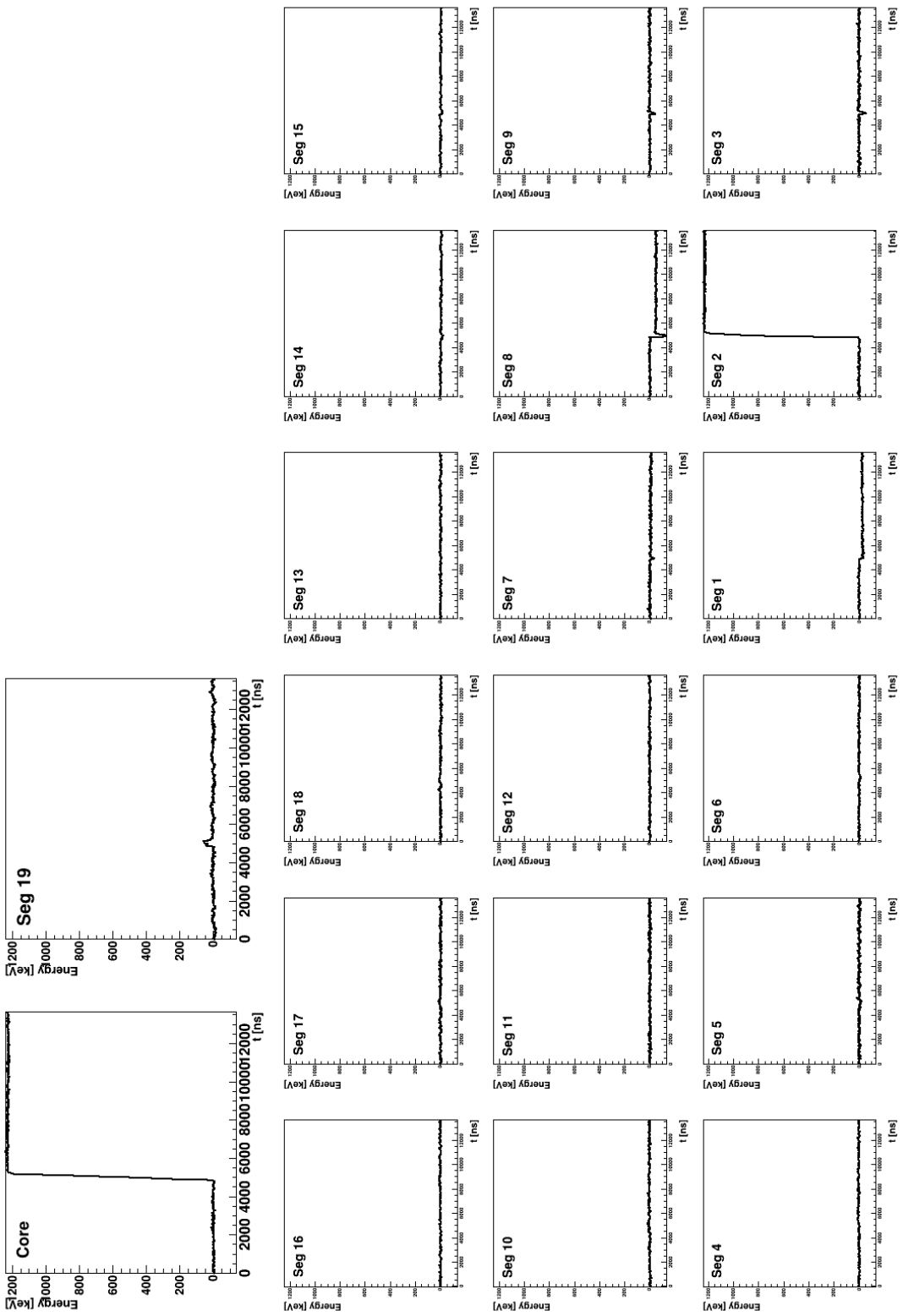

Figure 6.16: Calibrated and cross talk corrected pulses from the core (top left), from segment 19 (top right) and from the regular 18 segments for a typical event with electron trapping in segment 2.

Chapter 7

Probing Super Siegfried with ^{241}Am in GALATEA

Germanium detectors are probed with different kinds of radioactive sources inside the GALATEA test-stand (see chapter 4). In this chapter, the possibility to probe SuSie (see section 3.3.2) with low penetrating sources is discussed.

In section 7.1, the goals are formulated. The choice of ^{241}Am is motivated in section 7.2. In section 7.3, the expected signatures from alpha and gamma interactions are illustrated. Evidence for alpha interactions is presented in section 7.4. In sections 7.5 and 7.6, the selection criteria for alpha and gamma events, respectively, are given. In section 7.7, parameters extracted for pulses of alpha and gamma events are compared.

7.1 Goals

The goals are:

1. to characterize surface events induced by alpha particles and low-energy gammas. The characterization of alpha events should lead to suitable background reduction technique;
2. to improve the knowledge on charge trapping (e.g. [168]);
3. to extract the thickness of the dead layers down to few micrometers. This facilitates the exact determination of the active volumes of germanium detectors.

7.2 The isotope ^{241}Am

Americium is an artificial element produced by the neutron irradiation of uranium or plutonium inside a nuclear reactor. Its most common isotopes are ^{243}Am and ^{241}Am. The former is the most stable, with a half life of 7370 years. The latter is the isotope easiest to produce as pure samples and has a half life of 432.6 year. As shown in Fig. 7.1, ^{241}Am decays to ^{237}Np, emitting alpha particles with 5 different energies, predominantly with 5.49 MeV (branching ratio (BR) of 85.2%) and 5.44 MeV (BR = 12.8%). Many of the resulting states are metastable. They decay to their stable ground states emitting gamma rays, especially with 59.5 keV (BR = 35.9%) [172].

Emitting both alpha particles and low energy gammas, ^{241}Am is a perfect radioactive source to study surface events.

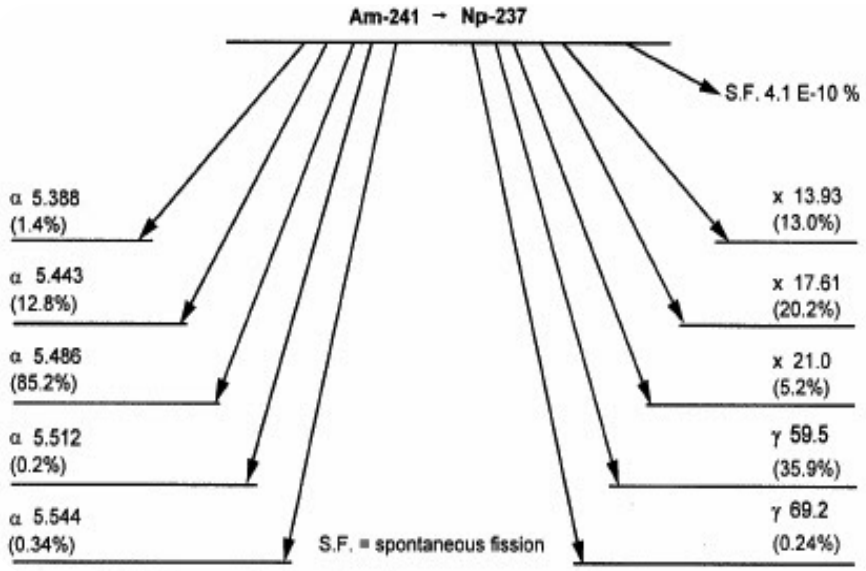

Figure 7.1: Decay scheme of ^{241}Am. The predominant alpha emission is at 5.49 MeV with a $BR = 85.2\%$. The gamma line with the highest BR of 35.9% has an energy of 59.50 keV.

While an alpha particle of about 5.5 MeV loses all its energy in as little as 32 μm of germanium, a gamma ray of 59.5 keV has a mean free path in germanium of about 0.9 mm. With a collimated ^{241}Am source:

1. alpha events can be used to study the characteristics of events very close to the surface;

2. alpha events can be used to study the depth of critical volumes right underneath the end-plates of a detector;

3. the gamma events can be used as a reference sample in the characterization process of surface events.

The comparison of the detector response to gamma and alpha particles basically compares the response of different volumes.

A 10 kBq ^{241}Am source was selected, which was placed inside a tungsten collimator [152]. The tungsten introduces two k-α emission lines k-α_1 at 59.32 keV and k-α_2 at 57.98 keV. These are unfortunately really close to the 59.5 keV from the ^{241}Am. The gammas from the k-α emission are not collimated and form an irreducible background to the collimated gammas from the ^{241}Am. Thus, the information from the gamma interactions is less localized.

7.3 Expected signatures from alpha and gamma interactions

Alpha particles interact with matter through ionization. Most of their energy is lost via scattering on atomic electrons. Although each individual collision causes little energy loss, the scattering cross-section is so high that alpha particles lose all their energy in the first thin layer of the detector. Photons, on the contrary, have a total scattering cross section about 10^2-10^3 times lower than the alpha particles. Typical values of the mean free path for the photons range from few mm for $E_\gamma = \mathcal{O}(10^2)\,\mathrm{keV}$ to tens of cm for $E_\gamma = \mathcal{O}(10^3)\,\mathrm{keV}$[1]. Photons, therefore, interact deeper inside the detector, than alpha particles.

True coaxial detectors, such as SuSie, present a symmetric and easy to understand electric field. However, distortions of the electric-field lines and surface-channels effect are expected close to the end-plates. The presence of the passivation layer and the distortion of the electric field lines reduce the charge collection efficiency in such critical volumes. Interactions happening within these so called "dead" layers create electron-hole pairs which recombine immediately and cannot be observed. Charge carriers drifting close to the surface have a certain probability to be trapped (see section 6.4). A strong effect is expected for low penetrating radiation like alpha particles.

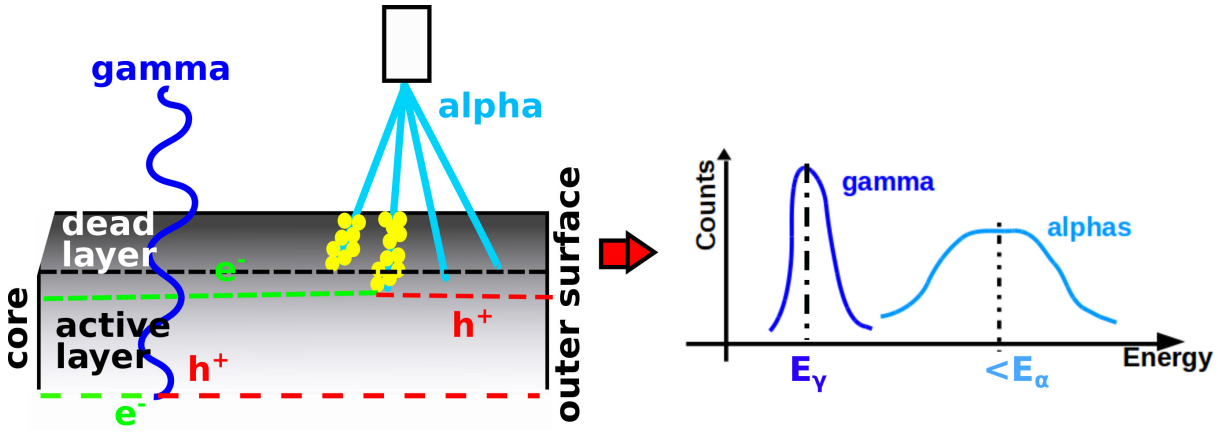

Figure 7.2: Schematic of expected line shapes from alpha and gamma radiation. The alpha line is broadened by geometrical effects and reduced in energy. Field distortions are expected close to the surface while the drift follows the radial field deeper inside the detector.

On the left part of Fig. 7.2, a vertical cut through of one half of SuSie is shown. The top surface is the passivated top end-plate. The left (right) side represents the inner (outer) surface of the detector. A naive model assumes a clear separation between a "dead" and an "active" zone. However the amount of charge actually collected increases slowly for charges deposited further from the surface. An effective dead layer, $\mathrm{DL}^{\mathrm{eff}}$, is defined corresponding to the amount

[1] The mean free path for 59.5 keV photons is 0.9 mm. Thus they have a high probability to interact in the top segment of SuSie.

of signal lost. A part of the signal loss is caused by the electric field lines being so distorted and weak, that charge carriers diffuse too slowly towards the electrodes to be registered. There are also effects due to the build-up of space charges, which can act as traps for charge carriers. The behaviour of charge carriers in such regions is unpredictable. The value of the thickness of DL^{eff} is affected by all effects which cause the loss of charge carriers during the drift.

The right part of Fig. 7.2 shows qualitative predictions for line shapes of gamma and alpha radiation. The line shapes for gamma radiation (dark blue line) with an incident energy, E_γ, is to first approximation a Gaussian (see App. B) with the mean value at E_γ. The width of the Gaussian is determined by electronic noise and by statistical fluctuations (i.e. the Fano factor, see section 3.3). The line shape for alpha radiation (light blue line) with an incident energy, E_α, is also a Gaussian. The mean value of the Gaussian is reduced. The width is the result of the combination of three effects:

geometrical effect (σ_{geom}): even though the ^{241}Am source is collimated, the beam spot has a finite size. A different incident angle corresponds to a different distance travelled inside the DL^{eff}, i.e. different amount of energy is lost inside the DL^{eff}. For a dead layer of 15 μm, the induced broadening is expected to be ≈ 0.1 keV (see appendix F). This effect can be neglected (see Appendix F);

protective window's effect (σ_{source}): the used ^{241}Am source is an encapsulated source with a plastic protective window [173]. For safety reasons, such a protective window is required. The window reduces the mean energy and introduces a spread of the energy at which alpha particles are emitted. A measurement on the side of a coaxial detector at a position where no dead layer is expected determined the reduced energy, E_α, to be $E_\alpha = 4.48$ MeV with a Gaussian width of about 0.18 MeV (see appendix F);

stochastic effect (σ_{stoch}): the amount of charge trapped during the drift can vary from one interaction to the other.

The total width of an alpha peak becomes:

$$\sigma_{tot} = \sqrt{\sigma_{geom}^2 + \sigma_{source}^2 + \sigma_{stoch}^2}\,. \tag{7.1}$$

7.4 Measurement of α-interactions

The ^{241}Am source was placed in the top collimator irradiating the top end-plate, i.e. segment 19, as shown in Fig. 7.3. On the left (right), a 3D view (top view) of SuSie, together with the sources, is shown.

All results shown in this chapter were obtained using the measurement referred to as AS01_5 from the azimuthal scan AS01 as listed in Tab. D.3. Figure 7.4 shows the energy spectra from the core, from segment 19 and from the 18 bulk segments.

The alpha peak is visible in the spectra from the core and from segment 19. The alpha peak is not observed in the summed spectrum from the 18 regular segments because of the extremely small penetration depth of alpha particles. The mean value of the alpha peak is different in the core and segment 19. This indicates different DL^{eff} for the electrons collected on the core electrode and the holes collected on the segment electrode.

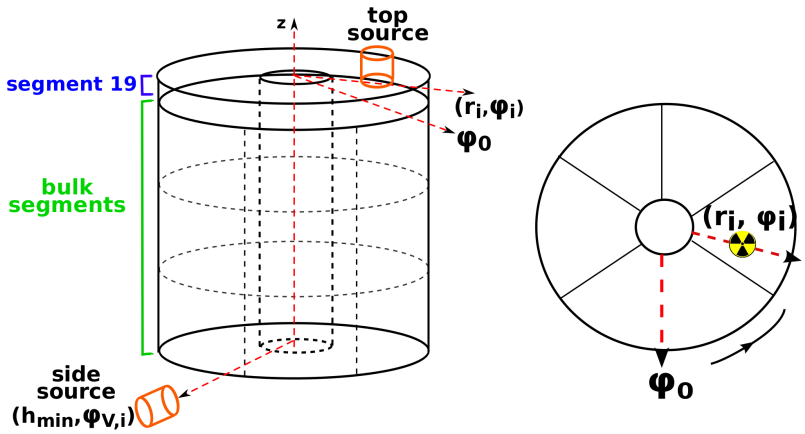

Figure 7.3: Position of the radioactive sources during a measurement with the α source at radius r_i and azimuthal angle ϕ_i. The side collimator is moved as far as possible away from the detector. The top collimator housing the ^{241}Am source can be moved in radial and azimuthal direction.

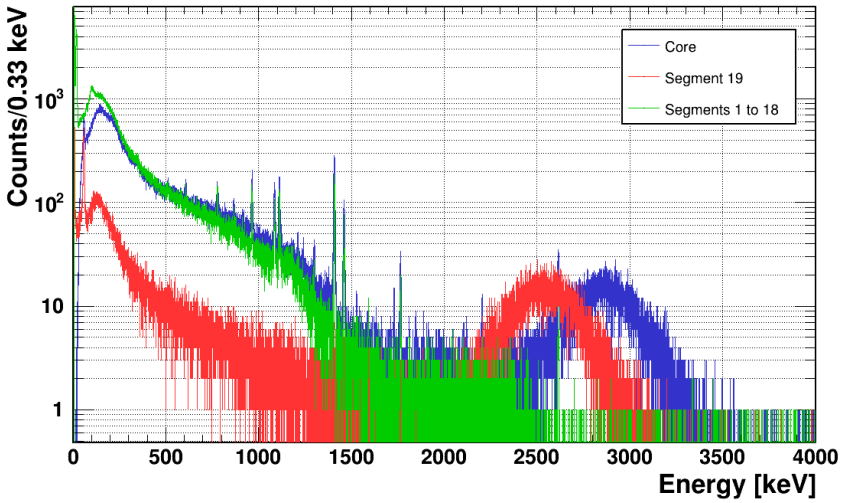

Figure 7.4: Comparison of the energy spectra from the core (blue), from segment 19 (red) and from the 18 regular segments (green), from the measurement AS01_5 as listed in Table D.3.

Figure 7.5 shows the energy spectrum and the result of a Gaussian fit for the core and segment 19. The values of the parameters extracted from the fitting procedure are listed. The Gaussian distribution is extremely wide in both spectra. The edges of the alpha peaks, $E_{min}(\alpha^{peak}_{0(19)})$ and $E_{max}(\alpha^{peak}_{0(19)})$, are defined as:

$$\begin{aligned} E_{min}(\alpha^{peak}_{0(19)}) &= \mu_{0(19)} - 3 \cdot \sigma_{0(19)} \\ E_{max}(\alpha^{peak}_{0(19)}) &= \mu_{0(19)} + 3 \cdot \sigma_{0(19)} \,, \end{aligned} \tag{7.2}$$

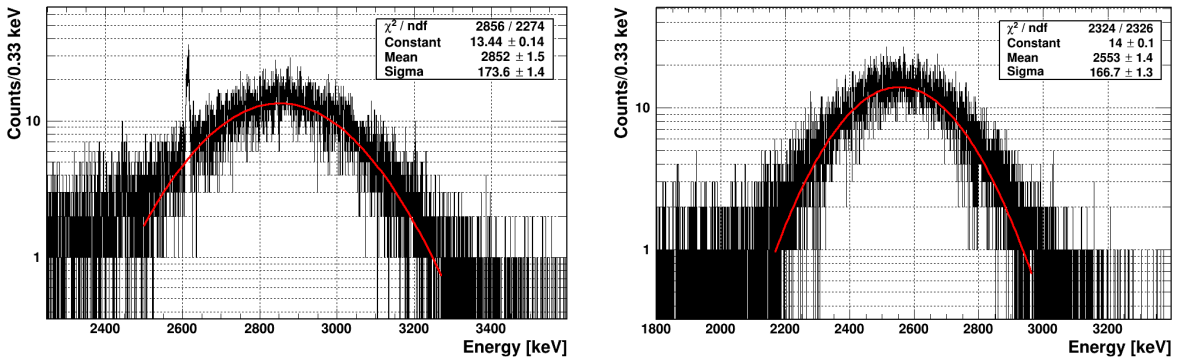

(a) (b)

Figure 7.5: a) Core energy spectrum around the alpha peak (black histogram) and the result of a fit performed with a Gaussian function in red; b) segment-19 energy spectrum zoomed around the alpha peak (black histogram) and the result of a fit performed with a Gaussian function in red. The results of the fit are also listed.

where $\mu_{0(19)}$ is the mean value of alpha peak in the core (segment 19) spectrum and $\sigma_{0(19)}$ is the standard deviation of the alpha peak in the core (segment 19) spectrum.

7.5 Alpha event selection

Figure 7.6 shows the correlation between the calibrated energy from the core and from segment 19. Several populations of events are identified:

1. single segment events (SSE) on the diagonal,
2. multi segment events (MSE) between the SSE diagonal and the x axis,
3. a class of events, observed only by probing the end-plate with the ^{241}Am source, in a band below the diagonal. These are associated with α-interactions.

The densest part of the α-band (inside the elliptical red area) contains the events with:

$$\begin{aligned} E_{min}(\alpha_0^{peak}) < E_0 < E_{max}(\alpha_0^{peak})\,, \\ E_{min}(\alpha_{19}^{peak}) < E_{19} < E_{max}(\alpha_{19}^{peak})\,. \end{aligned} \tag{7.3}$$

A pure alpha sample was selected by requiring the conditions of Eq. 7.3. The energies at which alphas are observed are so high that only the ^{208}Tl line is relevant. The probability for a photon above 2.5 MeV to be fully observed in segment 19 is low due to its limited thickness of 5 mm. Figure 7.7 shows the effect of the selection of alpha events on the core spectrum. The ^{208}Tl line is clearly visible in the spectrum of all events. It is not observable in the spectrum of selected events. From the events used for Fig. 7.6, 2.6% passed the selection. These are 20087 events. The contamination with gammas is negligible.

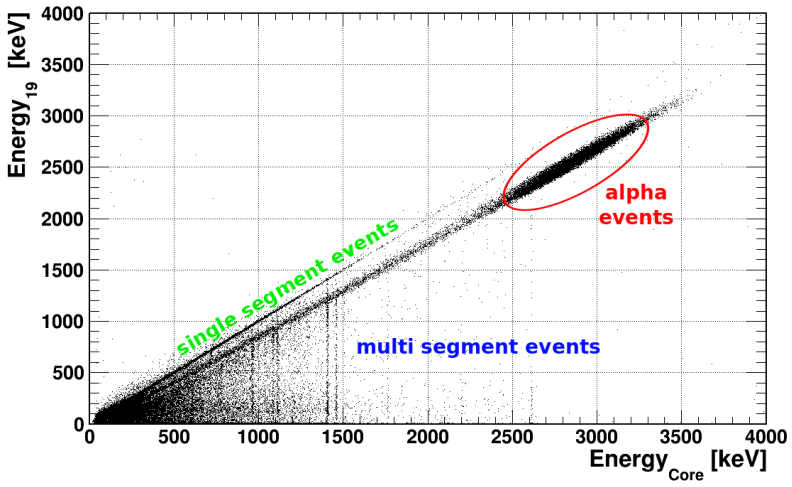

Figure 7.6: Correlation plot of the calibrated energies from the core and from segment 19. The population of events in the red elliptical area are the events for which the conditions of Eq. 7.3 are fulfilled.

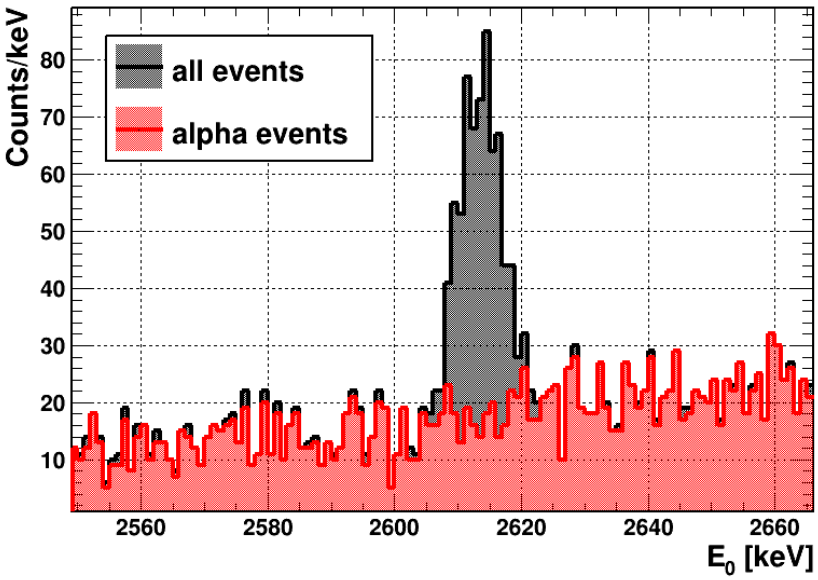

Figure 7.7: Comparison of the core energy spectra for all the event (black filled histogram) and for selected alpha events (red filled histogram) around the 2.6 MeV ^{208}Tl line.

The events in the entire alpha band in Fig. 7.6 have wider ranges of energy, both in the core and in segment 19. These events are harder to select into a pure sample. Any selection based on energy alone will have a larger gamma contamination. They were ignored as the analysis strategy is the following:

1. select the purest sample of alpha events requiring the conditions of Eq. 7.3;

2. proceed with the characterization of the alpha events, thereby obtaining characteristic parameters for alpha events;

3. use the parameters from 2. in order to later select alpha events in the rest of the alpha band.

Figure 7.8 depicts an event selected requiring the conditions of Eq. 7.3 from the measurement AS01_5 as listed in Table D.3. Calibrated and cross talk corrected pulses from the core (top left), from segment 19 (top right) and from the 18 regular segments are shown in the same time range and with the same energy scale.

Characteristics of alpha events at this location are:

1. core pulse and segment-19 pulse show different pulse-heights. This difference is about 7% for all selected events;

2. the risetime of the segment 19 pulse is larger than the risetime of the core pulse. This is a signature of slow hole drift due to a reduced field close to the surface;

3. the segments in the upper layer show either positive mirror (segments 13, 16, 17, 18) or positive truncated (segments 14 and 15) mirror pulses. These pulses are induced by the holes drifting to the collecting segment-19 electrode. The segment showing the highest mirror pulse is the segment located below the ^{241}Am source and is referred to as the "segment underneath", s_U;

4. segment-14 and segment-15 pulses are classified as positive truncated mirror pulses by the algorithm described in section 6.3.1. Truncated positive mirror pulses indicate hole trapping, see section 6.4. Adding the pulse-heights of the truncated mirror pulses to the pulse-height of segment 19, the pulse-height of the core pulse is obtained, i.e. the energy is balanced;

5. the segment-19 pulse shows a spike at around 4900 ns; the spike appears after the pulse is cross-talk corrected and calibrated, see section 6.1.3. The spike is due to core-to-segment 19 differential cross talk. The effect is visible only after the correction for proportional first order cross talk is applied. The spike in the segment 19 pulse follows the timing of the core pulse as shown in Figure 7.9. As pointed out in section 6.1.3, no proper method to correct differential cross talk is available. However, the presence of the spike does in general not affect any parameter extracted for the pulse (see section 6.2) and is thus irrelevant for this analysis.

Characteristics as defined here for a particular position have to be extracted for each position on each surface to characterize a detector completely.

7.6 Gamma events

The 59.5 keV photons, associated with the ^{241}Am source are selected using the following criteria:

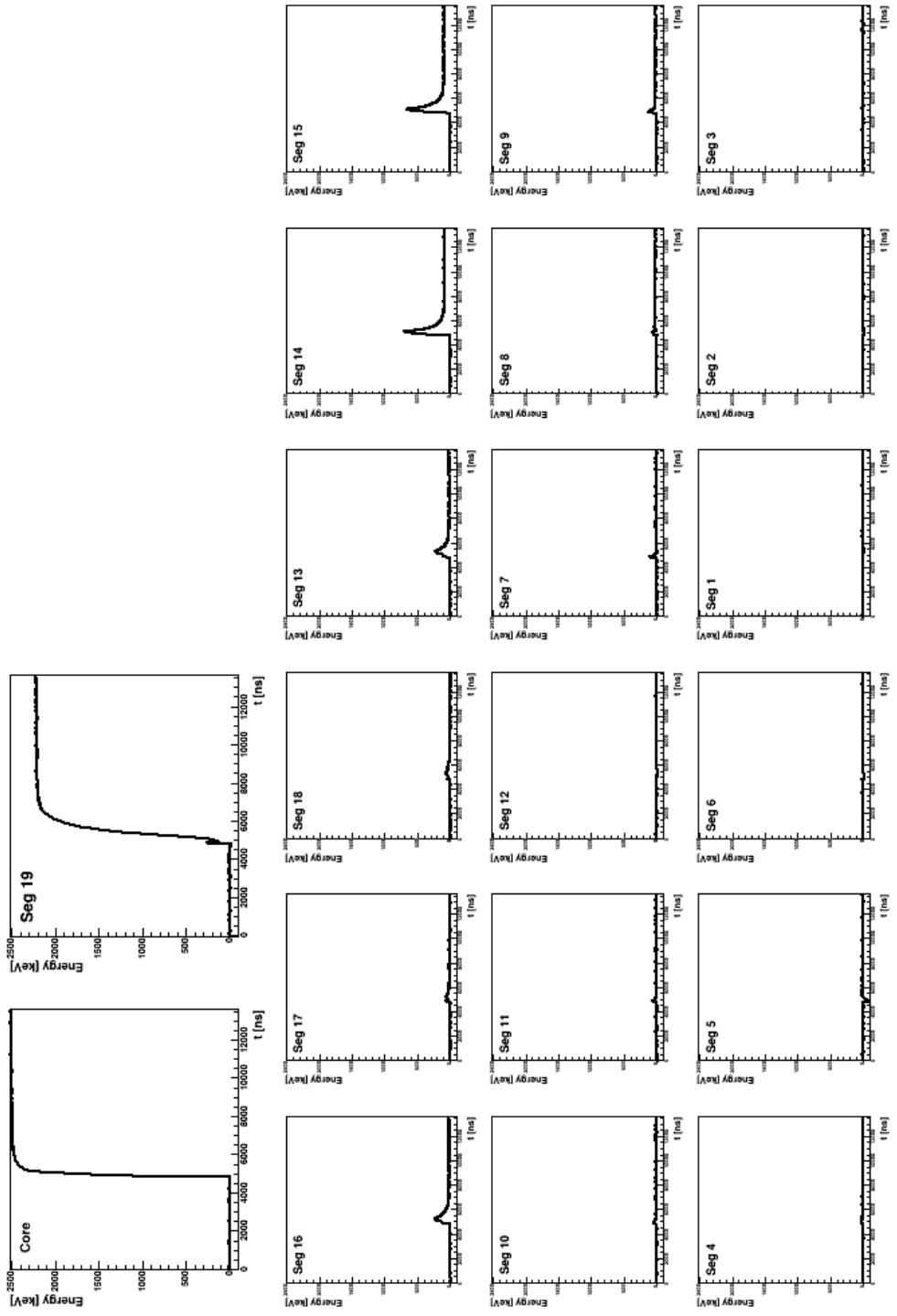

Figure 7.8: Cross-talk corrected and calibrated pulses from the core (top left), segment 19 (top right) and the 18 regular segments of a typical alpha event from the top scan measurement AS01_5 as listed in Table D.3. The source was located at $r = 26.0\,\mathrm{mm}$ and $\phi = 118°$ above segment 14 and segment 15.

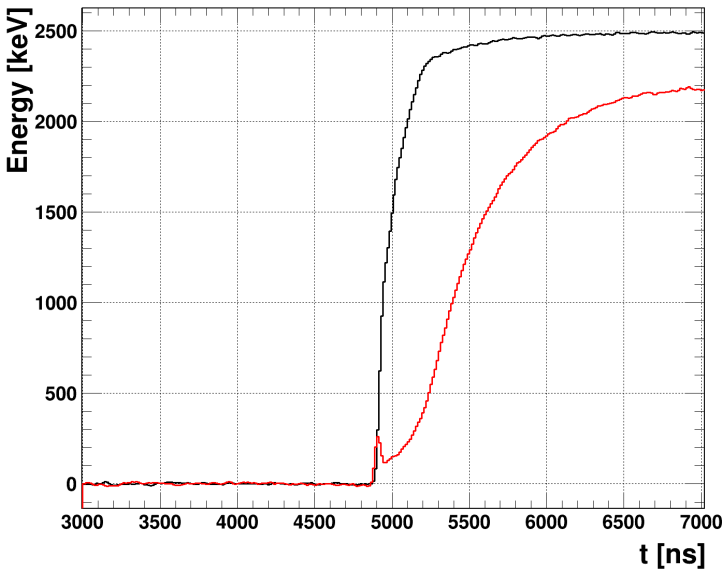

Figure 7.9: Core (black) and segment 19 (red) pulse. The pulses are from the alpha event depicted in Fig. 7.8.

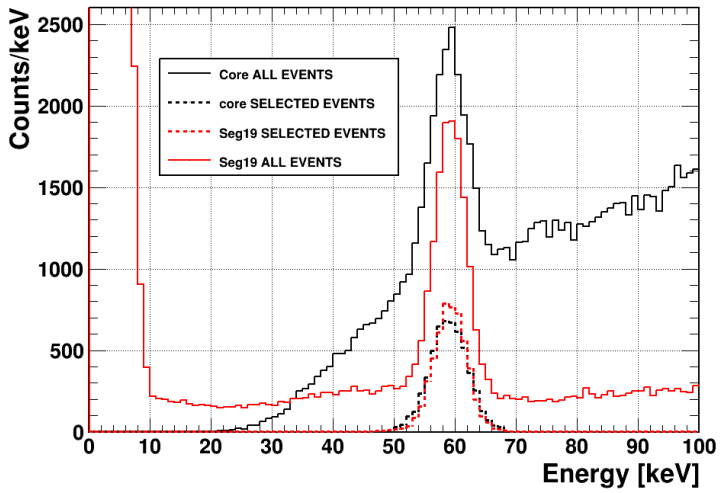

Figure 7.10: Core (black) and segment 19 (red) spectra before (solid lines) and after (dashed lines) the gamma event selection.

1. the energy measured in the core, E_0, is:

$$(E(\gamma_0^{peak}) - 3 \cdot \sigma_0)\,\mathrm{keV} < \mathrm{E}_0 < (\mathrm{E}(\gamma_0^{\mathrm{peak}}) + 3 \cdot \sigma_0)\,\mathrm{keV}\,, \tag{7.4}$$

   where $E(\gamma_0^{peak}) = 59.5\,\mathrm{keV}$ and σ_0 is the width of the peak in the full spectrum;

2. the segment 19 pulse is classified as standard using the classification algorithm introduced

in section 6.3.1;

3. s_U shows either a mirror or a truncated mirror pulse.

From the events shown in Fig. 7.6, 1.2% passed the selection. These are 5629 events.

Figure 7.10 shows the spectra from the core and from segment 19, before and after the selection criteria were applied. The events in the Compton continuum from gamma lines at energies higher than 59.5 keV are effectively removed from both spectra. The 1.2% of the events passing the selection form an extremely pure sample.

Figure 7.11 shows a typical event from the sample. Pulses from the core, from segment 19 and from the 18 regular segments are shown in the same time range and with the same energy scale. The electronic noise is more important for the gamma events than for the alpha events because of their much lower energy. The events shown in Figs. 7.8 and 7.11 were both selected from the measurement referred to as AS01_5 and listed in Table D.3.

The features of low-energy gamma events are:

1. the core pulse and segment 19 pulse have the same pulse-height. Segment 19 has more noise;

2. the segments in the upper layer show only normal mirror pulses. No truncated mirror pulses are observed, i.e. there is no evidence for charge trapping;

3. the segment 19 pulse is longer than the core pulse, but the effect is less pronounced than for alpha events;

4. if the different time developments affecting the cross-talk correction introduce a spike in segment 19, it is too small to be observable in the presence of noise.

7.7 Comparison of alpha and gamma pulses

7.7.1 Risetime

Figures 7.8 and 7.11 show that the time structure of alpha and gamma events is different. This is reflected in the risetime distributions. Figure 7.12a (7.12b) shows the distributions of RT_i^{10-90} (RT_i^{10-30}) for the core, $i = 0$, and segment 19, $i = 19$, for alpha and gamma events.

A big difference is observed in both the RT_i^{10-90} and RT_i^{10-30} distributions between alpha and gamma events. Both the RT_i^{10-90} and RT_i^{10-30} distributions for gamma events are much broader, because the events are less localized due to the component from the k-α radiation from tungsten. In addition the extraction of the risetime of low energy gamma events is more affected by the noise, especially in segment 19, where the noise level is 2 times larger than for the core. This affects in particular the RT_i^{10-30} distributions.

The distributions for the core and segment 19 show clear differences for both alpha and gamma events. They are more pronounced for alpha events, for which the RT_0^{10-90} distribution ranges from about 100 to 350 ns while the RT_{19}^{10-90} extends from about 900 to 1000 ns. Segment 19 collects holes at the outer surface of the detector. The drift of the holes at large radii is slower than the drift of the electrons close to the core. Due to the different weighting potentials, the pulses are affected differently. The last part of the hole drift has basically no influence on the

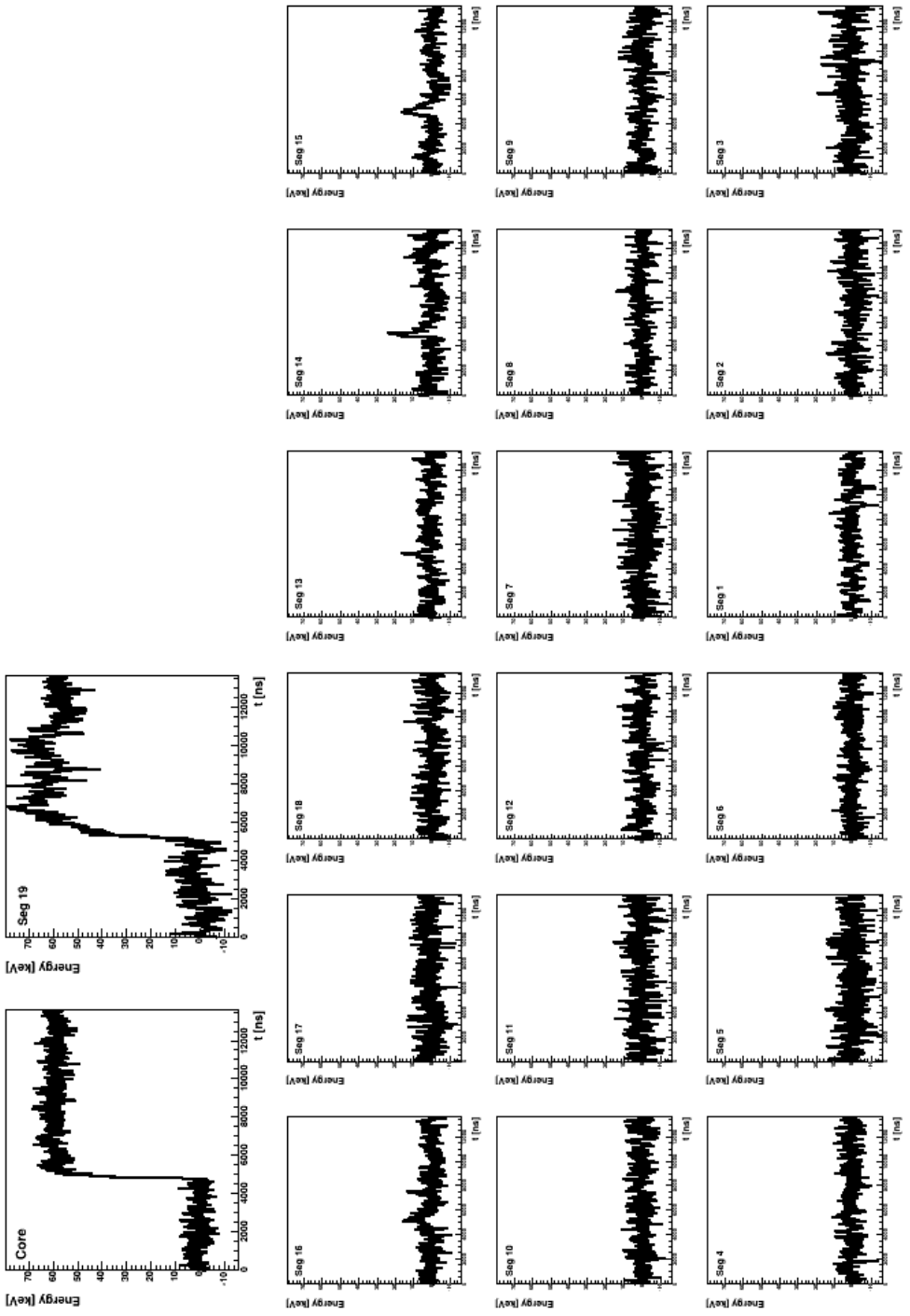

Figure 7.11: Cross-talk corrected and calibrated pulses from the core (top left), segment 19 (top right) and the 18 regular segments of a typical gamma event from the top scan measurement AS01_5 as listed in Table D.3. The source was located at $r = 26.0\,\mathrm{mm}$ and $\phi = 118°$ above segment 14 and segment 15.

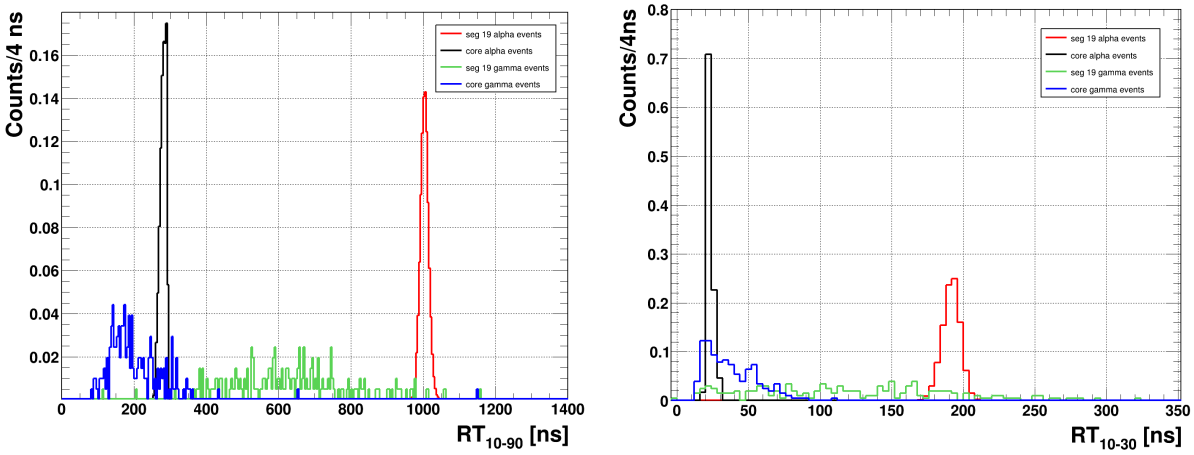

(a) (b)

Figure 7.12: Risetime distributions for alpha and gamma events: a) RT_0^{10-90} for alpha (gamma) events is shown in black (blue). RT_{19}^{10-90} for alpha (gamma) events is shown in red (green); b) $RT_{0(19)}^{10-30}$ distributions are shown with the same color code as in a). The distributions of selected events were obtained from the AS01_5 measurement as listed in Table D.3.

core pulse. The different risetimes for gammas show that large parts of the volume of segment 19 are affected by a low electric field.

7.7.2 Mirror pulse statistics

The classification algorithm described in section 6.3.1 was used to quantify the occurrence of truncated mirror pulses in the s_U and neighbouring segments. For any pulse-type, pt, a fraction, f^{pt}, is defined for segment s as:

$$f_{\alpha(\gamma)}^{\mathrm{pt,s}} = \frac{n_{\alpha(\gamma)}^{\mathrm{pt,s}}}{N_{\alpha(\gamma)}} \tag{7.5}$$

where:

$n_{\alpha(\gamma)}^{\mathrm{pt,s}}(s)$ is the number of selected alpha (gamma) events where the segment-s pulse was classified as pt;

$N_{\alpha(\gamma)}$ is the total number of selected alpha (gamma) events.

Table 7.1 shows the f^{pt} both for alpha and gamma events for $s_U = 14$ and its neighbours (segments 13 and 15) as extracted for the measurement AS01_5 as listed in Table D.3. The collection of all the f^{pt} values is referred to as "pulse statistics". The slow drift of the holes creates positive mirror pulses in $s_U = 14$ and with high probability also in its neighbours for both alpha and gamma events. In the alpha events, the positive mirror pulses in $s_U = 14$ are almost always truncated. This is not observed for the gamma events. The gammas interact deeper inside

the detector than the alpha particles and the holes are not trapped even though they drift slower than the electrons. A very small number of negative (truncated) mirror pulses is observed in the alpha events. This is most likely due to the selection of very high energy events from the alpha band. In addition, any small amount of electron trapping could be obscured by stronger hole trapping. The small number of negative truncated mirror pulses listed for the gamma sample are introduced by noise. As the events were calculated based on core energy, electron trapping cannot be observed in this sample.

	Segment	**Standard pulses** $f^{\mathrm{S}}_{\alpha(\gamma)}$	**No pulses** $f^{\mathrm{N}}_{\alpha(\gamma)}$	**Mirror positive** $f^{\mathrm{MP}}_{\alpha(\gamma)}$	**Mirror negative** $f^{\mathrm{MN}}_{\alpha(\gamma)}$	**Truncated positive** $f^{\mathrm{TP}}_{\alpha(\gamma)}$	**Truncated negative** $f^{\mathrm{TN}}_{\alpha(\gamma)}$
Alpha	Core	1.00	–	–	–	–	
	19	1.00	–	–	–	–	–
	13	–	–	0.553	0.0001	0.446	0.0002
	14	–	–	0.002	0.0001	0.998	0.0001
	15	–	–	0.002	0.0002	0.998	0.0001
Gamma	Core	1.00	–	–	–	–	
	19	1.00	–	–	–	–	–
	13	–	0.994	0.006	–	–	0.0002
	14	–	–	0.998	–	–	0.002
	15	–	0.293	0.707	–	–	0.0002

Table 7.1: Pulse statistics for core, segment 19, $s_U = 14$ and its neighbours segments 13 and 15. The statistics are listed for alpha events and for gamma events.

Chapter 8

Alpha-event and surface characterization

A scan of the upper end-plate of SuSie I using a collimated 10 kBq ^{241}Am source was performed to characterize alpha events and the detector properties close to the detector surface. Four radial and two azimuthal scans were performed to cover the end-plate.

In section 8.1, a method to localize events using mirror pulses is introduced. The dependence of the characteristics of alpha and gamma events on the location of the interaction is presented in section 8.2. In section 8.3, the reproducibility of this dependence is discussed. The results on the thickness of the effective dead layer are shown in section 8.4. In section 8.5, the consequences for detectors design are discussed.

8.1 Reconstruction of the event position using mirror pulses

The reconstruction of the position of an energy deposit using mirror pulses is an established method for segmented detectors (e.g. [174]). Amplitudes and polarities of mirror pulses in segments close to the collecting segment are used to obtain information on the drift of the charge carriers and thus on the location of the interaction. The energy depositions for alpha particles are high, i.e. the mirror pulses are large and well observable. These events are localised energy depositions at the top of the detector and are recorded in segment 19. The mirror pulses are observed in the six segments right underneath. The mirror pulses are expected to contain information on the radial and azimuthal position of the events.

The polarity of the mirror pulses depends on the radial position of the event. In principle, positive (negative) mirror pulses are expected for interactions close to the bore hole (to the outer surface) of the detector due to the longer drift of holes (electrons). However due to the slow drift of the holes, the situation is modified such that mostly positive pulses are expected and the information on the radial position is mostly lost.

The information on the azimuthal angle is contained in the relative strength of the mirror pulses and should not be obscured by the slow drift of the holes. The first step is to identify the segment underneath, s_U, as defined in section 7.5:

a) positive, M_i^+, and negative, M_i^-, maxima are extracted as discussed in section 6.2, for each segment i in the upper layer of the regular 18 segments of SuSie I, see appendix C Fig. C.1;

b) the absolute values M_i^+ and $|M_i^-|$ are arranged in ascending order, thereby obtaining two segments k and l whose $M_k^+ = M^{+,\max}$ and $|M_l^-| = |M^{-,\max}|$ respectively;

c) a comparison between the two maximum values is performed. Therefore $s_U = k$ ($s_U = l$) if $M^{+,\max} > |M^{-,\max|}$ ($|M^{-,\max}| > M^{+,\max}$);

The relative strengths of the mirror pulses in s_U and its neighbours is used to refine the position. An asymmetry, $\mathcal{A}_{s_U,j}$, is defined as:

$$\mathcal{A}_{s_U,j} = \frac{M_j^{+(-)} - M_{s_U}^{+(-)}}{M_j^{+(-)} + M_{s_U}^{+(-)}}\,, \tag{8.1}$$

where segment j shows the second highest mirror pulse. Figure 8.1 shows the distribution of s_U on the left and the distribution of $\mathcal{A}_{s_U,j}$ on the right. The distributions are based on the measurement AS01_5, listed in Table D.3.

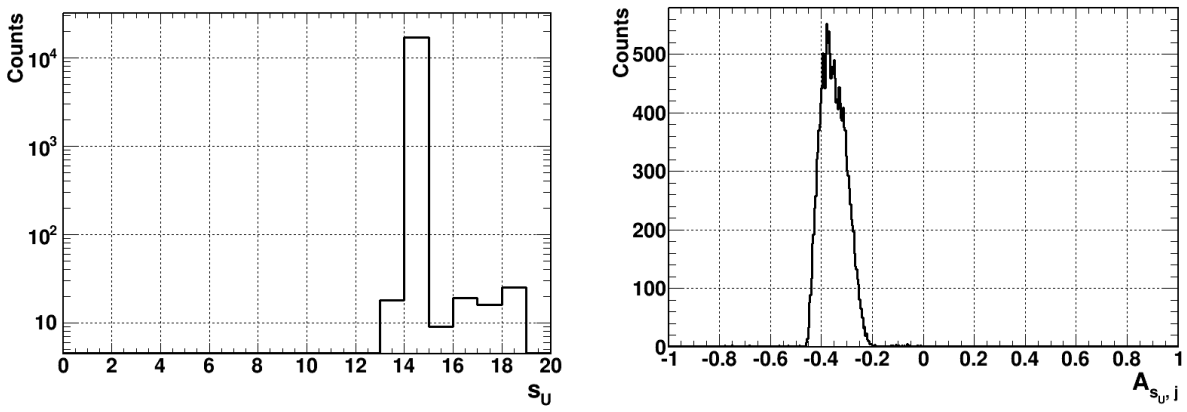

(a) (b)

Figure 8.1: a) Distribution of s_U; b) distribution of $\mathcal{A}_{s_U,j}$. The distributions were obtained using the measurement referred to as AS01_1, listed in Table D.3.

The distribution of s_U shows that in most of the events the identified $s_U = 14$. Events where other segments are identified as s_U are due to a small contamination of high energy gammas, e.g. from the 2.6 MeV ^{208}Tl line, see section 7.5. The distribution of $\mathcal{A}_{s_U,j}$ shows a peak at around -0.32 and a FWHM of about 0.11. A calibration is needed to convert the $\mathcal{A}_{s_U,j}$ values into azimuthal angles.

8.1.1 Calibration of the asymmetries and angular resolution

The known positions are used to convert the values of $\mathcal{A}_{s_U,j}$ to measured azimuthal angles. For the calibration, average asymmetries are used. This was implemented by computing average

values $\overline{M_i^+}$ and $\overline{M_i^-}$ before step b) in the procedure described in the previous section. Steps b) and c) were then performed for these average values, resulting in the averaged asymmetry, $\overline{\mathcal{A}}_{s_U,j}$.

Figure 8.2 shows the correlation between $\overline{\mathcal{A}}_{s_U,j}$ and the nominal source position. Only part of the data follow the expected linear dependence. The other data were affected by a motor problem as detailed below. The linear dependency is used for calibration. The distribution in Fig. 8.1b has a $\overline{\mathcal{A}}_{s_U,j} = -0.21$ and corresponds to an azimuthal angle of 98°. The slope is 0.014 and thus the FWHM of the distribution in Fig. 8.1b of 0.11 corresponds to an angular resolution of about 5° for single events.

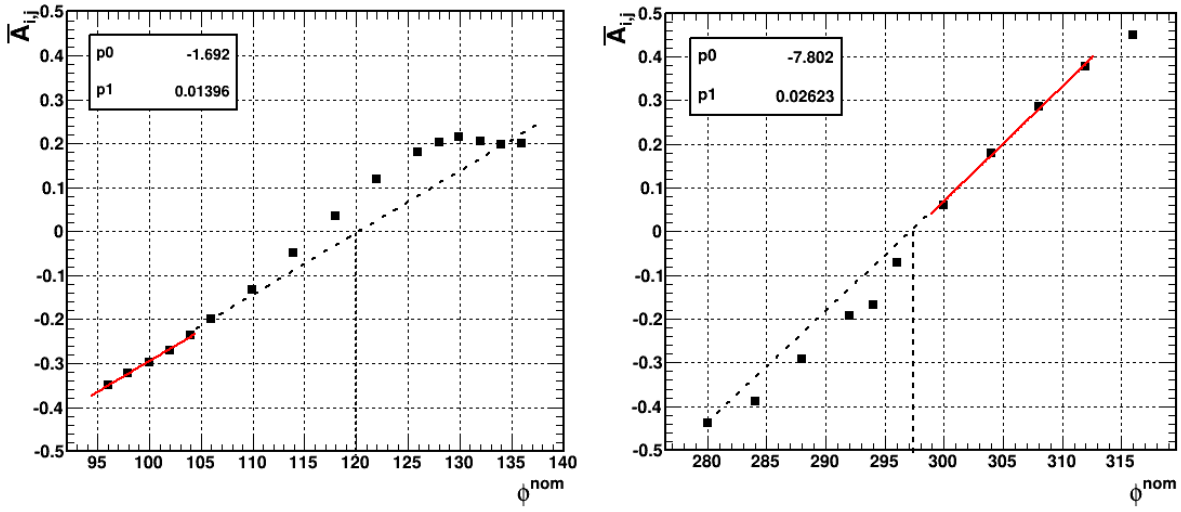

Figure 8.2: Correlation between $\overline{\mathcal{A}_{i,j}}$ and ϕ^{nom} at two different radii. On the left (right) the correlation obtained for $r = 26.0\,\text{mm}$ ($r = 30.0\,\text{mm}$) are shown. The error bars representing the uncertainties $\Delta\overline{\mathcal{A}}_{i,j}$ are smaller than the size of the symbols.

8.1.2 Corrections to nominal source positions

As mentioned in section 4.1, a problem with the rotation of the IR-shield was discovered during the data taking in Autumn 2013. The rotational stage dragged the detector holder along, thereby changing the relative azimuthal positions of the detector and the circular motor. The nominal values of the azimuthal angles were not describing the real position of the source. A reconstruction of the azimuthal position of the source was therefore necessary. The results of the calibration discussed in the previous section were used.

For each scan position, the $\overline{\mathcal{A}}_{s_U,j}$ was evaluated. By construction, $\overline{\mathcal{A}}_{s_U,j}$ is zero at the segment boundary between segment s_U and segment j. A shift from the segment boundary, ϕ^{shift}, is defined as:

$$\phi^{\text{shift}} = \frac{\bar{\mathcal{A}}_{s_U,j} - p_0}{p_1}\,, \tag{8.2}$$

where p_0 and p_1 are the offset and the slope of the fit function shown in Fig. 8.2. Thus, the

reconstructed azimuthal angle ϕ is defined as:

$$\phi = \begin{cases} \phi^{SB} + \phi^{\text{shift}} & \text{if } \overline{\mathcal{A}}_{s_U,j} > 0 \\ \phi^{SB} - \phi^{\text{shift}} & \text{if } \overline{\mathcal{A}}_{s_U,j} < 0\,, \end{cases} \tag{8.3}$$

where ϕ^{SB} is the azimuthal angle at the segment boundary between segment s_U and segment j.

The statistical uncertainty on ϕ is obtained propagating the statistical uncertainties of the fit. An estimate of the systematic uncertainty is obtained comparing the azimuthal position of the two segment boundaries obtained from the fit performed for $r = 26.0\,\text{mm}$ (Fig. 8.2 on the left) and for $r = 30.0\,\text{mm}$ (Fig. 8.2 on the right), i.e. $\phi_{26}^{SB} = 120°$ and $\phi_{30}^{SB} = 297.5°$ respectively. The systematic uncertainties on the azimuthal position of the source was found to be around 2.5°.

The scan positions showing an asymmetry around 0.2 on the left plot of Fig. 8.2, were performed close to metallic bars above the detector, which are part of the support of the detector (see section 3.3.2). The evaluated asymmetries are biased by the presence of the bar. A fraction of the solid angle from the opening of the source faced the bars. Thus only alpha particles emitted at very high angles reached the detector. This explains the almost constant value of the asymmetry.

8.2 Position dependence of event characteristics

The dependence on the radius and the azimuthal angle are investigated with two different kinds of scan:

1. **radial scans**: the azimuthal angle of the source was fixed while its radial position was varied;
2. **azimuthal scans**: the radial position of the source was fixed while its azimuthal position was varied. The azimuthal angles were corrected as described in section 8.1.

The azimuthal and radial positions are expressed with respect to the reference frame of SuSie described in appendix C. Even though radial scans were performed using the entire range of the horizontal motor, only measurements showing peaks associated with alpha interactions are considered in the following. Figure 8.3 shows all locations at which alpha measurements were performed. During all ^{241}Am measurements, the side collimator housing the ^{152}Eu source was moved as far as possible away from the detector. The event characteristics were extracted for each location separately using the parameters as specified in chapters 6 and 7.

All figures where the parameters are displayed for different source positions use the color code of Fig. 8.3 and the following structure (unless otherwise specified):

1. figures illustrating radial dependencies show the parameters as functions of the radial position for the four different azimuthal positions:
   (a) black squares represent measurements done at $\phi = 33.0°$, i.e. measurements listed as RS01 in Table D.2;
   (b) red squares represent measurements done at $\phi = 312.0°$, i.e. measurements listed as RS02 in Table D.2;
   (c) green squares represent measurements done at $\phi = 176.0°$, i.e. measurements listed as RS03 in Table D.2;

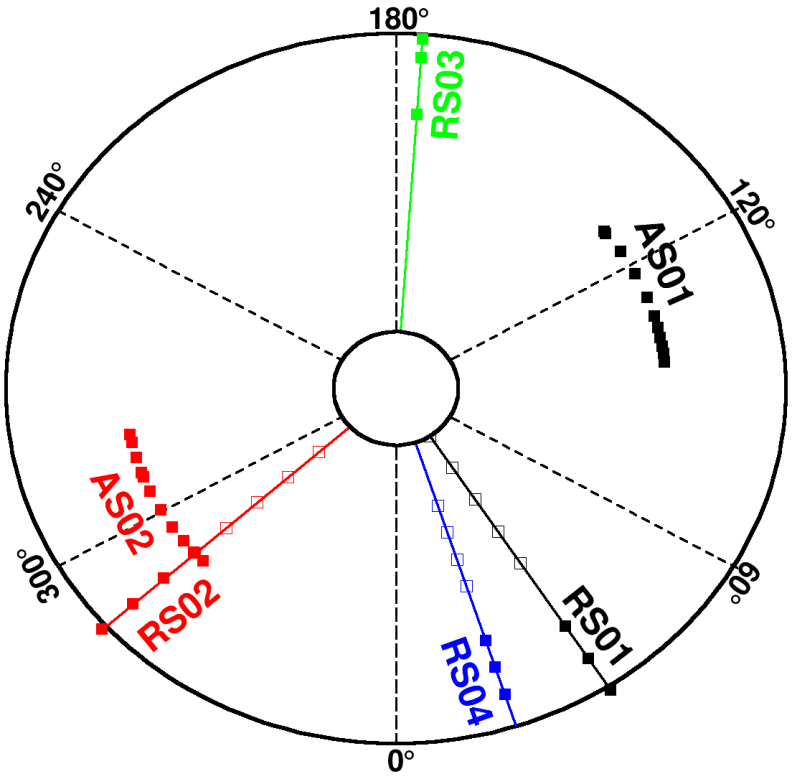

Figure 8.3: Location of scan positions on the top end-plate of SuSie I. The locations were corrected according to section 8.1. The dashed lines represent the segment boundaries between segments of the "upper-layer" (see Fig. C.1). Each filled square represents a source position, for which an alpha peak was identified. Open squares show positions for which no alpha peak was observed. All the scanning positions for both radial and azimuthal scans are listed in Tables D.2 and D.3.

(d) blue squares represent measurements done at $\phi = 18.0°$, i.e. measurements listed as RS04 in Table D.2.

2. Figures illustrating azimuthal dependencies show the parameters as functions of the azimuthal position for the two sectors with slightly different r:

   (a) black squares represent measurements done far from the metalization in segment 19 at $r = 26.0\,\text{mm}$, i.e. measurements listed as AS01 in Table D.3;

   (b) red squares represent measurements done close to the metalization in segment 19 at $r = 30.0\,\text{mm}$, i.e. measurements listed as AS02 in Table D.3.

8.2.1 Features of the spectral lines from alpha interactions

Alpha events were selected as described in section 7.5. The corresponding peaks in the spectra from the core and from segment 19 were fitted with Gaussian functions, as described in section 7.4.

The dependence of the event counts, C_i^α, the mean energies, μ_i^α, and the associated standard deviations, σ_i^α, was investigated.

Figure 8.4 shows the counts per second, C_0^α, of selected alpha events as a function of the radius and the azimuthal angle. The values of C_0^α were extracted with the fitting procedure described in section 7.4. The error bars represent the statistical uncertainties. The radial dependence is only shown for locations where alpha events were observed in a clear peak. The smallest radius at which this happened is $r = 26.0\,\text{mm}$ at $\phi = 312°$. This is close to the sector where segment 19 was metalized. At this ϕ and at $\phi = 18°$, an onset of the signal was observed while at the locations far away from the metalization, this was not the case. The count rate depends on the thickness of the effective dead layer. This seems to change very quickly around $r = 27.0\,\text{mm}$ and to be stable even up to very large radii. The detector ends at $r = 37.5\,\text{mm}$. It remains effective up to the very edge. Figure 8.4b shows the dependence of the count rate on the azimuthal angle for two different radii in the two different sectors. The count rate is reasonably stable over most of the two ranges. It is lower for the smaller radius of 26 mm. Both values are compatible to what was observed for $r = 26.0\,\text{mm}$ and $r = 30.0\,\text{mm}$ for other values of ϕ. The drop of count rate at $\phi = 135°$ is again associated to the metal holder above the detector. These points are excluded from the further analysis.

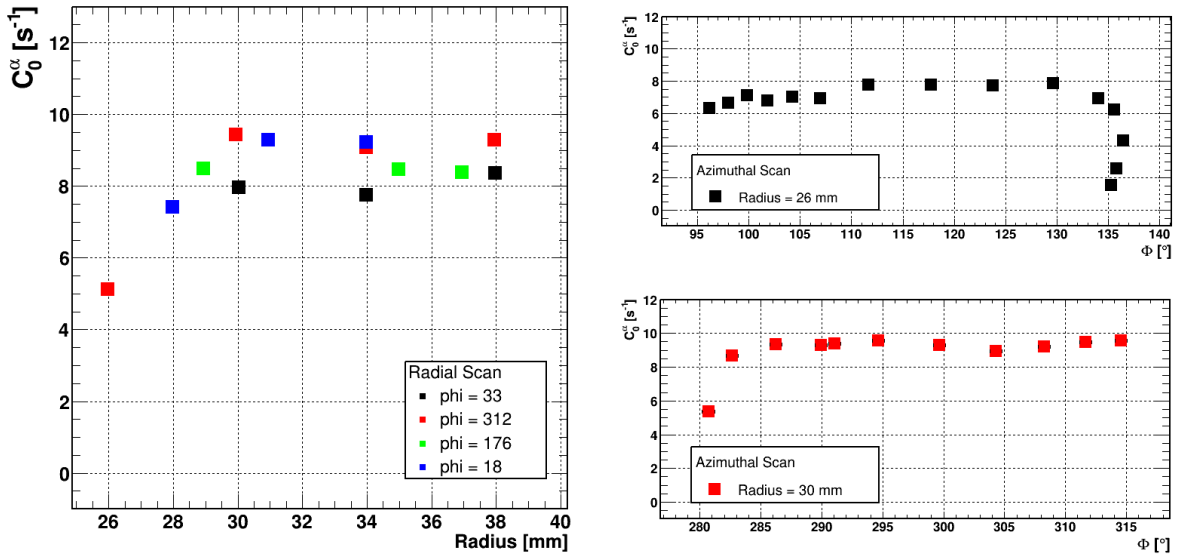

(a) (b)

Figure 8.4: Counts per second in the alpha peak a) as a function of the radius for four azimuthal angles; b) as a function of the azimuthal angle, in two sectors at two different radii. The error bars representing the statistical uncertainties are smaller than the size of the symbols.

Figure 8.5 shows the mean energies recorded for the selected alpha events in the core, μ_0^α, and in segment 19, μ_{19}^α, as a function of the radius, see section 7.4 for extraction details. There is a clear trend that the energy recorded in the core, μ_0^α, decreases with radius while the energy recorded in segment 19, μ_{19}^α increases. Due to the different weighting potentials, the former is

dominated by the drift of electrons while the latter is dominated by the drift of holes. The two different charge carriers are subject to different trapping effects. If the energy is deposited at large radii, the electrons have a higher probability to be trapped as the holes due to their longer path, hence lower μ_0^α. As the source is moved towards the core, i.e. smaller radii, holes are more likely to be trapped than electrons, hence lower μ_{19}^α.

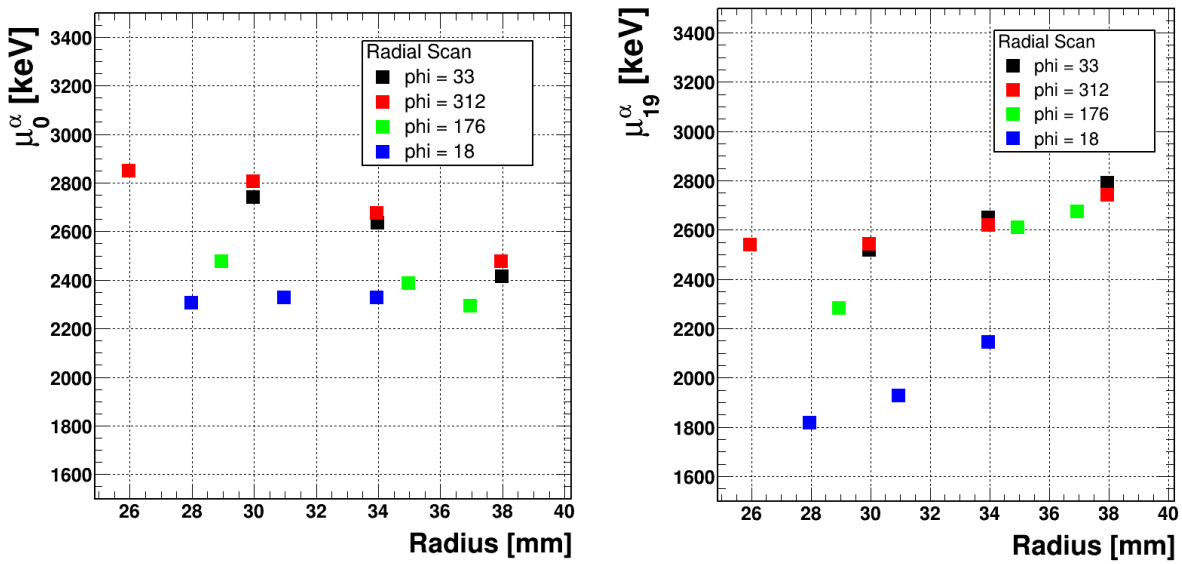

(a) (b)

Figure 8.5: Mean energy recorded, μ_i^α, as a function of the radius for different azimuthal angles, with $i = 0$ on the left and $i = 19$ on the right. The statistical uncertainties as determined by the fitting procedure are smaller than the symbol size.

Figure 8.6 shows the dependence of μ_i^α on ϕ for the core, $i = 0$, and the top segment, $i = 19$. μ_0^α is on average higher than μ_{19}^α for both azimuthal scans. This is in qualitative agreement with the results shown in Fig. 8.5. The mean recorded energies vary by about 200 keV for both scans. The variations of μ_0^α and μ_{19}^α with the azimuthal position indicates variations in the charge collection efficiency. AS02_1 (red) shows significantly higher μ_0^α and μ_{19}^α values around $\phi = 300°$, which is corresponding to the position of the metalization of the top segment in SuSie I (see Fig. 3.6). The electric field lines there are stronger and less distorted. That increases the drift velocity and reduces the probability of trapping for both electrons and holes.

Figure 8.7 shows the dependence of σ_i^α on the radius. The situation seems to be different for each set of measurements. Especially for the RS04 set, which shows a σ_{19}^α of about 270 keV at $r = 28.0$ mm. Such high values for σ_{19}^α in measurements from this set can however be explained by the vicinity of the Mercedes bar MB1, as shown in Fig. C.2. Figure 8.8 shows the dependence of σ_i^α on the azimuthal angle. Both σ_0^α and σ_{19}^α show the same value between 170 and 180 keV for most of the azimuthal angles. However, the standard deviations drastically increase around $\phi = 315°$.

As introduced in section 7.3, the standard deviation, σ_i^α (both $i = 0, 19$), is influenced by

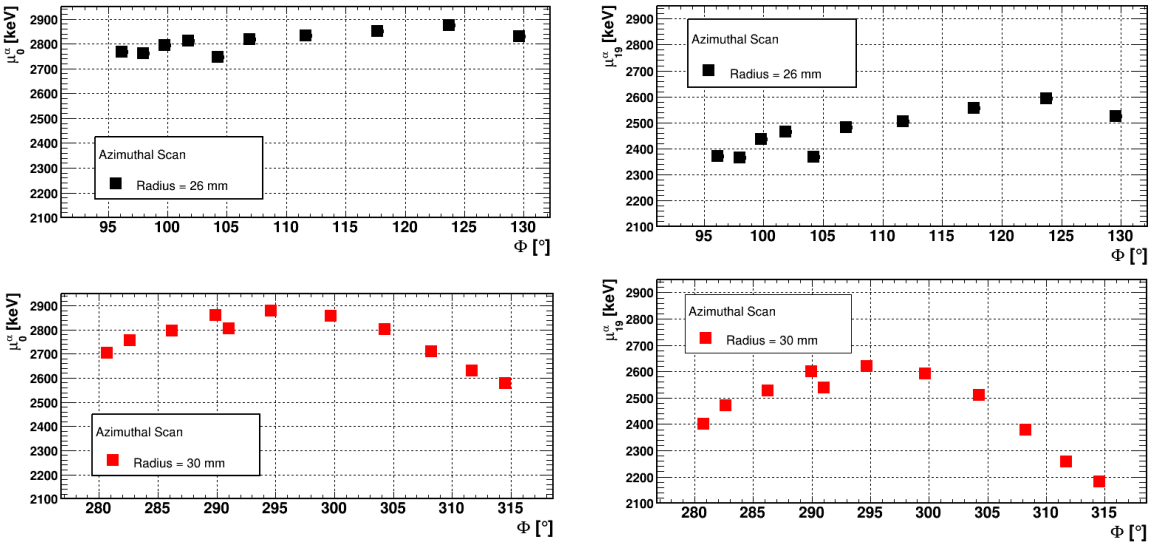

(a) (b)

Figure 8.6: μ_i^α as a function of the azimuthal angle for different radii, with $i = 0$ on the left and $i = 19$ on the right. The statistical uncertainties as determined by the fitting procedure are smaller than the symbol size.

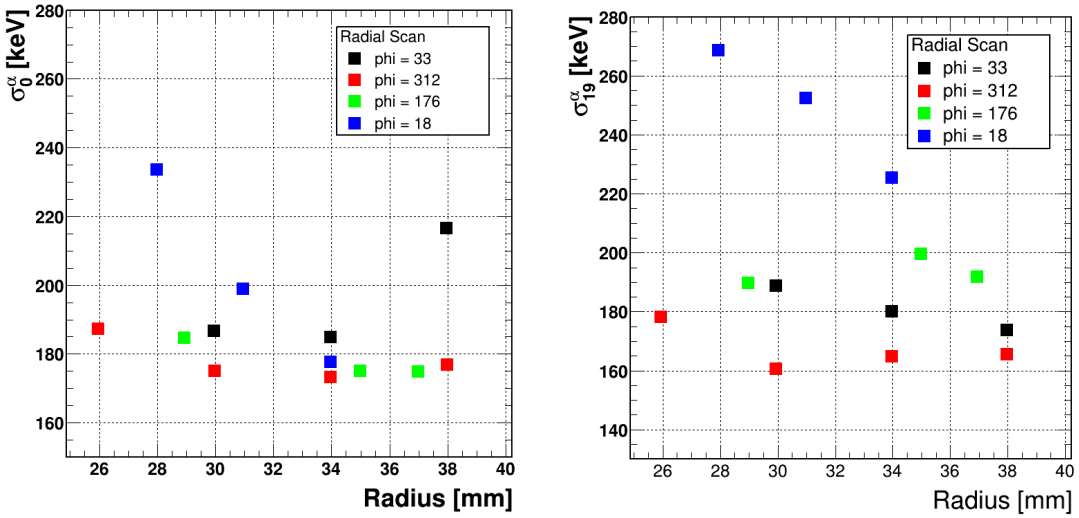

(a) (b)

Figure 8.7: σ_i^α as a function of the radius for different azimuthal angles, with $i = 0$ on the left and $i = 19$ on the right. The statistical uncertainties as determined by the fitting procedure are smaller than the symbol size.

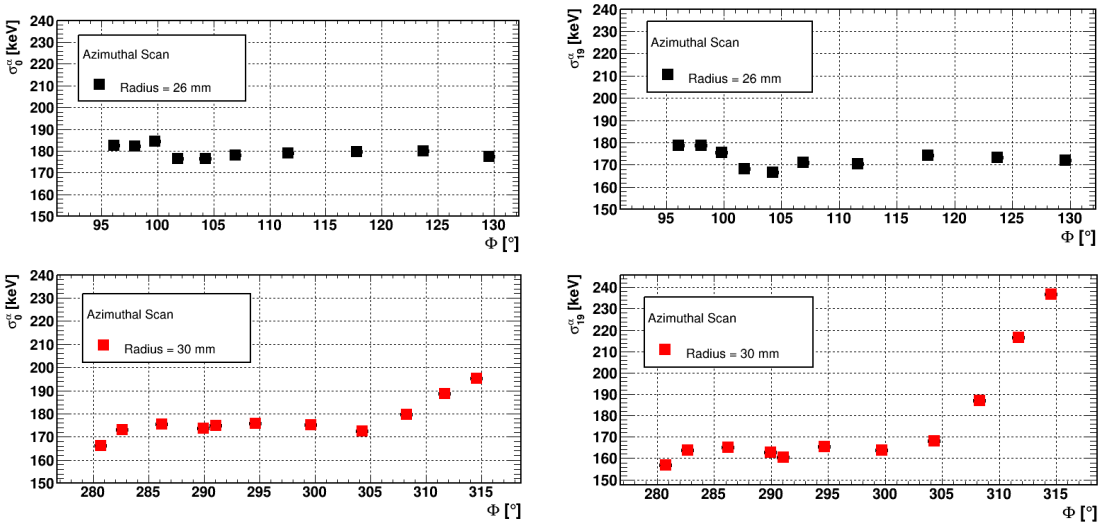

(a) (b)

Figure 8.8: σ_i^α as a function of the azimuthal angle for different radii, with $i = 0$ on the left and $i = 19$ on the right. The statistical uncertainties as determined by the fitting procedure are smaller than the symbol size.

three effects. The geometrical effect due to the angular spread of the alphas emerging from the collimator can be neglected (see appendix F). The intrinsic energy resolution of the detector (see section 3.3.1) increases at higher energies. However, its effect on σ_i^α is expected to be of $\mathcal{O}(0.1\%)$ and can also be neglected. The component due to the presence of the protective film of the source is independent of the scan position. The effect of the window was measured on the side of the detector (see appendix F). The measurement shows that the alpha energy is reduced to $\approx 4485\,\text{keV}$ with a spread of about 185 keV. The spread in energy introduced by the source accounts almost entirely for the σ_i^α observed at most locations of the top plate. This points to a relative reproducible effect of charge trapping for most of the positions. However, in some places significantly larger values for σ_0^α and σ_{19}^α are observed. For places which present such large standard deviations, the stochastic component is evaluated as:

$$\sigma_{stoch} \approx \sqrt{\sigma_i^2 - \sigma_{source}^2}\,, \tag{8.4}$$

The highest standard deviations are observed in the radial scans is $\sigma_{19}^\alpha = 270\,\text{keV}$, from the RS04 set at $r = 28.0\,\text{mm}$. The stochastic component there is thus $\sigma_{stoch}^{\alpha,RS04} \approx 200\,\text{keV}$. The highest standard deviation among the azimuthal scans is $\sigma_{19}^\alpha = 235\,\text{keV}$, from the AS02 at $\phi = 315°$. The stochastic component there is thus $\sigma_{stoch}^{\alpha,AS02} \approx 151\,\text{keV}$. Among these sets, the stochastic effect is the predominant one and it is stronger for holes than for electrons.

The correlation between σ_i^α and μ_i^α was investigated to disentangle the effect of the protective film in front of the source and the stochastic effect. The former is expected to be constant. The latter is expected to be correlated with the energy. Figure 8.9 shows the correlation between σ_i^α and μ_i^α for the radial scans listed in Table D.2. For most scans, the correlation is small. Only the scan at $\phi = 33$ shows a clear trend for segment 19. For this scan, a large stochastic effect is

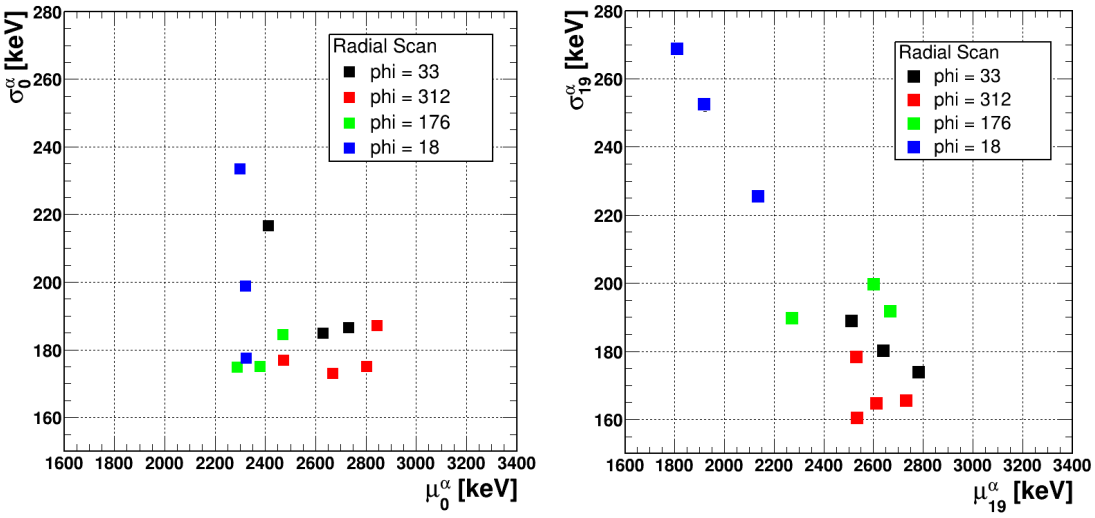

(a) (b)

Figure 8.9: σ_i^α as a function of μ_i^α in different radial scans for $i = 0$ on the left and $i = 19$ on the right. The statistical uncertainties as determined by the fitting procedure are smaller than the symbol size.

observed. This sector behaves differently than others, trapping seems to be more random.

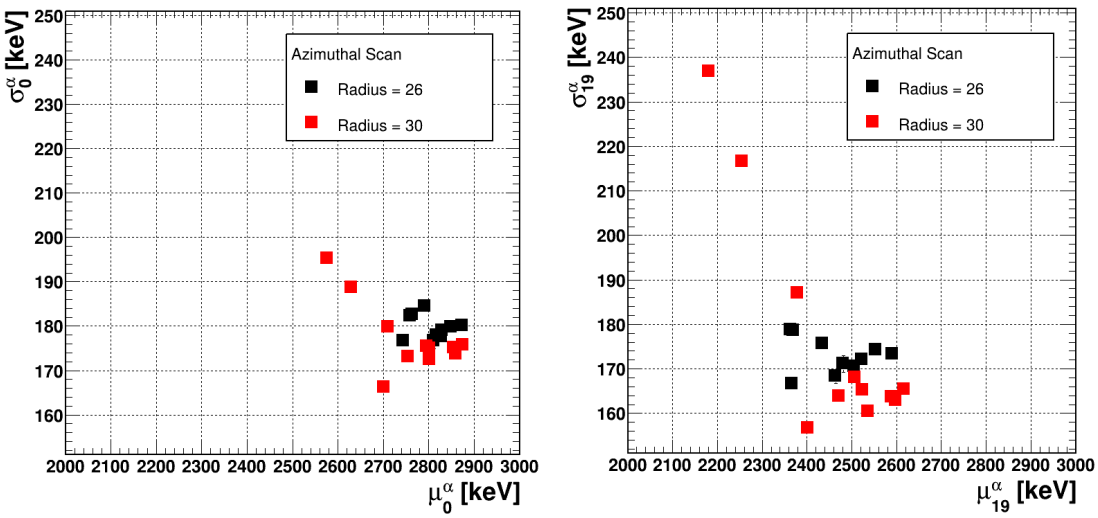

(a) (b)

Figure 8.10: σ_i^α as a function of μ_i^α in different azimuthal scans for $i = 0$ on the left and $i = 19$ on the right. The statistical uncertainties as determined by the fitting procedure are smaller than the symbol size.

Figure 8.10 shows the correlation between σ_i^α and μ_i^α for the azimuthal scans listed in Ta-

ble D.3. On average $\sigma_0^\alpha > \sigma_{19}^\alpha$. No clear correlation was observed but some points show high σ_{19}^α and low μ_{19}^α. This seems to be another part of the detector were stochastic trapping is more important than in most places.

Figure 8.11 shows the correlation between the energy recorded in the core, E_0, and in segment 19, E_{19} for the radial scan at $\phi = 33.0°$ from RS01 set listed in Table D.2. As discussed in section 7.5, events induced by alpha interactions populate the so called alpha band whose densest area contains the events fulfilling the conditions in Eq. 7.3. As the radial position of the source changes, the entire alpha band, from low to high energies, change its relative position to the diagonal of the single segment events. For small radii the band is below the diagonal, pointing to holes trapping. As the source is moved to bigger radii, the band gets thicker and it moves over the SSE diagonal, pointing to a higher effect from electron trapping. This is in agreement with the results obtained in Figs. 8.5 and 8.7.

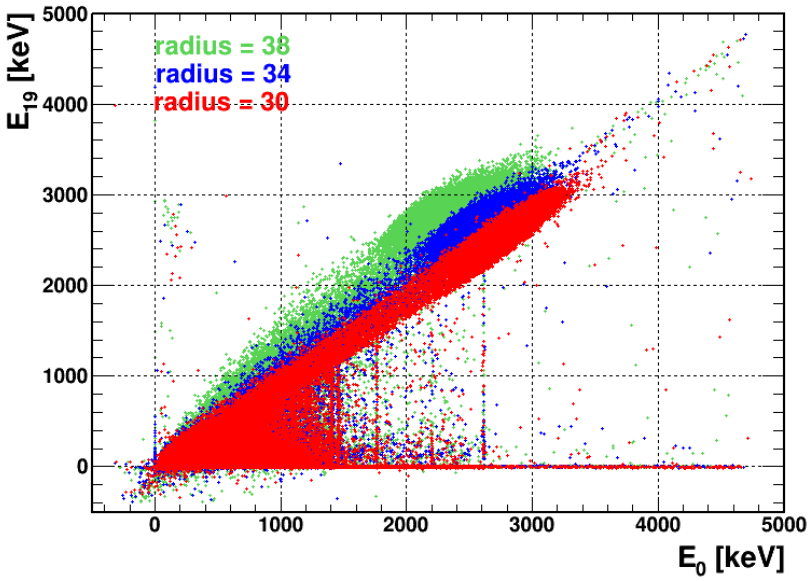

Figure 8.11: Correlation between E_0 and E_19, for different radii at $\phi = 33°$. The measurements were from the RS01 set, as listed in Table D.2.

8.2.2 Count rates in the 59.5 keV gamma line

Gamma events were selected as described in section 7.6. Spectral lines at 59.5 keV were fitted with the modified Gaussian as described in appendix B. Gammas do not loose part of their energy inside DL^{eff} like alpha particles do. Gammas either interact inside the DL^{eff} and are not registered as events or interact inside the active layer. Thus, the number of counts in the gamma peak is expected to vary with the thickness of the dead layer while the position of the peak is not expected to change

Figure 8.12 shows the count rate, C_0^γ, for the 59.5 keV gamma line in the core spectrum as a function of the source position. Figure 8.12a shows C_0^γ as a function of the radius for different azimuthal angles. The dependence on the radius for C_0^γ is observed in all the radial scans but the

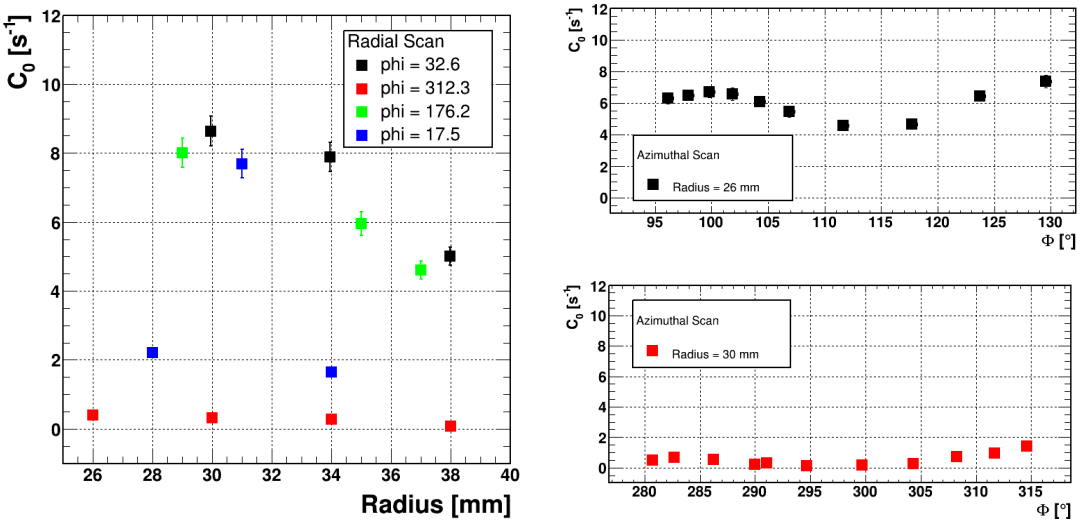

(a) (b)

Figure 8.12: Count rate in the 59.5 keV gamma line (a) as a function of the radius, for different azimuthal angles, (b) as a function of the azimuthal angle for different radii. The count rates were extracted as described in appendix B. The error bars represent statistical uncertainties.

one at $\phi = 18°$. The dependence follows the dependence obtained for the μ_0^α shown in Fig. 8.5a. Figure 8.12b shows C_0^γ as a function of the azimuthal angle for different radii. The count rate shows a minimum around $\phi = 115°$, which was not shown by the μ_0^α in Fig. 8.6a. The count rate is significantly lower in the AS02 (red), i.e. in front of the metalization.

The correlation of the reduction in C_i^γ for the spectral line at 59.5 keV with the reduction of the mean energy, μ_i^α, observed for alpha events is shown in Fig. 8.13 for the radial scans and in Fig. 8.14 for the azimuthal scans. For the radial scans, the correlation between μ_0^α and C_0^γ follows expectation in so far as the C_0^γ increases for increasing μ_0^α. The inverse observation for segment 19 cannot be easily understood. However, the influence of the small dead layer affecting the alphas is limited in the 59.5 keV gammas, as the average range for such a gamma is about 900 μm compared to the 20 μm of dead layer. From the azimuthal scans, a clear correlation is observed only for the scanning points in front of the metalization, i.e. AS02 (red). The negative correlation shown for AS02 is the same for the core and segment 19. The correlation is unexpected and not understood.

8.2.3 Charge trapping

The fractions $f^{\mathrm{pt}}_{\alpha(\gamma)}$, quantifying the occurrence of different pulse types as defined in Eq. 7.5, were evaluated for the segment underneath, s_U, for each data set, both for alpha and gamma events. The position dependence of $f^{\mathrm{pt}}_{\alpha(\gamma)}$ was studied. In all figures shown, the color of the marker represents the sign of the pulse while the shape represents the class of pulse, i.e. :

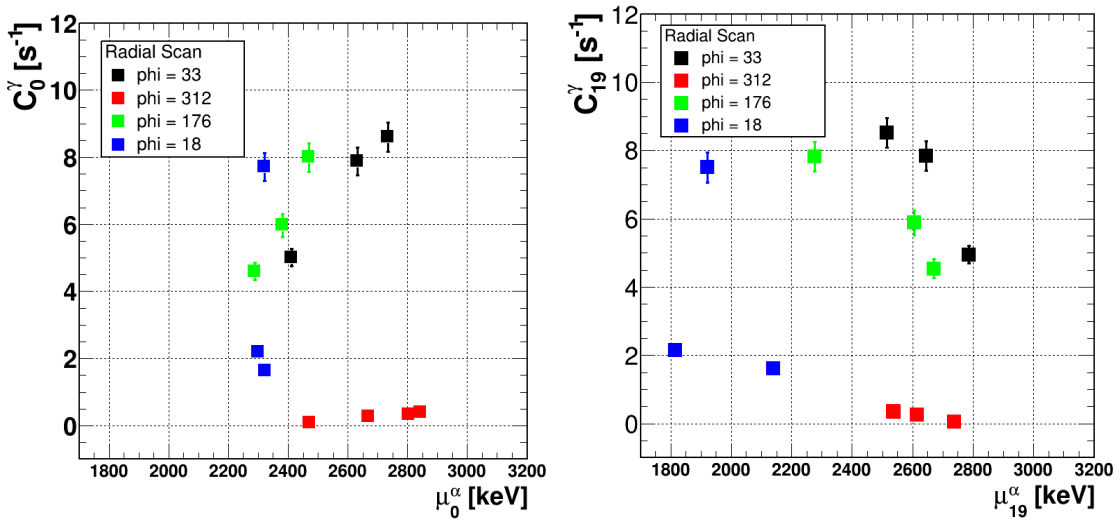

(a) (b)

Figure 8.13: Correlation between the count rate in the 59.5 keV gamma line and the mean energy of the alpha line for $i = 0$ on the left and $i = 19$ on the right. The error bars represent statistical uncertainties.

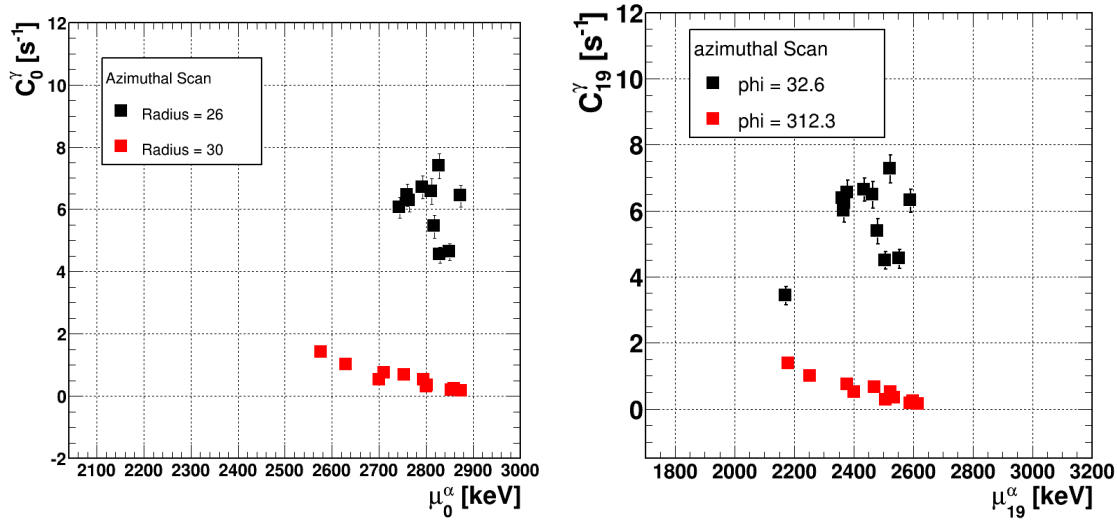

(a) (b)

Figure 8.14: Correlation between the count rate in the 59.5 keV gamma line and the mean energy of the alpha line for $i = 0$ on the left and $i = 19$ on the right. The error bars represent statistical uncertainties.

1. red circles represent the fraction of events with a "Mirror Positive" pulse in s_U, $f_{\alpha(\gamma)}^{\mathrm{MP}}$;

2. black circles represent the fraction of events with a "Mirror Negative" pulse in s_U, $f_{\alpha(\gamma)}^{\mathrm{MN}}$;

3. red crosses represent the fraction of events with a "Truncated Positive" pulse in s_U, $f^{\mathrm{TP}}_{\alpha(\gamma)}$;

4. black crosses represent the fraction of events with a "Truncated Negative" pulse in s_U, $f^{\mathrm{TN}}_{\alpha(\gamma)}$;

Alpha events Figure 8.15 shows f^{pt}_{α} as a function of the radius at four different azimuthal angles. A complete list of measurements belonging to these radial scans is available in Table D.2. Clear correlations between f^{pt}_{α} and the radial position of the source are observed:

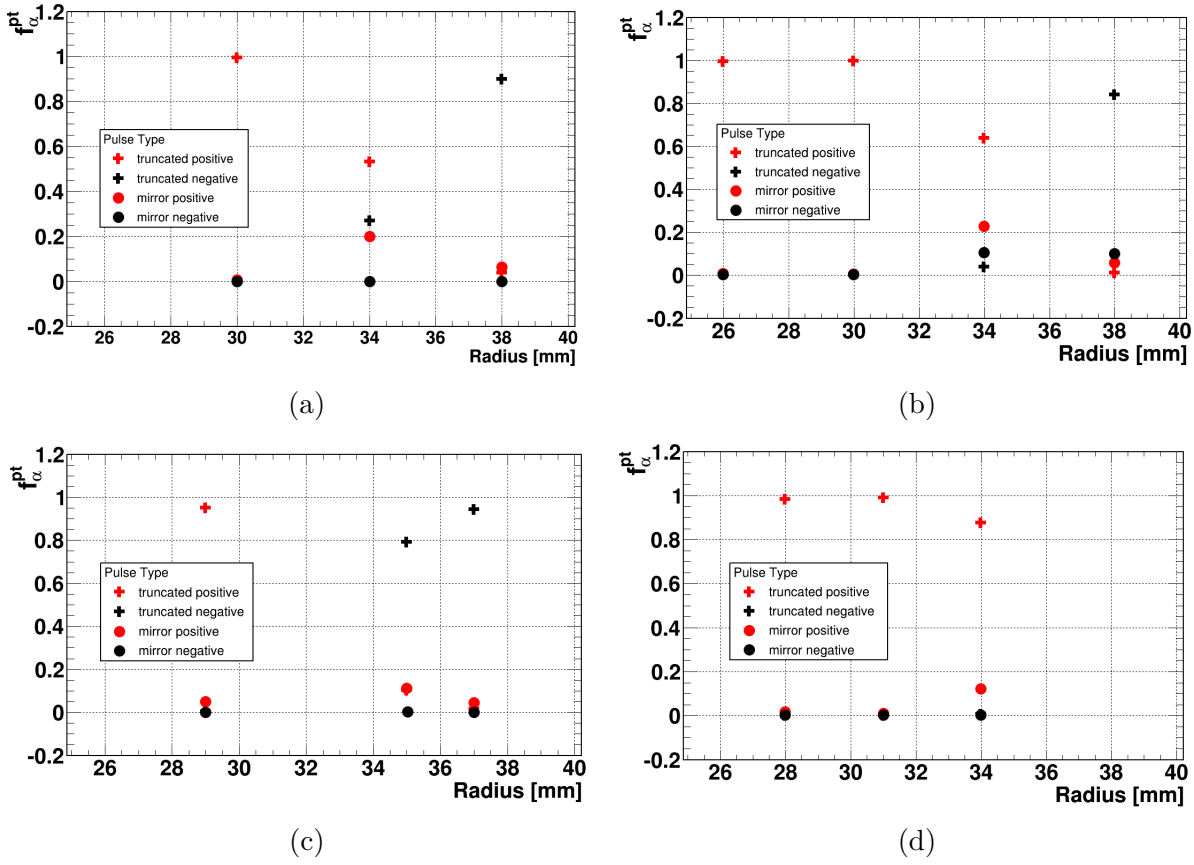

Figure 8.15: f^{pt}_{α} as a function of the radius at different azimuthal angles: a) at $\phi = 33°$, measurements belonging to RS01; b) at $\phi = 312°$ measurements belonging to RS02; c) at $\phi = 176°$ measurements belonging to RS03; d) $\phi = 18°$ measurements belonging to RS04.

a) towards lower radii, f^{TP}_{α} increases, indicating that the probability for holes to be trapped along their path towards the collecting electrode increases;

b) towards higher radii, the situation reverses: the fraction f^{TN}_{α} increases, indicating that the probability for electrons to be trapped along their path towards the core electrode increases;

c) at intermediate radii, significant fractions of positive and negative, both truncated or complete mirror pulses are observed.

This confirms that the different pulse height observed in core and segment 19 is indeed due to charge trapping. Only in areas for which no trapping is observed, the reduction of energy is essentially due to loss in a dead volume close to the surface. Even, if only holes are trapped, the core can still experience a small reduction in signal as the influence of the hole drift at large radii is small but not zero. For most radii, the fractions f_α^{TP} and f_α^{TN} both reach one at low or high radii, respectively, while dropping to zero at the other end of the range. The reduction of charge observed through the collecting electrode is entirely due to loss of energy close to the surface in a volume from which no charge carriers emerge.

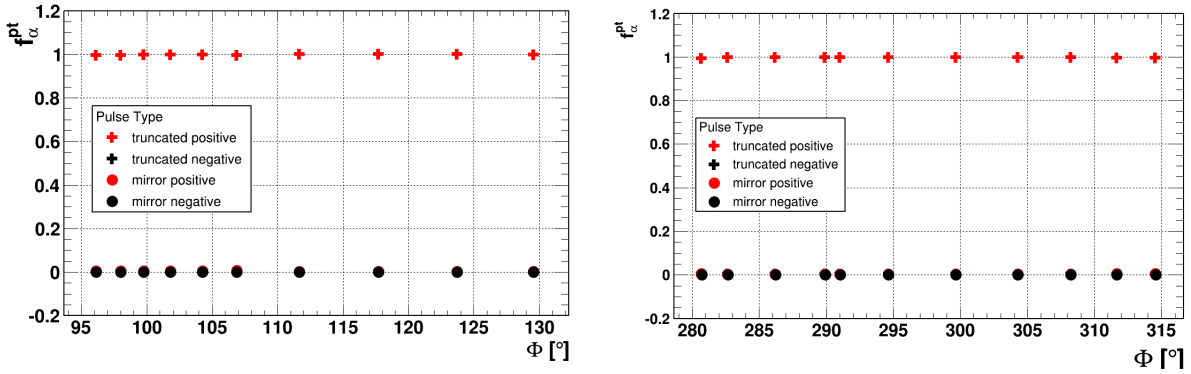

Figure 8.16: f_α^{pt} as a function of the azimuthal angle in two sectors at two different radii: a) at $r = 26.0\,\mathrm{mm}$ measurements belonging to AS01; b) at $r = 30.0\,\mathrm{mm}$ measurements belonging to AS02.

Figure 8.16 shows f_α^{pt} as a function of the azimuthal angle in two sectors at two different radii. A complete list of measurements belonging to these azimuthal scans is available in Table D.3. Some correlations between f_α^{pt} and the azimuthal angle are observed:

a) the fraction of events showing truncated positive pulses in s_U, f_α^{TP}, is one for all the azimuthal angles in both sectors;

b) the fraction of events showing truncated negative pulses in s_U, f_α^{TN}, is zero for all the azimuthal angles in both sectors;

The situation in both sectors is very similar even though one sector is close to the metalization and one is not and the radii are different. All events show positive truncated mirror pulses, indicating that all events were affected by hole trapping. The amount of charge trapped however, varies along ϕ as demonstrated in Fig. 8.6 which shows especially a reduction of collected charge for events further away from the metalization in the sector around $\phi = 110°$. The variations of collected charge, also observed in the core, can be explained by the influence of the hole drift on the core pulse. It can also not be excluded that small amounts of electron trapping occur which cannot be confirmed by a truncated negative mirror pulse because it is unobservable due to the

larger positive mirror charge induced. As the holes drift closer to the outer mantle of the detector than the electrons, they induce a larger mirror charge in the s_U electrode due to the stronger weighting potential of s_U in this volume.

Gamma events Figure 8.17 shows f_α^{pt} as a function of the radius at four different azimuthal angles. A complete list of measurements belonging to these radial scans is available in Table D.2.

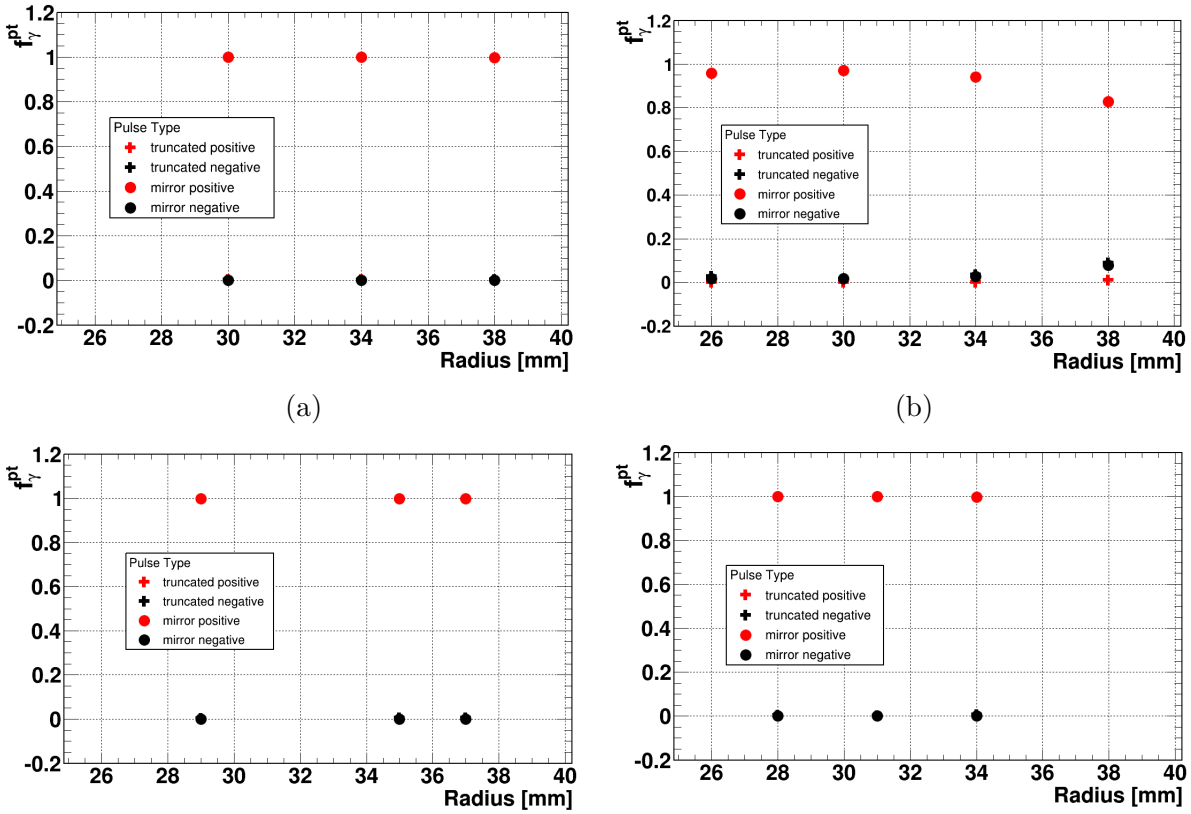

Figure 8.17: f_γ^{pt} as a function of the radius at different azimuthal angles: a) at $\phi = 33°$, measurements belonging to RS01; b) at $\phi = 312°$ measurements belonging to RS02; c) at $\phi = 176°$ measurements belonging to RS03; d) $\phi = 18°$ measurements belonging to RS04.

The gammas are less localized around the same position due to the $k-\alpha$ component and were selected demanding a pulse in s_U. At a low energy of 59.5 keV, only few events have observable mirror pulses. As a consequence, almost no correlations between f_γ^{pt} and the radial position of the source are observed:

a) the fraction of events showing positive mirror pulses in s_U, f_α^{MP}, is one for all radii at three different azimuthal angles;

b) only in Fig. 8.17b, towards higher radii f_γ^{MP} decreases and f_γ^{MN} increases;

c) the fraction of events showing truncated either negative or positive mirror pulses in s_U, f_γ^{TN} or f_γ^{TP}, is zero for all radii at all different azimuthal angles;

The drift of charge carriers created in the volume deeper below the surface is not affected by charge trapping. As the holes drift closer to the s_U than the electrons, mostly positive mirror pulses are observed. Only for events extremely close to the outer edge of the detector, negative mirror pulses are observed. The hole drift is very short for interactions in this region and the electron drift becomes visible.

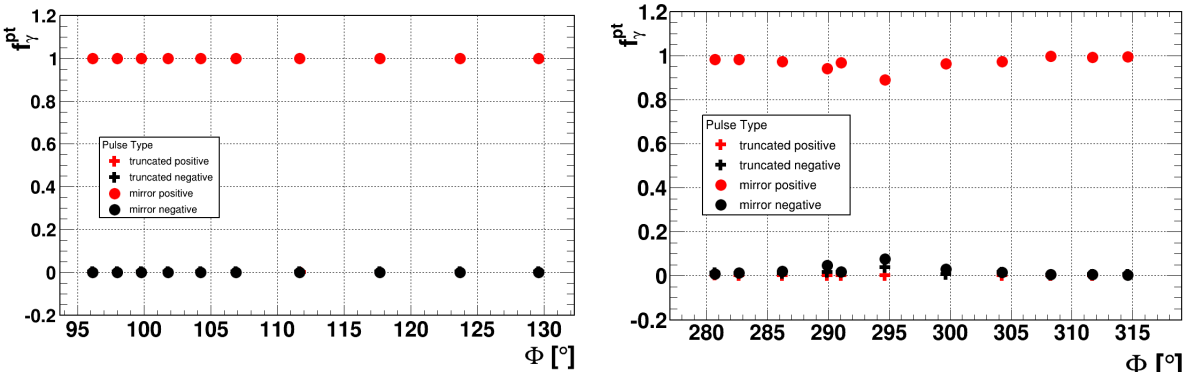

Figure 8.18: f_γ^{pt} as a function of the azimuthal angle in two sectors at two different radii: a) at $r = 26.0\,\mathrm{mm}$ measurements belonging to AS01; b) at $r = 30.0\,\mathrm{mm}$ measurements belonging to AS02.

Figure 8.18 shows f_γ^{pt} as a function of the azimuthal angle in two sectors at two different radii. A complete list of measurements belonging to these azimuthal scans is available in Table D.3. Almost no correlations between f_γ^{pt} and the azimuthal position of the source are observed:

a) the fraction of events showing mirror positive pulses in s_U, f_γ^{MP}, is one for all azimuthal angles in both sectors;

b) the fraction of events showing mirror negative pulses in s_U, f_γ^{MN}, is zero for most of the azimuthal angles in both sectors;

The situation is quite similar and stable for both sectors. However, very close to the metalization around $\phi = 295°$ negative mirror pulses emerge, and even some truncated negative pulses are observable. This area is expected to have the strongest field and the holes are expected to be collected faster such that the remaining electron drift can cause a negative mirror pulse. Again, it is possible that electron trapping remains unobservable at other ϕ values even though it occurs.

8.2.4 Risetime distributions

The RT_i^{10-30} and RT_i^{10-90} distributions for the core, $i = 0$, and for segment 19, $i = 19$, were obtained for each data set, both for gamma and alpha events. The values of RT_i^{10-90} and RT_i^{10-30} were calculated as described in section 6.2. Similar risetimes are expected for events happening in

the same volume of the detector. Alpha events are extremely localized. However, as introduced in section 7.7.1, charge trapping and distorted electric field lines might determine really different values of the risetime from event to event.

Figure 8.19 shows the $RT_{i,\alpha}^{10-90}$ distributions at $\phi = 33.0°$ at three different radii, for the core, $i = 0$, and segment 19, $i = 19$. All the distributions are normalized to one. The distributions obtained for alpha events show effects due to low fields and charge trapping. In general the $RT_{0,\alpha}^{10-90}$ values are much shorter than $RT_{19,\alpha}^{10-90}$ values. This indicates that the holes drift much slower which normally is not the case in germanium detector. The holes are slowed down by the reduced field and by being trapped and released. The shorter $RT_{0,\alpha}^{10-90}$ values are possible because the slow holes drift occurs in a volume where the weighting potential of the core is small. The core does not register this part of the drift in a 10-90 risetime. At $r = 30\,\text{mm}$, the core shows a risetime distribution according to expectations. The drift path is approximately 25 mm long and the normal velocities of $100\,\mu\text{m/ns}$ results in a drift-time of 250 ns. At $r = 34\,\text{mm}$, the risetime should increase by 40 ns. Indeed, longer risetimes are observed, but also events with shorter risetimes occurs. This can be explained by electron trapping. The pulse steps earlier. The value of 220 ns indicates that the drift path was maximally 22 mm long. Around the end of a bore hole, a volume of very low field is expected. Should electrons drift into these volumes, they are lost. At $r = 38\,\text{mm}$, a drift time of 330 ns is expected. The distribution is, however, very broad. Again, also very short $RT_{0,\alpha}^{10-90}$ values are observed. Indicating that the electrons do not make it to the core.

The situation in segment 19 is reversed. The closer the interactions are to the outer mantle, the shorter the $RT_{19,\alpha}^{10-90}$ values. The holes drift extremely slowly. At radii 34 and 38 mm, they should be collected within 50 ns. The mean value close to 1000 ns indicates a massive disturbance. As previously shown, the holes are trapped almost all of the times. That indicates that the velocity is at least reduced by a factor 20, possible more. The double peak at $r = 30\,\text{mm}$ is an artifact of the method to determine the risetime. It is caused by the spike in the pulse discussed in section 7.5. The higher values represent the "true" risetime 10-90.

The $RT_{0,\gamma}^{10-90}$ distributions for gamma events (Fig. 8.19c) range from 100 to 300 ns. They are broader than for alpha-induced events. The gamma interactions have a wider spread in r due to the k-α component. Nevertheless the reduction of $RT_{0,\gamma}^{10-90}$ for larger radii is unexpected. It points to electron trapping not observable trough truncated mirror pulses, because the pulses are obscured by larger positive mirror pulses. The $RT_{19,\gamma}^{10-90}$ distributions (Fig. 8.19b) are even broader than the one for the core. The values range from 200 to 1000 ns. Again, the segment pulses are much longer than the core pulses. In addition, the distributions are extremely broad and show no radial dependence. Gamma events basically probe the complete volume of segment 19. Some gammas interact close to critical areas of the detector where the charge collection is extremely slowed down. Some gammas, however, interact far away from such critical area. This cause the extremely broad risetime distributions.

The $RT_{i,\alpha}^{10-30}$ were investigated to look for effects of charge trapping in the first phase of the charge collection process. Figure 8.20 shows $RT_{i,\alpha}^{10-30}$ distributions with $i = 0$ on the left and $i = 19$ on the right. The distributions are normalized to one. Figure 8.20a does not show any effect due to charge trapping. The distributions have narrow Gaussian shapes. Figure 8.20b, however, shows effects similar to the ones observed in Fig. 8.19b. The first part of holes collection process is already affected by trapping. Holes, thus, seem to be subject to the charge trapping earlier in the drift than the electrons.

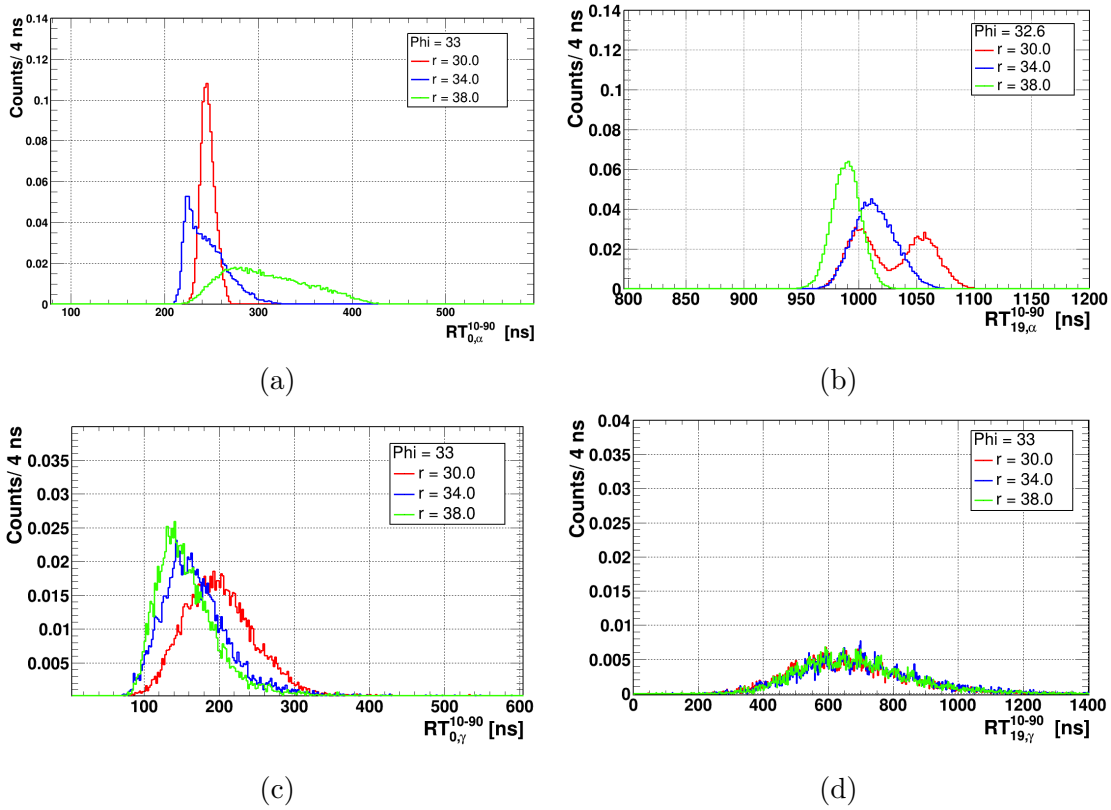

Figure 8.19: RT_i^{10-90} distributions, with $i = 0$ on the left and $i = 19$ on the right. The distributions obtained for selected alpha (gamma) events are shown on the top (bottom). The shown distributions are based on measurements from the RS01 data set (see Table D.2).

8.3 Reproducibility of surface conditions

The reduction of charge collected from an event in the top most layer of the detector has two main components:

1. charge carriers created in a "dead layer" at the very top of the detector immediately recombine and cannot be observed;

2. charge carriers are trapped on their way to the collecting electrodes.

Both effects are connected to distorted and weak field lines, which are affected by surface and space charge accumulating in or below the passivation layer on top of the detector. The configuration of the electric field lines can change after a depletion cycle of the detector. A comparison between measurements done before switching the detector off and after switching it back on was performed in order to study the reproducibility of the surface conditions. The measurements were taken at a fixed radius at three different azimuthal angles. The list of the measurements used for this study is available in Table D.4.

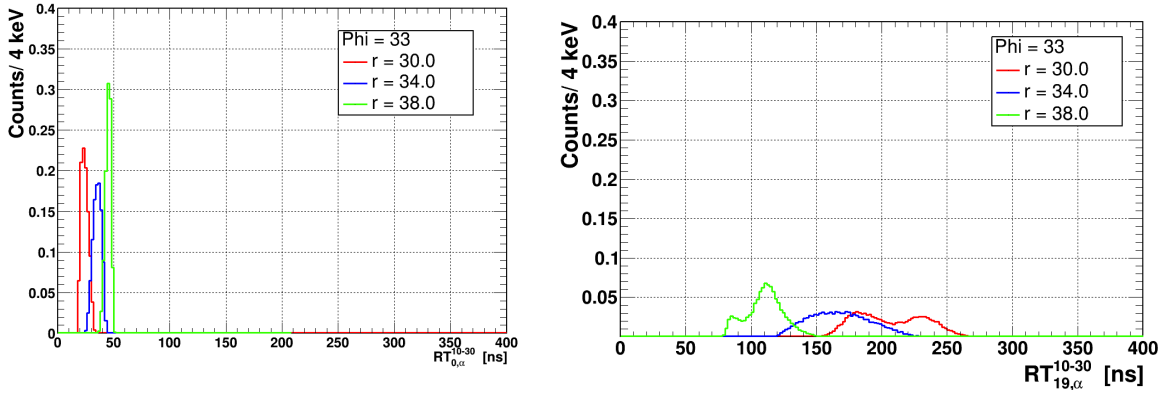

(a) (b)

Figure 8.20: $RT_{i,\alpha}^{10-30}$ distributions for the core, $i = 0$, on the left and for segment 19, $i = 19$, on the right. The shown distributions are based on measurements from the RS01 data set (see Table D.2).

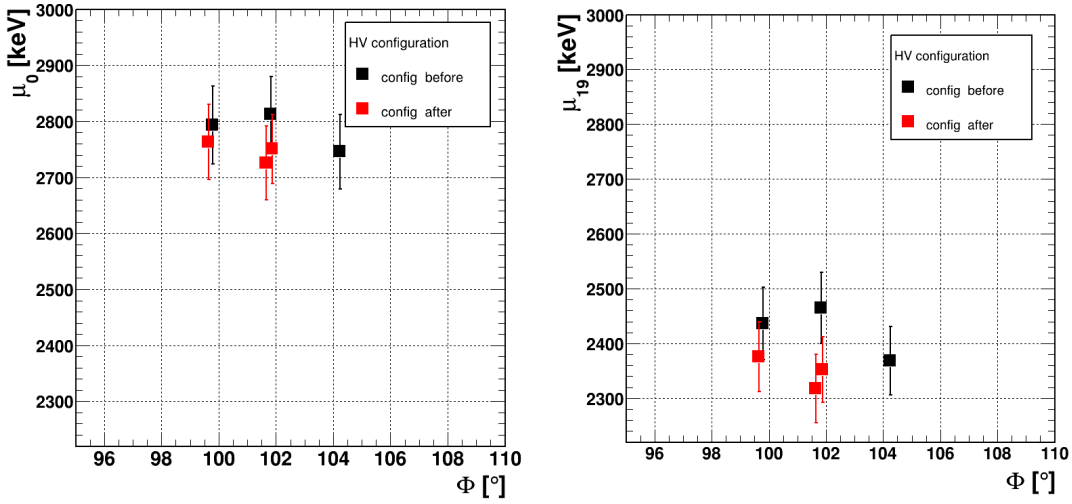

(a) (b)

Figure 8.21: μ_i as a function of the azimuthal angle before and after a depletion (HV) cycle for the core, $i = 0$, on the left and for segment 19, $i = 19$, on the right. μ_i are extracted as explained in section 7.4. The black squares represent the measurements performed before switching off SuSie I. The red squares represent the measurements performed after switching SuSie I back on. The measurements are listed in Table D.4. The error bars represent statistical uncertainties.

Alpha events were selected as described in section 7.5. Figure 8.21 shows the observed energies, μ_i, as a function of the azimuthal angle for the core, $i = 0$, and for segment 19, $i = 19$. The

uncertainties on μ_i were extracted as $\Delta\mu_i = \sigma_i/\sqrt{N}$, where N is the number of selected alpha events. The reconstructed azimuthal positions of the measurements "after" (red) are not exactly the same as for "before" (black). The motor did not move properly during this test. However, the μ_i are compatible within their uncertainties.

Figure 8.22 shows the width of the distributions, σ_i, as a function of the azimuthal angle for the core, $i = 0$, and for segment 19, $i = 19$. The uncertainties on σ_i are the statistical uncertainties as obtained from the fitting procedure. The standard deviations, σ_i, do not seem to be compatible. The difference is not explainable with the intrinsic energy resolution. The stochastic component (as introduced in section 8.2.1) of the σ_i has clearly changed. The depletion process changes the configuration of the electric-field lines and with it the spatial distribution of the traps, i.e. different charge trapping effect and a consequent different σ_i.

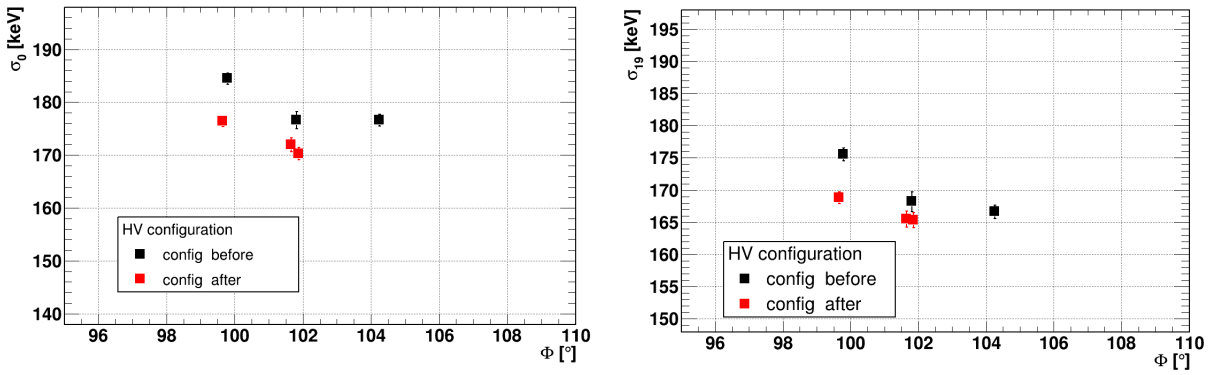

(a) (b)

Figure 8.22: σ_i as a function of the azimuthal angle before and after a depletion (HV) cycle for the core, $i = 0$, on the left and for segment 19, $i = 19$, on the right. μ_i are extracted as explained in section 7.4. The black squares represent the measurements performed before switching off SuSie I. The red squares represent the measurements performed after switching SuSie I back on. The measurements are listed in Table D.4. The error bars represent statistical uncertainties.

8.4 Extraction of the thickness of the effective dead layer

The mean value of an alpha peak is used to extract the thickness of the corresponding effective dead layer. This ignores that part of the reduction in the observed energy is due to later charge trapping. This is why it is called effective dead layer and can have a different thickness for electrons and holes. Given:

a) the energy loss per path unit of an alpha particle in germanium as:

$$\frac{dE}{dx} = 171.9\,\frac{\text{keV}}{\mu\text{m}}; \tag{8.5}$$

b) the energy of the incident alpha particle as:

$$E^{\text{ini}} = 4480.0\,\text{keV}\,, \tag{8.6}$$

obtained from alpha-dedicated measurements performed irradiating the side surface of a coaxial detector, see appendix F,

the thickness of the effective dead layer is obtained as:

$$\text{DL}_i^{\text{eff}} = \left(\frac{dE}{dx}\right)^{-1} (E^{\text{ini}} - \mu_i) \tag{8.7}$$

where $i = 0, 19$.

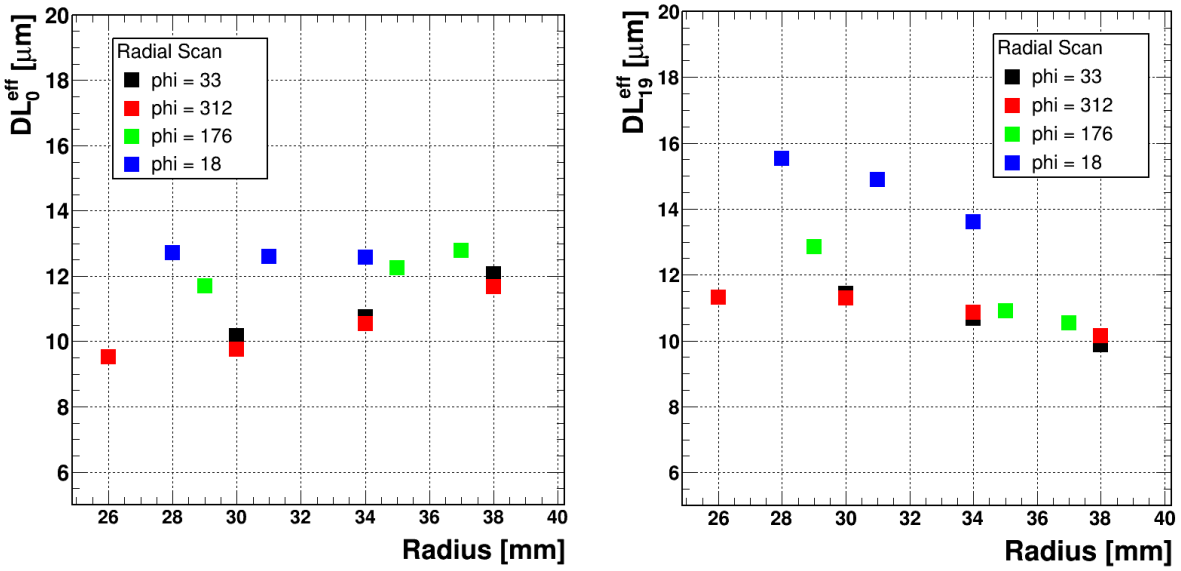

(a) (b)

Figure 8.23: DL_i^{eff} as a function of the radius, for $i = 0$ on the left and $i = 19$ on the right. DL^{eff} was obtained as defined in Eq. 8.7. The statistical uncertainties as determined by the fitting procedure are smaller than the symbol size.

The color scheme used for Figs. 8.23 and 8.24 is as introduced in section 8.2. Figure 8.23a shows DL_0^{eff} as a function of the radius at four different azimuthal angles. In general, the thickness of the effective dead layer observed by the core increases slightly with radius. DL_0^{eff} shows values between 9 μm and 13 μm. On average DL_0^{eff} is higher for $\phi = 17.5°$ and $\phi = 176.2°$. An azimuthal asymmetry is expected because of the partial metalization. In areas close to the metalization, the charge collection efficiency is higher and thus the effect of charge trapping is reduced. Fig. 8.23b shows $\text{DL}_{19}^{\text{eff}}$ as a function of the radius at four different azimuthal angles. The smaller the radius the thicker the $\text{DL}_{19}^{\text{eff}}$. $\text{DL}_{19}^{\text{eff}}$ shows values between 9 μm and 15 μm. On average DL_0^{eff} is higher for $\phi = 17.5°$. Alpha-dedicated measurements were performed at radii smaller than 25 mm. No

alpha peak was observed for such small radii. Only a lower limit on DL_0^{eff} and DL_{19}^{eff} was set at 26 μm confirming the rapid growth of the dead layer at small radii [145, 157].

Figure 8.24a shows DL_0^{eff} as a function of the azimuthal angle in two different sectors at two different radii. No strong correlation between DL_0^{eff} and the azimuthal angle was found, as for μ_0 in Fig. 8.6. The two azimuthal scans show the same DL_0^{eff} values around 10 μm. The effects of the radius and the metalization compensate each other. Figure 8.24b shows DL_{19}^{eff} as a function of the azimuthal angle for different radii. Both DL_0^{eff} and DL_{19}^{eff} show a shallow minimum around $\phi = 300°$ in front of the metalization where the effect of charge trapping is expected to be reduced.

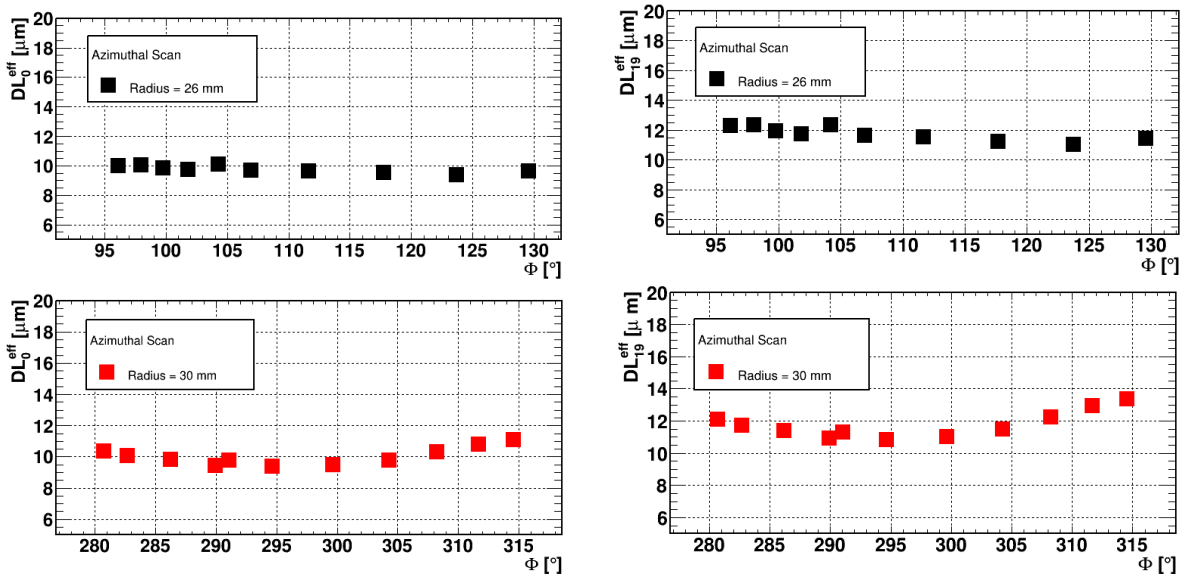

(a) (b)

Figure 8.24: DL_i^{eff} as a function of the azimuthal angle, for $i = 0$ on the left and $i = 19$ on the right. DL^{eff} was obtained as defined in Eq. 8.7. The statistical uncertainties as determined by the fitting procedure are smaller than the symbol size.

In all locations where alpha peaks were observed, the "real" dead layer can only be thinner than DL^{eff}. Such thin dead volumes were not expected.

8.5 Consequences of surface structure

The observation of the extremely thin dead layers observed at large radii at the top of SuSie was not expected. Studies with gammas injected from the top [157] could only place upper limits, but thickness of the order of 50 to 100 μm were expected [175].

One of the consequences of such thin layers is that an alpha penetrating from the top surface can be observed as an energy deposition of 2 MeV in the search window for $0\nu\beta\beta$ decay. The core pulse will not necessarily expose such an interaction as a surface event because at certain radii the pulse looks completely normal, especially it does not show a long risetime. Such an event can

only be identified as a surface event, if also the mantle is read out and a long risetime is observed there.

The long risetime of surface pulses is influenced by trapping which itself is influenced by the detector configuration. The metalization of the relevant mantle electrode influences the field and thus the capability to identify a surface pulse. This requires extra material close to the detector like cables. It is necessary to carefully evaluate whether this would introduce more background than it can avoid. R&D work on cables is on going.

If surface pulses are to be located and charge trapping is to be unambiguously identified, segmentation facilitating the observation of (truncated) mirror pulses is needed. Therefore, contrary to intuition, it might be advisable to not metalize the electrode close to the passivation layer. The resulting slow drift could be used to identify interactions in this volume. Alternatively, an extra layer of clean material could be added to the detector. However, this solution was discussed with the manufacturer and such a material is not available.

Summary, conclusions and outlook

The main goal of the work presented here was the characterization of interactions of alpha particles on a germanium detector. This was achieved by probing the passivated end-plate of a segmented true-coaxial detector with alpha particles from a ^{241}Am source.

To achieve this main goal, the test-facility GALATEA, located at the MPI für Physik in Munich, had to be finalized and commissioned. This was a major part of the work done for this thesis. The achievement of a stable vacuum at $\mathcal{O}(10^{-6})$ mbar over periods of weeks without pumping was a major effort. A system for environmental monitoring and for data-quality checks was developed for long physics runs. GALATEA was tested showing good and stable performance. Physics measurements were performed probing SuSie with a ^{152}Eu and a ^{241}Am sources from April to December 2013. During the data taking in Autumn 2013, the accident described in chapter 4 occurred. As a result, the analysis of the data was complicated by a lack of a priori knowledge of the source position. One of the achievements is that this problem was overcome. A major upgrade of GALATEA is still in the commissioning phase.

A complete analysis framework was developed to perform the analysis presented in this thesis. It includes a fully automized and robust calibration procedure for segmented germanium detectors as described in chapter 5 and a complete pulse-shape analysis package. One of the key element is the pulse-classification algorithm described in chapter 6. The results of the analysis, presented in chapters 7 and 8, are based on data obtained in a 2D scan of the upper end-plate of the special segmented true-coaxial detector Super Siegfried, SuSie, which has a 5 mm thick segment 19 underneath the end-plate.

Alpha events were identified and selected using the energy recorded in the core and in segment 19. For every scanning position, for which a spectral line due to alpha interactions was detected, the trapping of drifting charges was observed by identifying truncated mirror pulses in the segments below the segment 19. It was shown that electrons and holes experience different trapping effects with a clear dependence on the radial position of the interaction. The characteristics of the alpha-induced events depend on the details of the detector design. The metalization of segment 19 was restricted to a small sector. In areas far away from this partial metalization, the pulses from segment 19 were observed to have extremely long risetimes. This effect is very pronounced for alpha-induced events. A reference sample of low energy, 59.5 keV, gammas provided a risetime distribution for segment 19, which also showed long risetimes. The effect was not as pronounced as for the alpha-induced events right at the surface, but it shows that the lack of metalization also reduces the field in the volume of segment 19. In contrast, charge trapping was not observed for the gamma sample, indicating that this effect is limited to drift very close to the surface. Thus, alpha-induced surface events can be identified in an experiment, if both the core and the mantle electrodes are read out. The metalization of the relevant mantle electrode should

be optimized to provide the best identification of surface pulses. With a suitable segmentation scheme, it would furthermore be possible to unambiguously identify and localize such surface events trough truncated mirror pulses occurring due to charge trapping.

The dead layer at large radii was found to be much thinner than expected. The thickness was found to range between 9 and 14 μm compared to an expectation of between 50 and 100 μm. The values were extracted from the reduced energy as recorded in the core and segment 19. For these extractions, the energy reduction due to charge trapping during the drift was not separated out as it is small compared to the initial loss in the dead layer. For lower radii where no spectral line due to the alpha interaction was observed, a lower limit on the thickness of the effective dead layer was set at 26 μm.

In the future, more measurements with alpha particles are planned with SuSie II and other detectors. In addition, some data from SuSie II with full metalization are already available and will be analyzed. An accompanying Monte Carlo simulation with different models for charge trapping will help to sharper the conclusions on the characteristics of the detector. The next generation of germanium-based experiments will require extremely well understood detectors. The detailed design of the detectors including metalization schemes and passivation layers will be guided by studies like the one presented in this thesis.

Appendix A

Germanium detectors and natural radioactivity in food

The purpose of the study was to measure the potassium content of different food samples and evaluate the possible effects of soil and water.This work supported two bachelor thesis and is to be published in NIM A.

Measurements of the potassium content of food can be performed using several detection techniques: Atomic Absorption Spectrometers [176], Fluorometers [177], Sodium Iodide Based Detectors [178, 179] and High Purity Germanium (HPGe) Detectors [180–182]. In the following a detailed description of a simple and reproducible method to measure potassium content with HPGe detectors is provided.

Section A.1 provides a brief introduction: how potassium is present in food and how it can be detected with HPGe detectors. The experimental setup used for the measurements is described in section A.2. An overview of all measurements is given in section A.3. The method used to extract the potassium content of each food sample is discussed in section A.4. Results are reported in section A.5 and conclusions are drawn is section A.6.

A.1 Potassium and HPGe detectors

Potassium is one of the elements responsible for natural radioactivity. It is also a very important mineral for human life. It is found in soil and water and stored in food like beans, fruit and cacao. Samples of the same kind of food with different provenance are used to study the effect of the soil on the potassium content. The radioactive isotope ^{40}K has a natural abundance of 0.012% [183]. In 10.6% of the cases, it decays via a β^+ decay to a metastable state of ^{40}Ar. In the isomeric transition to the ground state, ^{40}Ar emits a photon of 1460 keV, which can be clearly identified by HPGe detectors.

The energy spectrum shown in Fig. A.1 was obtained with a potassium chloride (KCl) [184] calibration sample. The characteristic potassium peak at 1460 keV, has a FWHM of 2.03 keV, demonstrating the excellent energy resolution of HPGe detectors. All peaks expected from natural radioactivity are suppressed due to a lead shield (see section A.2) and the strength of the ^{40}K peak. Clearly visible is the 511 keV peak from pair production in the vicinity of the detector.

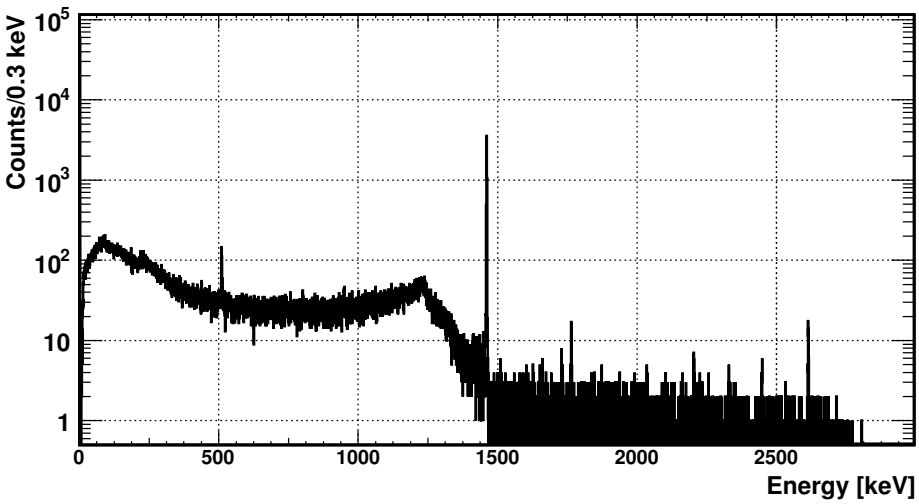

Figure A.1: Energy spectrum obtained with a potassium chloride calibration sample in a shielded environment.

A.2 Experimental setup

The experimental setup is shown in Fig. A.2. An HPGe detector produced by Canberra is surrounded by a multilayer shield with a cavity to place the samples.

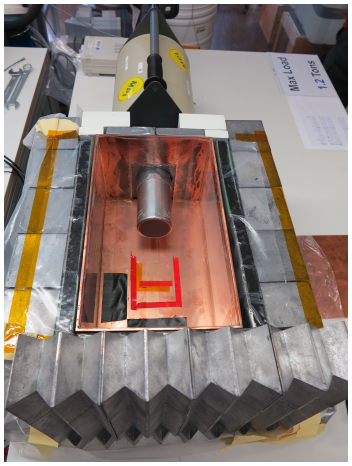

(a)

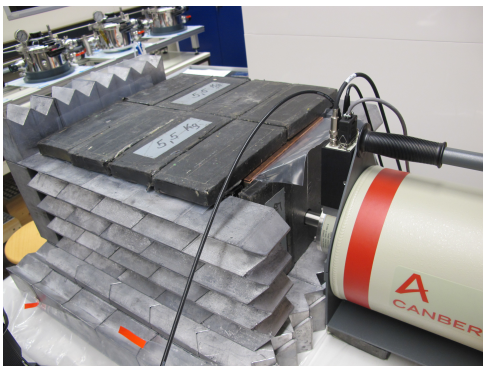

(b)

Figure A.2: Experimental setup: the high purity germanium detector is surrounded by a multilayer copper and lead shield leaving a cavity for the samples; (a) shows the open shield and (b) shows the closed shield.

The measurements reported here were performed with two different HPGe detectors: XtRa and REGe, already described in section 3.3.2. In order to be sensitive to the low level of radioactivity in food, it is necessary to reduce the environmental background. This was done with a

multilayer shield composed of an outer lead shield with a thickness of up to 10.5 cm and an inner copper shield with a thickness of 0.4 cm (see Fig. A.2).

Figure A.3 shows a comparison between energy spectra obtained with three different shield configurations. The side walls alone already substantially reduced the high energy gamma lines, especially the Thallium line at 2.6 MeV. This reduced also the Compton shoulder at medium energies.

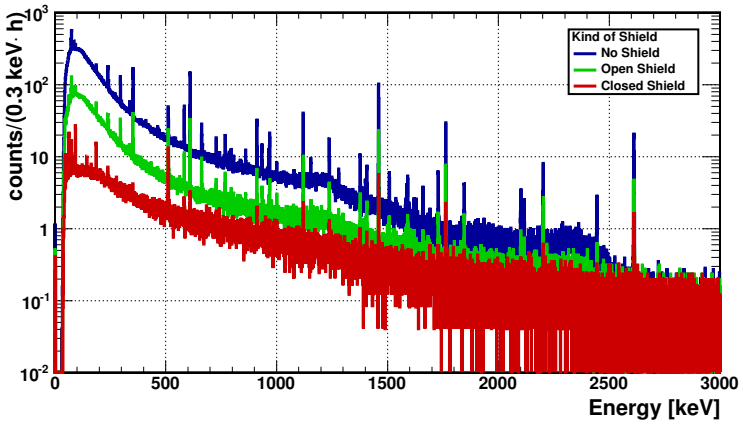

Figure A.3: Comparison of background energy spectra obtained with three different shield configurations. Top: no shield; middle: with the open shield (see Fig. A.2a), bottom with the closed shield (see Fig. A.2b).

Figure A.4 depicts the region around the ^{40}K peak. The full shield reduced the ^{40}K line by 95% and the continuous background in this region by 80%.

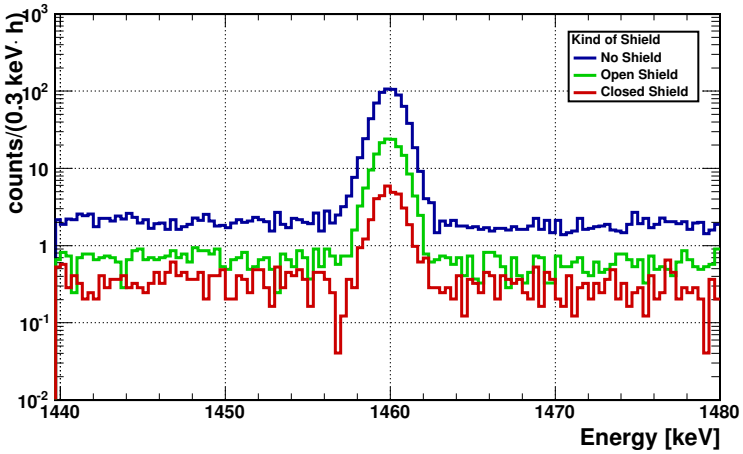

Figure A.4: Comparison of background spectra obtained with three different shield configurations, zoomed in the region of the potassium peak, i.e. around 1460 keV. For other details see Fig. A.3.

All the measurements presented here, were performed using a DGF Pixie-4 multichannel data acquisition system produced by XIA [158]. The software used to communicate with the Pixie-4 modules was a graphical user interface called IGOR from Wavemetrics [159].

A.3 Data taking

Tables A.1-A.4 provide an overview of all the food measurements discussed.

The relevant quantities for each measurement are its lifetime and the mass of the sample. The date of the measurement is also given as the samples were purchased shortly before the measurements and variations with production time are plausible.

The measurements listed in different tables were done with slightly different setups. A calibration measurement, as introduced in section A.1, was done for each of these configurations. All samples were weighed to a precision of 0.1 g. The samples were placed in plastic containers. The container and its relative position to the detector were the same for all the measurements in a given configuration to guarantee the same geometrical acceptance. Figure A.5 shows pictures of different samples as used in the measurements.

	ID	Sample	Date [dd/mm/yy]	Lifetime [h]	Mass [g]
	KCL_12	KCl	25/05/12	2.79	820.3
F_12	F01_12	bananas	30/05/12	13.47	453.6
	F02_12	kiwis	31/05/12	3.02	416.3
	F03_12	almonds	31/05/12	13.42	278.1
	F04_12	strawberries	01/06/12	2.99	458.6
	F05_12	dried prunes	01/06/12	2.70	400.1
	F06_12	pistachios	01/06/12	2.15	316.5
	F07_12	hazelnuts	04/06/12	2.78	405.0
	F08_12	raisins	04/06/12	2.71	469.9
	F09_12	dried apricots	04/06/12	1.72	594.4
DC_12	DC50_12	Lindt 50%	05/06/12	4.43	392.9
	DC70_12	Lindt 70%	05/06/12	2.56	401.1
	DC85_12	Lindt 85%	05/06/12	13.87	400.2
B_12	B01_12	background	29/05/12	18.70	-
	B02_12	background	01/06/12	53.65	-

Table A.1: List of measurements from summer 2012 using the XtRa detector: KCL_12 is the calibration measurement, F_12 contains measurements of fruit and nuts and DCN_12 contains measurements of samples of dark chocolate with N% of cacao; background measurements are listed in B_12.

The first phase of the study (see Table A.1) focused on fruit and nuts (F_12). In addition, a number of chocolates (DC_12) were investigated. In the DC_12 subset, the % values indicate the cacao content of the dark chocolates as listed by the producer Lindt. Fruit and chocolate samples were cut in small pieces to fill the container as shown in Fig. A.5.

	ID	Sample	Date [dd/mm/yy]	Lifetime [h]	Mass [g]
	KCL_13	KCl	09/10/13	2.53	334.7
DC_13	DC71_13	Vivani 71%	10/10/13	3.81	198.8
DC_13	DC85_13	Vivani 85%	11/10/13	3.71	186.8
DC_13	DC92_13	Vivani 92%	14/10/13	4.37	157.8
CC_13	CC01_13	Bonnat Ceylon	15/10/13	4.73	192.5
CC_13	CC02_13	Bonnat Chuao	16/10/13	4.10	190.7
CC_13	CC03_13	Bonnat Hacienda Rosario	28/10/13	7.93	191.2
CC_13	CC04_13	Bonnat Cote d'ivoire	29/10/13	3.61	195.0
CC_13	CC05_13	Bonnat Ecuador	29/10/13	3.81	196.3
CC_13	CC06_13	Bonnat Trinidad and Tobago	30/10/13	6.39	200.2
CC_13	CC07_13	Bonnat Madagascar	31/10/13	3.06	204.6
B_13	B01_13	background	09/10/13	20.29	-
B_13	B02_13	background	14/10/13	20.69	-

Table A.2: List of measurements from autumn 2013 using the XtRa detector: KCL_13 is the calibration measurement, DCN_13 contains measurements of samples of dark chocolate with N% of cacao and CC_13 contains measurements of samples of dark chocolate of 75% of cacao, with different places of origin; background measurements are listed in B_13.

The second and the third phases (see Tables A.2 and A.3) focused on chocolate. The DC_13 and DC_14 subsets contain dark chocolates with different nominal cacao content produced by Vivani and Lindt, respectively. Using these samples, together with the DC_12 samples, the connection between the cacao percentage and the potassium content was investigated. The CC_13 and CC_14 subsets contain dark chocolate with the same nominal cacao content (75%) but different places of origin of the cacao. Using these samples, the effect of the place of origin of the cacao on the potassium content was investigated. The chocolate samples listed in Tables A.2 and A.3 were chopped in order to obtain a uniform distribution of the chocolate in the container. This was not done in phase one. However, the effect of chopping was measured to be below 5% [185] and was neglected.

The fourth phase (see Table A.4) focused on legumes (L_14). Those were the samples for which the highest potassium content was expected.

The effect of the self absorption was estimated in a Monte Carlo study to be below 5% for the KCl, i.e. for the highest density of all the samples, and therefore neglected.

	ID	Sample	Date [dd/mm/yy]	lifetime [h]	mass [g]
	KCL01_14	KCl	13/05/14	2.16	817.5
DC_14	DC50_14	Lindt 50%	22/05/14	4.02	450.2
	DC70_14	Lindt 70%	02/06/14	3.79	499.3
	DC85_14	Lindt 85%	15/05/14	3.49	430.8
	DC90_14	Lindt 90%	13/05/14	2.63	429.9
CC_14	CC01_14	Bonnat Ceylon	09/06/14	3.70	471.5
	CC02_14	Bonnat Chuao	05/06/14	3.60	450.7
	CC03_14	Bonnat Hacienda Rosario	11/06/14	3.70	466.5
	CC04_14	Bonnat Cote d'ivoire	10/06/14	3.64	466.0
	CC05_14	Bonnat Ecuador	06/06/14	3.66	470.8
	CC06_14	Bonnat Trinidad and Tobago	09/06/14	3.77	462.2
	CC07_14	Bonnat Madagascar	05/06/14	3.67	469.0
	CC08_14	Bonnat Puerto Cabello	05/06/14	3.79	451.7
B_14	B01_14	background	06/05/14	39.97	-
	B02_14	background	13/05/14	40.06	-
	B03_14	background	22/05/14	87.26	-
	B04_14	background	02/06/14	63.13	-
	B05_14	background	05/06/14	14.83	-
	B06_14	background	09/06/14	14.71	-
	B07_14	background	10/06/14	14.97	-

Table A.3: List of measurements from summer 2014 using the REGe detector: KCL_14 is the calibration measurement, DCN_14 contains measurements of samples of dark chocolate with N% of cacao and CC_14 contains measurements of samples of dark chocolate of 75% of cacao, with different places of origin; background measurements are listed in B_14.

	ID	Sample	Date [dd/mm/yy]	lifetime [h]	mass [g]
	KCL02_14	KCl	08/05/14	1.86	1200.1
L_14	L01_14	white beans	26/05/14	2.57	900.0
	L02_14	green peas	26/05/14	3.31	900.0
	L03_14	red lentils	27/06/14	12.5	900.0
B_14	B08_14	background	26/05/14	94.02	-
	B09_14	background	29/05/14	28.07	-

Table A.4: List of measurements from summer 2014 using the REGe detector: KCL_14 is the calibration measurement, L_14 contains measurements of samples of legumes; background measurements are listed in B_14.

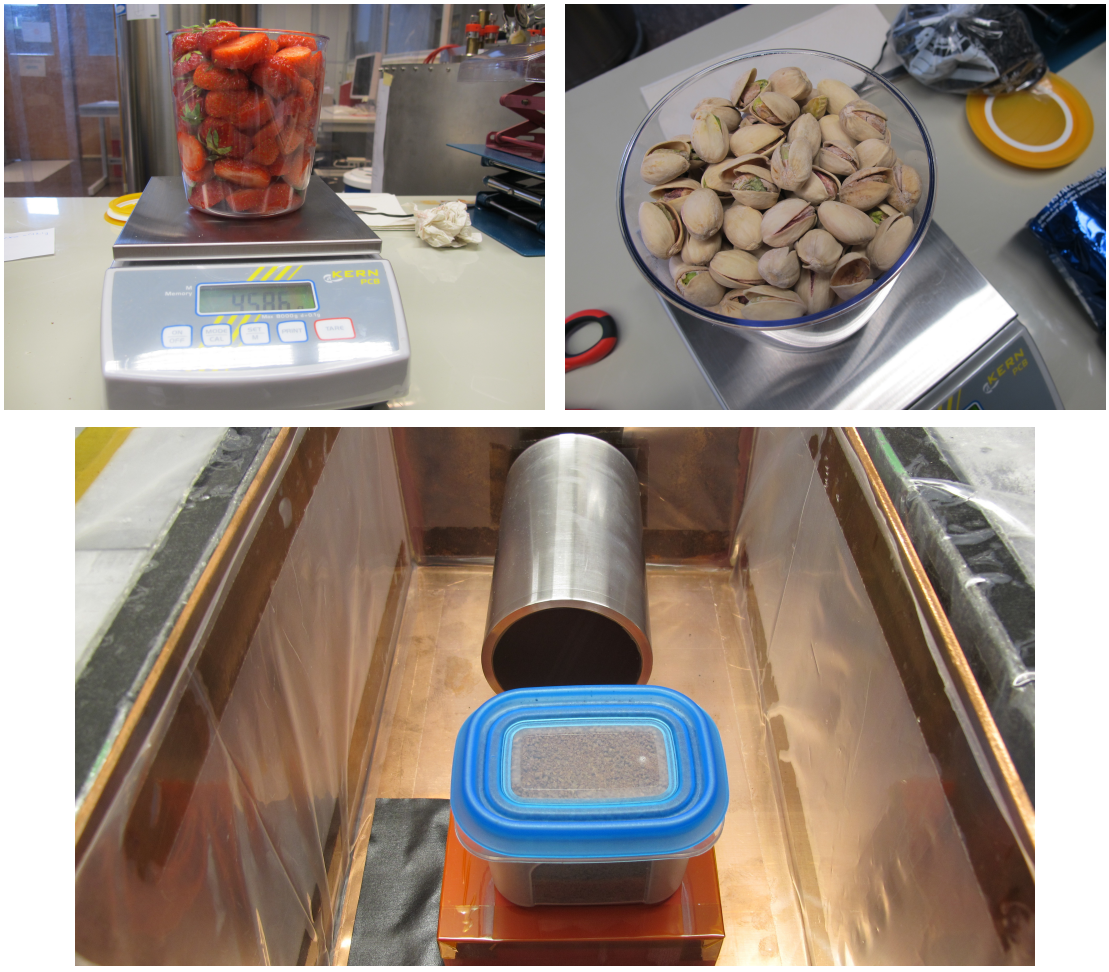

Figure A.5: Pictures of strawberries, pistachios and chocolate used in the measurements

A.4 Analysis method

Extraction of the peak area

The number of counts attributed to ^{40}K was obtained by fitting the peak with the function $F(E, \sigma, b)$ discussed in appendix B. The uncertainty on A was obtained from the fitting procedure as implemented in the ROOT [164] analysis framework. Figure B.1 shows an example of a fit performed for the chocolate sample CC06_14 listed in Table A.3.

Background subtraction

The lead shield does not completely remove the effect of the environmental potassium. The number of gammas coming from the sample was calculated as

$$A_S^{sample} = A_{S+BKG}^{sample} - A_{BKG}^{sample} \quad . \tag{A.1}$$

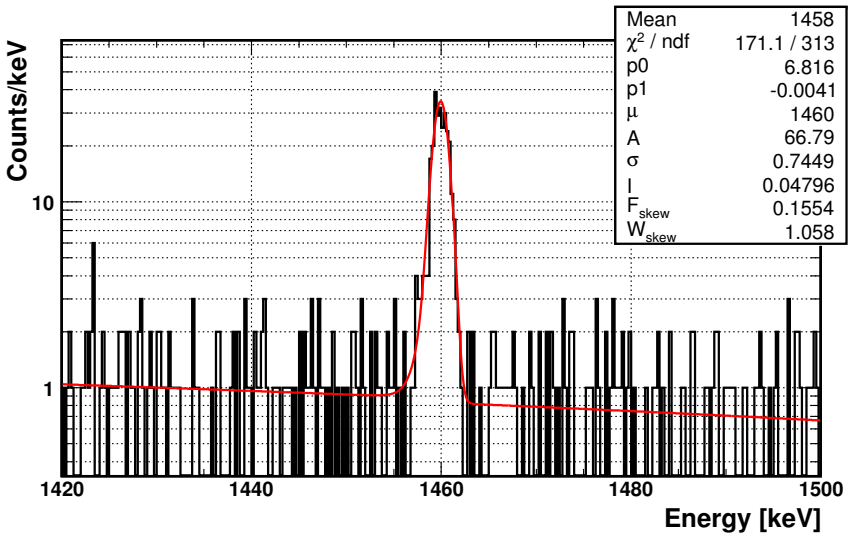

Figure A.6: Energy spectrum (histogram) of the chocolate sample CC06_14 from Table A.3 around the ^{40}K peak and the result of the fit performed using the function in Eqs. B.1, B.2 and B.3 plus a first order polynomial represented by the parameters p0 and p1 (line).

As the environmental background varies over time it is important to not only perform long enough background measurements, but to also do them in temporal proximity.

Detector calibration

The calibration of each setup was performed with KCl. The calibration factor was defined as:

$$\epsilon_{KCl} = \frac{C_K^{KCl}(\frac{\text{mg}}{100\text{g}})}{A_S^{KCl}} \ , \tag{A.2}$$

where C_K^{KCl} is the potassium content in the KCl sample in mg per 100 g, as specified in its data sheet, and A_S^{KCl} is the area underneath the ^{40}K peak in the KCl energy spectrum after background subtraction.

The uncertainty on ϵ_{KCl} can be asymmetric. It is evaluated varying C_K^{KCl} and A_S^{KCl} according to their uncertainties, in order to obtain the one sigma deviations $\Delta_{sys}^{+}(\epsilon_{KCl})$ and $\Delta_{sys}^{-}(\epsilon_{KCl})$. These uncertainties are taken as systematic uncertainties on the potassium content of the food samples.

Extraction of potassium content

Using the calibration factor ϵ_{KCl}, the potassium content in mg per 100 g, C_K, was calculated as

$$C_K\left(\frac{\text{mg}}{100\text{ g}}\right) = \frac{A_S^{food}}{m_{food}} \cdot \epsilon_{KCl} = F_{food} \cdot \epsilon_{KCl} \ , \tag{A.3}$$

where A_S^{food} from Eq. A.1 is the area underneath the ^{40}K peak measured for the food sample and m_{food} is its mass.

The statistical uncertainty is calculated from the fit uncertainty on A_S^{food} and the uncertainty of 0.1 g on m_{food}. The systematic uncertainty results from the uncertainty on ϵ_{KCl} (see Sec. A.4). The uncertainties are computed as asymmetric, but in many cases are symmetric and quoted as Δ_{stat} and Δ_{sys}.

A.5 Results

The measured potassium content, C_K^{meas}, for all samples listed in Tables A.1-A.4 are given in Tables A.5-A.8. Also given are expectations, C_K^{expec} [186], and statistical (Δ_{stat}) and systematic (Δ_{sys}) uncertainties. The statistical uncertainties dominate. The expected values [186] are reported without uncertainties.

	ID	$C_K^{expect}(\frac{\text{mg}}{100\text{ g}})$ **[186]**	$C_K^{meas}(\frac{mg}{100\ g})$	Δ_{stat}	Δ_{sys}	Δ_{tot}
F_12	F01_12	358	357	25	2	25
	F02_12	312	312	16	2	16
	F03_12	733	619	41	3	41
	F04_12	153	184	2	1	3
	F05_12	300	766	16	4	16
	F06_12	1025	733	37	4	38
	F07_12	680	640	54	3	54
	F08_12	746	1134	58	6	59
	F09_12	1162	1315	65	7	66
DC_12	DC50_12	762	417	40	2	41
	DC70_12	1067	512	19	3	19
	DC85_12	1296	1196	29	7	29

Table A.5: List of the expected (C_K^{expec}) and measured (C_K^{meas}) potassium content of the fruit, nuts and chocolates listed in Table A.1. The measured value is quoted together with the statistical uncertainty, Δ_{stat}, the systematic uncertainty, Δ_{sys}, and their quadratic sum Δ_{tot}.

Figure A.7 shows the F_12 results on fruit and nuts listed in Table A.5. The agreement between the expected and measured values is good for fresh fruit like bananas, kiwis and strawberries. The disagreement observed for processed food points to the influence of the processing techniques. The nuts show a potassium content lower than expected, while the dried fruit show a higher one. The more dehydrated the fruit, the higher is the relative potassium content. The ratios between expectation and measurement are not uniform but the trends are very clear.

The subset DC_12 of Table A.5 and Tables A.6 and A.7 list the results for chocolate. Given the cacao content, $C(\%)$, of a bar of chocolate of 100 g, the expected potassium content is calculated as

$$C_K^{bar}(\frac{mg}{100\,g}) = C_K^{cacao}(\frac{mg}{100\,g}) \cdot C(\%)\ , \tag{A.4}$$

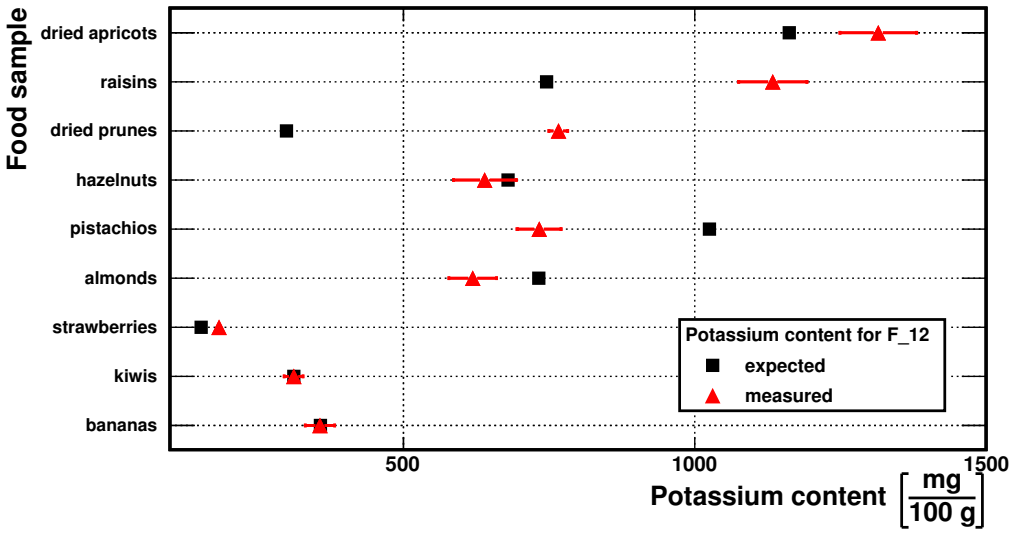

Figure A.7: Comparison between the expected (squares) and the measured (triangles) values of the potassium content of selected fruit and nuts as listed in Table A.5.

	ID	$C_K^{expect}(\frac{\text{mg}}{100\text{ g}})$ [186]	$C_K^{meas}(\frac{mg}{100\ g})$	Δ_{exp}	Δ_{sys}	Δ_{tot}
DC_13	DC71_13	1082	726	35	6	36
	DC85_13	1296	832	44	7	44
	DC92_13	1403	642	106	$^{+6}_{-5}$	106
CC_13	CC01_13	1143	590	85	5	85
	CC02_13	1143	814	41	7	42
	CC03_13	1143	660	52	6	53
	CC04_13	1143	529	93	$^{+4}_{-5}$	93
	CC05_13	1143	716	94	6	94
	CC06_13	1143	751	57	6	57
	CC07_13	1143	634	100	5	100

Table A.6: List of the expected (C_K^{expec}) and measured (C_K^{meas}) potassium content of the samples of chocolate listed in Table A.2. Other details as in Table A.5.

where $C_K^{cacao}(\frac{\text{mg}}{100\text{ g}})$ is the potassium content of pure cacao. Potassium is assumed to be contained only in cacao. Figure A.8 shows the correlation between the nominal content of cacao and the measured potassium content for samples produced by Lindt(DC_12 and DC_14, purchased in summer 2012 and summer 2014 respectively) and Vivani (DC_13), purchased in autumn 2013. The expected potassium content (Eq. A.4) are also shown. Both Lindt chocolates have higher potassium content for higher percentage of cacao. However, the proportionality is not as expected: for lower (higher) nominal cacao content the measured potassium content is lower (higher) than expected. For Vivani chocolates, the potassium content is basically independent of the nominal %

	ID	$C_K^{expect}(\frac{\text{mg}}{100\ \text{g}})$ [186]	$C_K^{meas}(\frac{mg}{100\ g})$	Δ_{exp}	Δ_{sys}	Δ_{tot}
DC_14	DC50_14	762	394	22	4	23
	DC70_14	1067	680	61	6	62
	DC85_14	1296	1498	25	14	29
	DC90_14	1372	1705	110	16	111
CC_14	CC01_14	1143	619	49	6	49
	CC02_14	1143	585	66	5	66
	CC03_14	1143	465	110	4	110
	CC04_14	1143	528	112	5	112
	CC05_14	1143	629	113	6	113
	CC06_14	1143	591	61	5	61
	CC07_14	1143	652	65	6	65
	CC08_14	1143	688	23	6	24

Table A.7: List of the expected (C_K^{expec}) and measured (C_K^{meas}) potassium content of the samples of chocolate listed in Table A.3. Other details as in Table A.5.

of cacao. This behavior could point to inaccurately quoted percentages of cacao or to production techniques influencing the potassium content of the product.

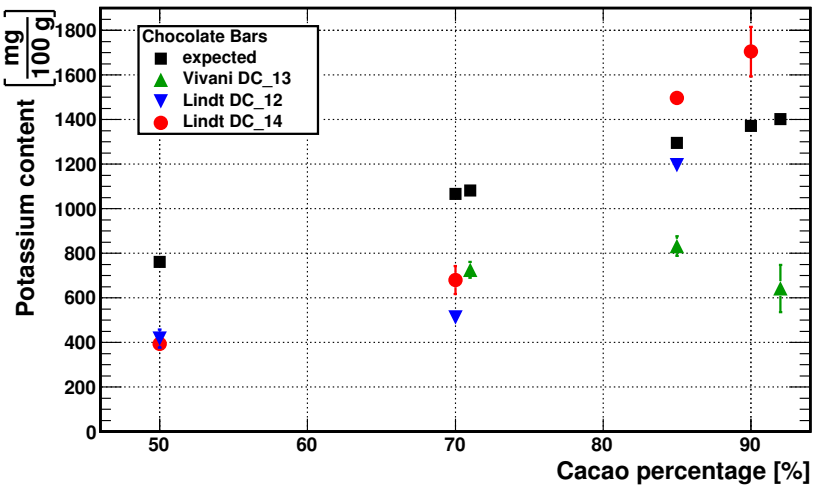

Figure A.8: Correlation between the measured potassium content and the quoted percentage of cacao in bars of chocolate for different brands: squares show the expected potassium content while up triangles show Vivani samples from autumn 2013, down triangles Lindt samples from summer 2012 and circles Lindt samples from summer 2014 (See Tables A.5–A.7)

Figure A.9 shows a comparison between the expected and the measured potassium content in bars of chocolate produced by Bonnat with cacao coming from different countries. Measurements for each place of origin were performed with two slightly different setups and using two samples of chocolate (75% of cacao) purchased in different years. The results are from autumn 2013 (CC_13 in Table A.6) and from summer 2014 (CC_14 in Table A.7). The two sets of measurements agree within the uncertainties. However, the measurements show a potassium content significantly lower than expected. This behavior could point either to a cacao content lower than declared or to specific production techniques that might influence the potassium content. No significant variations due to the place of origin are observed.

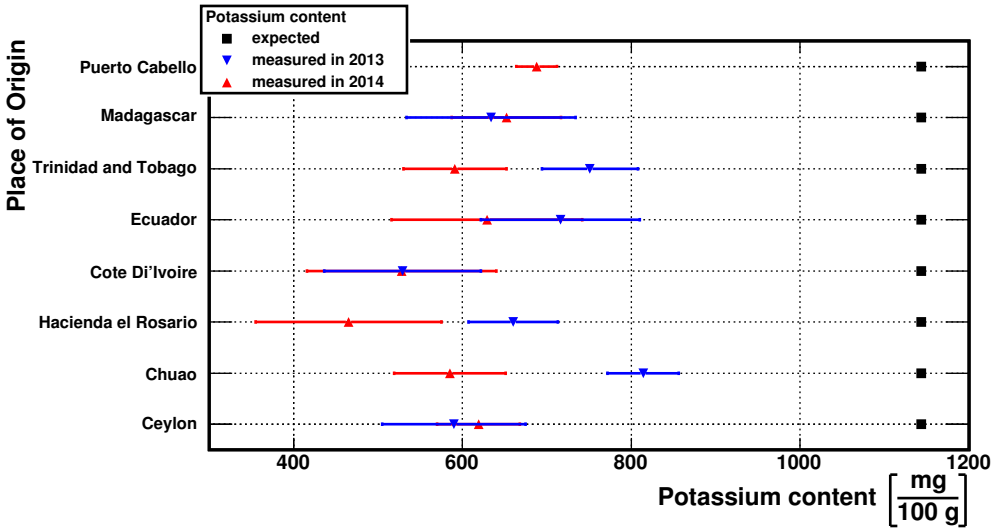

Figure A.9: Comparison between the expected (squares) and the measured (triangles) values of the potassium content in bars of dark-chocolate (75% of cacao), produced by Bonnat, with cacao coming from different countries as listed in Tables A.6 and A.7. No measurement for Puerto Cabello was performed in autumn 2013.

	ID	$C_K^{known}(\frac{\text{mg}}{100\text{ g}})$ [186]	$C_K^{meas}(\frac{mg}{100\ g})$	Δ_{stat}	Δ_{sys}	Δ_{tot}
L_14	L01_14	1795	1630	101	$^{+16}_{-17}$	103
	L02_14	244	1064	77	11	78
	L03_14	668	1100	21	11	24

Table A.8: List of the expected (C_K^{expec}) and measured (C_K^{meas}) potassium content of the legumes listed in Table A.4. Other details as in Table A.5.

Table A.8 shows the results for legumes. Figure A.10 shows the comparison between the expected and the measured potassium content. Both, red lentils and green peas, have a potassium

content higher than expected, while the white beans autumn short. However, the white beans still have the highest measured potassium content.

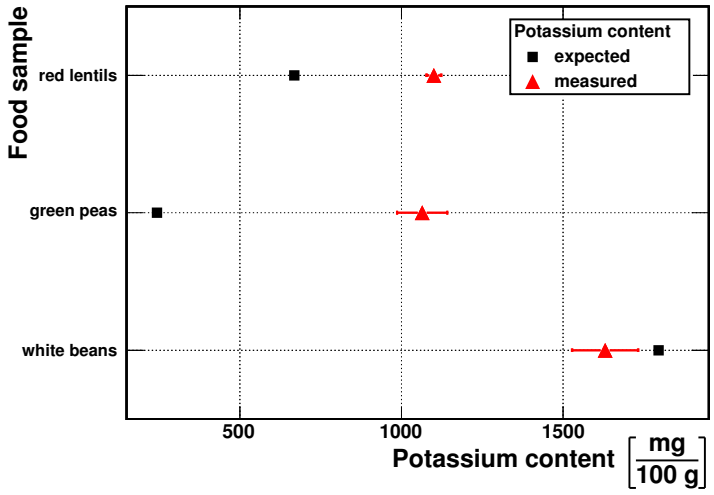

Figure A.10: Comparison between the expected (squares) and the measured (triangles) values of the potassium content for different kinds of legumes (see Table A.8).

A.6 Conclusions

In this appendix, a simple and clean method to measure the potassium content of samples of food with germanium detectors was presented. The results verify the high potassium content expected for fruit, nuts, chocolate and legumes. However, the expectations are not always met quantitatively. Especially the expected dependence of the potassium content of chocolate on the listed percentage of cacao could not be confirmed. No dependence on the origin of the samples could be established with statistical significance. The highest measured potassium contents are 1705 mg/100 g from dark chocolate with 90% of cacao and 1630 mg/100 g from white beans. Eating either 100 g of 90% cacao chocolate or 100 g of white beans provide approximately 50% of the daily recommendation of 3.5 g [187] of potassium.

Appendix B

Modelling photo-peaks in energy spectra from germanium detectors

An accurate analytical description of full-energy peaks in the energy spectrum is important for detailed analyses and calibration procedures. It is established (e.g. [188,189] and references therein) that a simple Gaussian with the width determined by statistical fluctuations and electronic noise is not enough to describe line shapes. It is necessary to introduce some deviations from a simple Gaussian to describe low energy tails from effects like incomplete charge collection and a step function to account for Compton Scattering enhancing the background below the peak.

The parametric function to model line shapes over a wide range of energies is chosen as:

$$F(E,\sigma,b) = A\cdot(1-F_{skew})\frac{1}{\sigma\sqrt{2\pi}}exp\left(-\left(\frac{E-\mu}{\sqrt{2}\sigma}\right)^2\right) \tag{B.1}$$

$$+A\cdot\frac{F_{skew}}{2b}exp\left(\frac{E-\mu}{b}+\frac{\sigma^2}{2b^2}\right)(1-erf\left(\frac{E-\mu}{\sqrt{2}\sigma}+\sigma\sqrt{2}b\right) \tag{B.2}$$

$$+I\cdot\frac{1}{2}erfc\left(\frac{E-\mu}{\sqrt{2}\sigma}\right)\,, \tag{B.3}$$

where:

B.1 describes the Gaussian component of the peak, where:

- E is the energy;
- A is the area underneath the peak;
- σ is the standard deviation of the Gaussian;
- μ is the center of the peak;

B.2 represents an exponentially modified Gaussian which describes the tail in the lower energy side of the peak, where:

- F_{skew} is the skewness factor;
- $b = W_{\text{skew}}\cdot\sigma$ is the relaxation time of the exponential component;

B.3 represent the step function which describes the Compton scattering component, where:

- I is the amplitude of the step function.

Figure B.1 shows the 1408 keV peak from the isotope ^{152}Eu in the energy spectrum from a ^{228}Th calibration measurement. The fit was performed using a function defined as the sum of Eqs. B.1, B.2 and B.3, plus a first order polynomial in order to describe the background.

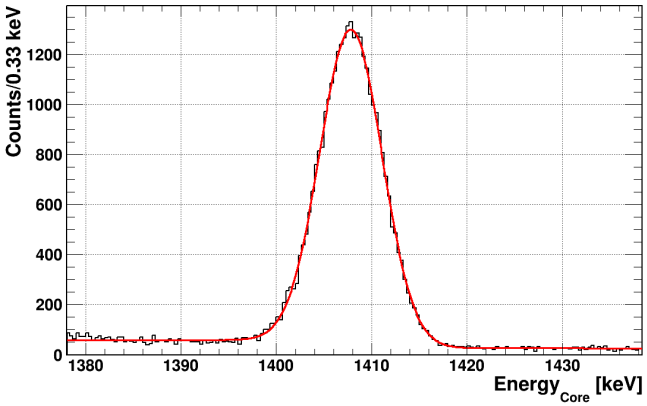

Parameter	Best Value
F_{skew}	0.01366
W_{skew}	0.0892
μ	1408.0
A	1.043×10^4
σ	3.26
I	30.93
p_0	64.3
p_1	-0.026

Figure B.1: On the left: energy spectrum (histogram) from a ^{228}Th calibration measurement around the ^{152}Eu peak and the result of the fit performed using a function defined as the sum of Eqs. B.1, B.2 and B.3 plus a first order polynomial (red line); on the right: a list of the best values of the fitting parameters.

Physical quantities are related to the fit parameters as follows:

Count rate: Fitting a binned histogram, the number of counts in the peak, C, is

$$C = \frac{A}{b_W}\,, \tag{B.4}$$

where b_W is the bin width. The uncertainty on C is obtained in terms of the statistical uncertainty on A, ΔA, from the fitting procedure.

Energy resolution: The Full Width Half Maximum (FWHM), introduced in section 3.3.1, can be expressed in terms of σ as

$$FWHM = 2.35 \cdot \sigma\,. \tag{B.5}$$

The uncertainty on FWHM is obtained in terms of the statistical uncertainty on σ, $\Delta\sigma$, from the fitting procedure.

Appendix C

Super Siegfried reference frame

The special segmented detector SuSie is described in detail in section 3.3.2. In the following, drawings with important information and conventions regarding SuSie are shown.

Figure C.1 shows the reference frame of SuSie. It is a cylindrical coordinate system where:

1. the vertical axis has its zero at the base of the detector and it is pointing upwards. The vertical position is denoted with z and measured in [mm]. The vertical sizes of the segments are shown;

2. the azimuthal coordinate is zero in correspondence to the readout cable (see Fig. 3.6, between segments 1 and 6 in the lower layer of segments. The azimuthal coordinate increases counter-clockwise and it is denoted with ϕ;

3. the radial coordinate has its zero at the center of the bore hole. The radial position is denoted as r. The radius of the cylinder is $r = 37.5\,\text{mm}$.

Positions of the radioactive sources inside Galatea are given always with respect to this reference frame. Conventions for each kind of measurement presented in this thesis follow:

1. background and calibration measurements: the internal radioactive sources are moved as far as possible away from the detector, as shown in Fig. 4.4. The side source is placed at $z = -5.0\,\text{mm}$ and the top source is placed at $r = 52.57\,\text{mm}$. These measurements are independent from the azimuthal position and therefore the latter is not specified;

2. alpha-dedicated measurements: the side source is placed as far as possible away from the detector, as in point 1. Only the radial, r, and azimuthal, ϕ, positions of the top source are given.

Figure C.2 shows a top view of SuSie. The Mercedes bars are metallic bars, part of the support of the detector. They are 120° apart ($\phi_{MB1} = 15°$, $\phi_{MB2} = 135°$, $\phi_{MB3} = 255°$) . The segment boundaries are depicted as dashed black lines and 60° apart. The position of the partial metalization as used for SuSie I is shown too and it is around 300°.

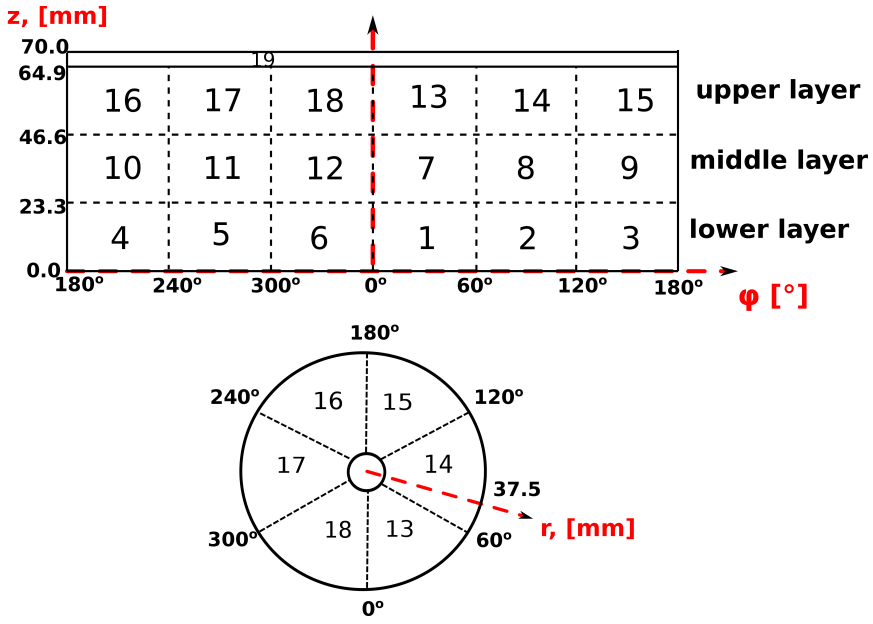

Figure C.1: SuSie: Segment numbering and reference frame. The axes of the reference frame are shown as dashed red lines. On top, an unfolded view of the detector is shown together with labels used for each layer of segments. At the bottom, a top view of the detector shows the azimuthal and radial coordinates.

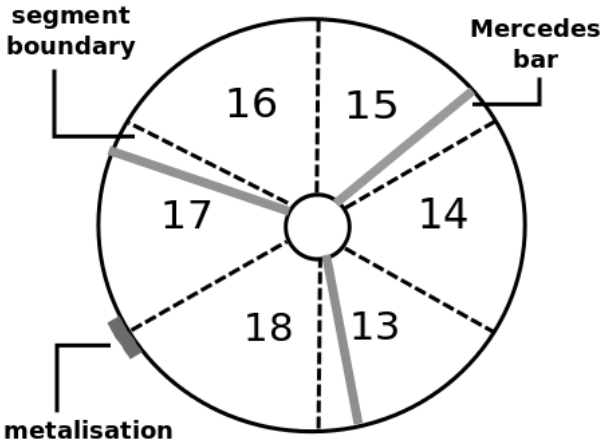

Figure C.2: Top view of SuSie I: segment boundaries are depicted as black dashed lines. Mercedes bars are depicted as thick grey lines. The partial metalization of the top segment of SuSie I is shown in correspondence to the segment boundary between segments 17 and 18.

Appendix D

Lists of measurements presented in the thesis

In the following, the measurements performed with SuSie I operated in GALATEA between June and December 2013 are listed. Measurements are grouped in types of measurements:

1. background and calibration measurements performed with SuSie I are listed in Table D.1. The relevant quantities for background and calibration measurements are their lifetimes and their date;

2. alpha dedicated measurements performed with SuSie I are divided into three groups:

   (a) measurements for the radial scans of the top end-plate, listed in Table D.2;

   (b) measurements for the azimuthal scans of the top end-plate, listed in Table D.3.

   (c) measurements for the reproducibility check, listed in Table D.4.

   The relevant quantities for each alpha-dedicated measurement is its lifetime, the date and the radial, r, and azimuthal, ϕ, position of the ^{241}Am source.

	ID	Date [dd/mm/yy]	Lifetime [s]
BKG	BKG01	29/08/13	40646.68
	BKG02	07/09/13	35912.26
	BKG03	17/09/13	16235.38
	BKG04	29/10/13	10040.78
	BKG05	08/11/13	11341.26
	BKG06	12/11/13	10252.84
	BKG07	13/11/13	10071.72
	BKG08	15/11/13	13364.58
	BKG09	27/11/13	20989.22
	BKG10	15/12/13	10861.32
	BKG11	17/12/13	24180.98
NOISE_EFF	all sensors ON	19/06/13	8256.77
	pressure ON others OFF	28/06/13	11768.27
	pressure OFF others ON	26/06/13	19410.20
	all sensors OFF	24/06/13	13660.05
	only Single Gauge ON	03/07/13	5976.07
	only BARION sensor ON	03/07/13	9579.35
	CAL01	23/10/13	11432.71

Table D.1: List of measurements from June 2013 to December 2013 using SuSie I in GALATEA: BKG contains background measurements, NOISE_EFF contains ^{228}Th calibration measurements done to study the effect of the monitoring sensors on the noise.

	ID	Date [dd/mm/yy]	Lifetime [s]	Top Source r [mm]	ϕ [◦]
RS01	RS01_1	11/11/13	3826.52	6.0	33.0
	RS01_2	17/11/13	2108.01	10.0	33.0
	RS01_3	17/11/13	2415.62	14.0	33.0
	RS01_4	17/11/13	2087.05	18.0	33.0
	RS01_2	17/11/13	2295.69	22.0	33.0
	RS01_3	15/11/13	2609.69	30.0	33.0
	RS01_4	15/11/13	2234.26	34.0	33.0
	RS01_2	13/11/13	3797.26	38.0	33.0
RS02	RS02_2	11/11/13	2197.64	10.0	312.0
	RS02_3	11/11/13	2146.54	14.0	312.0
	RS02_4	08/11/13	2382.57	18.0	312.0
	RS02_5	08/11/13	2028.05	22.0	312.0
	RS02_6	08/11/13	3736.54	26.0	312.0
	RS02_7	08/11/13	2401.55	30.0	312.0
	RS02_8	07/11/13	2119.95	34.0	312.0
	RS02_9	07/11/13	2657.29	38.0	312.0
RS03	RS03_1	19/09/13	2204.98	29.0	176.0
	RS03_2	19/09/13	2158.63	35.0	176.0
	RS03_3	19/09/13	2920.50	37.0	176.0
RS04	RS04_1	02/10/13	2681.48	13.0	18.0
	RS04_2	02/10/13	2948.84	16.0	18.0
	RS04_3	02/10/13	2296.08	19.0	18.0
	RS04_4	02/10/13	2877.17	22.0	18.0
	RS04_5	04/10/13	3636.42	28.0	18.0
	RS04_6	04/10/13	1952.48	31.0	18.0
	RS04_7	04/10/13	2281.49	34.0	18.0

Table D.2: List of measurements from August to November 2013 using SuSie I in GALATEA: RS01 contains alpha-dedicated measurements at $\phi = 33.0°$, . RS02 contains alpha-dedicated measurements at $\phi = 312.0°$, RS03 contains alpha-dedicated measurements at $\phi = 176.0°$, RS01 contains alpha-dedicated measurements at $\phi = 18.0°$.

	ID	Date [dd/mm/yy]	Lifetime [s]	Top Source r [mm]	ϕ [°]
AS01	AS01_1	01/10/13	2513.34	26.0	96.0
	AS01_2	01/10/13	2755.74	26.0	98.0
	AS01_3	01/10/13	3017.06	26.0	100.0
	AS01_4	27/09/13	1583.68	26.0	102.0
	AS01_5	26/09/13	2593.63	26.0	104.0
	AS01_6	25/09/13	1204.98	26.0	107.0
	AS01_7	25/09/13	2986.97	26.0	112.0
	AS01_8	25/09/13	2447.16	26.0	118.0
	AS01_9	25/09/13	2581.77	26.0	124.0
	AS01_10	25/09/13	1319.16	26.0	129.0
	AS01_11	24/09/13	1833.80	26.0	130.0
	AS01_12	24/09/13	1878.45	26.0	134.0
	AS01_13	24/09/13	2120.53	26.0	135.0
	AS01_14	23/09/13	2568.98	26.0	135.0
	AS01_15	23/09/13	3548.45	26.0	136.0
	AS01_16	23/09/13	2410.46	26.0	136.0
AS02	AS02_1	30/10/13	3416.67	30.0	281.0
	AS02_2	30/10/13	3802.15	30.0	283.0
	AS02_3	30/10/13	2188.97	30.0	287.0
	AS02_4	29/10/13	2343.72	30.0	290.0
	AS02_5	08/11/13	2401.55	30.0	291.0
	AS02_6	29/10/13	2462.13	30.0	295.0
	AS02_7	29/10/13	2543.32	30.0	300.0
	AS02_8	29/10/13	1550.38	30.0	304.0
	AS02_9	28/10/13	2212.13	30.0	308.0
	AS02_10	28/10/13	3313.06	30.0	312.0
	AS02_11	28/10/13	4015.13	30.0	315.0

Table D.3: List of measurements from August to November 2013 using SuSie I in GALATEA: AS01 contains alpha-dedicated measurements at $r = 26.0\,\text{mm}$, . RS02 contains alpha-dedicated measurements at $r = 30.0\,\text{mm}$.

	ID	Date [dd/mm/yy]	Lifetime [s]	Top Source r [mm]	ϕ [°]
before	before_1	01/10/13	3017.06	26.0	100.0
	before_2	27/09/13	1583.68	26.0	102.0
	before_3	26/09/13	2593.63	26.0	104.0
after	after_1	30/09/13	3539.49	26.0	100.0
	after_2	30/09/13	1906.59	26.0	102.0
	after_3	01/10/13	2089.03	26.0	102.0

Table D.4: List of measurements from September 2013 using SuSie I in GALATEA: **before** contains alpha-dedicated measurements done before switching OFF the detector, **after** contains alpha-dedicated measurements performed after switching the detector back on.

Appendix E

Example of the description of radioactive sources

Germanium detectors are mostly used as gamma-ray spectrometers with an excellent energy resolution. It is important to accurately describe known sources of gamma-rays close to the detector gamma-ray in order to quantitatively analyse energy spectra and identify unknown sources. Precise source descriptions are also important for the calibration process.

In the following an example of a source description used in the independent core calibration procedure described in section 5.2 is shown. The description is written in the open JavaScript Object Notation (JSON) [190] standard format. Radiation sources are divided in types: gamma, beta or alpha radiation. In the example, only gamma lines are listed. Each entry in the JSON file has two attributes: the name of the radionuclide and the energy of the gamma line. No information about the relative intensity of each gamma line is required.

```
1
2  {
3    "radiation" : {
4      "gamma": {
5        "1": {
6          "energy" : 609.380,
7          "name" : "Bi214"
8         }
9        "2": {
10         "energy" : 778.906,
11         "name" : "Eu152"
12       }
13       "3": {
14         "energy" : 964.082,
15         "name" : "Eu152"
16        }
17       "4": {
18         "energy" : 1085.841,
19         "name" : "Eu152"
20       }
21       "5": {
22         "energy" : 1112.080,
23         "name" : "Eu152"
24       }
25       "6": {
26         "energy" : 1408.006,
27         "name" : "Eu152"
28        }
29       "7": {
30         "energy" : 1764.680,
31         "name" : "Bi214"
32       }
33       "8": {
34         "energy" : 2614.533,
35         "name" : "Tl228"
36       }
37     }
38   }
39 }
```

Appendix F

Width of the spectral line due to alpha radiation

As discussed in section 7.3, the width of the spectral line due to alpha radiation is the result of a combination of three different effects. In the following, The extraction of the effects due to the plastic protective film in front of the source, σ_{source}, and the geometrical effect, σ_{geom}, are presented.

The effect of the protective film, σ_{source}, was estimated irradiating the mantle of an n-type coaxial detector with the ^{241}Am source. The detector is a segmented detector similar to SuSie. The source was placed at a medium height, thereby facing a volume of the detector with symmetric and strong electric field lines. The expected dead layer in this area is less than 300 nm. Thus, the width of the obtained spectral line is totally due to the protective window of the source.

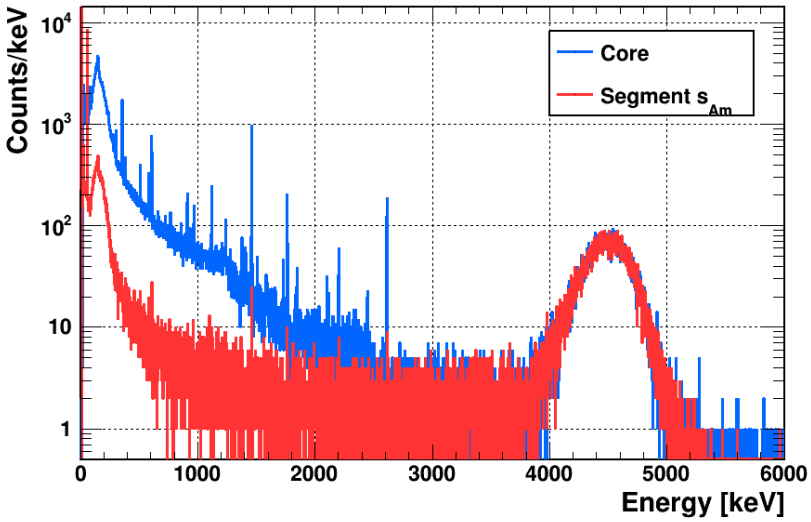

Figure F.1: Spectra from the core (blue) and from the segment in front of the ^{241}Am source, s_{Am}, (red).

Figure F.1 shows spectra from the core and from the segment in front of the ^{241}Am source,

s_{Am}. An alpha peak is visible in both spectra. Parameters of the alpha peak from the core and segment s_{Am} are listed in Table F.1. The listed parameters were extracted as described in section 7.4. These alpha peaks show the same mean values, $\mu_0 = \mu_{s_{\mathrm{Am}}}$. Thus, no trapping of drifting charges occurred.

	μ_i [keV]	σ_i [keV]
Core	4484	185
Segment s_{Am}	4487	185

Table F.1: List of the parameters of the spectral lines due to alpha radiation from a measurement performed probing the outer surface of a true coaxial segmented detector. Segment s_{Am} is the segment in front of the ^{241}Am source.

The reduction of energy of $\approx 1.2\,\mathrm{MeV}$ with a variation of about $0.2\,\mathrm{MeV}$ points inhomogeneities in the plastic window of 10%. The reduced energy is taken as reference for all calculations. The geometrical broadening of the line can easily be calculated for an assumed thickness of the dead layer of $20\,\mu\mathrm{m}$, the maximum penetration depth of a $4.5\,\mathrm{MeV}$ alpha particle. The trajectories of alpha particles emitted with the minimum and the maximum angles from the collimated source are depicted in Fig. F.2. A different incident angle corresponds to a different distance travelled inside the dead layer. The opening angle of the collimator, α_{true}, the radius of the resulting beam spot, r_{BS}, and the distance between the source and the detector, d, are listed.

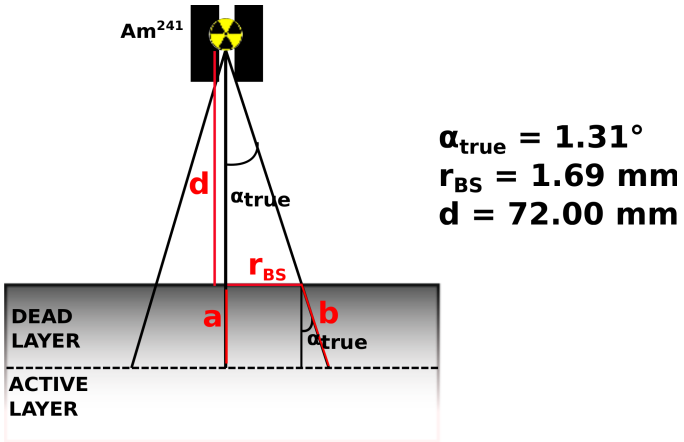

Figure F.2: Schematic view of trajectories of alpha particles emitted by the collimated ^{241}Am source with the minimum and the maximum incident angle (not to scale).

The following estimate of σ_{geom} is done assuming a clear distinction between dead and active layers of the detector. A particle emitted with the minimum incident angle (i.e downward trajectory) travels the minimum path, a, inside the "dead" layer. A particle emitted with the maximum incident angle travels the maximum path, b, inside the "dead" layer.

The energy loss of an alpha particle in germanium is about $170\,\mathrm{keV}/\mu\mathrm{m}$. For $a = 20\,\mu\mathrm{m}$, $b - a = 0.005\,\mu\mathrm{m}$, resulting in a different of energy loss of $0.85\,\mathrm{keV}$. Thus, this effect is negligible.

Bibliography

[1] Q. R. Ahmad *et al.*, "Measurement of the Rate of $\nu_e + d \rightarrow p + p + e^-$ Interactions Produced by ^{8}B Solar Neutrinos at the Sudbury Neutrino Observatory," *Phys. Rev. Lett.*, vol. 87, p. 071301, Jul 2001.

[2] Y. Fukuda *et al.*, "Evidence for oscillation of atmospheric neutrinos," *Phys.Rev.Lett.*, vol. 81, pp. 1562–1567, 1998.

[3] D. Hooper, "TASI 2008 Lectures on Dark Matter," pp. 709–764, 2009.

[4] S. Bilenky and C. Giunti, "Neutrinoless Double-Beta Decay: a Probe of Physics Beyond the Standard Model," *Int.J.Mod.Phys.*, vol. A30, no. 04n05, p. 1530001, 2015.

[5] R. Agnese *et al.*, "Search for Low-Mass Weakly Interacting Massive Particles with SuperCDMS," *Phys.Rev.Lett.*, vol. 112, no. 24, p. 241302, 2014.

[6] M. Agostini *et al.*, "Results on Neutrinoless Double-β Decay of ^{76}Ge from Phase I of the GERDA Experiment," *Phys.Rev.Lett.*, vol. 111, no. 12, p. 122503, 2013.

[7] R. Agnese *et al.*, "Improved WIMP-search reach of the CDMS II germanium data," *Phys.Rev.D*, 2015.

[8] J. Li, X. Ji, W. Haxton, and J. S. Y. Wang, "The second-phase development of the China JinPing underground Laboratory," *Phys.Procedia*, vol. 61, pp. 576–585, 2015.

[9] N. Smith, "The SNOLAB deep underground facility," *Eur.Phys.J.Plus*, vol. 127, p. 108, 2012.

[10] I. Abt, B. Dönmez, L. Garbini, S. Irlbeck, M. Palermo, and O. Schulz, "The GALATEA Test-facility," *Phys. Procedia*, vol. 61, pp. 750–758, 2015.

[11] S. Glashow, "Partial Symmetries of Weak Interactions," *Nucl.Phys.*, vol. 22, pp. 579–588, 1961.

[12] S. Weinberg, "A Model of Leptons," *Phys.Rev.Lett.*, vol. 19, pp. 1264–1266, 1967.

[13] A. Salam, "Weak and electromagnetic interactions," 1969. Proc. of the 8th Nobel Symposium on 'Elementary Particle Theory, Relativistic Groups and Analyticity', Stockholm, Sweden, 1968, edited by N. Svartholm, p. 367-377.

[14] M. Grunewald, "Experimental tests of the electroweak standard model at high-energies," *Phys.Rept.*, vol. 322, pp. 125–346, 1999.

[15] S. Chatrchyan *et al.*, "Observation of a new boson at a mass of 125 GeV with the CMS experiment at the LHC," *Phys.Lett.*, vol. B716, pp. 30–61, 2012.

[16] G. Aad *et al.*, "Observation of a new particle in the search for the Standard Model Higgs boson with the ATLAS detector at the LHC," *Phys.Lett.*, vol. B716, pp. 1–29, 2012.

[17] A. Anderson, J. Conrad, E. Figueroa-Feliciano, C. Ignarra, G. Karagiorgi, *et al.*, "Measuring Active-to-Sterile Neutrino Oscillations with Neutral Current Coherent Neutrino-Nucleus Scattering," *Phys.Rev.*, vol. D86, p. 013004, 2012.

[18] J. Chadwick, "Possible Existence of a Neutron," *Nature*, vol. 129, p. 312, 1932.

[19] C. Cowan, F. Reines, F. Harrison, H. Kruse, and A. McGuire, "Detection of the free neutrino: A Confirmation," *Science*, vol. 124, pp. 103–104, 1956.

[20] R. Ansari *et al.*, "Measurement of the Standard Model Parameters from a Study of W and Z Bosons," *Phys.Lett.*, vol. B186, pp. 440–451, 1987.

[21] H. Band *et al.*, "NEUTRINO COUNTING WITH THE SLD AT THE STANFORD LINEAR COLLIDER," *Annals N. Y. Acad. Sci.*, vol. 578, pp. 445–459, 1989.

[22] J. Adam *et al.*, "New limit on the lepton-flavour violating decay $\mu^+ \to e^+\gamma$," *Phys.Rev.Lett.*, vol. 107, p. 171801, 2011.

[23] J. N. Bahcall, M. Pinsonneault, and S. Basu, "Solar models: Current epoch and time dependences, neutrinos, and helioseismological properties," *Astrophys.J.*, vol. 555, pp. 990–1012, 2001.

[24] G. G. Raffelt, "Neutrinos and the stars," *Proc. Int. Sch. Phys. Fermi*, vol. 182, pp. 61–143, 2012.

[25] B. Cleveland, T. Daily, J. Davis, Raymond, J. R. Distel, K. Lande, *et al.*, "Measurement of the solar electron neutrino flux with the Homestake chlorine detector," *Astrophys.J.*, vol. 496, pp. 505–526, 1998.

[26] W. Hampel *et al.*, "GALLEX solar neutrino observations: Results for GALLEX IV," *Phys.Lett.*, vol. B447, pp. 127–133, 1999.

[27] M. Altmann *et al.*, "Complete results for five years of GNO solar neutrino observations," *Phys.Lett.*, vol. B616, pp. 174–190, 2005.

[28] J. Abdurashitov *et al.*, "Solar neutrino flux measurements by the Soviet-American Gallium Experiment (SAGE) for half the 22 year solar cycle," *J.Exp.Theor.Phys.*, vol. 95, pp. 181–193, 2002.

[29] Y. Fukuda *et al.*, "Solar neutrino data covering solar cycle 22," *Phys.Rev.Lett.*, vol. 77, pp. 1683–1686, 1996.

[30] S. Fukuda *et al.*, "Solar B-8 and hep neutrino measurements from 1258 days of Super-Kamiokande data," *Phys.Rev.Lett.*, vol. 86, pp. 5651–5655, 2001.

[31] V. Gribov and B. Pontecorvo, "Neutrino astronomy and lepton charge," *Physics Letters B*, vol. 28, no. 7, pp. 493 – 496, 1969.

[32] L. Wolfenstein, "Neutrino Oscillations in Matter," *Phys.Rev.*, vol. D17, pp. 2369–2374, 1978.

[33] S. Mikheev and A. Y. Smirnov, "Resonant amplification of neutrino oscillations in matter and solar neutrino spectroscopy," *Nuovo Cim.*, vol. C9, pp. 17–26, 1986.

[34] W. A. Mann, "Atmospheric neutrinos and the oscillations bonanza," *Int.J.Mod.Phys.*, vol. A15S1, pp. 229–256, 2000.

[35] T. J. Haines *et al.*, "Calculation of atmospheric neutrino-induced backgrounds in a nucleon-decay search," *Phys. Rev. Lett.*, vol. 57, pp. 1986–1989, Oct 1986.

[36] K. Hirata, T. Kajita, M. Koshiba, M. Nakahata, S. Ohara, Y. Oyama, N. Sato, A. Suzuki, M. Takita, Y. Totsuka, T. Kifune, T. Suda, K. Nakamura, K. Takahashi, T. Tanimori, K. Miyano, M. Yamada, E. Beier, L. Feldscher, E. Frank, W. Frati, S. Kim, A. Mann, F. Newcomer, R. V. Berg, W. Zhang, and B. Cortez, "Experimental study of the atmospheric neutrino flux," *Physics Letters B*, vol. 205, no. 2âĂŞ3, pp. 416 – 420, 1988.

[37] G. Battistoni *et al.*, "Fully contained events in the mont blanc nucleon decay detector," *Phys. Lett.*, vol. B118, p. 461, 1982.

[38] C. Berger *et al.*, "A Study of atmospheric neutrino oscillations in the FREJUS experiment," *Phys.Lett.*, vol. B245, pp. 305–310, 1990.

[39] T. Kafka, "Recent atmospheric neutrino results from Soudan-2," *Nucl.Phys.Proc.Suppl.*, vol. 87, pp. 186–188, 2000.

[40] Y. Fukuda *et al.*, "Measurement of the flux and zenith angle distribution of upward through going muons by Super-Kamiokande," *Phys.Rev.Lett.*, vol. 82, pp. 2644–2648, 1999.

[41] Z.-z. Xing, "Properties of CP Violation in Neutrino-Antineutrino Oscillations," *Phys. Rev.*, vol. D87, no. 5, p. 053019, 2013.

[42] B. Pontecorvo, "Mesonium and anti-mesonium," *Sov.Phys.JETP*, vol. 6, p. 429, 1957.

[43] S. F. King and C. Luhn, "Neutrino Mass and Mixing with Discrete Symmetry," *Rept.Prog.Phys.*, vol. 76, p. 056201, 2013.

[44] C. Giunti and C. W. Kim, "Fundamentals of Neutrino Physics and Astrophysics," 2007.

[45] M. Gonzalez-Garcia, M. Maltoni, and T. Schwetz, "Updated fit to three neutrino mixing: status of leptonic CP violation," *JHEP*, vol. 1411, p. 052, 2014.

[46] R. Mohapatra, "ICTP lectures on theoretical aspects of neutrino masses and mixings," 2002.

[47] S. Weinberg, "Baryon- and lepton-nonconserving processes," *Phys. Rev. Lett.*, vol. 43, pp. 1566–1570, Nov 1979.

[48] E. Ma, "Neutrino Mass: Mechanisms and Models," 2009.

[49] C. Weinheimer and K. Zuber, "Neutrino Masses," *Annalen Phys.*, vol. 525, no. 8-9, pp. 565–575, 2013.

[50] A. Strumia and F. Vissani, "Neutrino masses and mixings and...," 2006.

[51] S. Gershtein and Y. a. Zeldovich, "Rest Mass of Muonic Neutrino and Cosmology," *JETP Lett.*, vol. 4, pp. 120–122, 1966.

[52] R. Adam *et al.*, "Planck 2015 results. I. Overview of products and scientific results," 2015.

[53] T. J. Loredo and D. Q. Lamb, "Bayesian analysis of neutrinos observed from supernova SN-1987A," *Phys.Rev.*, vol. D65, p. 063002, 2002.

[54] G. Pagliaroli, F. Rossi-Torres, and F. Vissani, "Neutrino mass bound in the standard scenario for supernova electronic antineutrino emission," *Astroparticle Physics*, vol. 33, no. 5âĂŞ6, pp. 287 – 291, 2010.

[55] W. D. Arnett and J. L. Rosner, "Neutrino Mass Limits From Sn1987a," *Phys.Rev.Lett.*, vol. 58, p. 1906, 1987.

[56] C. Kraus, B. Bornschein, L. Bornschein, J. Bonn, B. Flatt, *et al.*, "Final results from phase II of the Mainz neutrino mass search in tritium beta decay," *Eur.Phys.J.*, vol. C40, pp. 447–468, 2005.

[57] V. Aseev *et al.*, "An upper limit on electron antineutrino mass from Troitsk experiment," *Phys.Rev.*, vol. D84, p. 112003, 2011.

[58] S. Mertens, "Status of the *KATRIN* Experiment and Prospects to Search for keV-mass Sterile Neutrinos in Tritium Îš-decay," *Physics Procedia*, vol. 61, no. 0, pp. 267 – 273, 2015. 13th International Conference on Topics in Astroparticle and Underground Physics, TAUP 2013.

[59] K. Assamagan, C. Brönnimann, M. Daum, H. Forrer, R. Frosch, P. Gheno, R. Horisberger, M. Janousch, P. R. Kettle, T. Spirig, and C. Wigger, "Upper limit of the muon-neutrino mass and charged-pion mass from momentum analysis of a surface muon beam," *Phys. Rev. D*, vol. 53, pp. 6065–6077, Jun 1996.

[60] R. Barate et al., "An upper limit on the τ neutrino mass from three- and five-prong tau decays," *The European Physical Journal C - Particles and Fields*, vol. 2, no. 3, pp. 395–406, 1998.

[61] M. Goeppert-Mayer, "Double beta-disintegration," *Phys.Rev.*, vol. 48, pp. 512–516, 1935.

[62] S. Elliott, M. Moe, M. Nelson, and M. Vient, "Observed double beta decay spectra from ^{82}Se, ^{110}Mo, and ^{150}Nd," *Nucl.Phys.Proc.Suppl.*, vol. 31, pp. 68–71, 1993.

[63] D. Dassie, "Two neutrino double beta decay of ^{116}Cd observed with the NEMO-2 detector," pp. 205–211, 1995.

[64] R. Arnold *et al.*, "Observation of two neutrino double beta decay of ^{116}Cd with the tracking detector NEMO-2," *JETP Lett.*, vol. 61, pp. 170–174, 1995.

[65] N. Ackerman *et al.*, "Observation of Two-Neutrino Double-Beta Decay in ^{136}Xe with EXO-200," *Phys.Rev.Lett.*, vol. 107, p. 212501, 2011.

[66] J. Barea, J. Kotila, and F. Iachello, "Nuclear matrix elements for double-β decay," *Phys.Rev.*, vol. C87, no. 1, p. 014315, 2013.

[67] G. Racah, "On the symmetry of particle and antiparticle," *Nuovo Cim.*, vol. 14, pp. 322–328, 1937.

[68] W. Furry, "On transition probabilities in double beta-disintegration," *Phys.Rev.*, vol. 56, pp. 1184–1193, 1939.

[69] I. Avignone, Frank T., S. R. Elliott, and J. Engel, "Double Beta Decay, Majorana Neutrinos, and Neutrino Mass," *Rev.Mod.Phys.*, vol. 80, pp. 481–516, 2008.

[70] A. Faessler, S. Kovalenko, F. Simkovic, and J. Schwieger, "Pion exchange currents in neutrinoless double beta decay and limits on supersymmetry," *Phys.Atom.Nucl.*, vol. 61, pp. 1229–1235, 1998.

[71] J. Vergados, "The Neutrinoless double beta decay from a modern perspective," *Phys.Rept.*, vol. 361, pp. 1–56, 2002.

[72] B. Schwingenheuer, "Status and prospects of searches for neutrinoless double beta decay," *Annalen Phys.*, vol. 525, pp. 269–280, 2013.

[73] J. Suhonen and O. Civitarese, "Weak-interaction and nuclear-structure aspects of nuclear double beta decay," *Phys.Rept.*, vol. 300, pp. 123–214, 1998.

[74] J. Kotila and F. Iachello, "Phase space factors for double-β decay," *Phys. Rev.*, vol. C85, p. 034316, 2012.

[75] S. M. Bilenky, C. Giunti, W. Grimus, B. Kayser, and S. T. Petcov, "Constraints from neutrino oscillation experiments on the effective Majorana mass in neutrinoless double beta decay," *Phys. Lett.*, vol. B465, pp. 193–202, 1999.

[76] F. Zwicky, "Die Rotverschiebung von extragalaktischen Nebeln," *Helv.Phys.Acta*, vol. 6, pp. 110–127, 1933.

[77] D. Clowe, M. Bradac, A. H. Gonzalez, M. Markevitch, S. W. Randall, *et al.*, "A direct empirical proof of the existence of dark matter," *Astrophys.J.*, vol. 648, pp. L109–L113, 2006.

[78] M. Milgrom, "A Modification of the Newtonian dynamics as a possible alternative to the hidden mass hypothesis," *Astrophys.J.*, vol. 270, pp. 365–370, 1983.

[79] G. Aad *et al.*, "Search for new phenomena in events with a photon and missing transverse momentum in pp collisions at $\sqrt{s} = 8$ TeV with the ATLAS detector," *Phys.Rev.*, vol. D91, no. 1, p. 012008, 2015.

[80] G. Aad *et al.*, "Search for invisible particles produced in association with single-top-quarks in proton-proton collisions at $\sqrt{s} = 8$ TeV with the ATLAS detector," *Eur.Phys.J.*, vol. C75, no. 2, p. 79, 2015.

[81] K. Begeman, A. Broeils, and R. Sanders, "Extended rotation curves of spiral galaxies: Dark haloes and modified dynamics," *Mon.Not.Roy.Astron.Soc.*, vol. 249, p. 523, 1991.

[82] H. Hoekstra, H. Yee, and M. Gladders, "Current status of weak gravitational lensing," *New Astron.Rev.*, vol. 46, pp. 767–781, 2002.

[83] M. Tegmark *et al.*, "The 3-D power spectrum of galaxies from the SDSS," *Astrophys.J.*, vol. 606, pp. 702–740, 2004.

[84] C. Csaki, "The Minimal supersymmetric standard model (MSSM)," *Mod.Phys.Lett.*, vol. A11, p. 599, 1996.

[85] T. Hemmick, D. Elmore, T. Gentile, P. Kubik, S. Olsen, *et al.*, "A Search for Anomalously Heavy Isotopes of Low Z Nuclei," *Phys.Rev.*, vol. D41, pp. 2074–2080, 1990.

[86] M. Schumann, "Dark Matter 2014," 2015.

[87] H. Baer, V. Barger, and A. Mustafayev, "Neutralino dark matter in mSUGRA/CMSSM with a 125 GeV light Higgs scalar," *JHEP*, vol. 1205, p. 091, 2012.

[88] H. Baer and J. List, "Post LHC8 SUSY benchmark points for ILC physics," *Phys.Rev.*, vol. D88, p. 055004, 2013.

[89] H.-C. Cheng, J. L. Feng, and K. T. Matchev, "Kaluza-klein dark matter," *Phys. Rev. Lett.*, vol. 89, p. 211301, Oct 2002.

[90] K. Kainulainen, K. Tuominen, and J. Virkajarvi, "The WIMP of a Minimal Technicolor Theory," *Phys.Rev.*, vol. D75, p. 085003, 2007.

[91] R. Foot, "Mirror dark matter: Cosmology, galaxy structure and direct detection," *Int.J.Mod.Phys.*, vol. A29, p. 1430013, 2014.

[92] R. Peccei and H. R. Quinn, "CP Conservation in the Presence of Instantons," *Phys.Rev.Lett.*, vol. 38, pp. 1440–1443, 1977.

[93] R. Creswick, I. Avignone, F.T., H. Farach, J. Collar, A. Gattone, *et al.*, "Theory for the direct detection of solar axions by coherent Primakoff conversion in germanium detectors," *Phys.Lett.*, vol. B427, pp. 235–240, 1998.

[94] Z. Ahmed *et al.*, "Search for Axions with the CDMS Experiment," *Phys.Rev.Lett.*, vol. 103, p. 141802, 2009.

[95] J. Simpson, "The AGATA Spectrometer: next generation gamma-ray spectroscopy," *J.Phys.Conf.Ser.*, vol. 606, no. 1, p. 012017, 2015.

[96] M. Cromaz, "The GRETINA Spectrometer," *J.Phys.Conf.Ser.*, vol. 606, no. 1, p. 012016, 2015.

[97] W. Maneschg, "Review of neutrinoless double beta decay experiments: Present status and near future," *Nuclear and Particle Physics Proceedings*, vol. 260, pp. 188 – 193, 2015. The 13th International Workshop on Tau Lepton PhysicsThe 13th International Workshop on Tau Lepton Physics (Tau2014).

[98] G. Audi, O. Bersillon, J. Blachot, and A. Wapstra, "The Nubase evaluation of nuclear and decay properties," *Nucl.Phys.*, vol. A729, pp. 3–128, 2003.

[99] S. R. Elliott and P. Vogel, "Double beta decay," *Ann.Rev.Nucl.Part.Sci.*, vol. 52, pp. 115–151, 2002.

[100] I. Barabanov, S. Belogurov, L. B. Bezrukov, A. Denisov, V. Kornoukhov, *et al.*, "Cosmogenic activation of germanium and its reduction for low background experiments," *Nucl.Instrum.Meth.*, vol. B251, pp. 115–120, 2006.

[101] H. Gomez, S. Cebrian, J. Morales, and J. A. Villar, "Background reduction and sensitivity for germanium double beta decay experiments," *Astropart. Phys.*, vol. 28, pp. 435–447, 2007.

[102] I. Abt, A. Caldwell, K. Kroninger, J. Liu, X. Liu, and B. Majorovits, "Pulse shapes from electron and photon induced events in segmented high-purity germanium detectors," *Eur. Phys. J.*, vol. C52, pp. 19–27, 2007.

[103] C. E. Aalseth *et al.*, "Neutrinoless double-β decay of^{76}ge: First results from the international germanium experiment (igex) with six isotopically enriched detectors," *Phys. Rev. C*, vol. 59, pp. 2108–2113, Apr 1999.

[104] M. Gunther, J. Hellmig, G. Heusser, M. Hirsch, H. Klapdor-Kleingrothaus, *et al.*, "Heidelberg - Moscow beta-beta experiment with Ge-76: Full setup with five detectors," *Phys.Rev.*, vol. D55, pp. 54–67, 1997.

[105] C. Aalseth *et al.*, "The IGEX Ge-76 neutrinoless double beta decay experiment: Prospects for next generation experiments," *Phys.Rev.*, vol. D65, p. 092007, 2002.

[106] H. Klapdor-Kleingrothaus, I. Krivosheina, A. Dietz, and O. Chkvorets, "Search for neutrinoless double beta decay with enriched Ge-76 in Gran Sasso 1990-2003," *Phys.Lett.*, vol. B586, pp. 198–212, 2004.

[107] H. Klapdor-Kleingrothaus, A. Dietz, L. Baudis, G. Heusser, I. Krivosheina, *et al.*, "Latest results from the Heidelberg-Moscow double beta decay experiment," *Eur.Phys.J.*, vol. A12, pp. 147–154, 2001.

[108] I. Abt *et al.*, "The GERmanium Detector Array for the search of neutrinoless $\beta\beta$ decays of ^{76}Ge at LNGS," *Proposal to the LNGS*, no. P38/04, 2004.

[109] N. Abgrall *et al.*, "The Majorana Demonstrator Neutrinoless Double-Beta Decay Experiment," *Adv.High Energy Phys.*, vol. 2014, p. 365432, 2014.

[110] "Gerda setup view." `https://www.mpi-hd.mpg.de/gerda/physics.html`. Accessed: 2016-01-25.

[111] C. Cuesta *et al.*, "Status of the MAJORANA DEMONSTRATOR," *AIP Conf. Proc.*, vol. 1686, p. 020005, 2015.

[112] M. Barnabe Heider *et al.*, "Operation of a GERDA Phase I prototype detector in liquid argon and nitrogen," in *14th International School on Particles and Cosmology Baksan Valley, Russia, April 16-21, 2007*, 2007.

[113] M. Agostini *et al.*, "Production, characterization and operation of ^{76}Ge enriched BEGe detectors in GERDA," *Eur. Phys. J.*, vol. C75, no. 2, p. 39, 2015.

[114] I. Abt, A. Caldwell, D. Gutknecht, K. Kroninger, M. Lampert, X. Liu, B. Majorovits, D. Quirion, F. Stelzer, and P. Wendling, "Characterization of the first true coaxial 18-fold segmented n-type prototype detector for the GERDA project," *Nucl. Instrum. Meth.*, vol. A577, pp. 574–584, 2007.

[115] S. Schönert, "New techniques in $0\nu\beta\beta$ germanium experiments," *Nuclear Physics B - Proceedings Supplements*, vol. 221, pp. 244 – 247, 2011. The Proceedings of the 22nd International Conference on Neutrino Physics and Astrophysics The Proceedings of the 22nd International Conference on Neutrino Physics and Astrophysics.

[116] A. de Cosa, "LHC results for dark matter from ATLAS and CMS," in *12th Conference on the Intersections of Particle and Nuclear Physics (CIPANP 2015) Vail, Colorado, USA, May 19-24, 2015*, 2015.

[117] J. Ahrens *et al.*, "Icecube - the next generation neutrino telescope at the south pole," *Nucl.Phys.Proc.Suppl.*, vol. 118, pp. 388–395, 2003.

[118] S. Desai *et al.*, "Search for dark matter WIMPs using upward through-going muons in Super-Kamiokande," *Phys.Rev.*, vol. D70, p. 083523, 2004.

[119] M. Boezio *et al.*, "The PAMELA space experiment: First year of operation," *J.Phys.Conf.Ser.*, vol. 110, p. 062002, 2008.

[120] F. Palmonari, V. Bindi, A. Contin, N. Masi, and L. Quadrani, "Search for dark matter in cosmic rays with the AMS-02 space spectrometer," *J.Phys.Conf.Ser.*, vol. 335, p. 012066, 2011.

[121] S. Peirani, R. Mohayaee, and J. A. de Freitas Pacheco, "Indirect search for dark matter: Prospects for GLAST," *Phys.Rev.*, vol. D70, p. 043503, 2004.

[122] J. Albert *et al.*, "Observation of gamma-rays from the galactic center with the magic telescope," *Astrophys.J.*, vol. 638, pp. L101–L104, 2006.

[123] D. Hooper and E. A. Baltz, "Strategies for Determining the Nature of Dark Matter," *Ann.Rev.Nucl.Part.Sci.*, vol. 58, pp. 293–314, 2008.

[124] T. Saab, "An Introduction to Dark Matter Direct Detection Searches and Techniques," in *The Dark Secrets of the Terascale (TASI 2011) - Proceedings of the 2011 Theoretical Advanced Study Institute in Elementary Particle Physics. Edited by Matchev Konstantin et al. Published by World Scientific Publishing Co. Pte. Ltd., 2013. ISBN #9789814390163, pp. 711-738* (K. Matchev and et al., eds.), pp. 711–738, Dec. 2013.

[125] B. Sadoulet, "Dark matter searches," *Int. J. Mod. Phys.*, vol. A15S1, pp. 687–714, 2000. [,687(1999)].

[126] T. MarrodÃąn Undagoitia and L. Rauch, "Dark matter direct-detection experiments," *J. Phys.*, vol. G43, no. 1, p. 013001, 2016.

[127] K. Freese, M. Lisanti, and C. Savage, "Colloquium: Annual modulation of dark matter," *Rev.Mod.Phys.*, vol. 85, pp. 1561–1581, 2013.

[128] B. J. Kavanagh, "Discretising the velocity distribution for directional dark matter experiments," *JCAP*, vol. 1507, no. 07, p. 019, 2015.

[129] C. Aalseth *et al.*, "CoGeNT: A Search for Low-Mass Dark Matter using p-type Point Contact Germanium Detectors," *Phys.Rev.*, vol. D88, no. 1, p. 012002, 2013.

[130] C. Aalseth *et al.*, "Search for An Annual Modulation in Three Years of CoGeNT Dark Matter Detector Data," 2014.

[131] K.-J. Kang *et al.*, "Introduction to the CDEX experiment," *Front.Phys.China*, vol. 8, pp. 412–437, 2013.

[132] K.-J. Kang, Q. Yue, Y.-C. Wu, J.-P. Cheng, Y.-J. Li, *et al.*, "CDEX-1 1 kg point-contact germanium detector for low mass dark matter searches," *Chin.Phys.*, vol. C37, no. 12, p. 126002, 2013.

[133] Q. Yue *et al.*, "Limits on light WIMPs from the CDEX-1 experiment with a p-type point-contact germanium detector at the China Jingping Underground Laboratory," *Phys.Rev.*, vol. D90, no. 9, p. 091701, 2014.

[134] K. T. Naoto Nihei and T. M. Nakanishi, "Inspections of radiocesium concentration levels in rice from fukushima prefecture after the fukushima dai-ichi nuclear power plant accident," *Scientific Reports 5, Article number: 8653*, March 2015.

[135] P. Hubert, F. Perrot, J. Gaye, B. Mèdina, and M. Pravikoff, "Radioactivity measurements applied to the dating and authentication of old wines," *Comptes Rendus Physique*, vol. 10, no. 7, pp. 622 – 629, 2009. Physics and heritagePhysique et patrimoine.

[136] P. Hubert, M. Pravikoff, and J. Gaye, "Possibility of wine dating using the natural pb-210 radioactive isotope," *Journal of Environmental Radioactivity*, vol. 142, pp. 132 – 135, 2015.

[137] X. R. Liu and J. Mott, "Low background techniques for SuperNEMO," *J. Phys. Conf. Ser.*, vol. 598, no. 1, p. 012022, 2015.

[138] V. Álvarez *et al.*, "Radiopurity control in the NEXT-100 double beta decay experiment: procedures and initial measurements," *Journal of Instrumentation*, vol. 8, p. 1002, Jan. 2013.

[139] G. Saha, *Physics and Radiobiology of Nuclear Medicine*. Springer New York, 2010.

[140] W. R. Leo, *Techniques for Nuclear and Particle Physics Experiments*. Springer-Verlag, second ed., 1987.

[141] R. D. Evans, *The Atomic Nucleus*. McGraw-Hill, 1955.

[142] J. D. Jackson, *Classical electrodynamics*. Jhon Wiley & sons, second ed., 1975.

[143] K. A. Olive *et al.*, "Review of Particle Physics," *Chin. Phys.*, vol. C38, p. 090001, 2014.

[144] G. F. Knoll, *Radiation Detection and Meausurement*. John Wiley & sons, Inc, 1999.

[145] S. Irlbeck, *The GALATEA Test Facility and a First Study of α-induced Surface Events in a Germanium Detector*. Phd thesis, Ludwig-Maximilians-Universität, March 2014.

[146] K. Vetter *et al.*, "Performance of the {GRETA} prototype detectors," *Nuclear Instruments and Methods in Physics Research Section A: Accelerators, Spectrometers, Detectors and Associated Equipment*, vol. 452, no. 1âĂŞ2, pp. 105 – 114, 2000.

[147] I. Abt, M. F. Altmann, A. Caldwell, K. Kroninger, X. Liu, B. Majorovits, L. Pandola, and C. Tomei, "Background reduction in neutrinoless double beta decay experiments using segmented detectors: A Monte Carlo study for the GERDA setup," *Nucl. Instrum. Meth.*, vol. A570, pp. 479–486, 2007.

[148] U. Fano, "Ionization yield of radiations. ii. the fluctuations of the number of ions," *Phys. Rev.*, vol. 72, pp. 26–29, Jul 1947.

[149] Canberra Industries, Inc., *Extended Range Coaxial Germanium Detector (XtRa)*, 4 2010.

[150] Canberra Industries, Inc., *Reverse Electrode Coaxial Germanium Detector (REGe)*, 11 2013.

[151] I. Abt, A. Caldwell, D. Gutknecht, J. Janicsko-Csáthy, M. Lampert, D. Lenz, X. Liu, J. Liu, B. Majorovits, D. Quirion, J. Schubert, F. Stelzer, and P. Wendling, "Operation of an 18-fold segmented n-type hpge detector in liquid nitrogen," *Journal of Instrumentation*, vol. 4, no. 11, p. P11008, 2009.

[152] I. Abt, A. Caldwell, B. Dönmez, L. Garbini, S. Irlbeck, B. Majorovits, M. Palermo, O. Schulz, H. Seitz, and F. Stelzer, "The GALATEA Test-Facility for High Purity Germanium Detectors," *Nucl. Instrum. Meth.*, vol. A782, pp. 56–62, 2015.

[153] Abt, I., Caldwell, A., Liu, J., Majorovits, B., and Volynets, O., "Measurement of the temperature dependence of pulse lengths in an n-type germanium detector," *Eur. Phys. J. Appl. Phys.*, vol. 56, no. 1, p. 10104, 2011.

[154] I. Abt, A. Caldwell, J. Liu, B. Majorovits, P. Petrov, and O. Volynets, "Axes determination for segmented true-coaxial HPGe detectors," *Eur. Phys. J.*, vol. C72, p. 1950, 2012.

[155] I. Abt, A. Caldwell, K. Kroninger, J. Liu, X. Liu, and B. Majorovits, "Neutron interactions as seen by a segmented germanium detector," *Eur. Phys. J.*, vol. A36, pp. 139–149, 2008.

[156] Canberra Industries, Inc., *EGC 75*70TC SEG 18+1 GERDA 74066*, 4 2008.

[157] D. Lenz, *Pulse Shapes and Surface Effects in Segmented Germanium Detectors*. Phd thesis, Technische Universität München, March 2010.

[158] XIA, *4-Channel 75 MHz PXI Digital Spectrometer*, 2013.

[159] "Wavemetrics." `www.wavemetrics.com`. Accessed: 2015-02-20.

[160] A. Wiens *et al.*, "Improved energy resolution of highly segmented HPGe detectors by noise reduction," *Eur. Phys. J.*, vol. A49, p. 47, 2013.

[161] B. Bruyneel, P. Reiter, and G. Pascovici, "Characterization of large volume {HPGe} detectors. part i: Electron and hole mobility parameterization," *Nuclear Instruments and Methods in Physics Research Section A: Accelerators, Spectrometers, Detectors and Associated Equipment*, vol. 569, no. 3, pp. 764 – 773, 2006.

[162] M. Dimmock, A. Boston, J. Cresswell, I. Lazarus, P. Medina, P. Nolan, C. Parisel, C. Santos, J. Simpson, and C. Unsworth, "Validation of pulse shape simulations for an agata prototype detector," *Nuclear Science, IEEE Transactions on*, vol. 56, pp. 2415–2425, Aug 2009.

[163] "Tspectrum class." `http://root.cern.ch/root/htmldoc/TSpectrum.html`. Accessed: 2015-12-20.

[164] "Root data analysis framework." `http://root.cern.ch/drupal/`. Accessed: 2015-03-10.

[165] A. Inc., "X-ray detection glossary." `http://www.amptek.com/pdf/glossary.pdf`. Accessed: 2016-02-17.

[166] S. Hemmer, "Mirror pulses and position reconstruction in segmented hpge detectors," Master's thesis, Ludwig-Maximilians-UniversitÃďt, München, September 2010.

[167] M. Martini and T. McMath, "Trapping and detrapping effects in lithium-drifted germanium and silicon detectors," *Nuclear Instruments and Methods*, vol. 79, no. 2, pp. 259 – 276, 1970.

[168] T. W. Raudorf and R. H. Pehl, "Effect of charge carrier trapping on germanium coaxial detector line shapes," *Nuclear Instruments and Methods in Physics Research Section A: Accelerators, Spectrometers, Detectors and Associated Equipment*, vol. 255, no. 3, pp. 538 – 551, 1987.

[169] W. Hansen, "High-purity germanium crystal growing," *Nuclear Instruments and Methods*, vol. 94, no. 2, pp. 377 – 380, 1971.

[170] R. Hall and T. Soltys, "High purity germanium for detector fabrication," *Nuclear Science, IEEE Transactions on*, vol. 18, pp. 160–165, Feb 1971.

[171] F. S. Goulding and R. H. Pehl, "A survey of radiation damage in semiconductor detectors," *Nuclear Science, IEEE Transactions on*, vol. 19, pp. 91–99, Feb 1972.

[172] N. Gray, Theodore W.Mann, *The elements :a visual exploration of every known atom in the universe*. Black Dog & Leventhal Publishers, 2009.

[173] R. for the radioactive sources at the MPI for Physics Munich. personal communication, 2015.

[174] M. Descovich, P. Nolan, A. Boston, J. Dobson, S. Gros, J. Cresswell, J. Simpson, I. Lazarus, P. Regan, J. Valiente-Dobon, P. Sellin, and C. Pearson, "The position response of a large-volume segmented germanium detector," *Nuclear Instruments and Methods in Physics*

Research Section A: Accelerators, Spectrometers, Detectors and Associated Equipment, vol. 553, no. 3, pp. 512 – 521, 2005.

[175] F. CANBERRA. private communication, 2015.

[176] C. G. d. K. H. A. M. G. Vaessen, "Sodium and potassium assay of foods and biological substrates by atomic absorption spectroscopy," *Pure Applied Chemistry*, vol. 61, pp. 113–120, 1989.

[177] K. Emumejaye, "Determination of ^{40}K concentration in some pwdered milk samples consumed in delta state, nigeria," *IOSR Journal of Applied Physics (IOSR-JAP)*, vol. 2, pp. 08–12, 2012.

[178] B. Hoeling, D. Reed and P. B. Siegele, "Going bananas in the radiation laboratory," *American Association of Physics Teachers*, 1999.

[179] E. E. no Juàrez and H. Vega-Carrillo, "^{40}K measurement to determine the total potassium content," *Revista Mexicana de Fisica*, vol. 58, pp. 211–214, 2012.

[180] M. P.-A. G. F. Acquaha, "Foodstuffs and cancer: Analysis of radionuclides and its radiation levels in common ghanaian maize," *International Journal of Sciences: Basic and Applied Research (IJSBAR)*, vol. 58, pp. 211–214, 2012.

[181] F. Abbasisiar, "Determination of ^{40}K concentration in milk samples consumed in tehran-iran and estimation of its annual effective dose," *IAEA, INI*, 2006.

[182] ORTEC, "Food monitoring notes," April 2011.

[183] "Potassium isotopes." `www.chemicalelements.com/elements/k.html`. Accessed: 2015-04-12.

[184] PanReac AppliChem, *Potassium Chloride*, 2014.

[185] M. Shuster, "Analysis of potassium induced radioactivity in chocolates based on γ spectra taken with high purity germanium detectors," bachelor thesis, Technische UniversitÃďt München, August 2014.

[186] United State Department of Agriculture, *National Nutrient Database for standard Reference*, December 2013.

[187] World health Organization, *Potassium intake for adults and children*, 2012.

[188] G. W. Phillips and K. W. Marlow, "Automatic analysis of gamma-ray spectra from germanium detectors," *Nuclear Instruments and Methods*, vol. 137, no. 3, pp. 525 – 536, 1976.

[189] L. McNelles and J. Campbell, "Analytic approximations to peak shapes produced by ge(li) and si(li) spectrometers," *Nuclear Instruments and Methods*, vol. 127, no. 1, pp. 73 – 81, 1975.

[190] E. international, *ECMA Script 2015 Language Specificatoin*. Standard ECMA-262, 6 ed., June 2015.

Thank you!

Finally I got to this page! The very last one! The one that makes you feel lighter! Without some really special people I would have never been able to reach it!

I would like to thank my official supervisor Prof. Dr. Jochen Schieck for his willingness to supervise this thesis. I want to express my deepest gratitude to my advisor Dr. Iris Abt, for her infinite support and her guidance in my work and in my life. Thank you for all the red pens you used to correct my thesis. A special thanks goes to PD Dr. Bela Majorovits for his helpful comments and his willingness to give us the honor to answer to interesting and sometimes nasty questions during our coffee breaks. I want to thank all the members of the group (past and present): Sabine I., Burcin D., Xiang L., Martin S., Lukas H., Heng-Ye L., Raphael K., Dimitris P., Oliver S., Chris G., Hans Z., Laura V., Fabiana C., Christopher O., Matteo P., Neslihan B. and Oleksander V.. Everybody in a way or another helped me to go through these long, intense and sometimes not easy years. A very heartfelt thanks goes to the best office mate ever: Sabine. Thank you for your suggestions, for your help but most of all thank you for your friendship! A special thanks goes to Hans and Chris. You have been always there whenever I would need you, as two precious angels. Your made the difference! A huge "thank you" goes also to Xiang for all his help. Your sincere willingness to learn from anyone and your humility makes you a special physicist (not many of us have them).

I want to thank several people that made my life in these years here in Munich nicer: Luca, Ettore, Jacky, Elisa C., Sonja, Elisa F., Michele and fagiolina.

Words (especially in my English) cannot express how grateful I am to my family. È quindi il momento di passare all'italiano. Senza l'incondizionato e infinito supporto da parte di mia madre Sonia e mio padre Danilo non sarei arrivata dove sono. Mi avete insegnato a tenere duro e a lavorare caparbiamente. Avete creduto sempre nelle mie capacità anche quando io per prima non lo ho fatto. Siete sempre con me! Un grazie speciale va alla mia gemella Elena. Che ha fatto e farà sempre il tifo per me. Tu mi hai sempre spronato a seguire i miei sogni anche se ci hanno tenuto lontane. Non immagini nemmeno la forza che mi dai. Il tuo sostegno è per me essenziale! Tutta la mia intera e grande famiglia (annessi e connessi, ternani e tuderti) mi è stata vicina e mi ha mostrato un sostegno senza pari soprattutto in un periodo difficile come quello di circa un anno fa. Ve ne sarò grata per sempre. E sarò sempre grata anche a Maria Stefania che mi ha re-insegnato ad avere il controllo del movimento: mi hai permesso di credere di nuovo nella possibilità di vivere senza dolore. GRAZIE!

Sono sicura che il Pacchetto Fisici mi concederà l'onore di canticchiare e leggermente modificare un motivetto a noi tutti estremamente caro: "Un dottorato così non è mica da tutti.... chi non è del pacchetto non lo prende". Le nostre strade ci hanno sparso in tutta Europa (e in America ultimamente). Ma il pacchetto ci sarà sempre e comunque. Nei momenti di difficoltà mi

sono immaginata al centro di un nostro abbraccio saltato! E quello si che aiutava! Grazie anche a voi!

Il GRAZIE più grande di tutti va alla persona che amo e che mi è stata più vicina in assoluto: Simone. GRAZIE perché in ogni singola pagina di questa tesi c'è anche un po' del tuo! GRAZIE perché Tu hai asciugato tante lacrime, ma hai fatto spuntare anche altrettanti sorrisi. GRAZIE perché Tu sei stato IL compagno di viaggio che tutti vorrebbero al loro fianco in un periodo così. GRAZIE perché hai condiviso con me questa difficile ma bellissima esperienza non solo di lavoro ma soprattutto di vita. GRAZIE perché hai scelto di condividerne anche di future :). Non vedo l'ora di viverle insieme!!